

Searching for new physics using the ATLAS and FASER detectors

THÈSE

présentée à la Faculté des sciences de l'Université de Genève
pour obtenir le grade de Docteur ès sciences, mention physique

par

Ondřej Theiner

de České Budějovice (Tchéquie)

Thèse N° 5854





**UNIVERSITÉ
DE GENÈVE**

FACULTÉ DES SCIENCES

DOCTORAT ÈS SCIENCES, MENTION PHYSIQUE

Thèse de Monsieur Ondrej THEINER

intitulée :

«Searching for new physics using the ATLAS and FASER detectors»

La Faculté des sciences, sur le préavis de

Madame A. SFYRLA, professeure associée et directrice de thèse
Département de physique nucléaire et corpusculaire

Monsieur T. GOLLING, professeur associé
Département de physique nucléaire et corpusculaire

Monsieur J. BOYD, docteur
Physics department, CERN, Genève

autorise l'impression de la présente thèse, sans exprimer d'opinion sur les propositions qui y sont énoncées.

Genève, le 1^{er} novembre 2024

Thèse - 5854 -



La Doyenne



Resumé

Certaines observations cosmologiques et données issues d'expériences de physique des particules suggèrent que le modèle standard de la physique des particules n'est pas une théorie complète. Des phénomènes tels que la matière noire, l'énergie noire et l'asymétrie matière-antimatière pourraient s'expliquer par l'existence de nouvelles particules plus lourdes que le quark top, la particule élémentaire connue la plus lourde, ou par des particules qui n'interagissent pas directement avec la matière ordinaire de l'univers et sont donc invisibles. La supersymétrie (SUSY) est une extension du modèle standard qui pourrait expliquer certains de ces phénomènes en introduisant une nouvelle symétrie entre les bosons et les fermions et en ajoutant de nouvelles particules à celles décrites par le modèle standard. Cependant, SUSY n'est pas la seule théorie viable. Il existe toute une nouvelle classe de particules hypothétiques beaucoup plus légères, avec des masses de l'ordre du MeV au GeV, qui pourraient produire de la matière noire avec la bonne densité relique. Au cours des dernières décennies, des recherches de nouvelle physique ont été menées à la frontière de l'énergie du TeV.

Les expériences ATLAS et FASER au Grand collisionneur de hadrons (LHC) du CERN recherchent de la nouvelle physique potentiellement générée par des collisions proton-proton à une énergie de centre de masse de 13-14 TeV, en utilisant deux approches différentes. ATLAS se concentre sur les régions où le moment transverse des produits de collision est élevé dans la zone centrale du détecteur. En revanche, l'expérience FASER, située à 480 mètres du point de collision d'ATLAS, recherche des particules à longue durée de vie et à faible interaction produites dans la direction très avant.

Cette thèse est divisée en trois parties principales. La première partie présente une introduction au domaine difficile de la physique des collisionneurs, en mettant l'accent sur la recherche de nouvelle physique. La deuxième partie se concentre sur l'expérience ATLAS. La troisième partie concerne l'expérience FASER.

Le détecteur ATLAS enregistre les données des collisions proton-proton à une fréquence d'environ 40 MHz, ce qui rend crucial un système de déclenchement et d'acquisition de données efficace pour un fonctionnement et des performances physiques optimales. Cette efficacité est vitale pour la sensibilité aux processus susceptibles d'indiquer une nouvelle physique. Cette partie détaille l'optimisation de l'algorithme d'extrapolation des traces utilisé pour la reconstruction des jets de Particle Flow au High-Level Trigger et explore les recherches de nouvelle physique. Elle introduit la recherche de la production de paires de higgsinos se désintégrant dans un état final avec plusieurs quarks b et un moment transverse manquant. En outre, elle présente de nouveaux résultats issus de la réinterprétation de cette recherche dans le contexte d'autres modèles intrigants de nouvelle physique : l'un lié à la supersymétrie et l'autre à une extension du secteur sombre du modèle standard.

La partie de la thèse consacrée à l'expérience FASER décrit le développement du système de déclenchement et d'acquisition de données du détecteur, suivi de la mise en service et des activités opérationnelles de l'expérience.



Abstract

Some cosmological observations and data from particle physics experiments suggest that the Standard Model (SM) of particle physics is not a complete theory. Phenomena such as dark matter, dark energy, and the matter-antimatter asymmetry could be explained by the existence of new particles that are heavier than the top quark, the heaviest known elementary particle, or by particles that do not directly interact with ordinary matter in the Universe and are therefore invisible. Supersymmetry (SUSY) is one extension of the Standard Model that could explain some of these phenomena by introducing a new symmetry between bosons and fermions and adding new particles to those described by the Standard Model. However, SUSY is not the only viable theory. There is a whole new class of hypothetical particles that are much lighter, with masses in the MeV to GeV range, which could produce dark matter with the correct relic density. In recent decades, searches for new physics have been conducted at the TeV energy frontier.

The ATLAS and FASER experiments at the CERN Large Hadron Collider (LHC) search for new physics potentially generated by proton-proton collisions at a center-of-mass energy of 13–14 TeV, employing two different approaches. ATLAS focuses on regions with high transverse momentum of collision products in the central area of the detector. In contrast, the FASER experiment, located 480 meters from the ATLAS collision point, searches for long-lived, weakly interacting particles produced in the very forward direction.

This thesis is divided into three main parts. The first part provides an introduction to the challenging field of collider physics with an emphasis on searches for new physics. The second part is focused on the ATLAS experiment. The third part concerns the FASER experiment.

The ATLAS detector records proton-proton collision data at approximately 40 MHz, making an efficient trigger and data acquisition system crucial for optimal operation and physics performance. This efficiency is vital for the sensitivity to processes that may indicate new physics. This part details the optimization

of the track extrapolation algorithm used for Particle Flow jet reconstruction at the High-Level Trigger and explores searches for new physics. It introduces the search for the pair production of higgsinos decaying into a final state with multiple b -quarks and missing transverse momentum. Additionally, it presents new results from the reinterpretation of this search in the context of other intriguing new physics models: one related to supersymmetry and another to a dark sector extension of the Standard Model.

The part of the thesis dedicated to the FASER experiment describes the development of the detector's trigger and data acquisition system, followed by the subsequent commissioning and operational activities of the experiment.



Acknowledgements

At this page, I would like to thank to several people who were important to me during these years of my doctoral studies. It is hard to mention everybody, I will try to do my best not to forget anybody.

First of all, I would like to express my utmost thanks to my supervisor, professor Anna Sfyrla. Her guidance has been essential during past five years on the journey through my Ph.D. studies, as well as and her feedback to this thesis.

I would also like to thank to postdocs who I worked with for their patience and willingness to explain me things when I needed it and invaluable help when I was battling through debug logs and error messages from any piece of software I worked with. Namely to Claire Antel, Pantelis Kontaxakis, Carlos Moreno, Chiara Rizzi, Marco Valente, Michael Hank - you all were important at different stages during these years I worked on FASER and ATLAS.

I also shouldn't forget about other Ph.D. students from our group with whom I shared office (and biscuits by our coffee machine). Thank you Kostas Axiotis, Lucas Bezio, Stefano Franchellucci, and Noshin Tarannum. I would also like to mention Tim Bruckler from the Oxford group, the other doctoral student who I worked with on the analysis and reinterpretations and with whom I could discuss about struggles with the analysis and talk about happy moments from the mountains.

I would, as well, like to thank to my colleagues from ATLAS and FASER who I got chance to work with and who helped me to solve numerous problems I came across.

Those who know me personally know, that when I am not in the office, I am probably in the mountains and I would like to express my gratitude to friends who I could share with (not only) my running, climbing and mountain adventures. The list is long and it is impossible to mention all but one of the most memorable adventures and discussions were with you Adri, Barča, Brch, Camille, Florian, "big" Florian, Georgiana, Giulietta, Hannes, Jana, Katrina,

Kibrom, Meg, Michal, Ronja, Yulia and Radim (the best Bro in this Universe). Also, I would like to apologize that I wasn't very active during the last months of writing of this thesis, but I promise, I will be back and I am already making plans while I am writing these lines.

Finally, the enormous thank you goes to my mum and dad who supports me in everything I do.



Contents

Introduction	2
Personal contributions	4
1 Standard Model	6
1.1 Introduction	6
1.2 Lagrangian of the Standard Model	6
1.3 Particle content of the Standard Model	8
1.3.1 Fermions	8
Leptons	9
Quarks	10
1.3.2 Bosons	11
Higgs mechanism	11
1.4 Shortcomings	13
2 Supersymmetry and other BSM theories	16
2.1 Introduction	16
2.2 Minimal Supersymmetric Standard Model	16
2.2.1 R-parity	19
2.2.2 Soft supersymmetry breaking	19
2.3 Selected beyond-Standard-Model theories	20
2.3.1 Dark photon	20
2.3.2 Axion-like particles	20
2.3.3 Heavy neutral leptons	21
3 Large Hadron Collider	22
3.1 Introduction	22
3.2 Source of particles	23
3.3 Acceleration	24

3.4	Beam bending and focusing	26
3.5	Collision	26
3.6	Large experiments	28
3.7	Smaller experiments	28
I	ATLAS	29
4	ATLAS Detector	30
4.1	Introduction	30
4.2	Coordinate system and commonly used variables	31
4.3	Inner Detector	33
4.4	Calorimeter	35
4.5	Magnets	36
4.6	Muon Spectrometer	38
4.7	Trigger and Data Acquisition System	40
5	Event reconstruction	44
5.1	Introduction	44
5.2	Track and vertex reconstruction	45
5.3	Topological clusters reconstruction	47
5.4	Particle Flow	48
5.4.1	Track selection	50
5.4.2	Matching tracks to topo-clusters	50
5.4.3	Energy subtraction	51
5.4.4	Remnant removal	52
5.4.5	Particle Flow jet building	52
5.5	Jet reconstruction	53
5.5.1	Jet building algorithms	53
5.5.2	Jet calibration	54
5.5.3	Jet-flavor tagging	56
5.6	Lepton and photon reconstruction	58
5.6.1	Electron and photon reconstruction	58
5.6.2	Muon reconstruction	59
5.6.3	Tau lepton reconstruction	60
5.7	Missing Transverse Momentum	60
6	Track extrapolation and its optimization for the HLT PFlow jet reconstruction	64
6.1	Introduction	64
6.2	Charged particle in magnetic field	65
6.3	Runge-Kutta methods	66
6.4	STEP algorithm	68
6.5	Track extrapolation optimization for the HLT	69
6.5.1	Tolerance τ	71
6.5.2	Material effects	75

6.5.3	Fast magnetic field	75
6.5.4	Momentum cut-off	75
6.5.5	The final parameter choice	77
6.6	Validation of the optimization	77
7	Statistical methods and data interpretation	82
7.1	Introduction	82
7.2	Probability density function	82
7.3	Estimation of parameters of physics model	83
7.4	Hypothesis testing	85
7.4.1	Discovery or exclusion	86
7.5	How to search for SUSY?	88
8	Search for the higgsino pair production	92
8.1	Introduction	92
8.2	Signal model	93
8.3	High-mass channel	93
8.3.1	Event selection	94
8.3.2	Background processes	96
8.3.3	Analysis regions definition	98
8.4	Low-mass channel	100
8.4.1	Analysis regions	100
8.4.2	Background processes	101
8.5	Systematic uncertainties	102
8.6	Results	103
9	Reinterpretation of the higgsino pair production analysis	106
9.1	Introduction	106
9.2	Heavy and light neutralino model	107
9.2.1	Signal model	107
9.2.2	Results	108
9.3	Dark-Higgs model	114
9.3.1	Signal model	114
9.3.2	Results	115
10	Analysis preservation	120
10.1	Introduction	120
10.2	RECAST	121
10.3	REANA	123
10.4	RECAST implementation of the Higgsino search	123
10.4.1	High-mass channel	124
	Ntuples production	125
	Merging	125
	Statistical fit	126
10.4.2	Low-mass channel	126
	Ntuples production	128

Skimming	128
Merging	128
Preparation of JSON workspaces	128
Statistical fit	129
10.4.3 Drawbacks for the dark-Higgs, and heavy and light neutralino models	129
11 Conclusion and outlook	132
II FASER	135
12 FASER Detector	136
12.1 Introduction	136
12.2 Physics motivation	136
12.3 Experiment location	137
12.4 Magnets	140
12.5 Scintillator system	140
12.6 Tracker	141
12.7 Calorimeter	142
12.8 FASER ν	143
13 Trigger and data acquisition system	146
13.1 Introduction	146
13.2 Design	147
13.3 DAQ software	148
13.4 GPIO boards	149
13.4.1 Communication protocol	150
13.4.2 Trigger Logic Board	151
13.4.3 Tracker Readout Board	152
13.5 Data readout error-detecting mechanisms	152
13.5.1 Cyclic redundancy check	153
13.5.2 Fletcher's checksum	154
13.5.3 Modified Fletcher's checksum used in FASER	155
13.6 Tests of communication with GPIO boards	156
14 Commissioning and detector operations	158
14.1 Introduction	158
14.2 Calorimeter commissioning	158
14.3 Silicon tracker commissioning	159
14.3.1 Threshold scan	161
14.3.2 Electronic tests and calibration procedure	162
14.4 TDAQ commissioning	164
14.4.1 Standalone tests	164
14.4.2 Combined measurements	166
14.5 Commissioning of the full detector	167

14.5.1	Commissioning with cosmic rays	168
14.5.2	Commissioning during the LHC pilot beam	168
14.6	Detector conditions monitoring	169
15	Conclusion and outlook	172
	Summary	174
	Appendix	176
A.1	ATLAS jet trigger naming convention	176
A.2	Interpolating in exclusion plots	177
A.3	RECAST workflow	181
A.4	TLB and TRB data format specifications	183
A.4.1	TRB data	183
A.4.2	TLB data	183
	List of Acronyms	186
	Bibliography	190



Introduction

The curiosity and desire to understand the world around us has been in human nature since thousands years ago, and sometimes, the explanation of a single phenomenon can lead to new theories and bring many new unanswered questions. Physics at the end of the 19th century seemed almost complete and could explain most of the phenomena people observed. In 1900, Lord Kelvin gave his lecture called "Nineteenth-century clouds over the dynamical theory of heat and light" [1], where he addressed two problems that he identified in physics of that time. He said:

"The beauty and clearness of the dynamical theory, which asserts heat and light to be modes of motion, is at present obscured by two clouds. I. The first came into existence with the undulatory theory of light and was dealt with by Fresnel and Dr. Thomas Young; it involved the question, How could the earth move through an elastic solid, such as essentially is the luminiferous ether? II. The second is the Maxwell-Boltzmann doctrine regarding the partition of energy."

While the first cloud was related to the relative motion of aether with respect to massive objects, which was resolved by denying the idea of aether and introducing the special theory of relativity, the second cloud referred to discrepancies in the explanation of specific heat capacity that could not be fully explained using equipartition theorem. The formulation of quantum mechanics resolved the second problem. However, with these theories, many new questions emerged, and they led to the invention of new theories. The Theory of General Relativity and the Standard Model of Particle physics are the most remarkable.

However, these theories give us excellent tools to better understand the Universe around us, and their results directly or indirectly lead to some of the greatest inventions in human history; they theories are not complete. An example is the inability of the Standard Model to include gravity in its description and to describe the Universe on large scales, while the Theory of General Rela-

tivity does not have predictive power at small scales. Some other problems are the unknown nature of dark matter and dark energy or the asymmetry between matter and anti-matter in our Universe. These issues lead to attempts to search for new physics that could explain these phenomena. An example of these theories are Supersymmetry, or extensions of the Standard Model assuming new particles, such as axion-like particles or dark photons, that would be able to address some of these problems.

The experiments ATLAS and FASER are two detectors at CERN that focus on searches of physics beyond the Standard Model. The ATLAS experiment is the largest experiment at the LHC, which contributed to the discovery of the Higgs boson in 2012 - the last big missing puzzle piece in the Standard Model and the FASER experiment is a small experiment built recently, which started taking data in 2022.

This thesis focuses on searches for physics beyond the Standard Model in ATLAS and FASER, each of which has its dedicated part. Each of these parts includes overview chapters for the introduction to the topic and chapters documenting the work of the author, which is always stated in the chapter's introduction.

Part I is focused on the ATLAS experiment, and in chapters 4 to 11 it describes the experiment, event reconstruction techniques, and optimization of the track extrapolation for the ATLAS High-Level Trigger Particle Flow jet reconstruction where one of the author's contributions lies. These chapters are followed by the chapter describing the search for higgsino pair production in the final state with multiple b -jets and missing transverse momentum. This search was then used by the author of the thesis as a base for the reinterpretation using the dark-Higgs model and the model with heavy and light neutralinos. The last chapter in part I is dedicated to the higgsino analysis preservation using RECAST, which was the author's main contribution to the search for higgsino pair production.

Part II is dedicated to the FASER experiment and, in chapters 12 to 15, it describes the detector, its TDAQ system, and the commissioning of the detector. It also briefly summarizes the first results of the experiment. The author's main contribution was to the development of the FASER TDAQ system and detector commissioning.

Unless stated otherwise, the thesis uses a natural system of units, where the speed of light in vacuum, the vacuum permittivity, and the reduced Planck constant are equal to 1, i.e., $c = \varepsilon_0 = \hbar = 1$.



Personal contributions

Particle physics studies the tiniest elementary particles that constitute matter to help understand the Universe on the largest scale. This is only possible thanks to thousands of physicists in many collaborations across the world. The author of this thesis has been working in two of these collaborations - ATLAS and FASER. Despite the sizes of these two collaborations being very different (ATLAS has about 5000 members, and FASER has about 100 members), they are only possible with the collaborative effort of all members who contribute through their work. That is why it is often challenging to pinpoint the main contributors to a given topic, as it is often based on other people's work. This section lists the main contributions of the author of this thesis to the ATLAS and FASER experiments .

ATLAS

The author was involved in the activities of the Jet Trigger Signature group. The main contribution consisted of the optimization of the track extrapolation for Particle Flow jet reconstruction for the High-Level Trigger, which was one of the bottlenecks blocking the Particle Flow jet reconstruction from being deployed at the High-Level Trigger due to the high CPU costs. Optimization of this step allowed us to save computing time and use the Particle Flow jet reconstruction online for triggering. During this work, several new monitoring metrics were introduced into the Athena reconstruction software to evaluate the extrapolation's performance. The author also validated the optimized version of the algorithm. This is described in detail in chapter 6. In addition to the abovementioned, the author was also involved in studies done by the Jet Trigger Signature group which are not part of this thesis, such as estimating gains for Particle Flow calo-based preselection chains.

Well-performing triggers are essential for the data recorded by the ATLAS

experiment and are used in physics analyses, such as searches for new physics. The author joined one of these searches, which was a search for higgsinos, where he helped to perform studies towards the final stage of the analysis and, most importantly, he did the RECAST implementation of this analysis, which is a crucial task that allows preserving the analysis workflow for the future use. This is described in chapter 9.

He also did the reinterpretation of the higgsino analysis using two other beyond Standard Model signal processes with the same final state, which allowed to set constraints on parameters of these signal processes. This is documented in chapter 9 dedicated to reinterpretations.

FASER

The author contributed to the FASER experiment mainly during the first year and a half of his Ph.D. studies.

The author contributed to the development of the FASER Trigger and Data Acquisition system, namely the development of drivers for the Trigger Logic Board and the Tracker Readout Board and by strain and reliability testing of the communication of these boards with the rest of the Trigger and Data Acquisition system, which is described in chapter 13.

The author was also involved in the detector's commissioning and installation. That included commissioning the detector's tracker system at ENH1 at CERN using cosmic muons, being one of the shifters during the first FASER test beam, which was used for commissioning of calorimeter modules, and participated in the detector cable installation inside the tunnel TI12. Finally, the author took part in the detector operations as one of the tracker shifters and run managers. He also developed software to automate presentation preparation for weekly reports, which most monitoring shifters have been using since the beginning of detector operations for its convenience and ability to save time when creating these reports. Operational aspects are discussed in chapter 14.

Standard Model

1.1 Introduction

The *Standard Model* (SM) is the theory describing all known elementary particles and the interaction between these particles through three fundamental forces - electromagnetic, weak, and strong. Gravity, the fourth fundamental interaction, is the only interaction not incorporated into the SM and is described by *general relativity*. The SM is a quantum field theory, the framework combining special relativity and quantum mechanics. It describes elementary particles as the quantization of fields spreading across the Universe. The interactions between different particles then arise due to symmetries of the Lagrangian describing the theory.

The Standard Model is described in terms of non-abelian Yang-Mills theory based on the invariance under $SU(3) \otimes SU(2) \otimes U(1)$ transformations. These symmetries can then be attributed to different parts of the SM. The $SU(3)$ symmetry can be attributed to *quantum chromodynamic*, which is the theory describing the strong interaction, and the $SU(2) \otimes U(1)$ symmetry is the part responsible for the *electroweak interaction*, which is the unification of the electromagnetic and weak interactions.

This chapter serves as a brief overview of the Standard Model, which forms the foundation of modern particle physics. The Lagrangian of the SM is briefly discussed in section 1.2, and particles included in the SM described by this Lagrangian are described in section 1.3. Section 1.4 lists some of the limitations of the SM and motivates the need for new theories that are discussed in the chapter 2.

1.2 Lagrangian of the Standard Model

The Lagrangian of the SM can be written as

$$\mathcal{L}_{SM} = -\frac{1}{4}F_{\mu\nu}F^{\mu\nu} + i\bar{\psi}\gamma^\mu D_\mu\psi + h.c. + \psi_i y_{ij} \psi_j \phi + h.c. + |D_\mu\phi|^2 - V(\phi). \quad (1.1)$$

This prescription uses several shorthand notations, putting the otherwise long formula into a nice, concise form. A detailed description of the Lagrangian is not the purpose of this text. However, it quickly discusses individual terms and their meaning.

- **Term** $-\frac{1}{4}\mathbf{F}_{\mu\nu}\mathbf{F}^{\mu\nu}$ in the Lagrangian contains the contraction of the field-strength tensor $F_{\mu\nu}$, is the kinetic term describing interactions between gauge bosons in the SM.
- **Terms** $i\bar{\psi}\gamma^\mu\mathbf{D}_\mu\psi + h.c.$ describe interactions of gauge bosons with fermions. Fermions are represented by their field ψ , and gauge bosons enter the equation in the form of the covariant derivative D_μ , which is the operator of the derivative that preserves the gauge transformation invariance of the Lagrangian, and γ^μ are the gamma matrices¹. The *h.c.* signifies Hermitian conjugate of the second term.

Before describing other terms of the Lagrangian, let's make a short remark about the covariant derivative. The covariant derivative is introduced in order to preserve invariance of the Lagrangian under the gauge transformations. The 'classical' derivative yields extra terms which modify the Lagrangian, and the covariant derivative is a modified operator of a derivative which help to cancel out these terms. The covariant derivative in the SM which is invariant under $SU(3) \otimes SU(2) \otimes U(1)$ transformation has form

$$D_\mu \equiv \partial_\mu - ig'YB_\mu - i\frac{g}{2}\sigma_j W_\mu^j - i\frac{g_s}{2}\lambda_\alpha G_\mu^\alpha. \quad (1.2)$$

Here g' , g , g_s are coupling constants associated to $U(1)$, $SU(2)$, $SU(3)$ groups, Y is the weak hypercharge associated to the $U(1)$ group, σ_j are generators of the $SU(2)$ group called *Pauli matrices*, and λ_a are generators of the $SU(3)$ group called *Gell-Mann matrices*. G_μ^α correspond to gauge boson fields called *gluons*. B_μ and W_μ^j are $U(1)$ and $SU(2)$ gauge fields which mix together and give rise to the SM gauge bosons Z , W^\pm and photon. It is also good to note that gauge invariance implies that the fields

¹Gamma matrices are a set of matrices $\{\gamma^0, \gamma^1, \gamma^2, \gamma^3\}$ satisfying anticommutation relations

$$\{\gamma^\mu, \gamma^\nu\} = 2\eta^{\mu\nu}I_4,$$

where $\eta^{\mu\nu}$ is the Minkowski metric with signature $(+---)$, and I_4 is 4×4 identity matrix. Covariant matrices γ_μ are defined by the contraction

$$\gamma_\mu = \eta_{\mu\nu}\gamma^\nu$$

B_μ , W_μ^j are massless and they acquire mass only after the introduction of the Higgs mechanism which is described in section 1.3.2.

- **Terms $\psi_i y_{ij} \psi_j \phi + \text{h.c.}$** describe Yukawa interaction of fermions with the Higgs field ϕ , which is responsible for the mass of the fermions. The term y_{ij} are the elements of the Yukawa matrix that describe coupling parameters of fermions to the Higgs field. The fifth term is the Hermitian conjugate of the fourth term and describes the interaction of the Higgs field and anti-fermions.
- **Term $|\mathbf{D}_\mu \phi|^2$** describes the interaction of gauge bosons with the Higgs field. This interaction is introduced to the equation through the covariant derivative D_μ .
- **Term $-\mathbf{V}(\phi)$** describes the potential of the Higgs field.

As we mentioned in the description of individual terms, these terms describe interaction of the SM particles through fundamental forces². The following section discusses different types of these particles included in the SM.

1.3 Particle content of the Standard Model

Elementary particles in the SM can be divided into two groups based on their *spin*, which is an intrinsic form of angular momentum carried by a particle. These groups are *fermions* and *bosons*, and they are discussed in the following subsections. The classification of particles in the SM is depicted schematically in figure 1.1.

1.3.1 Fermions

Fermions are particles of a half-integer spin and are the building blocks of matter. They are forming three generations, which is a division by their *flavor* quantum number and mass, but their strong and electric interactions are the same. Each of these generations then contains two types of *leptons* and two types of *quarks*. In addition to fermions shown in figure 1.1, each particle has a corresponding antiparticle with the same mass but opposite quantum numbers. That means that there are, in total, 24 different elementary fermions: six quarks, six leptons, and their antiparticles.

The SM fermions, with the exception of neutrinos, are believed to be *Dirac fermions*, which means that these fermions are different from their antiparticles. Contrary to Dirac fermions, there are *Majorana fermions*, their antiparticles. Until now, it has not been clear if neutrinos are Dirac or Majorana fermions.

²Excluding gravity.

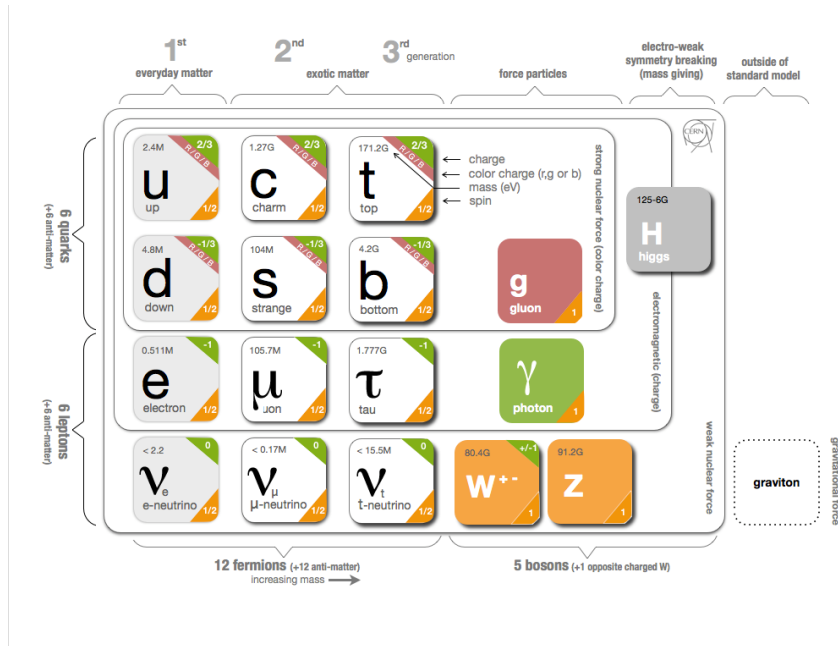


Figure 1.1: Particle content of the Standard Model. Graviton is the hypothetical particle mediating gravitational interaction and is not part of the SM. Despite attempts to include gravity in the Standard Model, none have succeeded. Figure taken from the reference [2].

Leptons

Leptons occur in nature in three different *flavors*, and they interact through electromagnetic and weak (electroweak) interactions. These flavors are ordered according to their mass, with the electron being the lightest and tau the heaviest. The leptons can be subdivided into electrically charged leptons and neutrinos with zero electric charge.

In nature, we observe three different types of charged leptons, each with its corresponding positively charged antiparticle: the electron, muon, and tau. Each of these charged leptons has a corresponding neutrino type, which is charged only under the weak interaction.

Neutrinos exist only in left-chiral states, while anti-neutrinos only exist in the right-chiral states. Their masses are very low compared to other particles, but experiments show they are non-zero. The peculiar property of neutrinos is that their mass eigenstates do not correspond to the flavor eigenstates (e, μ, τ), which leads to the phenomenon called *neutrino oscillations*. This phenomenon causes the freely propagating neutrinos to oscillate between the three flavors, and this phenomenon is described by means of the Pontecorvo–Maki–Nakagawa–Sakata (PMNS) matrix.

If we label the mass eigenstates by ν_i , where $i = 1, 2, 3$ and flavour eigenstates by ν_α , where $\alpha = e, \mu, \tau$, the PMNS matrix $U_{\alpha i}$ describes the transition between mass and flavour eigenstates. This can be expressed mathematically as

$$\begin{pmatrix} \nu_e \\ \nu_\mu \\ \nu_\tau \end{pmatrix} = \begin{bmatrix} U_{e1} & U_{e2} & U_{e3} \\ U_{\mu1} & U_{\mu2} & U_{\mu3} \\ U_{\tau1} & U_{\tau2} & U_{\tau3} \end{bmatrix} \begin{pmatrix} \nu_1 \\ \nu_2 \\ \nu_3 \end{pmatrix}, \quad (1.3)$$

and it means that the neutrino of flavor α is a mixed state of neutrinos with distinct mass. If one measured the neutrino's mass directly, it would be found to have mass m_i with probability equal to $|U_{\alpha i}|^2$. Here it is good to mention, that the neutrino oscillation is possible only when neutrinos are massive. However, the question of how neutrino masses arise has not been answered conclusively by the SM and it is one of the shortcomings briefly discussed in section 1.4.

Quarks

Similarly to charged leptons that are ordered into three generations according to their mass, quarks are ordered into three-generation doublets where quarks in lower generations are lighter than those in higher generations. The charge of the first component in the doublet is $+\frac{2}{3}$, and the second component has always charge $-\frac{1}{3}$ in terms of positron charge multiples.

Each quark has assigned one of three possible color charges (red, green, blue), thanks to which quarks also interact through the strong interaction. When quarks (and antiquarks) bind together, they form color-neutral particles called *hadrons*. This is the consequence of a phenomenon called *color confinement*, which makes it impossible to observe isolated quarks. Due to this effect, quarks (and antiquarks) bind together by gluons to form colorless hadrons. This process is called *hadronization*.

A direct consequence of color confinement are *jets*. Jets are one of the most common experimental signatures at the hadron collider experiments. They are narrow cones of hadrons and other particles produced by the hadronization of quarks and gluons from the colliding hadrons. When hadrons collide at high energies, each color-charged component carries away some color charge. However, as a consequence of the color confinement, these collision fragments create other colored objects around them in order to form colorless hadrons.

Hadrons have integer charge, and they can be either *mesons*, which are formed by an equal number of quarks and antiquarks, or *baryons*, which are composed by an odd number of quarks³. Due to the high number of possible combinations of quarks and antiquarks, there are a large number of mesons and baryons. However, most of them have in isolated form very short lifetimes. Proton and neutron are baryons with the longest lifetimes of known baryons. While the neutron lifetime is about $8.8 \cdot 10^2$ s, the proton decay has never been observed, and its lifetime is estimated to be 10^{31} years [3].

³To be precise, we should say valence quarks.

Force	Relative strength	Mediator
Strong	10	gluon
Electromagnetic	10^{-2}	photon
Weak	10^{-13}	W and Z
Gravitational	10^{-42}	graviton

Table 1.1: Relative strength of fundamental forces in nature and their mediators. [4] Gravitational force is typeset in grey because, as mentioned before, it is not included in the SM, and graviton has not been observed, but we include it for completeness.

1.3.2 Bosons

Bosons are particles with integer spin. So-called gauge bosons are fundamental⁴ bosons that arise in the SM as a consequence of a local gauge invariance. There are four fundamental-force-mediating bosons, and one *Higgs boson* which is responsible for particles having mass. Table 1.1 lists the relative strengths of known fundamental interactions and their mediating bosons.

The strong interaction is the strongest of all fundamental forces in nature and is responsible for binding quarks together. It is the force thanks to which the proton and neutron can exist as bound states of uud and udd quarks, respectively. The strong force is mediated by gluons, which are massless, electrically neutral particles, and they carry a color charge, which is responsible for gluons being able to interact with other gluons and quarks, collectively called *partons*. The strength of the strong force increases with distance.

Mediators of the weak interactions are the vector bosons W^+ , W^- , and Z , and the mediator of the electromagnetic force is the *photon*. Electromagnetic and weak interactions in the SM are treated as a unified electroweak interaction, which is due to the invariance under $SU(2)$ and $U(1)$ transformations, where gauge bosons arise as a consequence of the mixing of gauge fields that are introduced in order to preserve gauge invariance of the Lagrangian.

Special attention deserves to be given to the Higgs boson, the particle that was introduced to the Standard Model in 1964 by Peter Higgs⁵ to explain how particles acquire mass.

Higgs mechanism

Gauge invariance requires massless gauge bosons and fermions, which contradicts observations where the W^\pm , Z , and fermions are massive. The so-called Higgs mechanism suggests that there exists a complex scalar doublet of $SU(2)$

⁴not composed

⁵In fact, there were five different papers by six physicists (R. Brout, F. Englert, P. Higgs, G. Guralnik, C. Richard Hagen, T. Kibble) who proposed different but related approaches that were explaining how mass can arise in local gauge theories.

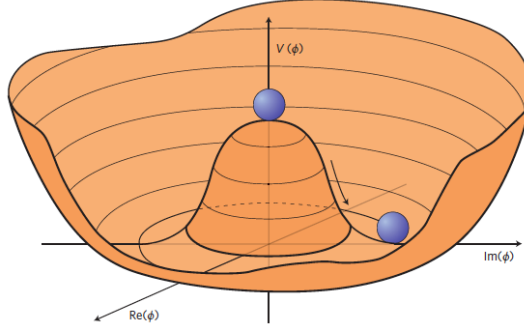


Figure 1.2: Shape of the Higgs potential for $\mu^2 < 0$ [5].

$$\Phi(x) = \begin{pmatrix} \varphi^+(x) \\ \varphi^0(x) \end{pmatrix} \quad (1.4)$$

for which we can write the interaction Lagrangian in the form

$$\mathcal{L}_{Higgs} = (D^\mu \Phi)^\dagger (D_\mu \Phi) - V(\Phi). \quad (1.5)$$

In the above equation, D^μ signifies the covariant derivative, which is the operator acting on the field Φ performing the derivative of the field but preserving $SU(2)$ gauge invariance. The $V(\Phi)$ in the equation 1.5 has form

$$V(\Phi) = \mu^2 \Phi^\dagger \Phi + \lambda (\Phi^\dagger \Phi)^2, \quad (1.6)$$

where μ and λ are real constants. It is also easy to see that this potential is invariant with respect to $U(1)$ transformation

$$\Phi(x) \longrightarrow e^{i\omega(x)} \Phi(x). \quad (1.7)$$

If the parameter μ^2 is positive, there exists a unique field configuration that corresponds to the minimum of the potential. However, if the $\mu^2 < 0$, the minimum does not correspond to the single field configuration but to a circle at the bottom of the potential well which has a so-called Mexican hat shape. The shape of this potential is shown in figure 1.2. In that case, the minimum of the potential is at the point where

$$|\Phi|^2 = \sqrt{-\frac{\mu^2}{2\lambda}}. \quad (1.8)$$

This result can be easily obtained in the following way. Since the potential $V(x)$ depends only on one real variable $|\Phi|^2 = \varphi^+ \varphi^+ + \varphi^0 \varphi^0$, we can do a substitution $|\Phi|^2 = \rho$ and find what is the value of ρ for which first derivative of potential $V(x)$ is zero. The finding in equation 1.8 allows us, without loss of generality, to choose a particular ground state

$$\varphi_{vac}^+ = 0 \quad , \quad \varphi_{vac}^0 = \sqrt{-\frac{\mu^2}{2\lambda}} + \frac{H(x)}{\sqrt{2}} \equiv \frac{v + H(x)}{\sqrt{2}}, \quad (1.9)$$

where $v = \sqrt{-\frac{\mu^2}{\lambda}}$ is the *vacuum expectation value*. This choice breaks both $SU(2)$ and $U(1)$ symmetries but preserves the residual $U(1)$ symmetry. The field $\Phi(x)$ can then be reparametrized as

$$\Phi(x) = \exp\left(i\frac{\tau^a}{2v}\pi^a(x)\right) \frac{1}{\sqrt{2}} \begin{pmatrix} 0 \\ H(x) + v \end{pmatrix} \quad (1.10)$$

where $\pi^a(x)$ are scalar fields representing *Nambu-Goldstone bosons*, τ^a , $a = 1, 2, 3$ are Pauli matrices, which are generators of the $SU(2)$ group, and $H(x)$ is the Higgs field. According to Goldstone's theorem [6, 7], there is one scalar particle called the Nambu-Goldstone boson for each generator of the symmetry that is broken. Since $SU(2)$ has three generators, there are three Nambu-Goldstone bosons. However, they are not observed in nature.

It can be shown that the Nambu-Goldstone bosons in the SM disappear since they get absorbed by the W and Z fields [5], thanks to which the W and Z acquire masses. The mass of the Higgs boson can be parametrized as $m_H = \sqrt{-2\mu^2} = \sqrt{2\lambda}v$; however, since parameters λ and μ are not constrained by the theory, the Higgs mass was not known until its discovery. Although the theory can give some mass range of the Higgs mass, the exact value was unknown because its exact value is not constrained by the SM⁶. This was also partly why detecting the Higgs boson took so long since it was unclear which mass it would have.

The Higgs boson, with a mass of 125GeV , was independently observed in the ATLAS and CMS experiments. Its discovery, announced in 2012, marked an important milestone in particle physics because it was the last missing puzzle piece in the SM as we know it today.

The Higgs boson gives masses to the W and Z bosons by the mechanism illustrated above. However, in order to allow fermions to have masses, another term to the SM Lagrangian has to be added. This term allows the preservation of the Lagrangian's symmetry for massive fermions through the additional interaction of the Higgs field with the fermions.

1.4 Shortcomings

Despite the Standard Model's strong predictive power, which can be demonstrated in figure 1.3, where comparison of the fiducial cross sections of several SM processes with values predicted by theory is shown, the Standard Model is not the final theory. Some phenomena cannot be explained in the scope of the Standard Model, which is why there are ongoing efforts to find physics beyond the Standard Model. This section briefly discusses some shortcomings of the Standard Model that give hints for the existence of physics beyond the Standard Model.

⁶Theoretical predictions about the Higgs boson mass, before the Higgs boson was discovered, are discussed, for example, in reference [8].

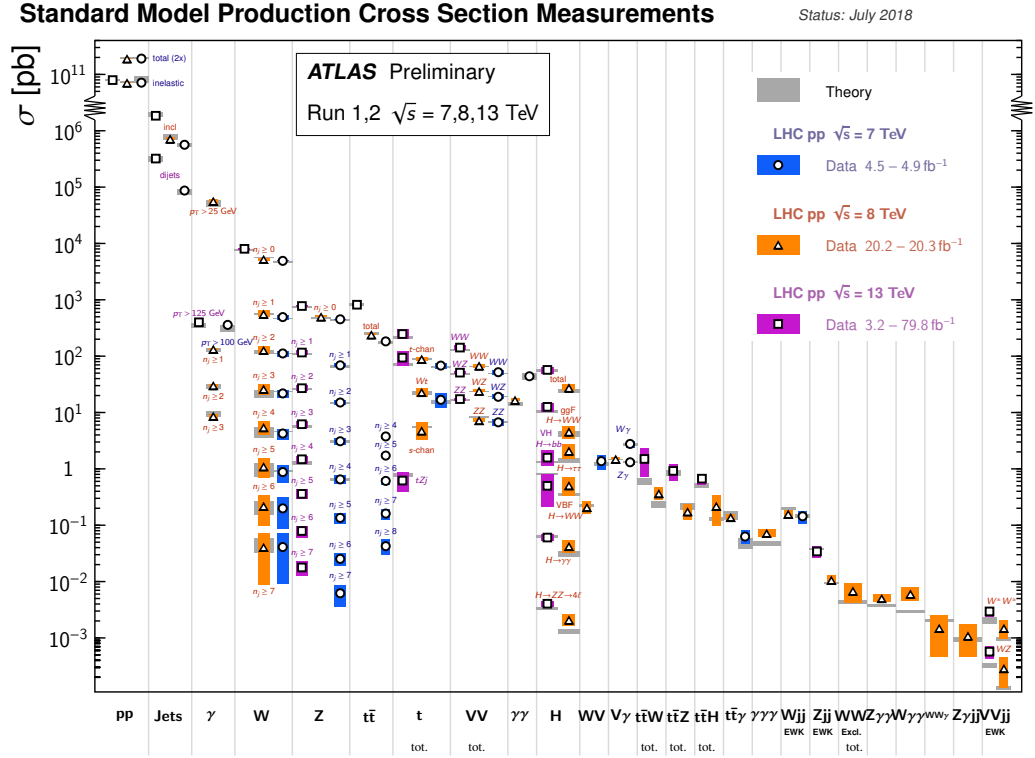


Figure 1.3: Summary of several Standard Model total and fiducial production cross section measurements and comparison with theoretically derived values. [9].

Based on the cosmological observations, the observed matter in the Universe accounts only for 5% of the ordinary matter formed by the Standard Model particles, while the remaining 26% and 69% are accounted for via dark matter and dark energy. The physical nature of these phenomena is unknown [10], which is why the explanation of these phenomena is being looked for beyond the scope of Standard Model physics. Some of the theories aiming to explain these phenomena assume the existence of long-lived weakly interacting particles [11], and these particles are then looked for in experiments such as FASER, which is discussed in the second part of this thesis.

As was mentioned in section 1.3.1, neutrino oscillations are experimentally observed phenomenon that are possible due to non-zero neutrino masses. However, the question of how neutrino masses arise has not been answered conclusively. In the SM, the other fermions have intrinsic mass because of the interactions with the Higgs field, which require left- and right-handed versions of the fermions. But only left-handed neutrinos have been observed so far, which is the problem when trying to explain how neutrinos gain mass, thanks to which neutrino oscillations could occur.

Another question that the Standard Model cannot answer in its present form is the asymmetry between matter and anti-matter. The Standard Model predicts that the lepton and baryon numbers are conserved in particle decays,

which is also an experimentally observed fact. Since our Universe is dominated by matter, and considering that before the Big Bang, nothing was supposed to exist, there has to be some fundamental force in higher energy that can violate the conservation of baryonic and leptonic numbers. CP-violation partly explains the asymmetry. However, the observed CP-violation in the quark sector (explained by the CKM matrix) is insufficient to explain the observed dominance of matter in the universe, which motivates the search for new sources of CP-violation.

The last example of the phenomenon that we are going to mention and that cannot be explained in terms of the Standard Model is the *hierarchy problem*. As mentioned in section 1.3.2, the Higgs mass is a free parameter of the Standard Model, and it is dictated by the Higgs potential and the vacuum expectation value. However, the sum of radiative loop correction affects the Higgs boson's physical mass. In this sense, the physical mass of the Higgs boson m_H that is observed in the experiment can be split into two terms: the so-called bare mass m_{bare} , and the mass term given by the radiative corrections m_{corr} .

$$m_H^2 = m_{bare}^2 + m_{corr}^2 \quad (1.11)$$

Since new physics is expected to be between the electroweak and Planck scales as a result of the unification of gravity with the Standard Model and the high number of unanswered questions. The term m_{corr}^2 is thus sensitive to new physics because these loop correction would also include other massive particles up to the Planck scale ($m_{Planck} \approx 10^{19}$ GeV) that we have not seen yet. The Planck mass is huge compared to the observed Higgs mass $m_H = 125$ GeV. It is known that the loop corrections are proportional to the mass of the particle in the loop, and bosons and fermions contribute to corrections with opposite signs. This could mean that in the case of particles with masses close to the Planck scale, their contributions might cancel out if there was a symmetry between bosons and fermions. Moreover, these loop corrections grow quadratically with the energy scale, making it unclear why the Higgs mass remains so small without fine-tuning. One solution is proposed by *Supersymmetry* (SUSY), which assumes symmetry between bosons and fermions and is discussed more in the following chapter 2.

Supersymmetry and other BSM theories

2.1 Introduction

As mentioned in section 1.4, the hierarchy problem is one of the questions the Standard Model does not answer. The radiative loop corrections to the Higgs boson mass grow quadratically with the particle's mass. Therefore, the Higgs boson mass is sensitive to the heaviest particle in the theory unless there is a symmetry between bosons and fermions that contribute to the loop corrections with the opposite sign.

Supersymmetry is the extension of the Standard model proposed in the 1970s, assuming a symmetry between fermions and bosons. Superpartners of fermions are usually spin-0 particles called *sfermions*, adding the "s" in front of the name of the SM fermion (superpartner of a quark is squark, of a muon is smuon, etc.). Fermionic superpartners of gauge bosons are spin- $\frac{1}{2}$ *gauginos*, and they append "ino" to the name of the boson (superpartner of a gluon is gluino, of W is wino, etc.). A tilde placed over a particle symbol represents the supersymmetric counterpart of this particle.

This chapter briefly presents the concept of the Minimal Supersymmetric extension of the SM in section 2.2, and also presents some other beyond SM theories relevant to experiments and searches presented in this thesis in section 2.3.

2.2 Minimal Supersymmetric Standard Model

The *Minimal Supersymmetric Standard Model* (MSSM) is a supersymmetric theory adding only the minimum number of additional free parameters. Each SM fermion has a complex scalar boson as a superpartner, and right- and left-chiral components of the fermionic fields are treated separately. The spin-1

2.2. Minimal Supersymmetric Standard Model

Names		spin 0	spin 1/2	spin 1	SU(3), SU(2), U(1)
squarks, quarks (\times families)	Q	$(\tilde{u}_L \tilde{d}_L)$	$(u_L d_L)$	-	$(3, 2, \frac{1}{6})$
	\bar{u}	u_R^*	u_R^\dagger		$(\bar{3}, 2, -\frac{2}{3})$
	\bar{d}	\tilde{d}_R^*	d_R^\dagger		$(\bar{3}, 2, \frac{1}{3})$
sleptons, leptons (\times families)	L	$(\tilde{\nu} \tilde{e}_L)$	(νe_L)	-	$(1, 2, -\frac{1}{2})$
	\bar{e}	\tilde{e}_R^*	e_R^\dagger		$(1, 1, 1)$
Higgs boson, higgsinos	H_u	$(H_u^+ H_u^0)$	$(\tilde{H}_u^+ \tilde{H}_u^0)$	-	$(1, 2, +\frac{1}{2})$
	H_d	$(H_d^0 H_d^-)$	$(\tilde{H}_d^0 \tilde{H}_d^-)$		$(1, 2, -\frac{1}{2})$
Gluon, gluino	\tilde{g}	-	\tilde{g}	g	$(8, 1, 0)$
W bosons, wino	\tilde{W}	-	$\tilde{W}^\pm, \tilde{W}^0$	W^\pm, W^0	$(1, 3, 0)$
B boson, bino	\tilde{B}	-	\tilde{B}	B	$(1, 1, 0)$

Table 2.1: Chiral supermultiplets (rows 1 to 3) and gauge supermultiplets (rows 4-6) in the MSSM. The spin-0 fields are complex scalars, and the spin-1/2 fields are left-handed two-component Weyl fermions. The last column lists the quantum numbers of each field with respect to the SM gauge symmetry group. Table adapted from [12].

bosons from the SM have spin-1/2 fermion superpartners. The list of chiral and gauge supermultiplets described by the MSSM is listed in table 2.1.

It is impossible to build SUSY theory with just a single Higgs doublet; two Higgs doublets are expected in the MSSM and four spin-1/2 superpartners of the Higgs boson are expected. The first, H_d , has weak hypercharge $Y = -\frac{1}{2}$ and couples to the down-type quarks and lepton. The second is marked H_u , and it has weak hypercharge $Y = +\frac{1}{2}$ and couples to up-type quarks. This leads to the phenomenological prediction of the existence of charged Higgs bosons H^\pm , while the remaining fields mix to produce two neutral CP-even Higgs bosons h^0 and H^0 , and a CP-odd neutral Higgs boson A^0 . Out of eight Higgs fields, the three remaining fields give mass to W^\pm and Z bosons. These superpartners are called higgsinos.

In such a theory, we can build the MSSM superpotential, which provides interaction terms of the Standard Model particles and their superpartners. This superpotential can be written as

$$W_{MSSM} = \bar{u}y_uQH_u - \bar{d}y_dQH_d - \bar{e}y_eLH_d + \mu H_uH_d, \quad (2.1)$$

where H_u , H_d are Higgs superfields; Q , \bar{u} and \bar{d} are quark superfields; and \bar{e} , L are lepton superfields. y_u , y_d and y_e are the dimensionless Yukawa coupling constants. Supersymmetry must be a broken symmetry. Otherwise, the superpartners would have the same masses as their SM counterparts and would have already been observed in nature.

It is important to note that the MSSM Higgs field interaction eigenstates in table 2.1 do not necessarily correspond to the physical observable states. In particular, it allows higgsinos to mix with winos and binos to form charged and neutral physical states referred to as *charginos* and *neutralinos*.

In the basis formed by the neutral Higgsinos (\tilde{H}_u^0 and \tilde{H}_d^0) and the neutral gauginos (\tilde{B} and \tilde{W}) $\psi^0 = (\tilde{B}, \tilde{W}, \tilde{H}_d^0, \tilde{H}_u^0)$, the Lagrangian that is associated to masses of these fields can be written as

$$\mathcal{L}_{\text{neutral mass}} = -\frac{1}{2} (\psi^0)^T \mathbf{M}_{\mathbf{N}} \psi^0 + \text{h.c.}, \quad (2.2)$$

where

$$\mathbf{M}_{\mathbf{N}} = \begin{pmatrix} M_1 & 0 & -g' \frac{\nu_d}{\sqrt{2}} & g' \frac{\nu_u}{\sqrt{2}} \\ 0 & M_2 & g' \frac{\nu_d}{\sqrt{2}} & -g' \frac{\nu_u}{\sqrt{2}} \\ -g' \frac{\nu_d}{\sqrt{2}} & g' \frac{\nu_d}{\sqrt{2}} & 0 & -\mu \\ g' \frac{\nu_u}{\sqrt{2}} & -g' \frac{\nu_u}{\sqrt{2}} & -\mu & 0 \end{pmatrix}. \quad (2.3)$$

M_1 and M_2 are masses of the bino (superpartner of $U(1)$ electroweak hypercharge) and the wino, respectively. In the expression 2.3, the terms of the diagonal provide the mixing interactions which, after the basis transformation, form four diagonal mass eigenstates. These states correspond to the neutralinos $\tilde{\chi}_1^0, \tilde{\chi}_2^0, \tilde{\chi}_3^0, \tilde{\chi}_4^0$, ordered in increasing mass.

Similarly charged higgsinos \tilde{H}_u^+ and \tilde{H}_d^- , and winos \tilde{W}^+, \tilde{W}^- undergo a similar mixing effects through the matrix

$$\mathbf{M}_{\mathbf{C}} = \begin{pmatrix} 0 & 0 & M_2 & g\nu_d \\ 0 & 0 & g\nu_u & \mu \\ M_2 & g\nu_u & 0 & 0 \\ g\nu_d & \mu & 0 & 0 \end{pmatrix}. \quad (2.4)$$

in the basis $(\tilde{W}^+, \tilde{H}_u^+, \tilde{W}^-, \tilde{H}_d^-)$. From the diagonalization of this matrix, we get four mass eigenstates, which are the charginos mentioned above. These are denoted $\tilde{\chi}_1^+, \tilde{\chi}_1^-, \tilde{\chi}_2^+, \tilde{\chi}_2^-$.

In the case of R-parity conservation, which is discussed in the next section, the lightest neutralino provides the dark matter candidate that can solve the dark matter issue in cosmology. This is why charginos and neutralinos are important for SUSY searches. In case these particles exist, they could be produced at the LHC in the following interactions:

$$q\bar{q} \rightarrow \tilde{\chi}_i^+ \tilde{\chi}_j^- \quad (2.5)$$

$$q\bar{q} \rightarrow \tilde{\chi}_i^0 \tilde{\chi}_j^0 \quad (2.6)$$

$$u\bar{d} \rightarrow \tilde{\chi}_i^+ \tilde{\chi}_j^0 \quad (2.7)$$

$$d\bar{u} \rightarrow \tilde{\chi}_i^- \tilde{\chi}_j^0 \quad (2.8)$$

here q signifies quarks of any flavour, and \bar{q} is its antiparticle. u and d are quarks up and down.

2.2.1 R-parity

There are many ways to build supersymmetric Lagrangians, and some of them are invariant under the $U(1)$ symmetry, commonly known as R -symmetry, which can be assigned the new quantum number called R -parity, defined as

$$P_R = (-1)^{3(B-L)+2s}, \quad (2.9)$$

where B , L and s are baryon number, lepton number and spin, respectively. All SM particles have R -parity +1 while their super-partners have R -parity of -1.

In case the R -parity is conserved¹, it leads to interesting phenomenological consequences for the model. In particular, since the SM particles have R -parity +1 and SUSY particles -1, the R -parity odd particles (SUSY particles) can be produced only in pairs. Also, since there are no interactions in the MSSM that would allow interaction of one superpartner and two SM particles, it suggests there would have to be a *lightest supersymmetric particle* (LSP) that cannot decay to pure SM states. This means that this particle has to be stable and therefore it is a good candidate for dark matter, which gives SUSY significance in explaining some of the cosmology questions.

2.2.2 Soft supersymmetry breaking

As it was mentioned above, if SUSY was a perfect symmetry, the masses of SM particles and their superpartners would have to be equal. However, this is not experimentally observed since no experiment observed a superpartner of any SM particle, and it is very likely that superpartners of light particles would have to be observed. That is why it is assumed that SUSY is not an exact symmetry but it is broken. In other words, the underlying model should have an invariant Lagrangian density under supersymmetry but a vacuum state that is not. [12] This effect is called *spontaneous supersymmetry breaking*.

In order to allow SUSY to solve the hierarchy problem and not to break loop corrections to the Higgs boson mass, the effect of the supersymmetry breaking has to be soft. In theory, there are many ways to achieve this, and no physical observation indicates exactly how this is done. The most general terms breaking supersymmetry in MSSM, conserving R -parity and gauge invariance are:

$$\begin{aligned} \mathcal{L}_{\text{soft}} = & -\frac{1}{2} \left(M_1 \tilde{B} \tilde{B} + M_2 \tilde{W} \tilde{W} + M_3 \tilde{g} \tilde{g} + h.c. \right) \\ & - \left(\tilde{u} a_u \tilde{Q} H_u - \tilde{d} a_d \tilde{Q} H_d - \tilde{e} a_e \tilde{L} H_d + h.c. \right) \\ & - \tilde{Q}^\dagger m_Q^2 \tilde{Q} - \tilde{L}^\dagger m_L^2 \tilde{L} - \tilde{u} m_u^2 \tilde{u}^\dagger - \tilde{d} m_d^2 \tilde{d}^\dagger - \tilde{e} m_e^2 \tilde{e}^\dagger \\ & - m_{H_u}^2 H_u^* H_u - m_{H_d}^2 H_d^* H_d - (b H_u H_d + h.c.). \end{aligned} \quad (2.10)$$

¹Model considering R -parity conservation are often referred to as RPC models, while those assuming that R -parity can be violated are referred to as RPV models.

Here, M_1 , M_2 , and M_3 are masses of the bino, wino, and gluino, and other terms represent masses of sfermions and symmetry-breaking contributions of the Higgs potential. However, this shows that supersymmetry breaking introduces a large number of new parameters in the MSSM².

2.3 Selected beyond-Standard-Model theories

As mentioned earlier, SUSY is one of the possible extensions of the SM that can explain problems presented in section 1.4. However, there are other models that can provide explanations for some phenomena. In this section, we briefly list some of them that are mentioned in this thesis, namely in part II, dedicated to FASER.

2.3.1 Dark photon

Dark photons [13] are a good example of light, weakly-coupled particles that arise when the SM is supplemented by a hidden sector. This can be motivated by the need for dark matter, where the existence of the dark photon can yield the right dark matter relic density. If the hidden has (broken) $U(1)$ symmetry, the new gauge boson mixes with the SM photon through coupling $\tilde{F}^{\mu\nu}\tilde{F}'_{\mu\nu}$, where $\tilde{F}^{\mu\nu}$ and $\tilde{F}'_{\mu\nu}$ are the field strengths of SM and hidden gauge boson. After the re-definition of the field to remove this kinetic coupling, a new boson A' , called a dark photon, with mass $m_{A'}$, is introduced to the SM. Similarly to the SM photon, it can interact with fermions. However, the strength of this interaction is modified by a new kinetic mixing parameter ϵ . The corresponding part of the Lagrangian then reads

$$\mathcal{L} = -\frac{1}{4}F_{\mu\nu}F^{\mu\nu} - \frac{1}{4}F'_{\mu\nu}F'^{\mu\nu} + \frac{1}{2}m_{A'}^2 A'^2 + \sum_f \bar{f}(i\not{\partial} - eq_f \not{A} - \epsilon eq_f \not{A}' - m_f)f, \quad (2.11)$$

where $F_{\mu\nu}$ and $F'_{\mu\nu}$ are field strengths of the photon A and the dark photon³.

Dark photons could be produced in meson decays, in the form of a proton bremsstrahlung, or directly during quark and gluon interactions. If their mass is high enough, they could decay to e^+e^- pairs. That is why they are interesting candidates for particles to be searched for at experiments like FASER.

2.3.2 Axion-like particles

Axion-like particles (ALPS) [14] are hypothetical particles proposed in order to solve various problems in particle physics and cosmology, and they are good candidates to explain dark matter.

²Coupling constants $a_u, a_d, a_e, m_Q, m_L, m_u, m_e$ are complex 3×3 matrices.

³The equation uses Feynman slash notation $\not{\partial} \equiv \gamma^\mu \partial_\mu$, where γ^μ are gamma matrices. And similarly for \not{A} .

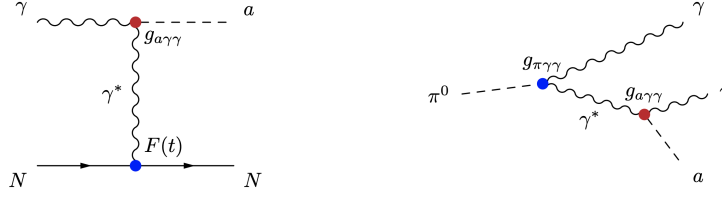


Figure 2.1: Production of an axion-like particle in Primakoff process (left) and light meson decay (right). [14].

They could be incorporated in SM by extending Lagrangian by terms where these axion-like particles a couple to vector bosons

$$\mathcal{L} = -\frac{1}{4}g_{aBB}aB_{\mu\nu}\tilde{B}^{\mu\nu} - \frac{1}{4}g_{aWW}aW_{\mu\nu}\tilde{W}^{\mu\nu}, \quad (2.12)$$

where $B_{\mu\nu}$ and $W_{\mu\nu}$ are $U(1)$ and $SU(2)$ field strength tensors, and g_{aBB} and g_{aWW} are the corresponding coupling constants. After electroweak symmetry breaking, these constants induce ALP coupling to $\gamma\gamma$, γZ , ZZ and W^+W^- . In particular, the coupling to two photons is interesting experimentally because they can be directly detected by a silicon tracking detector, as in the case of FASER⁴.

ALPs can be produced in any process involving photons by radiating an ALP off the photon line. Figure 2.1 shows two examples of these processes. The first example is the so-called Primakoff process, in which a photon converts into ALP when interacting with an atomic nucleus. The second example of a process where ALP can be produced is meson decay.

2.3.3 Heavy neutral leptons

The fact that non-zero neutrino masses are observed points to the possible existence of multiple SM neutral fermions. When these states are so heavy that they cannot be produced in neutrino oscillations, they are referred to as *heavy neutral leptons* (HNL). They can be introduced to the SM by adding the Standard Model Lagrangian interaction term [11]

$$\mathcal{L} = -\sum y_{\alpha I} \left(\bar{L}_\alpha H \right) N_I. \quad (2.13)$$

Here $y_{\alpha I}$ are Yukawa couplings, and the sum is over SM lepton doublets L_α and HNL fields N_I . After electroweak symmetry breaking, it is possible to find mixing between HNLs and SM neutrinos.

There are several ways they could be produced, but two examples are τ and heavy meson decays, such as $D \rightarrow K\ell N$, $D^\pm \rightarrow \ell^\pm N$ or $B \rightarrow D\ell N$, where ℓ signifies lepton, and N is the HNL.

⁴FASER, at the time of writing this thesis, does not have sensitivity for ALP two-photon signature due to the close separation of two photons. However, this should change with the planned upgrade of the preshower detector.

Large Hadron Collider

3.1 Introduction

Particle physics has undergone a very turbulent development over the past century. It went from a nearly newborn field at the beginning of the 20th century, where only an electron was known, and Albert Einstein hypothesized a photon to explain the photoelectric effect, to a field of large experiments operated by huge international collaborations of scientists where discoveries are possible only thanks to the cooperation of not only physicists but also engineers, software developers, civil construction workers and many more. It came from a field of physics where people knew almost nothing, to the point where we have one of the most tested and successful physics theories. The theory is called the Standard Model, and even though we know it is not the complete theory that would perfectly describe the Universe, it has a great predictive power. However, it was not always like that. After the discovery of the W and Z bosons in 1983 and the discovery of the top quark in 1995, all particles in the Standard Model were detected directly or indirectly in experiments except only one – the Higgs boson. A particle, the existence of which was predicted in 1964, but it was never observed before. This was the primary motivation for building the Large Hadron Collider (LHC). The machine which could help extend the reach of particle physics experiments beyond that available at the end of the 20th century.

The Large Hadron Collider (LHC) is a 27-kilometer-long circular collider located at the French-Swiss border near Geneva. The accelerator was built between 1998 and 2008 inside the tunnel where the previously Large Electron Positron collider (LEP) was located. It consists of two rings that can accelerate two proton or heavy ion beams orbiting in opposite directions and collide them afterward. These collisions serve as a probe of the physics of the Standard Model and even beyond.

The LHC is a proton-proton (pp) collider, on contrary to its precursor, the

Tevatron at Fermilab, which was a proton-antiproton ($p\bar{p}$) collider. Each approach has its pros and cons and requires different accelerator designs which we are going to quickly compare in this paragraph because each of these accelerators played an important role in the world of particle physics. The first difference in the $p\bar{p}$ and pp collider design is that $p\bar{p}$ colliders accelerate and collide two beams of oppositely charged particles, which require two separate accelerator pipes and magnets, while pp colliders can use a single pipe containing two beams orbiting in opposite directions.¹ Another difference is that proton-antiproton collisions can provide a cleaner collision environment due to the proton-antiproton annihilation process, whereas proton-proton collisions are more complex. Protons contain only quarks, so the collisions result from quark-quark, quark-gluon, or gluon-gluon interactions, leading to secondary particle production and higher background noise. Finally, proton-proton colliders can achieve higher collision rates more easily because protons are easier to extract and store, unlike antiprotons, which need to be cooled and stored using storage rings, resulting in fewer antiprotons in beams compared to protons. This makes it possible for the LHC to probe rare events at the intensity frontier.

This chapter is a brief overview of the basics of LHC accelerator physics, because the proton-proton collisions happening inside the LHC are a crucial ingredient for the ATLAS experiment, but also for the FASER experiment described in the part II of this thesis. This chapter also presents the LHC parameters, and introduces some important physical quantities.

3.2 Source of particles

At the beginning of the whole acceleration chain, there is the hydrogen gas source, which is used to extract protons from the hydrogen gas. The way of doing this was changing during the LHC operations and the approach described further has been used since the beginning of the Run 3. Instead of creating a proton from the hydrogen, an electron is added, which creates a negatively charged hydrogen ion H^- . The H^- is used for the acceleration as described in section 3.3. In case of heavy ion runs, there is a dedicated source and injector chain setup.

The curious reader of this text might wonder how much hydrogen is needed to fill the whole LHC ring with protons. The estimate can be done using the state equation of ideal gas, and because the numbers can be surprising, we are stating it here. During the LHC operations, in one fill, there can be about of

$$2 \text{ beams} \times 2808 \text{ bunches} \times 1.15 \cdot 10^{11} = 6.5 \cdot 10^{14} \text{ protons in two beams}^2.$$

A volume of 1 cm^3 of the ideal gas of molecular hydrogen H_2 at the room temperature of $T = 293 \text{ K}$ and atmospheric pressure of $p = 10^5 \text{ Pa}$ contains

¹In fact, the beams are kept separately even at the LHC by two close-by pipes, but they use common magnets, which is something that cannot be achieved in case of $p\bar{p}$ collider.

²Concept of bunches is explained in the section 3.3.

$$n = \frac{pV}{RT} = 4 \cdot 10^{-5} \text{ moles}$$

which translates into $2.5 \cdot 10^{19}$ hydrogen molecules and $5.0 \cdot 10^{19}$ hydrogen atoms. So theoretically, the LHC could be filled almost $7.7 \cdot 10^4$ times using a single cubic centimeter of hydrogen gas, assuming all atoms are used. The hydrogen gas usage is not fully efficient, but this still gives us a rough idea of how much hydrogen would be needed. Considering that the LHC is filled just a few times per day, it is impressive how little hydrogen gas is needed for proton-proton collisions in the research pushing the boundaries of human knowledge about matter in our Universe.

Despite the small amount of hydrogen needed, the bottle containing the hydrogen gas is replaced about twice per year in order to maintain the correct operational pressure. [15]

3.3 Acceleration

The particles go through several acceleration stages after obtaining the beam of protons or heavy ions. The following section describes the acceleration chain as it is used in Run 3. Hydrogen ions H^+ are extracted from the ion source, injected into the linear accelerator LINAC4, and accelerated to the energy of 160 MeV. After that, the two electrons are stripped off, and bare protons are injected into the Proton Synchrotron Booster, where they are accelerated to 2 GeV for the injection into Proton Synchrotron. The Proton Synchrotron accelerates protons further up to 26 GeV from where they are sent to the Super Proton Synchrotron (SPS), where they are accelerated up to 450 GeV. After that, they are finally injected into the main LHC ring. The schematics of the acceleration chain can be seen in figure 3.1.

For the acceleration, the electric field is used. If a charged particle gets into an electric field \mathbf{E} , it experiences the accelerating force

$$\mathbf{F} = q \mathbf{E} \tag{3.1}$$

where q is the charge of the particle. At the LHC, the accelerating electric field is applied inside radiofrequency cavities (RF cavities). RF cavities generate longitudinal oscillations in the voltage across isolated gaps, which creates the electromagnetic potential that can accelerate charged particles. Cavities are organized in an array, and a particle is always accelerated in the gap where it feels the potential that can accelerate it and cancels out as the particle travels through the rest of the machine. This leads to the simple condition, which says that the RF frequency f_{RF} has to be integer multiple h of the revolution frequency f_{rev} of the particle inside the ring.

$$h = \frac{f_{RF}}{f_{rev}} = \frac{f_{RF}}{\frac{\beta}{d}} \tag{3.2}$$

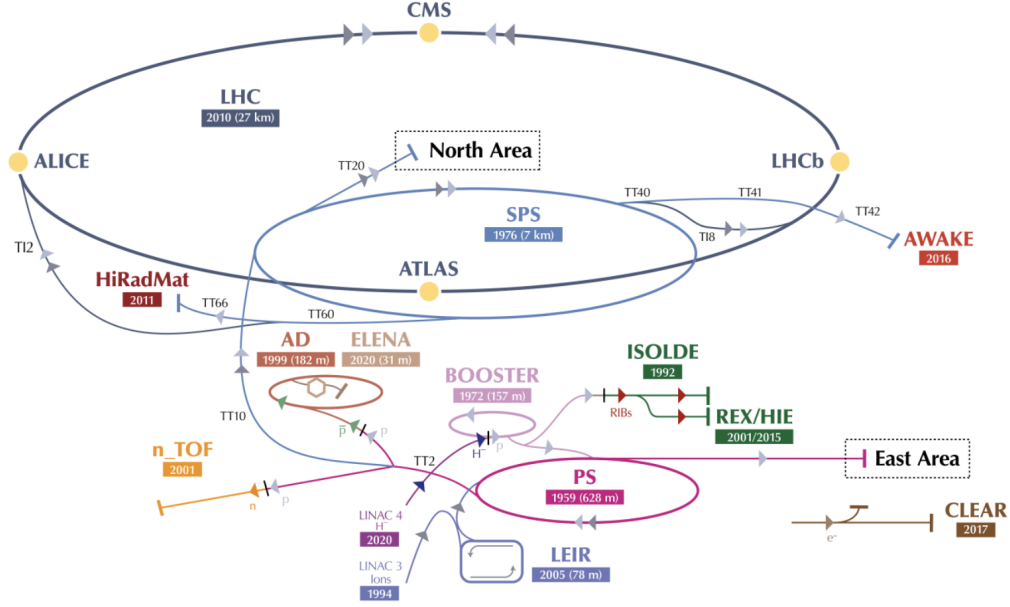


Figure 3.1: Schematic illustration of the whole LHC accelerator complex depicting locations of some CERN major experiments. Figure taken from [16].

where β is $\frac{v}{c}$ where v is the speed of the particle and d is the circumference of the ring. If we put parameters for the LHC where $f_{RF} = 400$ MHz, $\beta \approx c$, $d = 26659$ m [17] we get the harmonic number $h = 35640$. This leads to the fact that the beam is split into 35640 segments, which are called *buckets*. Particles grouped close to the centers of these segments get accelerated the most, and such a group of particles located in one bucket is called *bunch*. The LHC can have on its circumference up to about 3600 each containing $1.15 \cdot 10^{11}$ protons. Bunches are spaced by 25 ns; however, not all bunches have to be filled. In 2024, the LHC operates with a maximum of about 2350 bunches. Different types of bunch filling structures are referred to as *filling schemes*.

The advantage of the circular accelerator is that the particles can be accelerated multiple times before colliding, and particles that do not collide stay in their orbit and can be reused for future collisions. However, the process of acceleration is limited by another competing effect, which is the synchrotron radiation. It is photons that are irradiated when a charged particle changes momentum, which causes it to lose energy. The power that is carried out by the radiation is given by the Larmor formula

$$P = \frac{q^2 c \beta^4 \gamma^4}{6\pi \epsilon_0 \rho^2} \quad (3.3)$$

where γ is Lorentz factor, ϵ_0 is vacuum permittivity and ρ is the radius of curvature of particle trajectory. From a quick look at this formula, it can be seen that the faster the particle moves on a curved trajectory, the higher the losses are, and at the same time, the smaller the radius of curvature of the particle trajectory, the higher the losses are. So, the solution for reaching higher

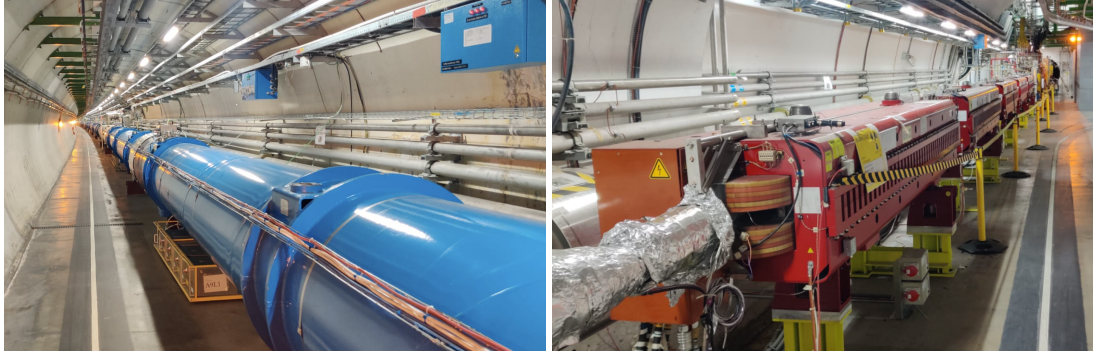


Figure 3.2: The view to the LHC tunnel close to the ATLAS experiment. The blue dipole magnets (left) and beam optics close to the entrance to the ATLAS cavern (right). These pictures were taken during the tunnel visit during the period of Long Shutdown 2.

energies is increasing the radius of the accelerator, but this also increases costs. Another limiting factor is how much we can bend the particle trajectory, which is the parameter discussed in the following section.

The LHC design allows the acceleration of a proton beam up to the energy of 7 TeV.

3.4 Beam bending and focusing

Because the LHC is a circular collider, it is clear that the particle trajectory has to be bent. A charged particle moving inside the magnetic field \mathbf{B} is perceiving force

$$\mathbf{F} = q \mathbf{v} \times \mathbf{B}, \quad (3.4)$$

which is bending its trajectory. LHC uses 1232 dipole superconducting magnets, each able to produce a magnetic field of 8.3 T, that is used to bend the trajectory of accelerated particles. These magnets are cooled down 1.9 K by superfluid helium.

In addition to dipole magnets, quadrupole magnets are used to squeeze the particle beam vertically or horizontally.

Photographs of the LHC dipole magnet and beam optics before the beam enters the ATLAS cavern are shown in figure 3.2.

3.5 Collision

If two highly relativistic particles collide head-on, the resulting energy available at the collision point is given by the formula

$$\sqrt{s} \approx 2\sqrt{E_1 E_2} \quad (3.5)$$

where E_1 and E_2 are energies of colliding particles in the laboratory reference frame. For two proton beams at the LHC accelerated to energy 7 TeV, this results in maximum collision energy of $\sqrt{s} = 14$ TeV³. These are the LHC design parameters that have not been reached yet. The collision energy in Run 3 (years 2022 – 2025 of data taking) is $\sqrt{s} = 13.6$ TeV.

This leads us to the definition of *instantaneous luminosity* \mathcal{L} , which is the quantity characterizing the ability of a particle accelerator to produce the required number of interactions N for the given process of the cross-section σ . In general, we can write

$$\mathcal{L} = \frac{1}{\sigma} \frac{dN}{dt}. \quad (3.6)$$

For the particle accelerator, which collides Gaussian beams head-on, the luminosity can be expressed as

$$\mathcal{L} = \frac{f N_b n_1 n_2}{4\pi \sigma_x \sigma_y} \quad (3.7)$$

where f is the revolution frequency of one bunch, N_b is the number of bunches inside the accelerator, n_1 and n_2 are the number of particles in colliding bunches and σ_x and σ_y are dimensions of the of the beam. In reality, beams are not colliding exactly head-on, which means that correction factors to the formula would have to be applied. By integrating the instantaneous luminosity over time, we get the *integrated luminosity*

$$L^{int} = \int \mathcal{L} dt, \quad (3.8)$$

which is the quantity directly related to the number of recorded collisions. This can be seen by substituting equation 3.6 into 3.8 and integrating over time.

$$N = L^{int} \sigma \quad (3.9)$$

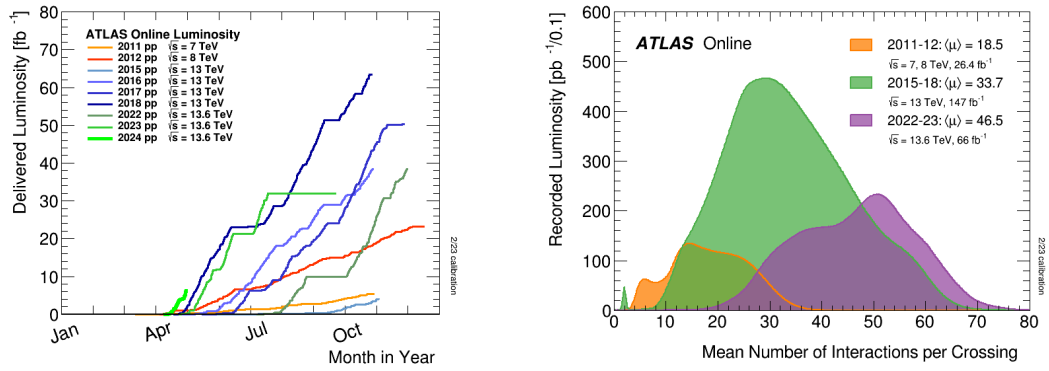
The evolution of the integrated luminosity for the ATLAS experiment during different years of data taking can be seen in figure 3.3a.

When two bunches of protons pass through each other, many collisions are usually happening. The mean number of collisions per bunch crossing is called *pile-up* and is generally denoted as $\langle\mu\rangle$. In general, we can distinguish between *in-time pile-up*, which is caused by multiple pp collisions in the same bunch crossing, and *out-of-time pile-up*, which is caused by multiple pp collisions in different bunch crossings.

Pile-up is directly influenced by the number of protons inside bunches, size of the beam, and the total inelastic cross-section⁴. This number was increased during the years of data taking, which can be seen in figure 3.3a.

³In case of heavy ion runs (lead–lead, xenon–xenon, proton–lead).

⁴This is 80 mb for 13 TeV pp collisions.



(a) Delivered integrated luminosity. [18]

(b) Distribution of $\langle\mu\rangle$. [18]

Figure 3.3: Two figures showing the delivered integrated luminosity and luminosity-weighted distribution of the mean number of collisions per bunch crossing $\langle\mu\rangle$ for the ATLAS experiment in years 2011–2024 (excluding two Long Shutdown periods when there was no data taking).

3.6 Large experiments

There are eight points at the LHC circumference where the the LHC construction would allow the two beams to cross each other. However, the crossing is actually happening only in four of them. These points are called *interactions points* (IP) and make the proton-proton (pp) collisions possible. These collision points house four major LHC experiments, each containing one. ATLAS and CMS are the two largest multipurpose LHC experiments, followed by ALICE and LHCb experiments. The placement of the experiments at the accelerating ring is shown in figure 3.1.

These experiments are sophisticated particle detectors that capture the products of collisions that happen inside them.

3.7 Smaller experiments

Apart from the four big experiments mentioned in the previous section, five more small experiments complement the physics program. Experiments TOTEM and LHCf focus on forward-scattered protons from collisions and forward hadron production. The next one is MoEDAL-MAPP, which searches for hypothesized magnetic monopoles. The newest experiments, FASER and SND@LHC, are focused on long-lived weakly interacting particles and neutrino physics.

PART I

ATLAS

The first part of the thesis is dedicated to the ATLAS experiment at the Large Hadron Collider at CERN. Chapter 4 describes one of the two largest LHC experiments - the ATLAS experiment and its subsystems, and chapter 5 focuses on the collision event reconstruction inside the ATLAS experiment. The next chapter, chapter 6 then discusses track extrapolation and the optimization of this algorithm for the online High Level Trigger Particle Flow jet reconstruction. Chapter 7 briefly summarizes statistical methods used for the interpretation of the data from the ATLAS experiment. These methods are used for the higgsino search discussed in chapter 8 and for the reinterpretation in chapter 9. The last chapter, chapter 10, is dedicated to the preservation and reinterpretation of the Higgsino analysis presented in chapter 8.

ATLAS Detector

4.1 Introduction

The ATLAS Collaboration is an international collaboration of about 6000 members from 42 countries, and approximately 4000 of the collaboration members are physicists. It was formed in 1992, and two years later, the proposal for the experiment in its current form was presented. The building of the experiment started at individual institutions that participated in the development of parts of the detector, and its construction was completed in 2008. The first proton-proton collisions were recorded in 2009 at 900 GeV, and physics data-taking started the year after, which marked the beginning of the first data-taking period.

These periods are called *Runs*, time intervals during which the LHC is running and experiments are taking data. Runs are interrupted by the planned technical stops called *Long Shutdowns*. The timeline of the LHC (and also ATLAS) operations is shown in table 4.1.

In 2012, during the Run 1, the ATLAS and CMS experiment announced the discovery of the last missing particle in the Standard Model, which was the Higgs boson. That year marked a significant milestone in the existence of the ATLAS experiment, and it opened a new window for discoveries of physics beyond the Standard Model using the Higgs boson. Apart from the new discoveries, ATLAS also focuses on precision measurements to refine the parameters of the Standard Model.

Understanding of the detector is important for the correct understanding of recorded data. This chapter serves as an overview of the detector and it describes the ATLAS experiment and its subdetectors.

Period name	Duration	Beam energy [TeV]
Run 1	2010 – 2012	7 - 8
Long Shutdown 1	2013 – 2014	-
Run 2	2015 – 2018	13
Long Shutdown 2	2019 – 2022	-
Run 3	2022 – 2025	13.6

Table 4.1: LHC and ATLAS operational timeline. The operational periods are called Runs. This is when collisions at LHC take place. These periods are interrupted by Long Shutdowns (LS), which are planned long technical stops used for the maintenance and upgrade of the LHC facilities and experiments.

4.2 Coordinate system and commonly used variables

In order to describe the geometry of events observed inside the ATLAS detector, let us describe the coordinate system used in the experiment. ATLAS uses a Cartesian right-handed coordinate system with the origin at the nominal interaction point. The x - y plane is transverse to the beam direction with a positive x -axis from the nominal interaction point to the center of the LHC ring, a positive y -axis pointing from the nominal interaction point upwards, and z -axis going along the beam direction, as shown in the figure 4.1. [19]

The whole ATLAS detector can be divided into the *barrel* region sections, where the detector instruments are positioned at open cylinders along the beam pipe, and *end-cap* region sections, where detector instruments are placed in wheels perpendicular to the beam axis.

When describing collision in highly relativistic events, it is useful to define other coordinates that are easy to use and better reflect the collision geometry. For this purpose, we can define the *azimuthal angle* ϕ , which is the angle measured around the beam axis in the transverse plane, and the *polar angle* θ is the angle with respect to the beam axis. The disadvantage of using a polar angle in the description of collision geometry is that it is not invariant under the Lorentz boost along the beam axis. That is why it is useful to define a quantity called *rapidity*

$$y = \frac{1}{2} \ln \left(\frac{E + p_z}{E - p_z} \right). \quad (4.1)$$

E is the energy of the particle, and p_z is the component of momentum along the beam axis. It can be shown that the difference between the two rapidities is, unlike the polar angle, invariant under the Lorentz boost along the z -axis.

We can also define *pseudorapidity* as

$$\eta = -\ln \left[\tan \left(\frac{\theta}{2} \right) \right], \quad (4.2)$$

, which becomes equal to rapidity for the limit where the mass of the particle is much smaller than its three-dimensional momentum ($m \ll |\mathbf{p}|$), which is, for protons at the LHC, a well-satisfied condition.

Finally, the distance in the pseudorapidity-azimuthal angle space is defined as

$$\Delta R = \sqrt{(\Delta\eta)^2 + (\Delta\phi)^2}. \quad (4.3)$$

At this place, it is also beneficial to introduce other boost-invariant quantities, which are the *transverse momentum* p_T and the *transverse energy* E_T , which are quantities defined in the transverse plane.

$$p_T = \sqrt{p_x^2 + p_y^2} \quad (4.4)$$

$$E_T = E \sin(\theta). \quad (4.5)$$

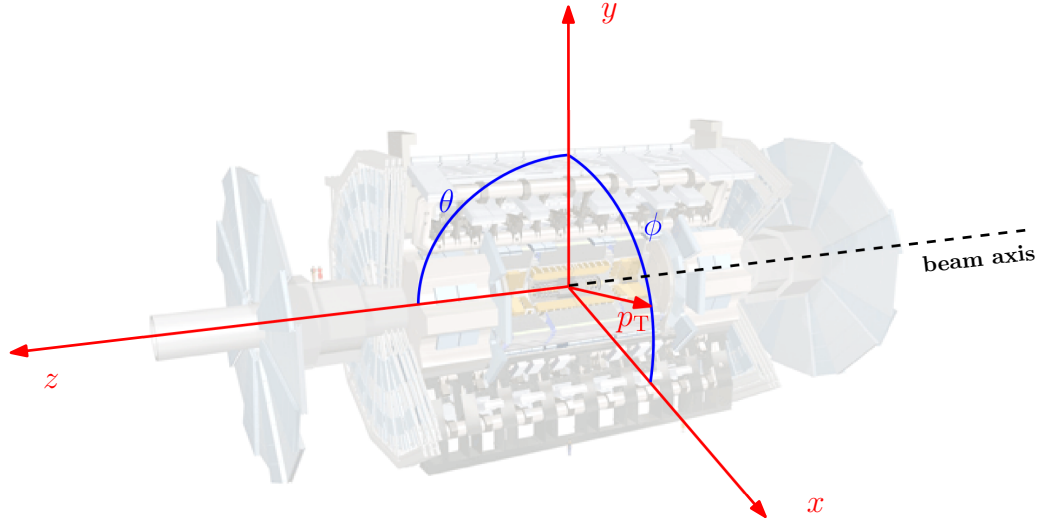


Figure 4.1: Schematic representation of the ATLAS coordinate system. 3D model of the ATLAS is from [20].

The definition of the transverse plane, as a plane that is perpendicular to the beam axis, is useful because before the collision happens, no momentum is in the direction perpendicular to the beam axis¹, and after the collision, some of the momenta gets distributed into the direction perpendicular to the beam axis. However, thanks to the momentum conservation, the transverse momenta of all particles have to be conserved before and after the collision, and their vector sum has to be zero. This concept is helpful for the definition of the missing transverse energy, which is described in section 5.7.

¹It is supposed that the transverse momentum of protons inside the beam, as well as transverse momentum of partons inside protons, is negligible.

4.3 Inner Detector

The first part of the ATLAS experiment that collided particles get in contact with is the *Inner Detector* (ID). The purpose of the inner detector is to provide extremely precise tracking information, excellent momentum resolution, and primary and secondary vertex identification. The detector is able to provide tracking information in the range of $|\eta| < 2.5$ for the particles with p_T down to 100 MeV. [19].

The tracking process is based on fitting the particle trajectory through hits of the particle in several layers of the tracking detector. It consists of three main parts, which are the *Pixel Detector*, the *Semiconductor Tracker* (SCT), and the *Transition Radiation Tracker* (TRT). The ID is contained within a cylindrical envelope of length 3512 mm and of radius 1150 mm, within a solenoidal magnetic field of 2 T. The cross-section through the ID and schematic illustration of the tracking principle can be seen in the figure 4.2. More details on track reconstruction are provided in section 5.2. A more detailed schema of the layout of individual subdetectors is shown in figure 4.3.

Pixel Detector

The Pixel Detector is the first part of the ATLAS detector to see the collision products. It consists of a total of 92 million pixels placed on four barrel layers and six end-cap disks (three on each side of the barrel). The pixel size varies from $50 \times 600 \mu\text{m}^2$ down to $50 \times 400 \mu\text{m}^2$ (which is approximately 90% of all pixels) for external layers all the way to $50 \times 250 \mu\text{m}^2$ for the innermost *Insertable B-Layer* (IBL). IBL is the pixel detector layer installed at 3.3 cm radius from the beam axis in 2014 to improve tracking performance [21, 19].

All pixel sensors were produced with leading-edge technology making them radiation hard and being able to withstand enormous particle fluxes produced during the proton-proton collisions.

The advantage of using pixel detectors is that they can provide very precise, unambiguous tracking information in the form of *hits*, which is necessary for vertex finding, but the technology is expensive for large-scale use. For this reason, strip detectors are used in the *Semiconductor Tracker* further from the collision point where a larger detector area needs to be covered.

Semiconductor Tracker

The Semiconductor Tracker (SCT) uses classic single-sided p-in-n silicon strip detectors. The strip detectors have the readout electrodes that are segmented as several centimeters long and tens of μm thin strips². This design provides excellent spatial resolution in the axis perpendicular to the strip direction while reducing the number of readout channels in comparison to the pixel detector

²Dimension of the strips depends on the location at the ATLAS detector with length ranging between roughly 57 – 65 mm and strip pitch approximately 60 – 94 μm .

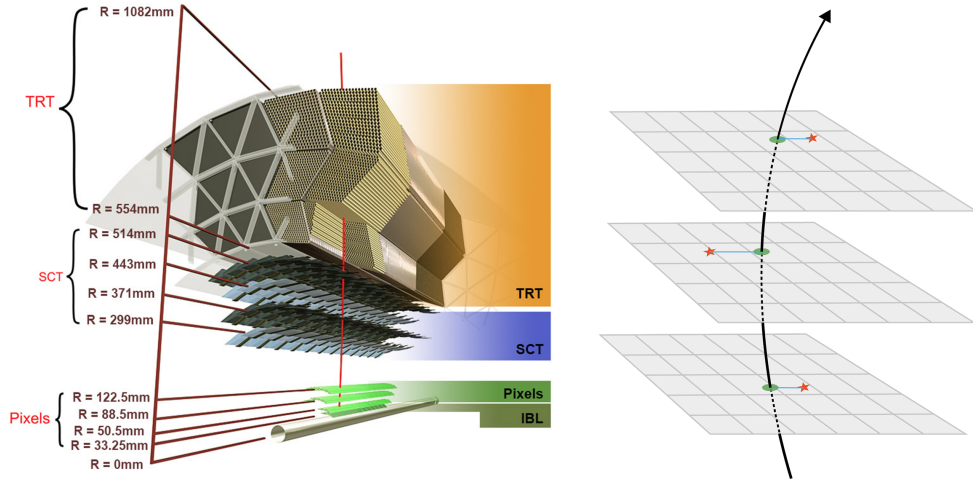


Figure 4.2: Visualisation of a cross-section through the Inner Detector. The closest to the interaction point is the Insertable B-Layer, which is the innermost layer of the pixel detectors. Right above the Insertable B-Layer, there are several layers of highly granular silicon pixels, followed by silicon strips and straw tubes forming the outermost layer of the ID (left). The other part of the figure is showing the schematic representation of the principle of tracking (right). A charged particle leaves hits in multiple layers of sub-detector planes. These hits are marked by red stars. Hits are subsequently fitted by the track represented by the black arrow. Green dots indicate the intersection of the track with each surface. The blue lines represent the track-to-hit residual of each layer. [22]

because the primary purpose of the SCT is to determine the curvature of the track inside the magnetic field. The inability of strip detectors to measure position precisely in the axis parallel to strip direction is mitigated by the fact that each module is composed of a double layer of strips tilted by a stereo angle of 40 mrad, which effectively creates a two-dimensional grid, allowing to measure a particle's position in both axes³. The small stereo angle is there to avoid massive fake hit measurements.

The sensor thickness of $285 \mu\text{m} \pm 15 \mu\text{m}$ is a compromise between the required operation voltage⁴ and the primary signal ionization. [19].

Transition Radiation Tracker

The detection principle of the Transition Radiation Tracker is based on the detection of the signal left by the charged particle that ionizes gas inside the thin straw tubes. The whole TRT consists of about 300 000 such thin polyamide

³Due to the fact that the stereo angle is small, the measurement in one axis is precise (axis perpendicular to the strip direction) and the estimate in the other axis is more coarse.

⁴Operation voltage of silicon strip detectors was about 150 V at the beginning of the ATLAS operations in Run 1 but is going to increase up to between 250 V and 350 V due to the radiation damage induced during the years of data taking [19].

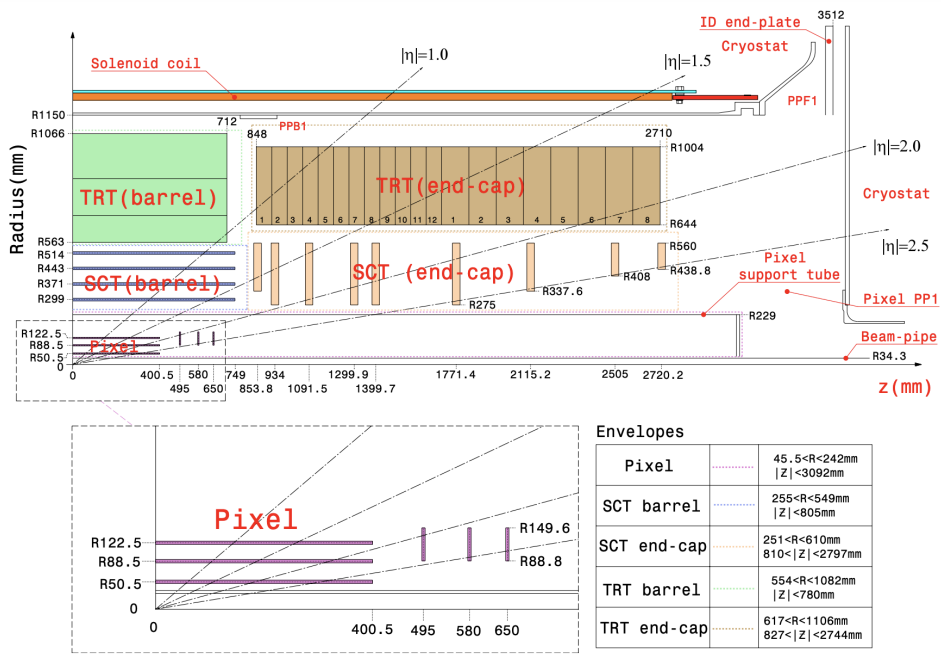


Figure 4.3: Planar view at a quarter section of the ATLAS Inner detector. [19]

straw tubes, each of them 4 mm in diameter, put next to each other (see figure 4.2). The length of the tubes varies across the detector from 144 cm long tubes in the barrel and 39 cm long tubes in the end-cap region. [19, 23] The TRT is used both for the tracking and electron identification by detecting transition radiation X-ray photons in an Xe-based working gas mixture.

4.4 Calorimeter

Calorimeters are detectors to measure the energy of produced particles. ATLAS calorimeters cover the range $|\eta| < 4.9$ and use various techniques suited for varying requirements of the physics processes of interest and of the radiation environment over this large pseudorapidity range. Over the pseudorapidity range corresponding to the inner detector, the fine granularity electromagnetic calorimeter is ideally suited for precision measurements of electrons and photons.

The thickness of the calorimeter is an important design parameter of the system because it has to contain electromagnetic and hadronic showers and must also limit punch-through to the muon system. For this reason, the thickness of the electromagnetic calorimeter, in radiation lengths, is in the barrel section $> 22 X_0$ and in the end-cap section $> 24 X_0$. The approximate 9.7 interaction lengths (λ) of active calorimeter in the barrel (10 λ in the end-caps) are adequate to provide good resolution for high energy jets. [19]

The section view through the ATLAS calorimeter system is shown in figure 4.4. The whole calorimeter is split into two major components based on their general purpose.

- **The electromagnetic calorimeter** is a detector to measure the energy of particles interacting through the electromagnetic interaction⁵. Because these particles get stopped first when traversing through matter, the electromagnetic calorimeter forms the inner part of the calorimeter system. As other parts of the ATLAS detector, it is divided into a barrel part ($|\eta| < 1.475$) and two end-cap components ($1.375 < |\eta| < 3.2$), and it is formed by a *LAr calorimeter* – the lead-liquid argon layers with accordion-shaped Kapton electrodes and lead absorber plates as an active medium over its full coverage.

On the one hand, the advantages of using liquid-argon technology are the detector uniformity, radiation hardness, and stability with time. On the other hand, it needs cryogenics for cooling, which adds dead material, and it has a slow charge collection time of 450 ns (see figure 4.5) at nominal operational voltage 2 kV. This is much longer than 25 ns spacing between bunches, and it could create problems when reading out the electromagnetic calorimeter. This is solved by integrating the signal current over a fixed time window of 50 ns, which is the pulse full width at half maximum given by the pulse pulse-shaping electronics. A bipolar shaping of the pulse with positive and negative output, as shown in figure 4.5, also ensures that the signal induced by out-of-time pile-up averages to zero.

- **Hadronic calorimeter** is designed to stop and measure energies of particles interacting through the strong interaction, and it consists of two different technologies. The first is a *tile calorimeter* covering the barrel sections in the range of $|\eta| < 1.7$. It is a sampling calorimeter using steel as the absorber and scintillating tiles as the active material. The second technology used in the hadronic calorimeter is again a liquid argon calorimeter installed in the two end-caps and forward regions. It consists of copper plates interleaved with LAr gaps, providing the active medium for this sampling calorimeter.
- **Forward calorimeters** are placed on both ends of ATLAS close to the beam axis in the very forward regions covering pseudorapidity range $3.1 < |\eta| < 4.9$. They are using LAr technology, and they are placed in the same cryostat as end-cap calorimeters. The forward calorimeters are split into three 45 cm deep modules, the first of which is the electromagnetic module, and two are hadronic modules.

4.5 Magnets

In order to be able to measure the momentum of charged particles, ATLAS features a unique system of four large superconducting magnets of size 22 m in

⁵these are mainly electrons, positrons, and photons

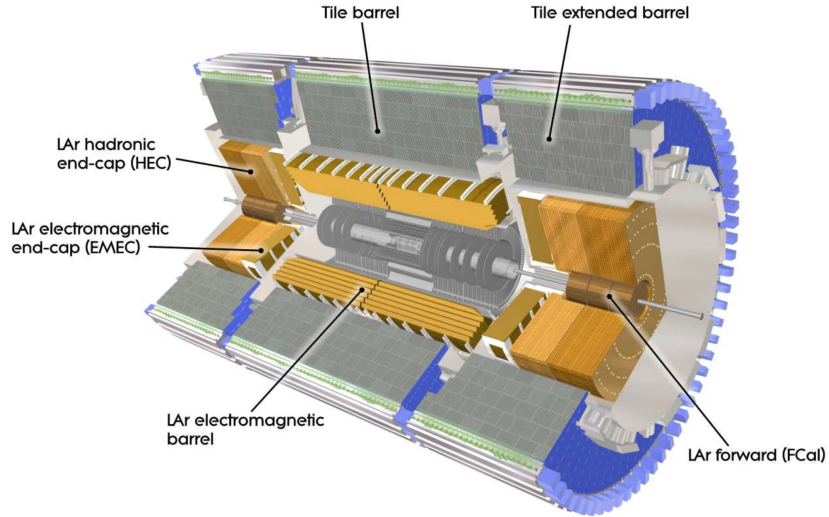


Figure 4.4: Visualisation of the ATLAS calorimeter system – cut-away view [19].

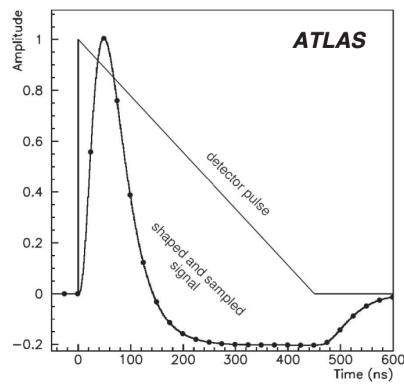


Figure 4.5: Shapes of the LAr calorimeter current pulse in the detector and of the signal output from the shaper chip [24]. The negative lobe of the pulse causes some cells in the calorimeter to have negative energy deposits.

diameter and 26 m in length. The magnet system can be split into two major components, which are:

- **a solenoid** – magnet aligned on the beam axis and providing an axial magnetic field of 2 T for the inner detector.
- **a toroid** – consisting of barrel toroid and two end-cap toroids which produce a toroidal magnetic field of approximately 0.5 T and 1 T for the muon detectors in the central and end-cap regions, respectively.

Central solenoid

The central solenoid is designed to provide an axial magnetic field of 2 T in the central barrel section, and stores energy of 38 MJ. In order to achieve the desired calorimeter performance, the layout was optimized carefully to keep the material thickness in front of the calorimeter as low as possible, resulting in the solenoid assembly contributing a total of 0.66 radiation lengths. The outer diameter of the solenoid is 2.56 m, and its axial length is 5.8 m.

Barrel toroid

The barrel toroid encloses the cylindrical volume surrounding the calorimeters and both end-cap toroids. It consists of eight coils, providing magnetic field of 4 T (value on the superconductor), with stored energy of 1.08 GJ. The barrel toroid overall size is 25.3 m in length, with inner and outer diameters of 9.4 m and 20.1 m, respectively, and its working point temperature is 4.7 K. [19] The picture of the ATLAS barrel toroid can be seen in figure 4.6a.

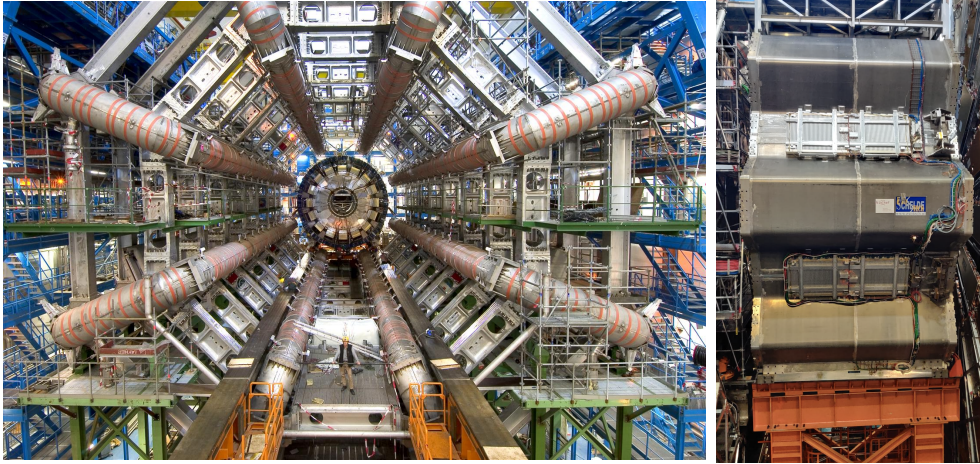
End-cap toroids

The purpose of end-cap toroids is to generate the magnetic field required for optimizing the bending power in the end-cap regions of the muon spectrometer. It provides magnetic field of 4 T (value on the superconductor) and each end-cap toroid can store energy of 0.25 GJ. The picture of the end-cap toroid taken during the year-end technical stop in 2023 can be seen in figure 4.6b.

4.6 Muon Spectrometer

The muon spectrometer (MS) is located at the outer part of the ATLAS detector and is designed to detect muons exiting the barrel and end-cap calorimeters and to measure their momentum in the pseudorapidity range $|\eta| < 2.7$. The momentum measurement is based on the estimation of the track bending inside the magnetic field provided by the ATLAS magnets.

In the barrel region, the precision momentum measurement is performed by the precision-tracking chambers located on and in between eight coils forming



(a) Barrel toroid during installation [25].

(b) End-cap toroid

Figure 4.6: The view at the barrel and end-cap toroid magnets.

the superconducting barrel toroid magnet. These chambers are arranged in the barrel section in three concentric cylindrical shells around the beam axis at radii of approximately 5 m, 7.5 m, and 10 m. On the contrary to the barrel region, muon chambers in the forward regions are organized into large wheels, perpendicular to the z -axis and located at distances of $|z| \approx 7.4$ m, 10.8 m, 14 m, 21.5 m from the interaction point.

In the range of $|\eta| < 2.7$, the precision measurement is performed by the *Monitor Drift Tube chambers* (MDT) that are composed of three to eight layers of drift tubes. These gaseous detectors are operated at an absolute pressure of 3 bar, achieving an average resolution of $80 \mu\text{m}$ per tube.

Until the end of Run 2, multiwire proportional chambers with cathode plates segmented into strips were used in the forward regions. ($2 < |\eta| < 2.7$). These were called *Cathode-Strip Chambers* (CSC), and they were used in the innermost tracking layer due to their higher rate capability and time resolution. During the Long Shutdown 2, the first muon station in the pseudorapidity region of $1.3 < |\eta| < 2.7$, called Small Wheel, was replaced by the new detector segment called New Small Wheel (NSW) [26]. NSW uses large-size multi-gap resistive strips Micromegas technology along with the small-strip Thin Gap Chambers, and it is part of the detector upgrade for the high luminosity stage of the LHC.

One of the essential design criteria of the muon system is the capability to trigger on muon tracks, which requires a system with low latency. For this reason, the set of precision-tracking chambers has been completed by the system of fast-tracking chambers, which are able to deliver track information within a few tens of nanoseconds after the passage of the particle. In the barrel region ($|\eta| < 1.05$), *Resistive Plate Chambers* (RPC) were installed for this purpose, while in the end-cap regions ($1.05 < |\eta| < 2.4$) *Thin Gap Chambers* (TGC) were chosen. [19]

The model of the ATLAS Muon Spectrometer is shown in figure 4.7.

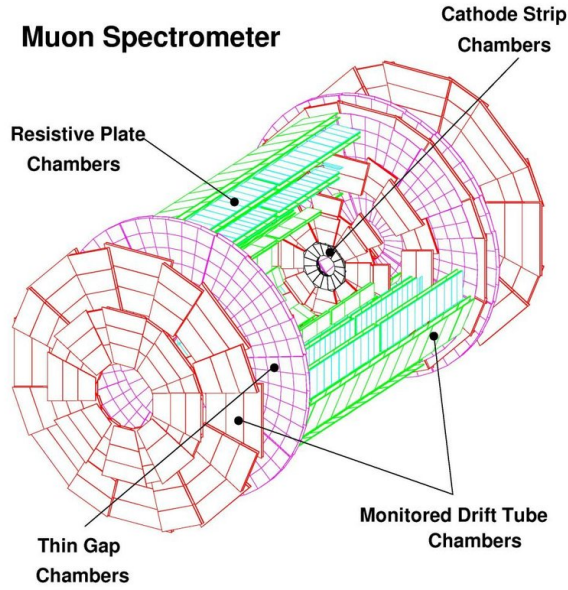


Figure 4.7: Model of the ATLAS Muon Spectrometer with different subdetector technologies highlighted in it. [27] Cathode-Strip Chambers were replaced, together with the rest of the first muon tracking station, with the New Small Wheel, which is not shown in the figure.

4.7 Trigger and Data Acquisition System

The rate of the collisions inside ATLAS is nearly 40 MHz⁶. If we wanted to store every event, where the average size of one event is about 2.5 MB, this would lead to the amount of data that would not be feasible to store and process. That's why we need the Trigger and Data Acquisition System (TDAQ), which is responsible for deciding which events are going to be stored. Because of the complex decision that has to be made, the trigger system is split into two levels: *Level-1 trigger* (L1) and the *High-Level Trigger* (HLT).

L1 makes the quick decision, and if the event passes selections at Level-1, the L1 accept (L1A) signal is issued, and the event is passed to the second processing stage, which is the HLT. The selection criteria at the HLT are based on more complex algorithms compared to those running at Level 1. The collection of all L1 and HLT selection criteria, called triggers, is called *trigger menu*.

L1 and HLT are discussed in subsections below.

Level-1 Trigger

The main goal of the Level-1 trigger is to limit the input rate of approximately 40 MHz to an output rate of 100 kHz, which can be further used as an input for the HLT. Due to the high event rate inside the ATLAS detector during LHC

⁶40 MHz is a bunch crossing frequency, but not all bunches are filled, which results in slightly lower collision rate.

data taking, the decision about which events will pass to the HLT has to be made within a latency of $2.5\,\mu\text{s}$. For this reason, only the information from the Muon Spectrometer and the Calorimeter is used.

Because the trigger decision has to be made in a very short time, only partial information about the event can be used at this stage. Such pieces of information are signatures from high- p_T muons, electrons, photons, jets, and τ -leptons decaying into hadrons. It also selects events with large missing transverse energy E_T^{miss} . These pieces of information are provided by *Level-1 Calo*, *Level-1 Muon*, and *Level-1 Topo* subsystems (see figure 4.8).

- **Level-1 Calo** (L1Calo) system is used to analyze analog signals coming from the ATLAS calorimeters. In Run 1 and 2, the system was receiving information from 7200 trigger towers, which are segments of the calorimeter formed by calorimeter cells of size 0.1×0.1 (barrel) up to 0.4×0.4 (end-cap) in $\eta - \phi$ plane. This information was passed to *Pre-processor* from where it went to *Cluster Processor* (CP) and *Jet/Energy-sum Processor* (JEP), which were used for the object identification. The so-called legacy system just mentioned was replaced by the new Level-1 Calo system using the *Feature Extractor* (FEX), which is further split into three subsystems:
 - electron Feature Extractor (eFEX) for the reconstruction of e/γ and τ candidates
 - jet Feature Extractor (jFEX) for identification of jet candidates, E_T^{miss} measurement, and τ candidates
 - global Feature Extractor (gFEX) for jet candidates and for the energy measurement

FEX uses information of the finer granularity from the calorimeter than the legacy system, where each calorimeter tower is split into ten *supercells*. Thanks to that it is able to provide better triggering decision than the legacy system.

- **Level-1 Muon** (L1Muon) is designed for fast muon reconstruction, and it searches for the coincident muon hits in the RPCs and TGCs. For the candidate muon objects, the *Regions of Interest* (RoIs) are created for subsequent processing by the HLT.
- **Level-1 Topo** (L1Topo) applies more complex topological cuts on electrons, jets, taus, and muons. It receives *Trigger Objects* containing kinematic and further quality information from the L1Calo and L1Muon systems, and it applies topological selection.

The essential function of the L1 trigger is to unambiguously identify a bunch crossing of interest, which is a challenging task, considering the 25 ns spacing between bunches and the fact that the time width of the calorimeter signal

spreads over several bunch crossings. That is why there have to be temporary memory buffers, called *Read-Out Buffers* (ROB), which allow waiting for the signal formation and decision-making but also for the propagation of the signal through cables. This all has to be achieved in the time window of fixed length of $2.5\,\mu\text{s}$.

The final decision if the event is going to be discarded or used for further processing is made by the *Central Trigger Processor* (CTP), which combines information about various object types and triggers on events defined in *trigger menus*. These L1 trigger menus can be programmed with up to 256 distinct items, each item being a combination of requirements on the input data [19]. Once the L1 accept decision has been made, the event goes as an input to the HLT.

High Level Trigger

The HLT is a software-based trigger, which means that it can apply more sophisticated event selection and reduces the rate of 100 kHz further down to 1 kHz. These algorithms are running on 2800 CPU cores using reconstruction techniques similar to those used in the offline event reconstruction described in more detail in chapter 5.

After the Level-1 trigger issues the L1 accept signal, data are passed to the HLT, which runs an online event reconstruction to be able to use more complex triggers. A typical online reconstruction sequence consists of dedicated fast triggering algorithms to provide early background rejection, followed by more precise CPU-intensive algorithms that are similar or identical to those used for offline reconstruction. Reconstruction algorithms process detector data to extract features, and hypothesis algorithms test the selection hypothesis for all active *trigger chains*, which is the set of L1 trigger items and series of HLT algorithms organized into distinct steps. The reconstruction is done either in the full detector volume or in restricted *Regions-of-Interest* (ROIs), which are seeded by the objects identified at Level-1. The approach employing ROIs significantly reduces processing time without negatively impacting the selection performance.

After the event passes the HLT selection, it is permanently stored. The resulting event rate of about 1 kHz passing the HLT selections is then organized according to the purpose of selections applied into different data *streams*. There are five different types of streams:

- **Physics streams** contain events collected for the offline analysis. This stream dominates the trigger rate and it is running in multiple instances for the different physics analysis groups.
- **The express stream** contains a small fraction of events from physics streams used for real-time reconstruction in order to provide quick data quality checks and monitoring
- **Debug streams** stores events for which the trigger could not make a decision. These are used for debugging purposes.

- **Calibration streams** are used for the HLT calibration or dedicated sub-detectors. In case the event is used for the sub-detector calibration, generally, only a fraction of the detector information is recorded in order to reduce bandwidth.
- **Trigger-Level Analysis streams** contains reduced detector information and reconstructed trigger objects for physics analysis at the trigger stage. In this approach, a bias introduced by trigger selections can be reduced, and events that could be otherwise discarded are stored. Contrary to physics streams, it lacks the precise object calibration that cannot be performed online.

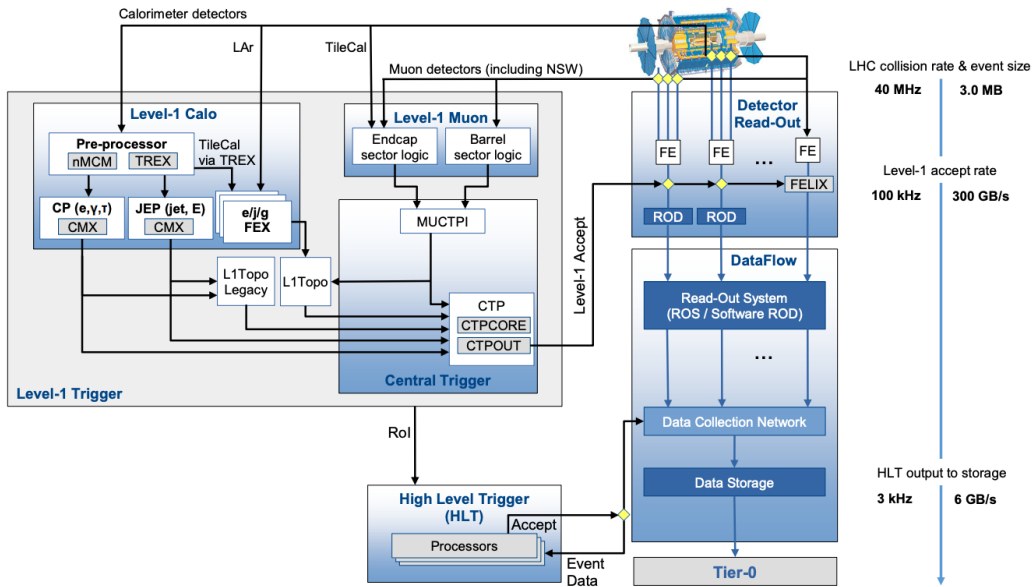


Figure 4.8: Schematic illustration of the structure of the ATLAS TDAQ system in Run 3 [28]. The data from L1Calo, L1Muon, L1Topo, and Central Trigger are sent to the readout system, which in Run 3 consists of Front-End Link Exchange (FELIX) readout system and software running on the commodity servers Software Read-Out Drivers (SW ROD). Data from SW ROD are then routed on-demand to HLT processing nodes.

Event reconstruction

5.1 Introduction

The complex information from various subdetectors described in the previous section must be combined to provide a detailed picture of what is happening during proton-proton collisions, which is the information that can be useful for physics searches. For this purpose, we want to know the four-vectors of physics objects rather than raw information from the detector. This process is called event reconstruction, and it is done by the reconstruction software called Athena [29].

The reconstruction is performed in two instances:

Online reconstruction is the real-time event reconstruction done while ATLAS takes the data. The information is used for triggering, and algorithms running in this stage have to be efficient in order to be able to be performed on data coming in high rates.

Offline reconstruction is performed on recorded data, not in real-time. Information reconstructed at this stage is used in physics analyses produced by the experiment since it does not have strict constraints on the processing time.

Both of these reconstructions are important. While the online reconstruction is used for the trigger decision and has to be done in a short time¹, the offline reconstruction is used for the majority of physics analyses. Due to the short time in which the online reconstruction has to be performed, the algorithms running at this level often need optimization, and the precision of this reconstruction

¹The HLT decision, where the online reconstruction is used, has to be made in order of $\mathcal{O}(100)$ ms.

might be slightly worse than the precision of the reconstruction done offline, which does not have strict time limitations.

This chapter is an overview of event reconstruction techniques used in ATLAS. It describes techniques used at the HLT level for Run 3, which is similar to offline reconstruction in many aspects; however, it runs an optimized or modified version of algorithms used offline. This, for example, is the case of the track extrapolation, which was optimized for Run 3 to allow running Particle Flow jet reconstruction at the HLT level, and will be discussed in the chapter 6.

In addition to the online reconstruction for the HLT in Run 3, some aspects of the offline reconstruction in Run 2 will also be discussed since this was used for searches described in chapter 8. More emphasis, however, will be on the jet reconstruction because the author of this thesis was involved in the optimization of track extrapolation for Particle Flow jet reconstruction at the HLT and also because searches presented in chapter 8 are targeting the final state with multiple b -jets.

5.2 Track and vertex reconstruction

The essential part of the event reconstruction consists of reconstructing the trajectories of tracks inside the detector. This is important in order to find the primary vertex of the interaction, which is considered to be the hard scatter point of two interacting protons and having this information is crucial for pile-up suppression. The second purpose of tracking is to determine the track parameters.

This section describes tracking inside ID. Tracking in the muon spectrometer used for the muon reconstruction is described separately in the subsection 5.6.2.

There are five distinct track parameters describing the track. The first is the *transverse impact parameter* d_0 , defined as the closest distance in the transverse plane to the reference position. The second parameter is the *longitudinal impact parameter* z_0 defined, similarly as a previous parameter d_0 , as a distance in the longitudinal plane to the reference position. The third and fourth parameters are polar and azimuthal angles θ and ϕ , which are the angles describing the three-dimensional momentum of a track at the point of the closest approach specified by transverse and longitudinal impact parameters. The last parameter describing the track is the ratio of $|q|/p$, which is inversely proportional to the radius of curvature of the track. The sign of the charge can be determined from the direction of curvature in the transverse plane in which the trajectories are curved. The track reconstruction, also called tracking, in ATLAS uses two strategies [30].

The first is *inside-out* track finding. In this step, the algorithm looks for a track seed in the pixel and SCT detectors, which are collections of three space points from unique layers of the pixel or SCT detectors. If the seed passes certain quality criteria, such as p_T and impact parameter selection, they are grouped together by a window search, which is performed using a combinatorial Kalman

filter² [31]. During this process, ambiguities due to incomplete track segments or purely random hit combinations can arise, and they can be resolved by selecting the best tracks using the score assigned based on the track quality criteria, such as number of hits along the track and χ^2 . After resolving the ambiguities in the track-finding process, the extension of tracks from the pixel and SCT detectors to the TRT is then performed. Any track successfully extended from the silicon detector to the TRT is said to have a TRT extension.

The inside-out tracking is then followed by *outside-in* tracking, which extends tracks from the TRT back to the silicon tracker. This extension is seeded by the electromagnetic calorimeter, and it uses only hits that are not already used for existing tracks from the inside-out pass.

Resulting tracks from both inside-out and outside-in strategies form the final set of reconstructed tracks used to reconstruct primary vertices. This step is divided into two stages: a) the primary vertex finding algorithm, dedicated to associating reconstructed tracks to the vertex candidates, and b) the vertex fitting algorithm, dedicated to reconstructing the vertex position and its corresponding error matrix [32].

After the inside-out and outside-in tracking, the *large radius tracking* [33] is executed. The large radius tracking sequence is executed after the primary tracking iteration using exclusively the detector hits not already assigned to primary tracks, ensuring a completely independent collection of tracks. This third instance of tracking is used to reconstruct tracks with a large radius or impact parameter. It operates in a similar way as inside-out tracking iteration, but it is specifically optimized for the long-lived particle signatures, with looser requirements on the track parameters compared to the first two iterations of tracking. Moreover, the seed extension uses a sequential instead of a combinatorial Kalman filter.

The approach above is used for the offline tracking. The online tracking sequence used at the HLT is modified and consists of the following steps. The track reconstruction starts with the data preparation in the ID, where space points using information from the pixel and the SCT are used. This step makes use of the *Regions-of-Interest* (RoIs), which are formed by the Level-1 trigger based on the information available from calorimeters and muon spectrometer. After the data preparation, the fast-tracking step takes place, which runs a custom pattern recognition and fast-track fit. Following this, a precision tracking step takes the tracks reconstructed by the fast-tracking and fits them again but with the offline reconstruction code, where the pattern recognition is done by a specifically trained neural network. Additionally, tracks are extended to the TRT.

In Run 2, the track reconstruction accounted for around 64% of the total ATLAS event reconstruction CPU time. This fraction was reduced for Run 3 down to 40% at $\langle\mu\rangle = 50$ [34].

The efficiency of the online versus offline reconstruction is assessed as a ratio of reconstructed tracks between online and offline reconstruction, and despite

²The silicon pattern recognition algorithm that combines track seeds together.

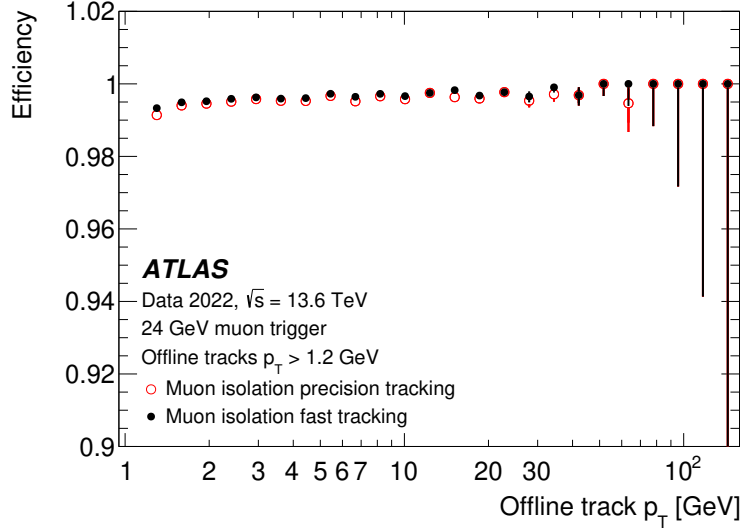


Figure 5.1: The tracking efficiency for non-muon tracks reconstructed in the muon isolation RoI centred on the trigger muon selected by the 24 GeV [35]

it being dependent on the type of object, it is close to 99%. As an example, the tracking efficiency for non-muon tracks reconstructed inside muon isolation ROIs³ of muon energy 24 GeV is shown in figure 5.1.

5.3 Topological clusters reconstruction

In order to correctly attribute energy deposits in the calorimeter to individual objects, reconstruction of which is described in later sections of this chapter, deposits from calorimeter cells are grouped together to form three-dimensional regions of space called *clusters*. This section briefly describes the reconstruction of calorimeter clusters using a topological cell clustering algorithm. These clusters are then called topological clusters, or simply *topo-clusters*, and they are currently used for the higher object reconstruction as described in the rest of the chapter 5.

The topo-clustering algorithm is based on the absolute value of the cell energy significance [36] defined as

$$\epsilon_{\text{cell}}^{\text{EM}} = \frac{E_{\text{cell}}^{\text{EM}}}{\sigma_{\text{noise,cell}}^{\text{EM}}}, \quad (5.1)$$

which can be viewed as a ratio of the cell signal over the expected noise $\sigma_{\text{noise,cell}}^{\text{EM}}$. Both $E_{\text{cell}}^{\text{EM}}$ and $\sigma_{\text{noise,cell}}^{\text{EM}}$ are measured at the electromagnetic scale. This reconstructs energy deposits by electrons and photons correctly but does not include any corrections for the loss of signal for hadrons due to the non-compensating character of the ATLAS calorimeters.

³A muon track is required to be isolated with respect to other tracks from the interaction.

Topo-clusters are formed by a growing-volume algorithm, which can be described as follows:

1. The clustering starts from a cell with $|\epsilon_{\text{cell}}^{\text{EM}}| > 4$. This value was derived from the response optimizations and the relative energy resolution for charged pions in test beam experiments.
2. The cluster is then extended around previously selected cell and neighboring cells are added. Added cells significance has to fulfill $|\epsilon_{\text{cell}}^{\text{EM}}| > 2$.
3. The last step adds the cluster boundaries by adding cells with $|\epsilon_{\text{cell}}^{\text{EM}}| > 0$

The above algorithm is repeated until all topologically connected cells are found. However, clusters built in this way can be too large to provide a good measurement of the energy flow from the particles generated in the recorded event. In particular, local signal maxima within a cluster typically indicate the presence of multiple particles in close proximity. The local maximum in this case is defined by $E_{\text{cell}}^{\text{EM}} > 500 \text{ MeV}$ and only electromagnetic sampling layers EMB2, EMB3, EME2, EME3, FCALO are considered.

The calorimeter cell can be shared by only two signal maxima. In case there are more signal maxima, the cell is assigned to the two highest-energy clusters after the splitting, which is done in the following way. The sharing of signal between two clusters with energies $E_{\text{cluster},1}^{\text{EM}}, E_{\text{cluster},2}^{\text{EM}}$ is expressed in terms of two geometrical weights $w_{\text{cell},1}, w_{\text{cell},2}$, which are computed based on the distance of the cell to the center of gravity of two clusters (d_1, d_2).

$$w_{\text{cell},1} = \frac{E_{\text{cluster},1}^{\text{EM}}}{E_{\text{cluster},1}^{\text{EM}} + r E_{\text{cluster},1}^{\text{EM}}} \quad (5.2)$$

$$w_{\text{cell},2} = 1 - w_{\text{cell},1} \quad (5.3)$$

$$r = e^{d_1 - d_2} \quad (5.4)$$

Topo-clusters reconstructed in this way are used as inputs in further reconstruction steps described in the following sections.

5.4 Particle Flow

The ultimate goal of collider experiments is to accurately reconstruct all particles and objects created during collisions because detailed information about these objects can help to understand underlying physics processes better. The task becomes more difficult in an environment with a higher pile-up, which is the case of the big LHC experiments, such as ATLAS. The goal of Particle Flow algorithms is to identify the individual particles inside the detector and combine information from the different subdetectors in an optimal way. One of the typical Particle Flow approaches uses a combination of tracker and calorimeter

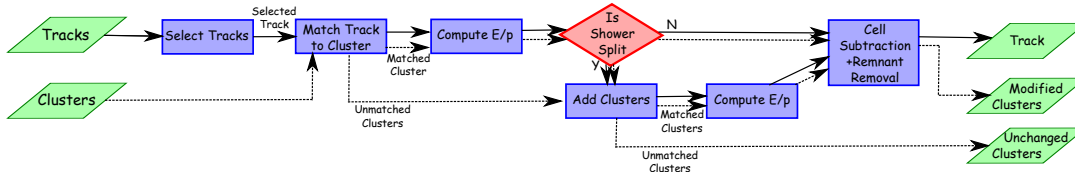


Figure 5.2: Flow chart showing individual steps of the ATLAS Particle Flow algorithm. [37]

subsystems. It exploits the fact that the charged particles can be measured much better with the tracker when their p_T is low because the track bending inside the magnetic field is bigger. At the same time, the calorimeter provides a better measurement of high p_T where track bending is not so significant. In addition to the facts mentioned above, it can help to identify neutral particles close to charged objects after the association between charged tracks and calorimeter objects. It also helps to mitigate pile-up jets and it improves the E_T^{miss} resolution.

The Particle Flow algorithm has been used in ATLAS since Run 2 for offline event reconstruction and, since the beginning of Run 3, it is also used for reconstruction at the HLT. It combines information from the inner detector and calorimeter, and it can reconstruct hadronic jets, as well as the soft activity in the event, which is crucial for the E_T^{miss} reconstruction as described in sections 5.5 and 5.7.

The input to the algorithm are tracks and topo-clusters, and the output is the *Particle Flow Objects* (PFOs), which represent particles inside the detector. These reconstructed objects are then used for the jet reconstruction. The strength of this approach is based on the combination of the information from two subdetectors, which mitigates double energy counting and can better identify neutral particles that do not leave tracks inside the tracking detector.

The reasons why Particle Flow used in ATLAS improves the resolution of individual particles are summarized below [37]:

- The momentum resolution of the tracker is better than the resolution of the calorimeter for low-energy charged particles.
- Angular resolution of the single charged particle reconstructed using the tracker is much better than that of the calorimeter.
- Charged particles with low p_T from hadronic jets are swept out of the jet cone by the magnetic field. However, thanks to using the track's azimuthal coordinate at perigee, these particles are clustered into the jet correctly.
- In-time pile-up interactions can be mitigated by using the information about the hard-scatter vertex, simply by rejecting signals originating from pile-up vertices.

The algorithm consists of five main steps, which are depicted in figure 5.2 and described more in detail in subsections 5.4.1 - 5.4.4.

5.4.1 Track selection

The first step is the track selection step, which aims to select tracks that fulfill stringent quality criteria. Each selected track must have at least nine hits in the silicon tracker and must have no missing pixel hits when such hits would be expected [38, 37]. This is to minimize the number of badly measured tracks. In addition, tracks are required to be within $|\eta| < 2.5$ and $p_T > 0.5$ GeV. Tracks with $p_T > 40$ GeV are excluded from the algorithm because such energetic particles are often poorly isolated from nearby activity, compromising the accurate removal of the calorimeter energy associated with the track. Finally, tracks matched to medium-quality electrons or muons are excluded as well because the algorithm is optimized for hadronic shower subtraction.

5.4.2 Matching tracks to topo-clusters

In order to remove energy from the calorimeter where particle formed a single topo-cluster, the algorithm attempts to match each selected track to one topo-cluster. In order to do that, tracks need to be extrapolated from the tracker to the calorimeter because the precise spatial information about the particle's position is available only inside the tracker. This part is computationally expensive, and it was one of the bottlenecks in using the Particle Flow algorithm at the HLT level before the start of Run 3. Track extrapolation and its optimization for the HLT Particle Flow jet reconstruction for Run 3 is discussed in detail in the separate chapter 6.

The distance $\Delta\phi$ and $\Delta\eta$ between the barycentre of the topo-cluster and the track, extrapolated to the second layer of the EM calorimeter, are computed for each topo-cluster. The distance metric defined in equation 5.5 is introduced and used to rank topo-clusters for each track.

$$\Delta R' = \sqrt{\left(\frac{\Delta\phi}{\sigma_\phi}\right)^2 + \left(\frac{\Delta\eta}{\sigma_\eta}\right)^2} \quad (5.5)$$

σ_η and σ_ϕ are the angular widths of topo-clusters computed as a standard deviation of the displacement of cells constituting the topo-cluster with respect to its barycentre.

The preliminary selection of topo-clusters to be matched to the tracks is performed by requiring that $E^{\text{clus}}/p^{\text{trk}} > 0.1$, where E^{clus} is the energy of the cluster and p^{trk} is the track momentum. This selection criterion can reject about 10% of incorrect topo-clusters for particles in the range $1 < p_T < 2$ GeV, and about 30 – 40% for incorrect topo-clusters for tracks with $p_T > 5$ GeV.

Next, the attempt to match tracks to one of the preselected topo-clusters is made based on the $\Delta R'$ metric. Figure 5.3 shows that the correct topo-cluster almost always lies at a small $\Delta R'$ relative to other clusters. The closest preselected topo-cluster in $\Delta R'$ is taken to be the matched topo-cluster, and if no preselected topo-cluster is found in a cone of size $\Delta R' = 1.64$, it is assumed

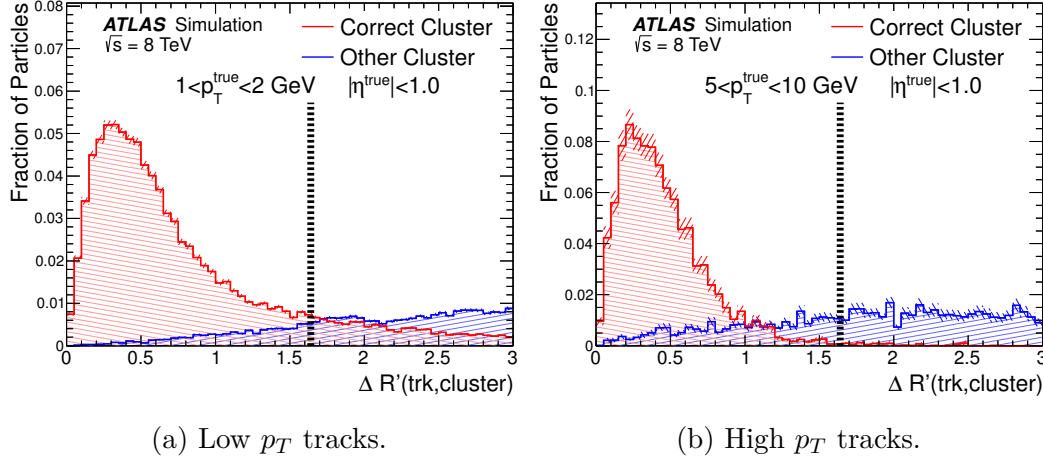


Figure 5.3: The distributions of $\Delta R'$ for the topo-cluster with $> 90\%$ of the true energy of the particle and the closest other topo-cluster, both satisfying $E^{\text{clus}}/p^{\text{trk}} > 0.1$, for the data from the dijet sample in the central region. The black vertical line marks the cut of $\Delta R' = 1.64$. [37]

that this particle did not form a topo-cluster in the calorimeter. In that case, no energy subtraction is done for such a track.

5.4.3 Energy subtraction

The energy subtraction step is the procedure that removes deposits of charged particles from the calorimeter and allows the identification of neutral clusters that were merged with these charged objects.

In order to remove energy corresponding to the given track correctly from the calorimeter, the expected energy deposit has to be estimated. That is based on the fact that the expected energy deposit of the track can be computed as

$$\langle E_{\text{dep}} \rangle = p^{\text{trk}} \langle E_{\text{ref}}^{\text{clus}} / p_{\text{ref}}^{\text{trk}} \rangle. \quad (5.6)$$

The scaling factor $\langle E_{\text{ref}}^{\text{clus}} / p_{\text{ref}}^{\text{trk}} \rangle$ depends on the detector geometry and the shower development is captured by binning the scaling factor by p_T and η of the track, as well as the layer of highest energy density.

The layer of the highest energy density is the layer of the calorimeter having the most significant increase in energy density as a function of the number of interaction lengths from the front face of the calorimeter for a given topo-cluster. Estimating the layer of the highest energy density is crucial for energy subtraction because the subtraction starts in this layer before progressing to the less regular shower periphery. The energy density is calculated for the j -th cell in the i -th layer of the calorimeter as

$$\rho_{ij} = \frac{E_{ij}}{V_{ij}} \left(\text{GeV}/X_0^3 \right) \quad (5.7)$$

where V_{ij} is the cell volume expressed in radiation lengths.

It is not always the case that the particle deposits the energy only in one cluster. In that case, the split shower recovery procedure is performed to attribute the energy to the track correctly. This step is done before proceeding to the energy subtraction itself and is based on estimating the significance of the difference between the expected energy and that of the matched topo-cluster.

After estimating expected energy deposits and recovering split showers, the energy subtraction can start. If the energy of a cluster is smaller than the expected energy deposit, the cluster is removed. In case the expected energy deposit is smaller than the energy in the topo-cluster, the iterative process of energy removal starts. The removal starts in the layer of the highest energy density, and proceeds in concentric rings centered around the layer with the highest energy density [37].

5.4.4 Remnant removal

If the energy remaining in the cells and topo-clusters that stay after the energy subtraction is consistent with the width of $E_{\text{ref}}^{\text{clus}}/p_{\text{ref}}^{\text{trk}}$ distribution⁴, then the topo-cluster is considered to be produced by the shower fluctuation of a single particle and the remaining energy in these cells is removed. However, if it is not consistent with $E_{\text{ref}}^{\text{clus}}/p_{\text{ref}}^{\text{trk}}$ distribution, then the deposit was probably created by multiple close-by particles and the energy is retained. After this last step, the set of selected tracks and remaining topo-clusters in the calorimeter should represent the reconstructed event with no double counting of the energy between the subdetectors, which is why the Particle Flow approach is so powerful.

5.4.5 Particle Flow jet building

After matching tracks to topo-clusters and identifying neutral clusters, the Particle Flow Objects are used as an input to the anti- k_T jet clustering algorithm, which is described in more detail in section 5.5.1.

The algorithm is executed on two different types of inputs. The first are the charged PFOs, formed by isolated tracks or tracks and topo-clusters matched by the PFlow algorithm associated to the primary vertex. The second type of input are neutral PFOs, which are formed by topo-clusters not associated with any track or calorimeter signals surviving the subtraction procedure.

The Particle Flow algorithm improves the jet energy and mass resolution at low transverse momentum. It leads to better pile-up stability than the one obtained from jets reconstructed from topo-clusters [39]. This is also why using Particle Flow jet reconstruction for the HLT trigger helped improve the ATLAS overall triggering capability.

⁴If the energy is less than $1.5\sigma(E_{\text{dep}})$

5.5 Jet reconstruction

Jets are the most common signature at the LHC and are the key ingredient for many searches in ATLAS. They are sprays of collimated particles created in high energy regimes thanks to the radiative showering of strongly interacting particles, such as quarks and gluons.

When these collimated sprays of particles travel through the detector, they usually leave high energy deposits inside the calorimeter localized within the narrow cone, leading to significant signals in groups of adjacent calorimeter cells. These are called topo-clusters and are identified by dedicated clustering algorithms as described in section 5.3.

When the topo-clusters are formed, they are used as an input for the jet-building algorithm described in section 5.5.1.

5.5.1 Jet building algorithms

Algorithms used for the jet reconstruction take four-momenta of input objects and cluster them together. There are different approaches to doing that. Objects used for the clustering can be either topo-clusters or Particle Flow objects described more in detail in sections 5.3 and 5.4 respectively. In Runs 1 and 2, EMTopo algorithm [40] was used for the jet reconstruction. This algorithm uses topo-clusters as an input. However, in Run 3, EMTopo jet reconstruction was replaced by Particle Flow, which uses Particle Flow Objects that combine information from the ID and the calorimeter⁵ as described in section 5.4. The advantage of using Particle Flow objects over simple topo-clusters is the improvement of jet momentum measurements and higher acceptance for low- p_T regimes since the ID can measure tracks of particles with energies as low as a few MeV.

For the jet reconstruction, the ATLAS experiment uses the anti- k_t algorithm, which belongs to the family of k_t algorithms [42, 43]. They are all sequential algorithms that work on the same principle, and we can divide them into three steps that can be summarized as follows:

1. For each pair of objects i, j , distance d_{ij} between these objects is calculated, as well as the distance d_{iB} of each object i from the beam. These distances are defined as

$$d_{ij} = \min(p_{T,i}^{2n}, p_{T,j}^{2n}) \frac{(\Delta R_{i,j})^2}{R^2} \quad (5.8)$$

$$d_{iB} = p_{T,i}^{2n} \quad (5.9)$$

⁵EMTopo is still used in a few cases such as long-lived particle searches where PFlow's track use is suboptimal. [41]

where $p_{T,i}$ and $p_{T,j}$ are four-momenta of objects⁶, ΔR_{ij} is the geometrical distance between objects i and j in $\eta - \phi$ plane defined as

$$\Delta R_{ij}^2 = (\eta_i - \eta_j)^2 + (\phi_i - \phi_j)^2. \quad (5.10)$$

R is generally called the jet radius and represents the only free parameter of the algorithm that is configurable by the user. Finally, n is the parameter distinguishing individual k_t algorithms, and we will discuss it later.

2. From distances computed in the previous step, find the smallest d_{ij} and d_{iB} . If $d_{ij} < d_{iB}$, recombine objects i and j into single object. If the $d_{ij} > d_{iB}$, call i the jet and remove it from the list of objects.
3. Recalculate distances and repeat the steps above until no objects are left in the list.

As mentioned previously, parameter n in equation 5.8 can have different values, which distinguishes different modifications of the k_t algorithms.

- a) $\mathbf{n} = \mathbf{1}$ is known as k_t algorithm. In this case, jets are formed from the soft object first, which can be problematic since the pile-up jets⁷ typically have lower transverse momenta.
- b) $\mathbf{n} = \mathbf{0}$ defines Cambridge-Aachen algorithm. In this case, dependence on transverse momenta vanishes, and jets are formed only based on the geometrical requirements.
- c) $\mathbf{n} = -\mathbf{1}$ is called the anti- k_t algorithm, which is the most widely used case in ATLAS analyses. It uses transverse momenta similarly to k_t algorithm but because of the $\min(\frac{1}{p_{T,i}^2}, \frac{1}{p_{T,j}^2})$, jet formation starts from objects with the highest p_T .

5.5.2 Jet calibration

The ATLAS calorimeters are *non-compensating*, which means that a fraction of the energy invested into breaking nuclear bonds in particles traveling through the detector is not measured. The jet energy scale calibration addresses this issue, but also the fact that the energy scale is influenced by the primary vertex not being directly at the center of the detector, as well as the effect of the pile-up. It is done in several steps, which are shown in figure 5.4 and described in more detail in the text below.

⁶In the original papers [43, 42] transverse momenta are designated by k_t , from which comes the name of this class of algorithms. We decided to keep p_T to keep consistent notation throughout the thesis.

⁷Due to the pile-up, fake jets can be reconstructed. These jets are called pile-up jets and they can be the result of pure stochastic fluctuations of particles inside a specific part of the ATLAS detector, or they can be the result of hard pileup interactions creating real jets having back-to-back topologies.

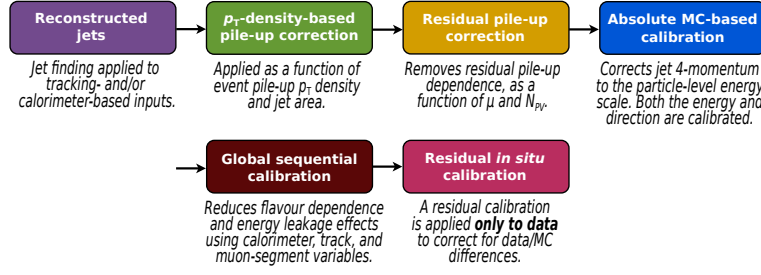


Figure 5.4: Jet calibration procedure used in ATLAS. [44]

- The first step of the calibration procedure accounts for the fact that particles are not coming directly from the center of the detector but from the primary vertex that can be slightly displaced with respect to the detector's center. Considering this fact, coordinates of topo-clusters are recomputed with respect to the primary vertex, resulting in improved η resolution.
- Particles coming from the pile-up collisions can pose a problem in the jet energy estimation because they can be wrongly added to jets from the hard scatter. The second step of the calibration removes the pile-up in two stages. First, the average energy due to the pile-up, estimated by the *random cones* method,⁸ is subtracted from the event. After that, the residual correction is applied. Based on the number of interactions and the event's bunch crossing ID, the effects of in-time and out-of-time pile-up can be disentangled.
- The absolute calibration is to correct jet four-momenta and energy scale. It is derived from Monte-Carlo simulations, where truth jet energy and directions are available.
- The global sequential calibration is also based on the Monte-Carlo simulations, and it uses the jet's global properties, such as the longitudinal structure of the energy depositions within the calorimeters, tracking information associated with the jet, and information related to the activity in the muon chambers behind a jet. This calibration aims to reduce the difference in the calorimeter energy response from jets of different flavors, and also differing responses to quark- and gluon-initiated jets.
- Finally, the in-situ calibration is derived from data to correct the difference between the actual detector data and the Monte-Carlo simulation.

The procedure presented above is used in the offline reconstruction. A similar correction is also made at the HLT level one more step before the residual in-situ

⁸Random cones method is the method to estimate the noise. The energy deposits in the calorimeter are summed at the energy scale of the constituents in circular areas analogous to the jet area for anti- k_t $R = 0.4$ jets. Two such random cone sums, p_T^{c1} and p_T^{c2} , are obtained at random ϕ values and within opposite $\pm\Delta\eta$ regions and the difference between them, Δp_T^{RC} , provides a measure of the random fluctuations of deposited energy.

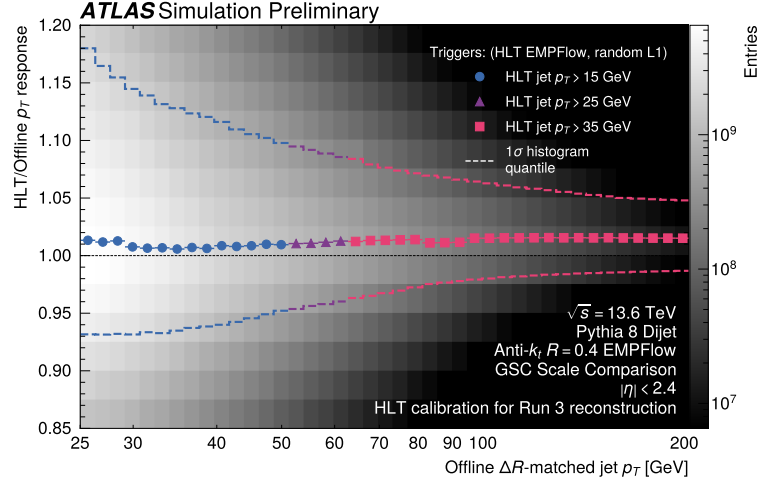


Figure 5.5: HLT jet calibration performance for the year 2023. The plot shows the HLT versus offline jet response as a function of jet p_T . The closer the ratio is to unity, the more similar the performance of offline and online calibration is. [45]

calibration, which corrects trigger-level jets to the scale of offline reconstructed jets. A comparison of HLT versus offline response at the final energy scale in the calibration sequence of the jets for 2023 data is shown in figure 5.5.

5.5.3 Jet-flavor tagging

Jets' properties differ based on the parton from which they were initiated. If the jet is initiated by quarks u or d , it is referred to as *light jet*. When the jet is initiated by c -quark, we call it a c -jet, and if it was initiated by b quark, we call it a b -jet. Identifying the jet type is crucial for offline data analysis and for the trigger to target many processes of interest. The process of the jet flavor identification is called *flavor tagging*.

Many SUSY searches, such as those presented in the chapter 8, consider final states containing b quarks, and the correct b -jet identification, referred to as b -tagging, is essential because it helps to identify given final state and has been studied closely by the ATLAS collaboration. Different multivariate techniques for b -tagging in Runs 2 and 3 involve machine learning algorithms, and due to the rapid development of machine learning, these algorithms have also been evolving quickly in recent years. The fundamental principle used by these algorithms relies on properties of b -hadrons, which typically have a lifetime of about 1.5 ps. Due to that, b -hadrons travel inside the detector of about $c\tau \approx 4.5$ mm, which creates a displaced secondary vertex. This property is shown in figure 5.6 and can be used to identify b -jet, which is why b -tagging algorithms use as inputs reconstructed tracks, primary vertex position, and jets.

In Run 2 at the HLT level, tracks were reconstructed within ROIs for primary vertex finding, and precision tracks were reconstructed within EMTopo jets that pass minimum E_T cut. Then, the probability that the jet originates

from b -quark was evaluated. This was done in two steps. The first step used low-level algorithms that matched tracks to jets, reconstructed secondary vertices, and identified tracks with large impact parameters. The second step ran machine learning algorithms that could discriminate between b -jets, c -jets, or light jets. Since, in Run 2, the precision tracking was performed in all jet-ROIs above a minimum E_T , b -jet selections were the most CPU-intensive selections at the ATLAS HLT. [46].

In Run 3, a new approach was introduced to reduce the CPU needs for b -jet trigger finding while maintaining excellent efficiency for key physics processes. Moreover, ATLAS also unified HLT algorithms with their offline counterparts, meaning that the same algorithms are used in online and offline reconstruction. The new approach consists of running the preselection step referred to as *fast b -tagging* [46], which exploits machine learning techniques, followed by the b -tagging algorithm, which is based on the neural network. This algorithm evolved during Run 3, and the DL1d used at the beginning was replaced by the graph neural network GN1, which was replaced by the improved graph neural network called GN2. A comparison of the performance of the different b -tagging algorithms is shown in figure 5.7.

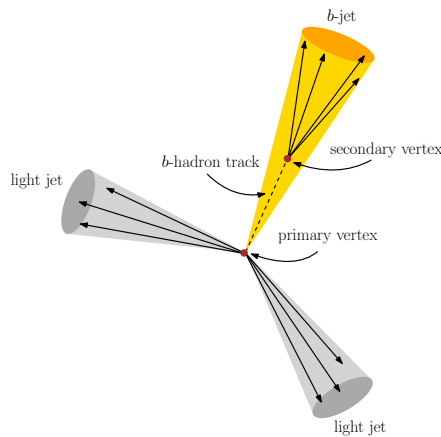


Figure 5.6: Typical decay topology of a b -hadron-induced jet. The secondary vertex is displaced from the hard scatter primary vertex.

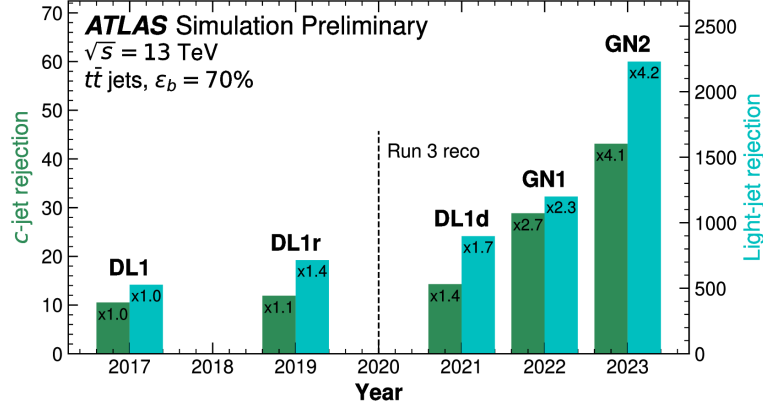


Figure 5.7: Comparison of different b -tagging algorithms used in Run 2 and at the beginning of Run 3. [47]

5.6 Lepton and photon reconstruction

When leptons and photons travel through the detector, they leave characteristic signatures that allow them to be reconstructed and identified inside the detector. Subsections 5.6.1 - 5.6.3 describe these reconstruction steps in more detail.

5.6.1 Electron and photon reconstruction

The reconstruction of electrons and photons is based on the similar energy deposits in electromagnetic calorimeter, thanks to the electromagnetic showers with similar properties they produce. Photons are reconstructed only from the calorimeter information, while electrons also use the information from the ID because electrons create tracks leading from the interaction vertex to the deposit in the calorimeter. However, the situation gets more complicated due to the bremsstrahlung photons created by electron or positron particles or the conversion of photons into electron-positron pairs. Until 2017, the clusters were identified using the sliding-window algorithm with fixed cluster size, which was replaced by the algorithm assuming variable cluster size. The cluster with variable size is called *supercluster* [48].

Superclusters are formed from topo-clusters in two steps. The first step is cluster seeding, where the electron supercluster seed is required to have $E_T \geq 1$ GeV with matched track from the ID, and photon supercluster seed $E_T \geq 1.5$ GeV with no requirement on tracks. The second step identifies so-called supercluster satellites, which are clusters adjacent to the supercluster seed but they are coming from the same interaction. The topocluster is considered to be a satellite if it is located in $\Delta\eta \times \Delta\phi = 0.075 \times 0.125$ range from the seed barycentre for topoclusters formed by electron, positrons, or photon, and $\Delta\eta \times \Delta\phi = 0.125 \times 0.300$ for electrons-only topo-clusters. Finally, the cluster seeds and satellite topoclusters are grouped together to form superclusters.

The second stage of the electron and photon reconstruction is the calibration. Superclusters formed in the previous step are calibrated for several effects. The

first correction consists of the correction to the truth electron/photon calorimeter energy, which is done by means of a multivariate algorithm trained on MC simulation. The second correction is the residual correction for the non-uniformities in the response of some parts of the calorimeter. The third correction is to improve agreement between data and simulation using the high-purity $Z \rightarrow e^+e^-$ data events. This third correction is applied to simulated events in order to better match the data.

After the calibration step, the electron and photon identification is performed. The electron identification is based on the likelihood discriminant build from the information on the track quality, the longitudinal and lateral development of the electromagnetic shower, and cluster-to-track matching, which is applied to distinguish real and fake electrons. The three working points, *Loose*, *Medium*, *Tight*, are based on the likelihood discriminant, with average electron efficiencies 98%, 90%, and 80%, respectively. The Medium and Tight electrons require additional cuts on E_T and track quality. Details of the photon identification are described in more detail in reference [48].

The sequence presented above is used in the offline reconstruction. The online reconstruction used in the HLT is localized into ROIs selected by the L1 trigger.

5.6.2 Muon reconstruction

Muons leave much lower energy deposits in calorimeters, so their reconstruction relies on the signal from the ID and hits inside muon chambers. The reconstruction inside the ID is the same as for all other tracks, which is described in section 5.2. The reconstruction inside the Muon Spectrometer starts with a search for the track patterns inside each muon chamber. In the Cathode-Strip Chambers, track segments are built using separate combinatorial search in the $\eta - \phi$ plane. The muon tracks are then constructed by fitting together tracks identified in individual layers. When the muon tracks from the Muon Spectrometer are formed, they are combined with tracks from the Inner Detector.

When the muon tracks are reconstructed, the calibration step comes into play. The correction factors are derived by comparing MC simulation and data by looking at $Z \rightarrow \mu^+\mu^-$ and $J/\Psi \rightarrow \mu^+\mu^-$ processes. [49]

After reconstruction and calibration, muon identification is performed to identify signal muons from the background induced by the decay of hadrons, such as pions and kaons. Similar to the electron identification, the muon identification recognizes *Loose*, *Medium*, *Tight*, and it adds the fourth *High- p_T* , which is designed to improve momentum resolution of tracks above 100 GeV. These working points use various cuts, and they form four inclusive categories, with each selection defined by tighter requirements applied on top of the previous working point. The tightest selection, the High- p_T working point, has a muon identification efficiency of 78%, which goes up to 97% for Loose muons.

The approach presented above is used in the offline reconstruction. Online reconstruction is divided into two steps: fast reconstruction and precision

reconstruction. The fast reconstruction is trigger-specific and uses L1 muon candidates. It refines them by including precision data from the MDT chambers in the ROI defined by the L1 candidate. A track fit is then performed using the MDT drift times and positions as well as the information from the TGC and Micromegas detector. The Muon-Spectrometer-only fit is then back extrapolated to the interaction point and combined with tracks reconstructed in the ID to form a combined muon candidate. The precision step then uses the same software as offline reconstruction with some adaptations for online running. [28]

5.6.3 Tau lepton reconstruction

Tau leptons have typically short lifetime due to their high mass, and they are expected to decay leptonically, in which case the electron/muon is reconstructed, or hadronically into jets that are reconstructed as discussed later in this chapter. Since tau leptons are not used in any work presented later in this thesis, we are skipping the detailed description of tau lepton reconstruction, and we are referring to the papers [50], and [51], in which improvements of the algorithm employed during the Run 3 are presented.

Tau leptons are also reconstructed at the HLT level, but only those decaying hadronically. Events with taus decaying leptonically are recorded by electron and muon triggers. [28]

5.7 Missing Transverse Momentum

The *missing transverse momentum* (E_T^{miss}) is an important quantity that can give us information about invisible particles produced in proton-proton collisions. It can be the Standard Model particles (neutrinos), or possibly some BSM particles we are trying to find in searches. The measurement of E_T^{miss} is based on the perfect conservation of transverse momentum. In the case of proton-proton collisions, two beams of protons of the same energy collide head-on, which means that the net momentum in the transverse plane of all particles created inside a collision has to be zero. That can be written as

$$\sum_{\text{all particles}} \mathbf{p}_T = \sum_{\text{visible particles}} \mathbf{p}_T + \sum_{\text{invisible particles}} \mathbf{p}_T = 0 \quad (5.11)$$

If we attribute the E_T^{miss} as a momentum carried away by invisible particles, we can, based on the equation 5.13, define E_T^{miss} as

$$E_T^{\text{miss}} = - \sum_{\text{visible particles}} \mathbf{p}_T. \quad (5.12)$$

Visible particles in the equations above are all possible objects reconstructed by ATLAS: electrons, muons, photons, tau leptons, and jets. However, we also must consider particles that cannot be well identified and calibrated in the detector.

In order to account for that, we are adding so-called *soft term*, which accounts for these effects. Having said that, we can rewrite E_T^{miss} defined in equation 5.12 by individual components as

$$E_T^{\text{miss}} = -\sum \mathbf{p}_T^e - \sum \mathbf{p}_T^\mu - \sum \mathbf{p}_T^\tau - \sum \mathbf{p}_T^\gamma - \sum \mathbf{p}_T^{\text{jet}} - \sum \mathbf{p}_T^{\text{soft}}. \quad (5.13)$$

The soft term ($\sum \mathbf{p}_T^{\text{soft}}$) is estimated either based on energy deposits in calorimeters that are not linked to any reconstructed objects in the event (*calorimeter soft term*), or based solely on the track information (*track soft term*) [52].

The E_T^{miss} reconstruction is dependent on the good functioning of the ATLAS detector, but also the accuracy of reconstruction of all physics objects, and the data-taking conditions. In this sense, the E_T^{miss} reconstruction is very sensitive to the pile-up conditions. In order to mitigate the effect of the pile-up, several techniques are used in ATLAS. The first is the use of a discriminant called *Jet Vertex Tagger* (JVT) [53], which uses the tracking information to mitigate pile-up jets. The second technique uses the definition of E_T^{miss} working points, allowing different analyses to use two different jet selections. The third technique is the definition of the E_T^{miss} soft term which is stable to pile-up, which is possible thanks to the use of tracking information where the soft term is estimated using the tracks not associated with any hard object and associated with the hard-scatter primary vertex.

The mismeasurement of the energy has a direct impact on the amount of E_T^{miss} measured in the event, and the real (carried away by undetected particles, e.g., neutrinos) and fake (mismeasurement) sources are indistinguishable in the data. One way to define "realness" of the E_T^{miss} in event is to use event-based E_T^{miss} significance, which is defined as

$$S_\Sigma = \frac{E_T^{\text{miss}}}{\sqrt{\sum \mathbf{p}_T}}, \quad (5.14)$$

where $\sum \mathbf{p}_T$ is the sum of transverse momenta of all reconstructed objects. This quantity is defined per event only for E_T^{miss} reconstructed from the calorimeter. The distribution of S_Σ for Run 2 data is shown in figure 5.8. The low values are dominated by events with an expected truth E_T^{miss} of zero, which have some fake E_T^{miss} . The high values in tails are more dominated by events from other processes that have a high energy neutrino produced and satisfy the $Z \rightarrow \mu^+ \mu^-$ selection in data.

The reconstruction described above is done offline, where detailed information about all reconstructed objects is available. The main difference in how E_T^{miss} is computed in the trigger involves details of which constituents to utilize in the sum of transverse moments. These constituents are not necessarily physical objects. In fact, there are different variations of E_T^{miss} reconstruction algorithms at the HLT level used for the sum of transverse momenta calorimeter cells, topo-clusters, PFOs, or jets.

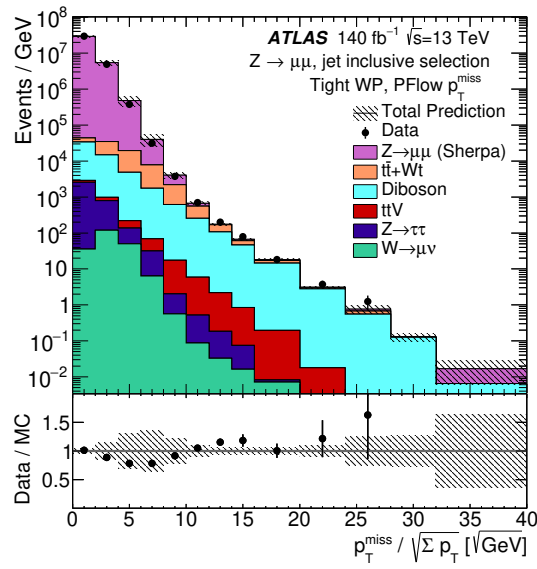


Figure 5.8: Calorimeter-only event-based E_T^{miss} significance in $z \rightarrow \mu\mu$ events in Run 2. Figure taken from [54].

Track extrapolation and its optimization for the HLT PFlow jet reconstruction

6.1 Introduction

As mentioned in the previous chapter, track extrapolation is one of the key ingredients of event reconstruction. The goal is to match the precise position information from the tracker with energy deposits in individual calorimeter layers to get more complex information about the event. This requires extending the reconstructed track from tracker to calorimeter, which is done in several steps. They involve propagating track parameters and related uncertainties in the presence of an inhomogeneous magnetic field and considering stochastic processes due to particle interactions with material inside the detector. This is a computationally nontrivial task because equations of motion have to be solved numerically due to the inhomogeneous nature of the magnetic field inside the ATLAS detector.

The track extrapolation is an important step in the Particle Flow reconstruction. Since it has been used at the HLT level since the beginning of Run 3, it was necessary to optimize it in order to save valuable CPU resources during the online reconstruction. Track extrapolation is one of the most CPU-expensive steps in the PFlow reconstruction, and it had to be optimized. This chapter introduces the general concept of the track extrapolation and presents the optimization of the track extrapolation for the HLT PFlow jet reconstruction, which was the subject of the author's qualification task¹. Validation of the optimized algorithm is also discussed in this chapter.

¹In order to become signing author of the ATLAS papers, each member has to complete so-called qualification task, which is the task assigned to the author and the whole ATLAS collaboration should benefit from results of the task.

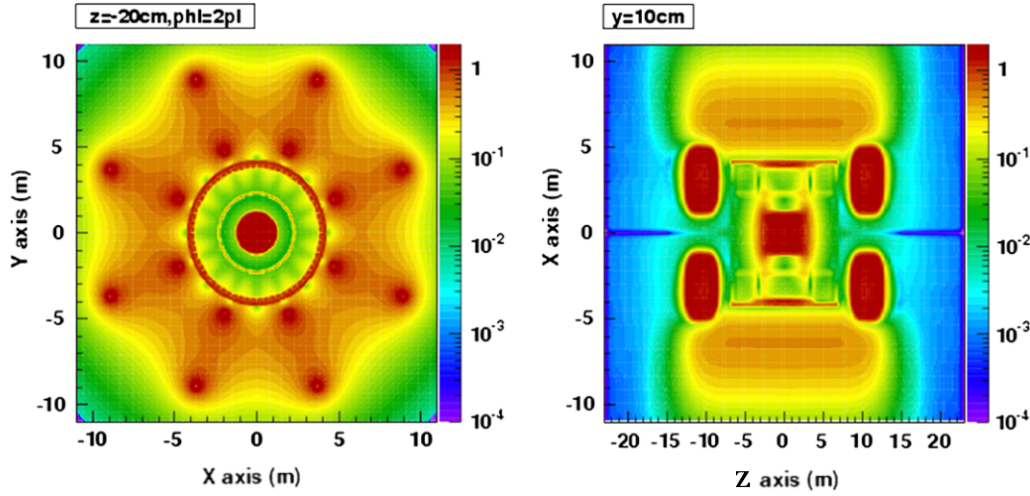


Figure 6.1: Magnetic field map in two planar sections. The section in the transverse plane (left) and along the beam axis (right). The color scale corresponds to the magnetic field strength in Tesla. [56]

6.2 Charged particle in magnetic field

There are several representations of the equation of motion of charged particle in magnetic field, each better suited for certain experimental setup. In collider experiments, such as ATLAS, the natural choice of the coordinates would be spherical or cylindrical coordinates. However, due to the magnetic field, the integration becomes difficult and error-prone. For that reason, using the arc length s and integrating along the particle's trajectory solves this problem. [55]

Let's designate \mathbf{r} the three-dimensional position vector. Using the arc length parametrization, the equation of motion of charged particle inside the magnetic field becomes

$$\frac{d^2\mathbf{r}}{ds^2} = \frac{q}{p} \left(\frac{d\mathbf{r}}{ds} \times \mathbf{B}(\mathbf{r}) \right) = \lambda (\mathbf{T} \times \mathbf{B}(\mathbf{r})). \quad (6.1)$$

$\mathbf{T} = \frac{d\mathbf{r}}{ds}$ is the normalized tangent² vector to the track, $\mathbf{B}(\mathbf{r})$ is the magnetic field and $\lambda \equiv q/p$. The electric field component is neglected in this equation because it is negligible inside the detector. The complexity of the ATLAS magnetic field can be seen in the section through the magnetic field in figure 6.1.

Solving the equation 6.1 analytically becomes impossible due to the presence of the inhomogeneous magnetic field. Many numerical methods are available, but one set, called Runge-Kutta methods, is particularly useful for this case. The basic idea of this method is to divide the integration interval into steps and solve these independently in an iterative procedure. The solution to each step is estimated by evaluating the equation of motion at different points —

²This can be easily shown by looking at the definition of velocity $\mathbf{v} = d\mathbf{r}/dt$, and the arc length $ds = vdt$. Derivative $\frac{d\mathbf{r}}{ds}$ then becomes $\frac{d\mathbf{r}}{ds} = \frac{d\mathbf{r}}{vdt} = \frac{\mathbf{v}}{v} = \mathbf{T}$.

often referred to as stages — along the step. [55] The most straightforward approach is keeping the step size constant through the solution, but that is not the optimal approach because the step size would have to be very small due to significant gradients of the magnetic field in some parts of the detector. This would make solving inefficient in parts of the detector where the magnetic field does not change so much. That is why the Runge-Kutta method with adaptive step size is used.

6.3 Runge-Kutta methods

In order to solve the equation of motion 6.1, the fourth order Runge-Kutta method is used, and the integration is done in curvilinear coordinates along the trajectory of a particle. However, before getting more into the method, let us first illustrate the principle of the Runge-Kutta method in the simplest case of the classical Runge-Kutta method for the first order differential equation, which can be easily schematically depicted as is done in figure 6.2.

Let us assume we have a differential equation:

$$\frac{dy}{dt} = f(x, y), \quad y(x_n) = y_n \quad (6.2)$$

The classical Runge-Kutta method evaluates the solution of the equation in four stages:

$$k_1 = f(x_n, y_n) \quad (6.3)$$

$$k_2 = f\left(x_n + \frac{h}{2}, y_n + \frac{h}{2}k_1\right) \quad (6.4)$$

$$k_3 = f\left(x_n + \frac{h}{2}, y_n + \frac{h}{2}k_2\right) \quad (6.5)$$

$$k_4 = f(x_n + h, y_n + hk_3) \quad (6.6)$$

and the final solution can then be written as

$$y_{n+1} = y_n + h \sum_{i=1}^4 a_i k_i \quad (6.7)$$

where coefficients a_i can be estimated by substituting equations 6.3 - 6.6 into 6.7 and comparing terms in front of derivatives with Taylor expansion of y_{x+h} around x . This leads to the solution of form:

$$y_{n+1} = y_n + \frac{1}{6}h(k_1 + 2k_2 + 2k_3 + k_4). \quad (6.8)$$

In reality, the equation 6.1 is the second-order differential equation expressed in curvilinear coordinates in the form:

$$\frac{d^2 r(s)}{ds^2} = f(s_n, r_n, r'_n), \quad (6.9)$$

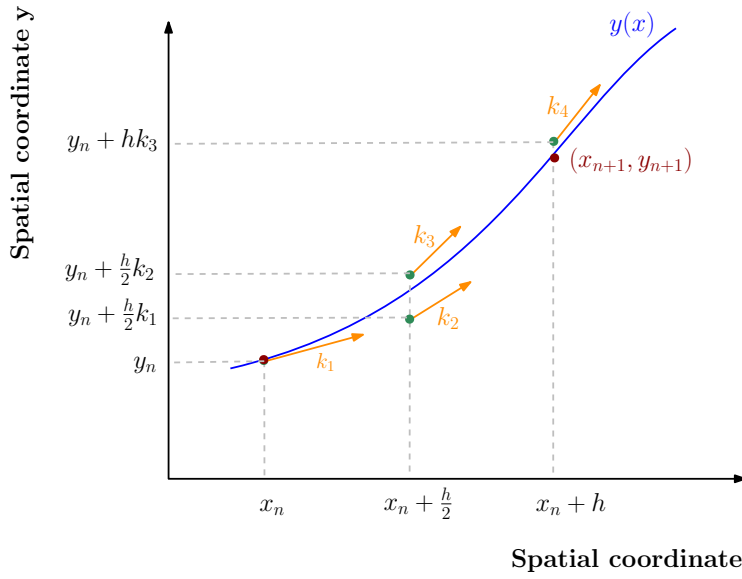


Figure 6.2: Schematic illustration of classical Runge-Kutta method. The solution is evaluated in four stages k_1, k_2, k_3, k_4 and the final solution of the step in point (x_{n+1}, y_{n+1}) is obtained as a linear combination of these stages.

where $r'_n \equiv \frac{dr_n(s)}{ds}$. The fourth order Runge-Kutta method with four evaluation stages is used for the numerical solution. The principle is the same as in the case of the first-order equation, but the graphical representation would be less demonstrative, so we only express evaluation stages and the solution in the same way as in [55].

$$k_1 = f(s_n, r_n, r'_n) \quad (6.10)$$

$$k_2 = f\left(s_n + \frac{h}{2}, r_n + \frac{h}{2}r'_n + \frac{h^2}{8}k_1, r'_n + \frac{h}{2}k_1\right) \quad (6.11)$$

$$k_3 = f\left(s_n + \frac{h}{2}, r_n + \frac{h}{2}r'_n + \frac{h^2}{8}k_1, r'_n + \frac{h}{2}k_2\right) \quad (6.12)$$

$$k_4 = f\left(s_n + h, r_n + hr'_n + \frac{h^2}{2}k_3, r'_n + \frac{h}{2}k_3\right) \quad (6.13)$$

$$r'_{n+1} = r'_n + \frac{h}{6}(k_1 + 2k_2 + 2k_3 + k_4) \quad (6.14)$$

$$r_{n+1} = r_n + hr'_n + \frac{h^2}{6}(k_1 + k_2 + k_3) \quad (6.15)$$

In this case, the step size h is constant, but as mentioned above, the Runge-Kutta method with adaptive step is used to perform propagation faster in detector regions where the magnetic field is not changing much and slower in regions with high magnetic field gradients, where higher precision is needed.

The most straightforward method of adjusting step size is step doubling. Every step is taken twice, first as a full step producing solution \hat{y}_{n+1} , and then as two half-steps producing a solution of higher order y_{n+1} . The difference between these solutions gives an estimate of the *local error* ε of each step.

$$\varepsilon = y_{n+1} - \hat{y}_{n+1} \quad (6.16)$$

The local error is then checked against a user-specified criterion, the *error tolerance* τ , and if the error is bigger than the error tolerance, the step fails. It is then shortened and redone. If the local error is smaller than the error tolerance, the step is successful, and the step size of the following step is increased to minimize the number of steps needed for the integration.

An alternative way of estimating the local error of a step is based on the embedded Runge-Kutta formulae - the so-called embedded pairs. The most well-known Runge-Kutta-Fehlberg method is a fifth-order method with six stages, where another combination of these six stages gives a fourth-order method. As in step doubling, the difference between these two solutions is used to estimate the local error of the lower-order solution of the step.

In the algorithm used for the propagation in ATLAS, the step size is not doubled but

$$h_{n+1} = h_n \left(\frac{\tau}{|\varepsilon|} \right)^{\frac{1}{q+1}}, \quad (6.17)$$

where h_{n+1} is the new step size, which is given by the local error of the current step ε , the current step length h_n , the user-specified error tolerance τ , and the order q of the lower-order solution \hat{y}_{n+1} . The algorithm's core is the fraction $\frac{\tau}{|\varepsilon|}$, which becomes less than one if the local error is bigger than the error tolerance, reducing the step length and vice versa.

6.4 STEP algorithm

The STEP algorithm (Simultaneous Track and Error Propagation) is the algorithm used for the track parameters propagation through the detector, and its goal is to estimate crossing points of the track with a given layer of the calorimeter. It uses the Runge-Kutta method with adaptive step size as described in subsection 6.3. Only when the propagation is close to the target surface describing one of the calorimeter layers, the distance to the surface is used as a maximum limit to the new step size to avoid stepping through the target surface. When the distance to the target surface is down to $10\mu\text{m}$ or less, the Runge-Kutta propagation is stopped, leaving the remaining propagation to a simple Taylor expansion. Like this, intersection points of tracks with calorimeter layers are found.

Propagation stops when the momentum cut-off of 50 MeV is reached, or the particle leaves the detector.

The equation 6.1 does not include material effects, such as the effect of multiple scattering of the particle coming through the detector. These effects must also be considered when propagating particles through the detector. Since these effects are stochastic, they are reflected in the uncertainty propagated together with the track as described more in detail in [57].

Algorithm	Fraction of the total run time in %
Fast Track Finding	62.1%
Track Extrapolation	3.3%
...	...
Full Scan Topo clustering	2.0%
Particle Flow	1.2%
Primary vertex finding	0.6%
...	...

Table 6.1: Overview of the overall fraction run time for selected HLT algorithms before track extrapolation optimization. Track extrapolation was the second most expensive algorithms, after the fast track finding algorithm. A few other selected algorithms are listed for the reference run time values.

6.5 Track extrapolation optimization for the HLT

Track extrapolation as described in section 6.3 is computationally expensive task, which was one of the reasons why the Particle Flow jet reconstruction could not be used at the HLT as it was used at the offline reconstruction, because, even though the track extrapolation takes only a few percent of the total processing time, it is still one of the most CPU expensive tasks. Saving just a few percent in an overall run time was necessary in order to make it possible for Particle Flow jet reconstruction to run at the HLT online event reconstruction. An overview of run times for some of the HLT algorithms discussed in the sections above is listed in table 6.1. These times are before the track extrapolation optimization, which will be discussed later in this section.

It can be noted that the track extrapolation is the second most CPU-expensive algorithm after the Fast Track Finding algorithm, which is the track reconstruction algorithm used for the track reconstruction for the HLT [58] and is 2.7% slower than the rest of the Particle Flow algorithm³.

The goal was to reduce the CPU time of the track extrapolation step while preserving the performance of the track-to-cluster matching. Several parameters impacting the performance of the track extrapolation were studied, and finally, the one having the most significant impact was selected, and its value was tuned to lower the CPU costs but maintain approximately the same performance. The most promising parameters that were studied are listed below:

Tolerance τ - Parameter introduced in equation 6.17. This parameter directly influences the accuracy of the track extrapolation by setting the size of the integration step.

³The track extrapolation stage is isolated from the rest of the Particle Flow algorithm and the cost monitoring for these stages are provided separately.

Material effects - Track propagation through the detector allows turning off the material effects, such as multiple scattering, which are the effects adding complexity to the computation.

Fast magnetic field - STEP algorithm has the option of using *Fast Magnetic Field*, which is effectively a simplified map of the magnetic field, reducing the number of calls to the map when solving the equation of motion 6.1.

Momentum cut-off - Particle propagation stops when the particle's energy reaches the momentum cut-off. Propagating particles with low momenta is computationally more difficult than those with high momenta because of the more substantial bending of the track inside the magnetic field and larger material effects. Increasing the cut on momentum cut-off also changes propagation time.

A dedicated approach was developed for the evaluation of performance. We wanted to see that the total processing time goes down, but the overall performance of the track-to-cluster matching does not change. The timing of the algorithm and the global behavior that can be captured by plotting histograms for selected variables was done thanks to the implementation of the new monitoring metrics into the Athena reconstruction software. The global metrics, such as the number of matched tracks to clusters for different regions of the detector, p_T and energy distribution of matched clusters, and distribution of the extrapolation time per track, are helpful but cannot necessarily capture the slight changes in the extrapolation of individual tracks. That is why we temporarily added⁴ into Athena a piece of code that could dump information about all extrapolated positions of tracks into all different calorimeter layers for the given configuration. Analyzing files with information corresponding to two different extrapolation setups allowed us to check for the differences in the extrapolated position of individual tracks. Each line in the file corresponded to a hit in one calorimeter layer, and columns uniquely indexed these hits and tracks to compare them across different configurations.

This file allowed us to identify what we will call in this section *missing tracks*. Missing track in the given calorimeter layer is a track that we would expect to have hit in a given layer when comparing to the same track extrapolated with default configuration, but the hit does not exist. This is illustrated in figure 6.3. Extrapolation always starts from the last hit inside the Inner Detector and can evolve differently due to the different configuration of the STEP algorithm.

The file also allowed the comparison of extrapolated positions of a given track into selected calorimeter layers. The difference between extrapolated positions in the $\eta - \phi$ plane will be denoted as ΔR in this chapter. In figure 6.3, the ΔR for track t in layer 1 between configurations a and b would be the difference in extrapolated positions x_{1a} and x_{1b} .

⁴This piece of the code was used only for the local evaluation of changes during the optimization process. However, it was not included in the official Athena release because it

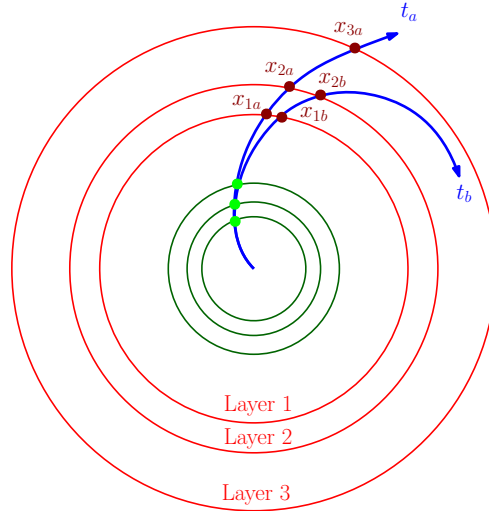


Figure 6.3: Schematic illustration of the track extrapolation for the same track t but using two different configurations leading to extrapolated tracks t_a and t_b . The number of layers inside the calorimeter and tracker is only illustrative. Extrapolation starts from the track reconstructed from hits (green dots) inside the tracking detector layers (green circles). Hits inside the calorimeter layers 1, 2 and 3 (red circles) for track t_a are indexed x_{1a} , x_{2a} , x_{3a} respectively. Track t_b has hits only in layers 1 and 2. The hit in the third layer for track t_b is missing, and we would see it as a *missing track* in layer 3.

A detailed discussion of the optimization of track extrapolation using the four parameters listed above follows.

6.5.1 Tolerance τ

The tolerance τ was one of the studied parameters. The default value of this parameter was 10^{-5} , and we expected that increasing its value would lead to the speed-up in the extrapolation time due to possibly longer integration steps, as can be seen in equation 6.17. We scanned the range of values of this parameter, and we checked the distribution of the extrapolation time per track; see figure 6.4. We can see that the distribution is complicated, which is the effect caused by the detector geometry and the fact that extrapolation close to the transition between the barrel and end-cap regions has to be done more precisely. The mean of this distribution served as the primary metric to measure the reduction of the extrapolation time. The distribution of an extrapolation time per track for different values of tolerance is shown in figure 6.4, and the relative comparison in the mean extrapolation time per track with respect to the default configuration as a function of τ is shown in 6.4.

The next quantity we studied was the distribution of the number of matched clusters binned by the cluster energy, which served as a first sanity check that

was specific only for this particular task.

6. Track extrapolation and its optimization for the HLT PFlow jet reconstruction

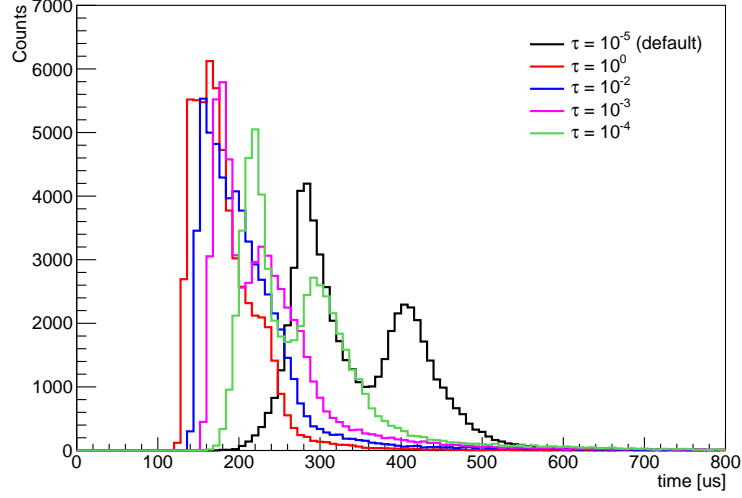


Figure 6.4: Distribution of the extrapolation time per track for different values of the tolerance parameter τ . The double peak structure of the distribution is caused by different track extrapolation times per track in different parts of the detector. In particular, the right lower peak is formed by tracks close to the transition between barrel and end-cap layers, where extrapolation has to be performed with high precision. Since the extrapolation accuracy drops, the double peak structure gets blurred when the parameter τ increases.

the new configuration does not influence the reconstruction's performance. This is shown in figure 6.6.

We also checked the mean distance $\Delta R = \sqrt{(\eta_a - \eta_b)^2 + (\phi_a - \phi_b)^2}$, where η and ϕ are coordinates of the intersection between the track and calorimeter layer, and a and b index two different configurations, for every calorimeter layer. We considered that extrapolated positions with the default configuration are obtained with absolute precision, and any deviations from these positions mean a worsening of the extrapolation result. The reference values for us were the sizes of calorimeter cells, which range from 0.025×0.025 up to 0.1×0.1 in $\eta - \phi$ plane, and we wanted to make sure that the mean distance ΔR is never significantly bigger than the size of the cell. The dependence of the mean ΔR per calorimeter layer for different values of τ is shown in figure 6.7.

Finally, we were looking to see if changing τ leads to missing tracks in some calorimeter layers. The fraction of hits present with respect to the default configuration is shown in figure 6.8.

From all tested values, the value of $\tau = 10^{-2}$ was chosen as a good trade-off between the improvement of the extrapolation time per track and precision, which did not change much.

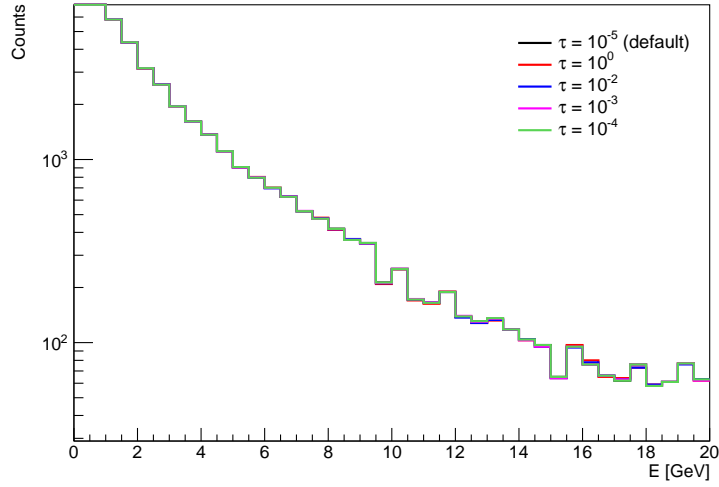


Figure 6.6: Number of clusters matched to a track for different cluster energies for several values of τ .

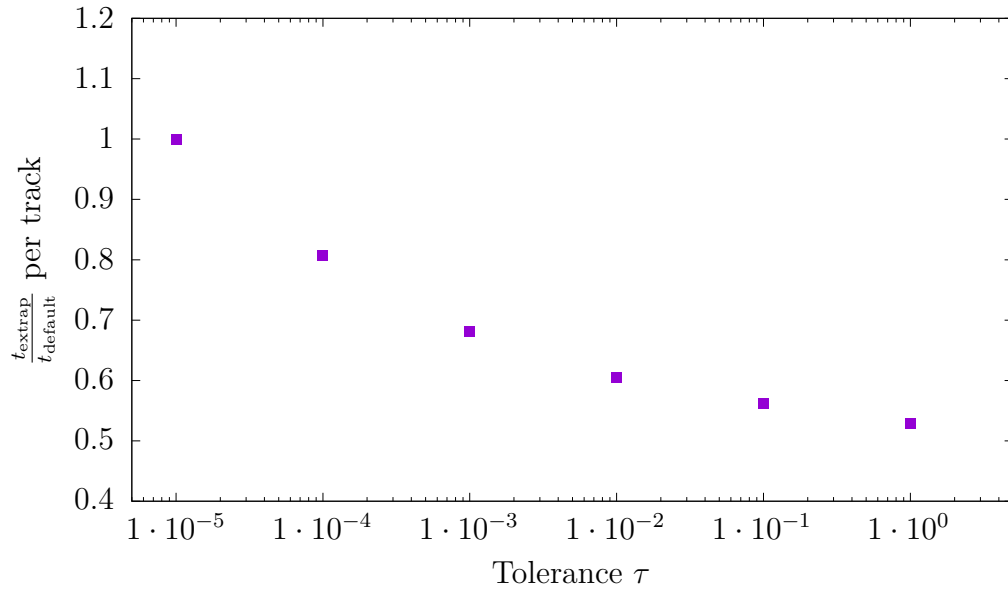


Figure 6.5: The mean extrapolation time per track for different values of tolerance τ in comparison to the extrapolation with default configuration with $\tau = 10^{-5}$.

6. Track extrapolation and its optimization for the HLT PFlow jet reconstruction

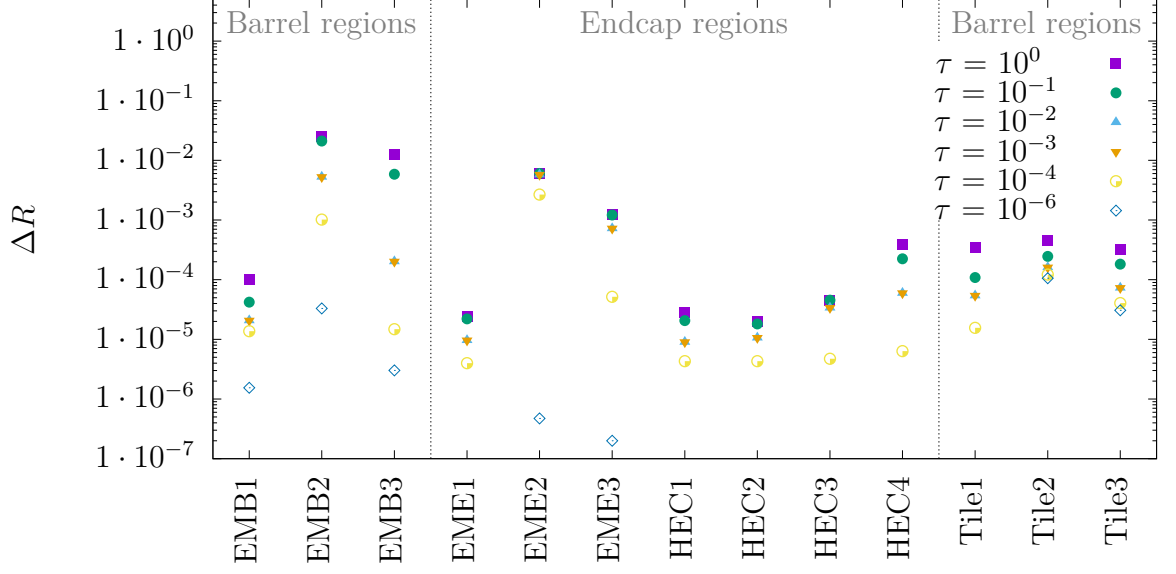


Figure 6.7: The mean ΔR of the track in given calorimeter layer. Distance is computed like an Euclidean distance between extrapolated positions with changed and default configurations in the $\eta - \phi$ plane. Tolerance value $\tau = 10^{-5}$ is used as a reference value.

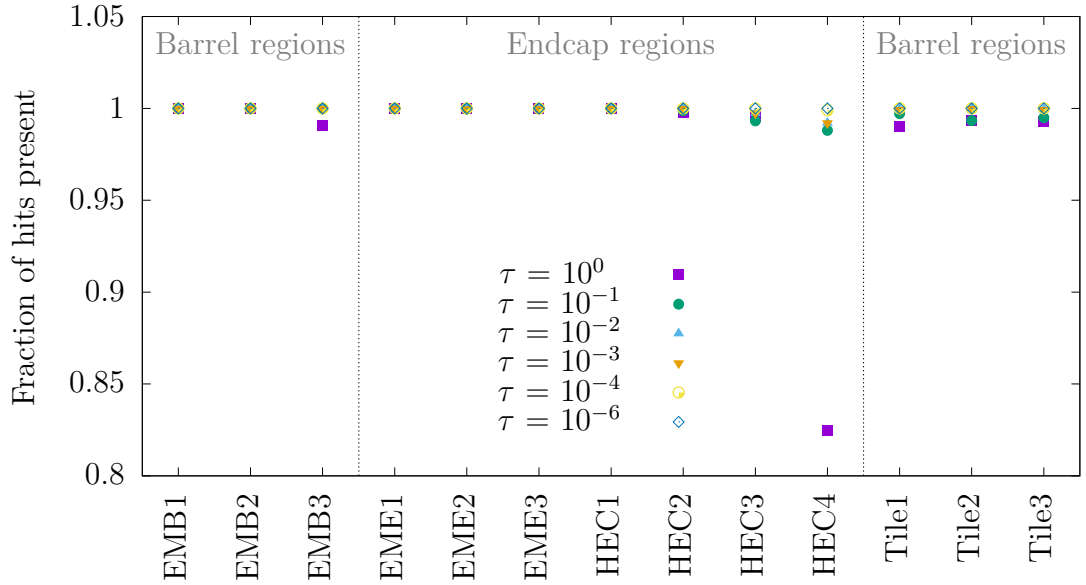


Figure 6.8: The fraction of missing hits for individual calorimeter layers for different parameter configurations τ . Comparison was done with respect to the configuration of $\tau = 10^{-5}$.

6.5.2 Material effects

Turning off material effects during the propagation had little influence on the extrapolation quality, which could be seen in a zero ΔR and no missing tracks for individual layers. Mean extrapolation time per track almost did not change, so turning off material effects would not improve performance.

6.5.3 Fast magnetic field

When solving the equation of motion 6.1, the knowledge of the magnetic field in every integration step is crucial. The ATLAS magnetic field map, which is shown in figure 6.1, is stored as a three-dimensional map, which is segmented into cells in z, r, ϕ coordinates, as shown on the left side in figure 6.9, and values of the magnetic field are given for these cells. This means that if the particle moves inside one cell, it feels the same magnetic field no matter where in the cell it is located. Reading the value of the magnetic field map is an expensive operation. In order to reduce the number of calls into the magnetic field map, the concept of cache is introduced. This means that the properties of the local magnetic field inside the cell are stored in the memory. If the particle is inside the same cell, the value of the field is taken from the memory instead of accessing the magnetic field map itself. This approach makes the computation more efficient.

The fast magnetic field map is the concept that can reduce access to the magnetic field map and allow the use of the magnetic field stored inside the cache more often. It is based on the assumption that the ATLAS magnetic is approximately axially symmetric, and it is assumed that the value of the magnetic field is constant inside the ring given by coordinates z, r , and it doesn't change with the ϕ coordinate. The concept of the fast magnetic field is illustrated in figure 6.9.

We studied the effect of the fast magnetic field and observed only 8% reduction in the total number of calls to the magnetic field ⁵. Despite the slight reduction in the number of accesses to the magnetic field map, we did not see any significant change in the extrapolation time.

6.5.4 Momentum cut-off

The last studied parameter was the cut-off on the momentum of the propagated particle. Increasing the cut means that particles will stop in the detector earlier, reducing the propagation time.

Similarly to previous parameters, we looked at the mean extrapolation time per track, which was the primary metric for the measurement of the reduction of the processing time. This is shown in figure 6.10. It can be seen that the extrapolation time gets shorter for higher values of the momentum cut-off. If we compare this to improvements achieved by the change of the tolerance τ , we

⁵The study was done on 200 events. In the case of the standard magnetic field map, the magnetic field was called $\sim 6.1 \cdot 10^6$ times, and using the fast magnetic field option reduced the total number of calls to $\sim 5.5 \cdot 10^6$.

6. Track extrapolation and its optimization for the HLT PFlow jet reconstruction

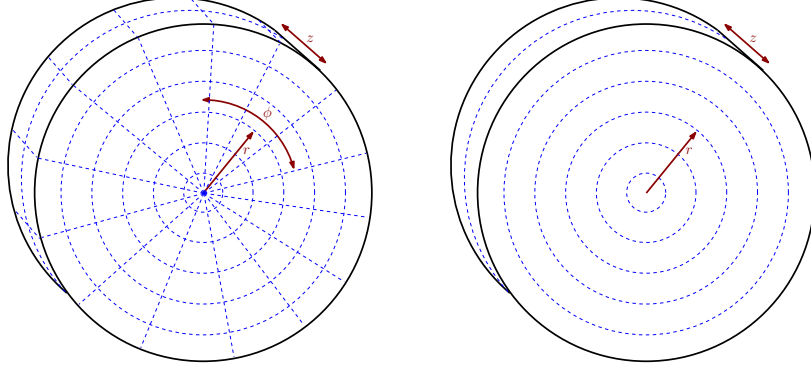


Figure 6.9: Segmentation of the ATLAS magnetic field map (left) and simplified segmentation of the magnetic field used for the fast magnetic field option (right). This is just a schematic illustration and the number of divisions in the real magnetic field map is much higher.

can see that the cut-off value of 1000 MeV achieves a similar reduction of the extrapolation time per track. However, this is expected to cause a considerable fraction of missing tracks since tracks reaching momentum 1000 MeV will not propagate further, causing missing hits in further calorimeter layers. This can be seen in figure 6.11, and we can notice that cut-off 1000 MeV has a high number of missing tracks in some layers. This is the effect that would have a significant effect on the event (jet) reconstruction performance.

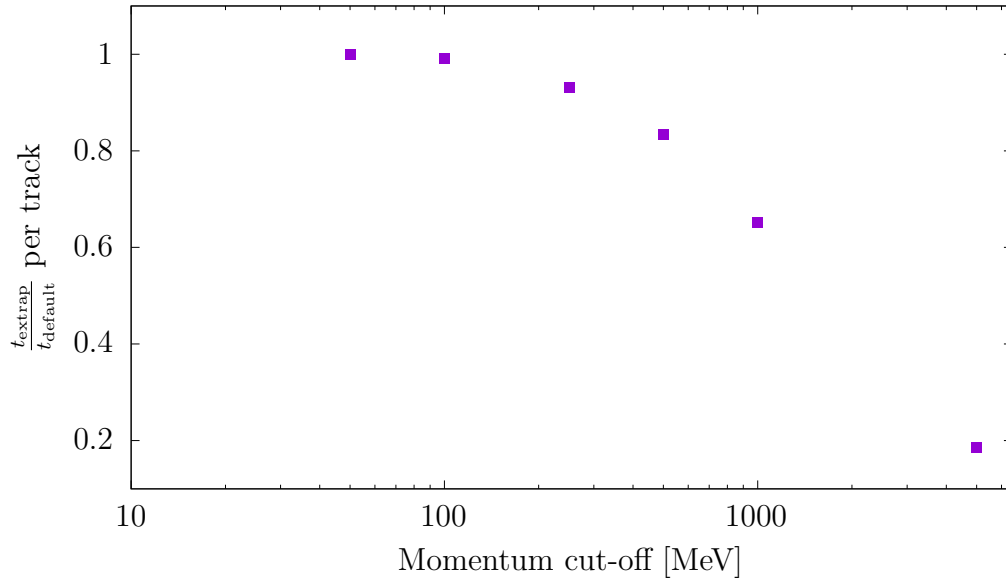


Figure 6.10: The mean extrapolation time per track with respect to the default configuration for different values of the momentum cut-off. The default value of the momentum cut-off is 50 MeV.

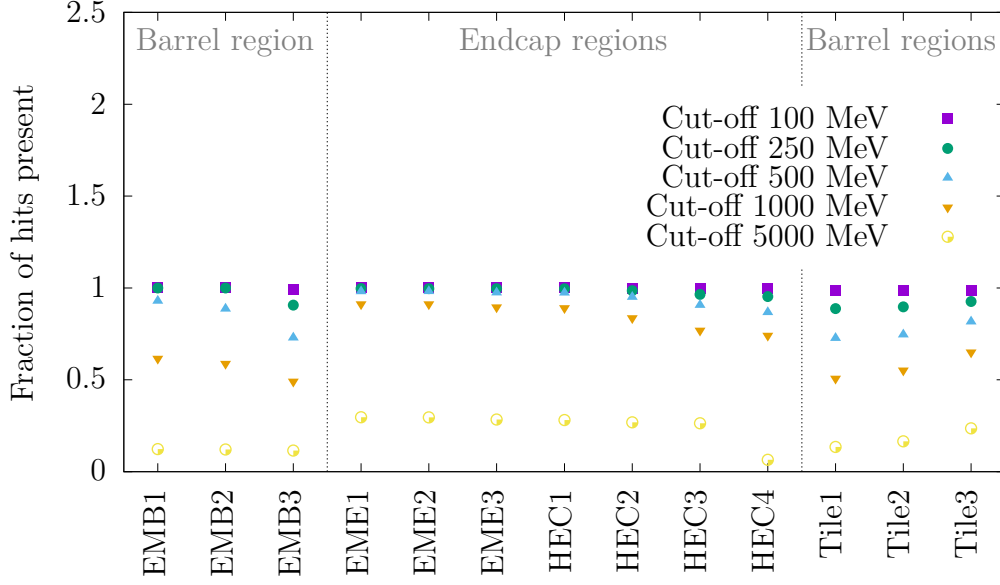


Figure 6.11: The fraction of missing hits for individual calorimeter layers for different configurations of momentum cut-off. Comparison was done with respect to the default cut-off of 50 MeV.

6.5.5 The final parameter choice

After the evaluation of the effects discussed above, the tolerance parameter τ was chosen as the best parameter, which can make the extrapolation run faster. Other studied parameters either did not affect the extrapolation time or changing them would significantly worsen the performance of event reconstruction. The new configuration was validated by reprocessing ATLAS collision data with the new configuration and comparing results to the original configuration's performance as described in subsection 6.6.

6.6 Validation of the optimization

Athena reconstruction software is under continuous development to improve the ATLAS experiment's overall performance. However, when a new feature is implemented, we want to ensure that it does not impact the performance in an undesired way. This can be done through reprocessing, which is when we reconstruct data with old and new versions of the software and compare the performance. This is done under standardized conditions so we can also accurately measure the runtime of the individual algorithms.

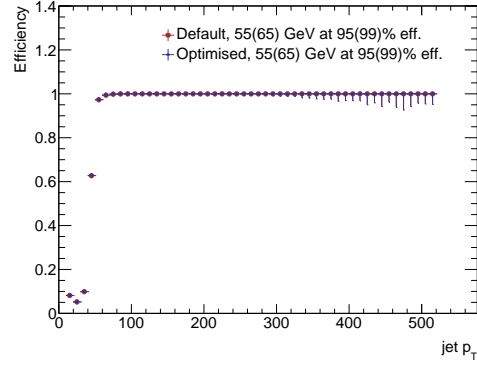
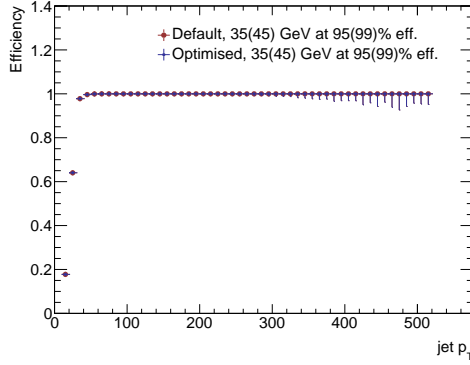
After changing the tolerance inside Athena for the HLT reconstruction and implementing the new monitoring metrics, we previously requested the reprocessing of physics data taken by the ATLAS. The purpose of this reprocessing was to

6. Track extrapolation and its optimization for the HLT PFlow jet reconstruction

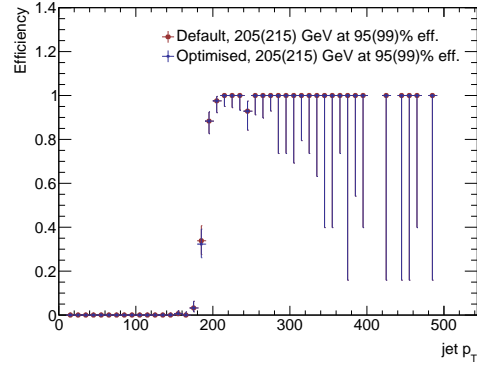
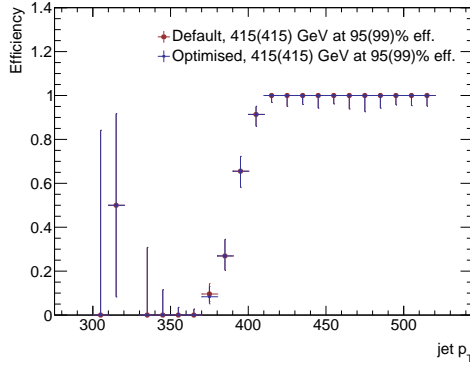
1. Check that the performance of jet triggers using Particle Flow jets, which will be affected by the change of τ , does not change.
2. Measure the total run time of the track extrapolation algorithm.

In order to assess the performance of jet triggers, we plotted trigger efficiencies of several triggers, some of which are shown in figure 6.12. Triggers were selected to cover low and high- p_T jets and include single-jet and multi-jet triggers. Since we do not have the truth information about events in physics data, we have to calculate trigger efficiency with respect to the reference trigger that we chose such that it is 100% efficient in events where the studied trigger is expected to fire. We studied trigger efficiencies for single jet triggers low and high p_T jets as is shown in figures 6.12a, 6.12b, 6.12c, and also 3-jet triggers as shown in figure 6.12d, and we observed good agreement between trigger efficiencies before and after the change of τ . It means that the change of the parameter does not impact trigger performance.

Based on the result presented in the section dedicated to the optimization of τ , the value of τ was changed from the default value of 10^{-5} to 10^{-2} , leading to $\sim 30\%$ decrease of the total extrapolation time and saving of approximately 1.2% of the total CPU processing time used by HLT algorithms. The average run time of the extrapolation per event got shorter by nearly 30%. The distribution of the extrapolation time per track obtained after reprocessing using the actual physics data from the ATLAS is shown in figure 6.13.



(a) HLT_j25_pf_ftf_L1RD0_FILLED, (b) HLT_j45_pf_ftf_preselj20_L1RD0_FILLED,
 ref. :HLT_j0_perf_pf_ftf_L1RD0_FILLED ref. :HLT_j25_pf_ftf_L1RD0_FILLED



(c) HLT_j400_pf_ftf_preselj225, (d) HLT_3j190_pf_ftf_presel3j150,
 ref. :HLT_j360_pf_ftf_preselj225_L1J100 ref. :HLT_j110_pf_ftf_preselj80_L1J30

Figure 6.12: Trigger efficiencies for different triggers, jet p_T is in GeV. The reference trigger with respect to which the efficiency was computed is always noted in the second line. Trigger names follow the standard ATLAS trigger naming convention described in appendix A.1.

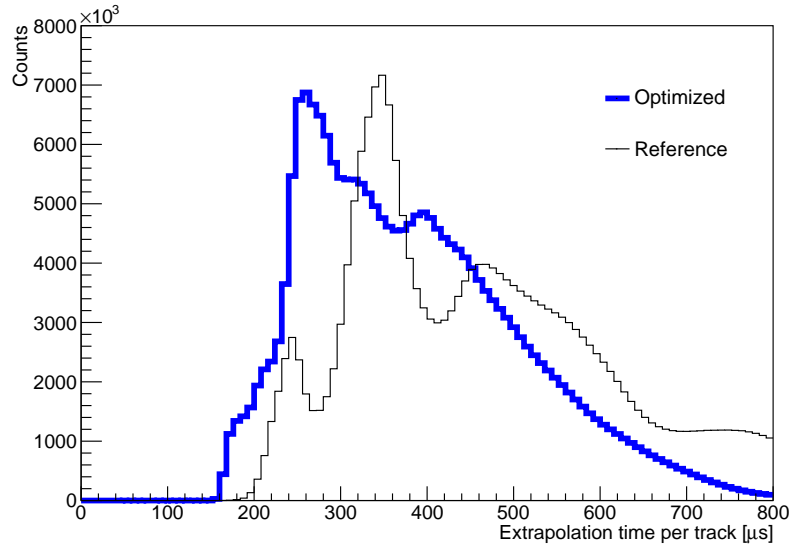


Figure 6.13: Comparison of the extrapolation time per single track for the old value of tolerance and newly optimized value. The multiple-peak structure of the distribution is caused by different track extrapolation times per track in different parts of the detector. In particular, the right-most peak is formed by tracks close to the transition between barrel and end-cap layers, where extrapolation has to be performed with high precision, and the middle peak is the majority of tracks inside the barrel region. The multiple-peak structure gets blurred when increasing the parameter τ since the extrapolation's accuracy drops.

Statistical methods and data interpretation

7.1 Introduction

The LHC is colliding proton-proton bunches at a rate of approximately 40 MHz, with 20 to 60 collisions per bunch crossing. As a result, a large amount of data is collected, allowing for the exploration of events that occur with a very low probability. Probability is the key concept in quantum physics that governs these processes, but it is also important for statistical data evaluation. Imagine there is a physics process that appears on average once in a billion experiment repetitions. The probability that we observe the process in the first experiment repetition is very low. However, it is the same probability that we get this outcome in the last repetition. We know that the process occurs on average once in a billion repetitions. Nevertheless, there is a certain smaller chance that it will appear twice and a smaller chance that it will appear three times. It can be unlikely, but it is not impossible. The statistical data evaluation aims to tell whether the observation agrees with our expectations or if the result can be a hint for the new physics.

This chapter serves as a brief overview of concepts from statistics, namely the probability density function, estimation of parameters of a physics model, and hypothesis testing. These are the key ingredients used in evaluating the data at the LHC and in physics searches presented in the thesis.

7.2 Probability density function

The data at the LHC come from the proton-proton collisions, which can be understood as a separate, statistically independent¹, measurements. The probability of an outcome of the measurement can be described by the *probability*

¹One collision does not influence the other.

density function (PDF). Let us have the continuous observable x ; $x \in M$, where M is the set of all possible measured values of x . The PDF is then a continuous function $p(x)$ expressing the probability of x being in the interval $[a; b]$.

$$P(x \in [a; b]) = \int_a^b p(x) dx \quad (7.1)$$

Since the result of measurement on x has to be from M by definition, the integral of $p(x)$ over M has to be equal to one.

$$P(x \in M) = \int_M p(x) dx = 1 \quad (7.2)$$

In the case of two continuous random independent variables $x \in M$ and $y \in N$, we can write for the joint probability density function

$$p(x, y) = p(x)p(y) \quad (7.3)$$

$$P(x \in M \wedge y \in N) = \int_M \int_N p(x)p(y) dy dx = 1 \quad (7.4)$$

which is true if and only if x and y are independent. This can be easily extended to the case of multiple variables.

We often work with a few prominent PDFs with specific properties in particle physics. The first example of such a probability density function is the Poisson distribution, which describes the result of the counting experiment. It characterizes the probability of n events being found inside a given interval, assuming that the expected number of events inside this interval is λ , where λ is the parameter of the PDF.

$$p_{\text{Pois}}(n; \lambda) = e^{-\lambda} \frac{\lambda^n}{n!} \quad (7.5)$$

Another essential PDF is the Gaussian, or normal, distribution $p_{\text{Gauss}}(n; \mu, \sigma)$. Unlike Poisson distribution, it is characterized by two parameters: μ and σ . The parameter μ is the mean of the distribution, and σ is the standard deviation. We can write

$$p_{\text{Gauss}}(x; \mu, \sigma) = \frac{1}{\sigma\sqrt{2\pi}} e^{-\frac{(x-\mu)^2}{2\sigma^2}}. \quad (7.6)$$

The importance of a Gaussian distribution is also due to the central limit theorem, which states that the average of many observations of a random variable with a finite mean and variance is also a random distribution that converges to Gaussian distribution as n goes higher.

7.3 Estimation of parameters of physics model

In physics experiments we usually do measurement on a set of n random variables $\mathbf{x} = (x_1, x_2, \dots, x_n)$, where each variable takes a particular value $\bar{\mathbf{x}} = (\bar{x}_1, \bar{x}_2, \dots, \bar{x}_n)$. The measured data can be described by some physics model,

which is characterized by the set of parameters $\boldsymbol{\theta} = (\theta_1, \theta_2, \dots, \theta_m)$ and the typical task of the physics analysis is to estimate these parameters. In terms of probability density functions, we can write $f(\mathbf{x}|\boldsymbol{\theta})$, which is the PDF of the joint probability of outcome \mathbf{x} , given the set of parameters $\boldsymbol{\theta}$.

Not all parameters are of our imminent interest. Some parameters, such as the cross-section of a given process or the mass of a particle, directly describe the physics model we want to study. These are in the case of the analysis and reinterpretation discussed in the following chapters *parameters of interest*. The PDF, however, also has to reflect the effect of the detector response, such as, for example, energy resolution, trigger efficiencies, or different particle misidentification rates, which are not of our direct interest but have to be included as well. These are called *nuisance parameters*. The uncertainty on the nuisance parameter is reflected in the accuracy of the estimate of the parameter of interest. We can differentiate between two types of uncertainties in physics measurement, which are *statistical uncertainties* and *systematic uncertainties*. Statistical uncertainties are uncertainties arising purely from the statistical fluctuations in the data. Systematic uncertainties are inaccuracies caused by the propagation of our imperfect knowledge of nuisance parameters.

If the outcome of the experiment is known, we can use *likelihood function* $\mathcal{L}(\boldsymbol{\theta}|\mathbf{x})$ to extract the information about the PDF. The likelihood function is obtained by evaluating $p(\mathbf{x}|\boldsymbol{\theta})$ for a specific value of \mathbf{x} and examining how it varies as $\boldsymbol{\theta}$ changes.

$$\mathcal{L}(\boldsymbol{\theta}) \equiv \mathcal{L}(\boldsymbol{\theta}|\mathbf{x}) = p(\mathbf{x}|\boldsymbol{\theta}) \quad (7.7)$$

The main distinction between likelihood and probability is that the integral of the likelihood function over the whole parameter space does not necessarily add up to one.

The way how to estimate the parameters of the model is to use the likelihood function and find the set of parameters $\boldsymbol{\theta} = \hat{\boldsymbol{\theta}}$ which maximizes its value. $\hat{\boldsymbol{\theta}}$ found through this way is then called the *maximum likelihood estimator*. This approach is equivalent to finding a minimum of $-\log \mathcal{L}(\boldsymbol{\theta})$, which is often used because it is better suited for numerical computations.

$$\hat{\boldsymbol{\theta}} = \arg \min (-\log \mathcal{L}(\boldsymbol{\theta})) \quad (7.8)$$

In the case of multiple measurements, which we encounter in the ATLAS experiment since each pp collision is a separate measurement, the likelihood function can be written as a product of individual probability density functions. This is clear from the equation 7.3 and the fact that individual collisions inside the LHC are entirely independent events. If the results of N measurements are described by the set of vectors

$$\bar{\mathbf{X}} \equiv \{\bar{\mathbf{x}}^1, \bar{\mathbf{x}}^2, \dots, \bar{\mathbf{x}}^N\} = \{(\bar{x}_1^1, \dots, \bar{x}_n^1), \dots, (\bar{x}_1^N, \dots, \bar{x}_n^N)\}, \quad (7.9)$$

then the likelihood function can be written in the form

$$\mathcal{L}(\boldsymbol{\theta}|\bar{\mathbf{X}}) = \prod_{i=1}^N p(\bar{\mathbf{x}}^i|\boldsymbol{\theta}). \quad (7.10)$$

If the number of measurements is too high, which is the case in the LHC experiments, the minimization procedure would not be feasible. That is why we can store the resulting distribution into histograms and split it into M_b bins, where one bin can contain multiple measurements. If the measurements are all independent, the expected number of events in each bin, n_i , is Poisson-distributed, with the average number of expected events being determined by the original PDF $p(\mathbf{x}|\boldsymbol{\theta})$. In this case, we can rewrite the likelihood function into the following form:

$$\mathcal{L}(\boldsymbol{\theta}|\bar{\mathbf{X}}) = \prod_{i=1}^{M_b} \frac{\mu_i(\boldsymbol{\theta})^{n_i} e^{-\mu_i(\boldsymbol{\theta})}}{n_i!} \prod_{j=1}^{M_{NP}} \rho(\theta_j^{NP}). \quad (7.11)$$

In this case, $\mu(\boldsymbol{\theta})$ is the expected number of events in the i -th bin, which depends on the original PDF, and $\rho(\theta_k^{NP})$ is the constraint on the j -th nuisance parameter which, in case of unknown nuisance parameters, can be considered to be described by the Gaussian distribution.

7.4 Hypothesis testing

In physics, we do measurements and want to see if the data we get are more compatible with the null hypothesis H_0 or alternative hypothesis H_1 . This process is called hypothesis testing and will be described in the following section. However, before doing so, let us introduce one crucial concept in hypothesis testing, and that is the *test statistic*.

Let's assume we measure data $\mathbf{x} = (x_1, x_2, \dots, x_n)$ and these data are following probability density function $p(\mathbf{x})$. The probability density function is different under each of the hypotheses, saying $p(\mathbf{x}|H_0)$ and $p(\mathbf{x}|H_1)$ are, in general, different. The test statistic is the function t based on the probability distribution function distributed differently for each hypothesis. The test statistic $t = t(\mathbf{x})$ is a function of a random variable evaluated on observed values. The smaller the overlap of the two probability density functions under two hypotheses is, the easier it is to tell which hypothesis should be rejected.

The Neyman-Person lemma says that the optimal test statistic is built as a likelihood ratio

$$\lambda(\mathbf{x}) = \frac{\mathcal{L}(\mathbf{x}|H_1)}{\mathcal{L}(\mathbf{x}|H_0)}. \quad (7.12)$$

In case we are testing two hypotheses where one says that the cross section of the signal process is greater or equal to zero, and the other says that the cross section of the signal process is precisely zero, it is useful to define *signal strength* $\mu = \sigma/\sigma_{\text{theo}}$. In this expression, σ is the actual cross section of the process, and the σ_{theo} is the cross section predicted by theory. Assuming that

the null hypothesis can be viewed as a hypothesis $\mu = \mu_0 = 0$ and the alternative hypothesis is the one with $\mu = \hat{\mu}$ that can take arbitrary positive value, the test statistic can be constructed as

$$\lambda(\mu_0) = \frac{\mathcal{L}(\mathbf{x}|\mu_0, \hat{\boldsymbol{\theta}}(\mu_0))}{\mathcal{L}(\mathbf{x}|\hat{\mu}, \hat{\boldsymbol{\theta}})}, \quad (7.13)$$

where $\hat{\mu}$ and $\hat{\boldsymbol{\theta}}$ are estimated from the data, and the $\hat{\boldsymbol{\theta}}(\mu_0)$ are the values that maximize the likelihood function under assumption $\mu = \mu_0$. These values are obtained by the two separate fits². Values in the numerator are obtained by performing the background-only fit, while values in the denominator are obtained by performing the fit on signal plus background hypothesis. The test statistic constructed in this way is often used at the LHC to estimate the exclusion limit in case of no discovery, and it is called the *profile likelihood ratio*.

7.4.1 Discovery or exclusion

The ultimate goal of the statistical analysis is to determine whether the collected data are more compatible with a background-only hypothesis or if the alternative theory, assuming a new signal model, describes data more accurately. The compatibility of data with one or the other hypothesis can be estimated using the test statistic, as shown in the paragraphs above.

For further discussion in this section, let us define *p-value* and a *significance*. The *p-value* for a given observation \bar{t} is the probability of obtaining the test result t at least as extreme as \bar{t} , in case the null hypothesis is correct. This can be written as

$$p = \Pr(t \geq \bar{t} | H_0), \quad (7.14)$$

meaning that the smaller the *p-value* is, the less compatible the observation is with the hypothesis. Closely related to the *p-value* is the concept of significance, which is the measure related to how certain we are that the null hypothesis can be excluded given the measurement \bar{t} . It is often expressed as the number of standard deviations the observed test statistic is away from the average of the null hypothesis. For example, if the test statistic is distributed according to the normal distribution, the random measurement will be within 1σ from the mean 68% of the time. The *p-value* and significance of the measurement \bar{t} are graphically illustrated in figure 7.1.

This can be formally written as

$$p = \int_Z^{\infty} p(t|H_0) dt = 1 - \Phi(Z) \quad (7.15)$$

where $p(t|H_0)$ is the normalized probability density function of the test statistic t , and $\Phi(Z)$ is the value of the cumulative distribution function of $p(t|H_0)$. The

²The concept of statistical fits is described in more detail in section 7.5

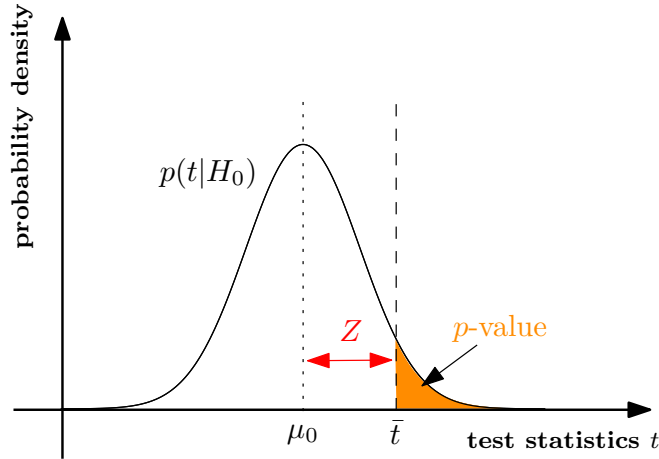


Figure 7.1: Illustration of the concept of p -value and significance Z for the measured value \bar{t} of the test statistic t given the null hypothesis H_0 with mean μ_0 .

integral can be hard to evaluate since the probability density function of the test statistic does not have to be known. However, there is a way of doing that thanks to Wilk's theorem [59]. It states that the logarithm of the likelihood ratio³ is asymptotically normal. In case we define the test statistic in the following way

$$q_0 = \begin{cases} -2 \ln \lambda(0) & \text{if } \hat{\mu} \geq 0 \\ 0 & \text{if } \hat{\mu} < 0, \end{cases} \quad (7.16)$$

Wilk's theorem assures that q_0 will become a normal distribution for many measurements. $\hat{\mu}$ must be greater than zero to prevent excluding negative cross sections. This is very convenient because it allows us to compute the p -value of the result, as defined in equation 7.15, and the associated significance level, without knowing the prescription for the original probability distribution function.

$$p_0 = \int_Z^\infty p(q_0|H_0) dq_0 = \int_Z^\infty p(q_0|\mu = 0) dq_0 \quad (7.17)$$

Tests statistics q_0 is useful when claiming a discovery where the background-only hypothesis is the hypothesis we want to reject.

The usual convention in particle physics is to claim the evidence for the alternative hypothesis when the significance of the measurement is at least 3σ and to claim discovery when the significance of the measurement is at least 5σ .

Suppose the alternative hypothesis is in agreement with observations, and there is no evidence for the new physics. In that case, we might be questioning values of the signal strength μ that are not compatible with the observation and can be excluded. Moreover, since the signal strength is directly proportional to the cross section of the signal process, this method allows us to set limits on the

³Which is according to Neyman-Pearson lemma the optimal test statistic.

cross section predictions. Similar to the equation 7.16, we define tests statistics called the *one-sided profile likelihood ratio*

$$q_\mu = \begin{cases} -2\ln\lambda(\mu) & \text{if } \hat{\mu} \leq \mu \\ 0 & \text{if } \hat{\mu} > \mu, \end{cases} \quad (7.18)$$

with associated p -value

$$p_\mu = \int_z^\infty p(q_\mu|H_0)dq_\mu \quad (7.19)$$

and exclusion limit can be set by estimating the number of events for which the p_μ corresponds to 5%. However, if the analysis has no sensitivity for the new physics, the low p -value is easily achievable, leading to the high exclusion due to the non-optimal analysis strategy. In order to avoid this problem, the ATLAS SUSY group is using the conservative CL_s technique, which normalizes p_μ by the power $1 - p_0$.

$$CL_s = \frac{p_\mu}{1 - p_0} \quad (7.20)$$

This quantity replaces p_μ and represents a new p -value for given signal strength μ . This method is used to estimate exclusion limits, which are presented in the following chapters.

7.5 How to search for SUSY?

When we look for new physics processes, such as the production of SUSY particles, we usually look for a weak signal on top of the SM background. In order to be able to identify potential SUSY signal, it is crucial to understand the underlying physics and the way how we perform the experiment, which means understanding the detector, physics object reconstruction, and knowing uncertainties of measured quantities. Only then we can correctly interpret measured data and we can make statements about observed physics. In the case of big complex experiments, such as ATLAS, this process can be complicated and it can take years to get from the initial analysis idea to the physics results.

In the previous sections, we presented some statistical methods used in the physics analyses. These are also used in the analysis and reinterpretations presented later in this thesis. This section aims to briefly present a general idea of how these methods are used in the searches for new physics.

The new search starts by selecting the physics process we want to study and the way how we expect this process to manifest itself in our experiment. This usually means picking a well-defined final state with a signature specific to the given process. Let us use the higgsino search presented in chapter 8 as an example. Here we are looking for the production of a higgsino pair, where each of higgsinos decays to gravitino and the Higgs boson and we focus only on the case in which the Higgs boson decays to $b\bar{b}$, producing two b -jets. Since

the gravitinos can't be directly detected, we will identify them as E_T^{miss} in the event, and so the final state we want to study is the final state with E_T^{miss} and four b -jets⁴.

However, the signal process, which is described by SUSY, is not the only process able to produce the final state with four b -jets and E_T^{miss} since other SM processes can mimic this signal. Before continuing further, it is a good point to present the concept of different *analysis regions*. The analysis region is a set of selection rules, also called *cuts*, that select a well-defined subset of the data. We can define three different types of analysis regions, each of them having a specific purpose.

- *Signal region* (SR) - A signal region is a subset of our dataset where we expect to find possible evidence of new physics. For this reason, the signal region is designed based on criteria that maximize sensitivity to the hypothesized signal while minimizing the presence of background processes.
- *Control region* (CR) - This is the analysis region that is kinematically similar to the signal region but we ideally expect there no signal events, and a majority of events originating from the background. The purpose of this region is to constraint the background estimate that can be used in the signal region where we expect our SUSY signal on top of the SM background.
- *Validation region* (VR) - A validation region is typically designed to have similar characteristics to the signal region but without significant overlap. The purpose of the validation region is to verify that the background estimate derived in the control region matches our expectations, before applying it to the signal region. The validation region may have looser or alternative selection criteria compared to the signal region but still has a relatively low signal contribution.

Having defined analysis regions, we can describe the general analysis strategy and how these regions are used. The aforementioned background can be estimated using Monte-Carlo methods, or by data-driven methods as discussed more in detail in chapter 8. In order to make sure these estimates correctly describe our observed data, we use these estimates inside the control regions and we do a statistical fit of our predictions to the data using the maximum likelihood method as described in section 7.3. In order to be able to have robust background estimates, it is also important to quantify the uncertainty of our estimates, which include estimating experimental uncertainties (detector measurements, calibrations,...), theory uncertainties (physics processes modeling), and data-driven background estimates uncertainties, if the data-driven background estimates were used. These systematic uncertainties enter the fit as nuisance parameters. Since this fit assumes the presence of only background

⁴The higgsino analysis requires actually more than three b -tagged jets, which is discussed more in chapter 8, but we will now use the simplified example just to demonstrate the concept.

events inside the control regions, it is called *background-only fit* and it helps us to scale our background estimates such that they describe actual data in signal regions.

However, before applying these background corrections in the signal region, we use the validation region first to verify that our background modeling is correct. This step helps us verify our background estimates, before looking into the signal region which is important to avoid unwanted biases. Until this moment, the signal region is usually blinded.

Only after we make sure that we model the background correctly, we unblind signal regions and we apply the background correction factors derived in the control regions to the signal regions. At this moment, we can see if there is an excess between data and our predictions. The excess above three standard deviations (3σ) is considered to be a hint for new physics and excess above five standard deviations (5σ) can be claimed as discovery.

If the background modeling in the SR describes the data well, we can estimate the so-called model-independent limit by performing a *discovery fit*, which aims at determining the largest possible contribution for any signal model in the fitted bins without ruling out the background hypothesis. This fit uses both the signal and control regions that enter the fit to data, and the signal yield is added as a new parameter of interest to be estimated from the data. The upper limit is then estimated by scanning signal yields using profile likelihood ratio as a test statistic and excluding those values with $CL_s \leq 0.05$. Another approach is estimating model-dependent upper limits through an *exclusion fit*. This fit aims to derive upper limits on the cross section of the signal process under study. This fit is also performed both in signal and control regions, and the scan in a broad range of values of signal strength is performed and all values corresponding to $CL_s \leq 0.05$ are excluded.

Search for the higgsino pair production

8.1 Introduction

After the raw data from the experiment have been reconstructed, they can be used for data analysis. The aims of analyses can range from studies of the detector performance to precision measurements of parameters of the Standard Model to searches for new physics.

Supersymmetry predicts a vast amount of new particles. Although no direct evidence of SUSY has been found so far, it is still an appealing theory because, if found to be true, it could help solve many issues, such as the hierarchy problem, the existence of dark matter, or the unification of forces. Due to the large number of particles the SUSY predicts, searches for SUSY can be done in many ways. One of the possible ways is to search for squarks and gluinos since they should be abundantly produced at the LHC. Nevertheless, no signs for the gluinos and squarks have been found yet, and the searches have set limits on gluinos and squark masses of around 2 TeV. [60, 61]

The more difficult supersymmetric particles to search for are rare, electroweak-produced superpartners of W, Z, and Higgs bosons: the charginos and neutralinos. Discovery of the Higgs boson in 2012 opened a new window of search for these particles since they are predicted to decay into the final states containing the Higgs boson (among other possible decays) and other SUSY particles that can be seen as E_T^{miss} . Due to the high branching ratio of $h \rightarrow b\bar{b}$, the final state with multiple b -jets coming from the decay of the Higgs boson, and E_T^{miss} , representing invisible particles, is an interesting final state for searches for SUSY.

The analysis [62] described in this chapter searches for higgsino pair production in the final state with the two Standard Model Higgs bosons and E_T^{miss} . It uses the complete Run 2 data set with integrated luminosity of 139 fb^{-1} and is divided into two branches. One targets higher higgsino masses, referred to as the *high-mass channel*, and the other targets lower higgsino masses, referred to

as the *low-mass channel*. Approaches for these two branches are entirely different, including different analysis region definitions and background estimates. While the high-mass analysis exploits the high E_T^{miss} resulting from the boosted gravitinos, the low-mass analysis relies on b -jet triggers because E_T^{miss} is lower in these events than in the high-mass case and cannot be used efficiently. The results of these two branches were combined into the final exclusion.

The high-mass part of the analysis was used for the reinterpretation with the two different signal models, which is described in chapter 9, and for this reason, it is going to be described in more detail than the low-mass part of the analysis. The author of the thesis joined the analysis team in the final stages of the analysis, and he helped to do a few studies, such as cut flow. He also implemented RECAST of the analysis, which is described in detail in chapter 10.

8.2 Signal model

This analysis searches for the higgsino pair production in the model, inspired by general gauge mediation or gauge-mediated supersymmetry breaking.¹ These models are characterized by the existence of the lightest neutralino $\tilde{\chi}_1^0$, which is the neutral particle originating from mixing between the SUSY partners of the SM electroweak bosons and the particle associated with the spontaneous symmetry breaking of the global supersymmetry. This analysis studies a scenario in which the particle associated with supersymmetry breaking is absorbed by the superpartner of the graviton, the gravitino \tilde{G} , and due to the SUSY breaking being mediated at low energy, the gravitino is nearly massless. The $\tilde{\chi}_1^0$ in these models is dominated by the higgsino component and treated as a pure higgsino. It allows the higgsino, produced in mass-degenerate pairs, to decay into the SM Higgs boson and the nearly massless gravitino, which is the scenario studied by this analysis.

In this search, higgsinos are assumed to be produced in pairs, resulting in the final state with two SM Higgs bosons and missing transverse momentum E_T^{miss} . Due to the high branching ratio of $h \rightarrow b\bar{b}$, this decay channel is an ideal target for this model. Figure 8.1 shows the Feynman diagram of this particular scenario.

8.3 High-mass channel

The high-mass channel can be characterized by significant E_T^{miss} in the final state and relies on E_T^{miss} -based triggers, and it targets higgsino masses in the range of $[200, 1200]$ GeV. The following sections describe the analysis strategy, from

¹There is a number of proposed mechanisms through which the SUSY breaking effects are mediated to the visible sector. Gauge-mediated SUSY (GMSB) breaking models describe scenarios in which the SM gauge interactions mediate between hidden and visible sectors. For more information about this class of model, the reader can refer, for example, to [63].

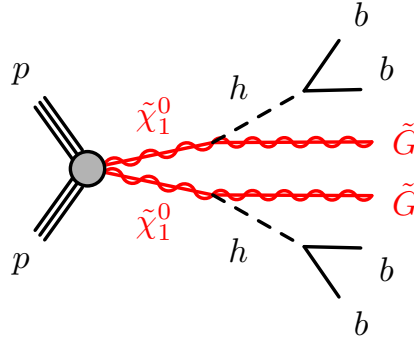


Figure 8.1: Feynman diagram of the simplified SUSY model targeted by the analysis. $\tilde{\chi}_1^0$ neutralino is treated as a pure higgsino.

event selection to background estimation and analysis region definition. It also briefly discusses systematic uncertainties considered in the analysis. Results are presented in the subsection 8.6 together with results from the low-mass channel of the analysis.

8.3.1 Event selection

All events used for the analysis must pass specific data quality criteria, ensuring that the entire ATLAS detector was fully operational. These selections reject events containing corrupted data from the ID and calorimeters and spurious jets caused by noncollision backgrounds. Also, events containing signal-quality leptons (electrons, muons) ² are discarded in order to minimize background due to the leptonic decays of W boson, and events containing loose leptons with $p_T > 8$ GeV in order to minimize overlap with ATLAS analyses using leptonic final states.

After these criteria have been satisfied, the following preselection criteria are applied.

- Between 4 and 7 small-radius jets with $p_T > 25$ GeV are reconstructed in the event to reduce backgrounds with a large number of additional jets.
- At least 3 b -tagged jets, as expected for the signal topology.
- $E_T^{\text{miss}} > 150$ GeV, for consistency with the production of invisible particles, because the lightest higgsino mass targeted by this branch of the analysis is 200 GeV.

²When reconstructing electrons or muons, multivariate techniques are employed, and the likelihood of the object being an electron is computed. There can be defined three types of leptons - *loose*, *baseline*, *signal-quality* based on several criteria. The signal-quality leptons are required to survive the overlap removal procedure, which is the procedure to resolve reconstruction ambiguities between electrons, muons, and small-radius jets, and satisfy *MediumLH* likelihood identification criteria [64].

- The minimum azimuthal angle between E_T^{miss} and any of the four leading jets ($\Delta\phi_{\text{min}}^{4j}$) is greater than 0.4, to reduce backgrounds with spuriously large E_T^{miss} resulting from the mismeasurement of the momentum of the jet. The reason for this choice is that events with large mismeasurement of jets can artificially enhance E_T^{miss} that would be then close to some of these jet.

The key element of this analysis is based on identifying two Higgs bosons originating from the decay of two higgsinos. Masses of the Higgs boson candidates are later denoted as $m(h_1)$ and $m(h_2)$. If the event contains at least 4 b -jets, the four with the highest p_T are used. If the event contains only 3 b -jets, the b -jet with the highest p_T above 100 GeV is considered to be the boosted Higgs candidate with two b -jets being merged into one. If there are only 3 b -jets and none have $p_T > 100$ GeV, the fourth jet is selected as the untagged small-radius jet that minimizes the $m(h_1)$ value.

The selected jets are paired into Higgs candidates in the following way. The quantity $\Delta R_{\text{max}}^{bb} = \max(\Delta R(h_1), \Delta R(h_2))$ is computed for all different pairings of candidate jets, where $\Delta R(h_{1,2})$ is the ΔR separation of two jets, and the pairing which minimizes $\Delta R_{\text{max}}^{bb}$ is selected.

In order to separate signal events from the background, a *Boosted Decision Tree* (BDT) is used. The BDTs are the machine learning technique using decision trees, which are simple classifiers that classify inputs based on several decision criteria that can be schematically represented as a binomial tree. These criteria are represented as cuts on selected variables, and the process of adjusting these criteria to ensure the best input classification is called *training*. The tree *boosting* is the process of combining the results of several simple decision trees into the final result by adding individual results together and reweighting them based on the accuracy of individual decision trees. This method can be used in the task of classification of inputs (events) into categories (signal or background), and its power is based on the fact that selection criteria can be directly interpreted and understood, contrary to, for example, neural networks where understanding the selection process is much more complicated.

BDTs used in the high-mass analysis exploit the following variables for the event classification.

- Number of jets and number of b -jets in the event.
- The scalar sum of the transverse momenta associated with small-radius jets in the event called H_T .
- Magnitude of E_T^{miss} and the object-based E_T^{miss} significance. [65]. The object-base E_T^{miss} significance is the quantity defined to test the hypothesis that the total transverse momentum carried by invisible particles equals zero against the hypothesis that it is different from zero.
- $\Delta\phi_{\text{min}}^{4j}$ as defined in the preselection criteria.

- the minimum transverse mass of the E_T^{miss} and the three leading b -jets in the event

$$m_{T,\min}^{b\text{-jets}} = \min_{i \leq 3} \sqrt{(E_T^{\text{miss}} + p_T^{j_i})^2 - (E_T^{\text{miss}} + p_x^{j_i})^2 - (E_T^{\text{miss}} + p_y^{j_i})^2}$$

- $\Delta R_{\text{max}}^{bb}$ as defined in the construction of the Higgs boson candidates
- The scalar sum of the masses of the reclustered large-radius jets in the event M_J^Σ . The reclusterization of jets is done at the object reconstruction level and increases the sensitivity for topologies where two b -jets originating from the Higgs boson are merged. It takes the small- R jets with $R = 0.4$ and uses another iteration of the anti- k_t algorithm to recluster them to jets with distance parameter $R = 0.8$.
- Masses of reconstructed Higgs bosons $m(h_1)$ and $m(h_2)$.
- Angular distances between the jets associated to Higgs boson candidates $\Delta R(h_1)$ and $\Delta R(h_2)$.

In order to ensure the optimal training for each of the higgsino mass hypotheses, the BDT is parametrized as a function of the higgsino mass. All the available samples of the simulated signal events are used together, with the higgsino mass for each sample used as an input variable in the training. To prevent the BDT from learning to distinguish signal from the background based on the higgsino mass variable, the same distribution of higgsino mass is assigned randomly to background events. The BDT then gives one output score per mass hypothesis. In total, eleven different mass hypotheses were set:

$$m_{\tilde{H}} = \{200, 250, 300, 400, 500, 600, 700, 800, 900, 1000, 1100\} \text{ GeV}$$

8.3.2 Background processes

The event selection described above also has acceptance for the SM processes with high E_T^{miss} and several b -jets. Several processes can contribute, and they need to be carefully modeled, which is done using Monte-Carlo simulation, with the only exception of QCD, which is estimated by the data-driven method. Further description of the individual processes follows.

- **Top quark pair background:** The $t\bar{t}$ production is one of the largest backgrounds in the analysis. The main decay mode for top quarks in the SM is $t \rightarrow W + b$, which results in two b -quarks in the final state. If the W decays hadronically, it can decay into $W \rightarrow c\bar{s}$ and c -quark, with a certain probability, can be mistagged as a b -jet, which results in the final state with at least 3 b -quarks.

In addition to $t\bar{t}$, additional parton can be radiated in the hard scattering. Simulation of $t\bar{t}$ production can be split into the following three production modes based on their truth information.

- If the radiated jet contains a B -meson at the truth level, the jet is considered a b -jet, and the event is marked as $t\bar{t}+ \geq 1b$.
 - If there is a radiated jet with D -meson at the truth level, the jet is considered to be from the hadronization of c -quark, and the event is marked as $t\bar{t}+ \geq 1c$.
 - If the radiated jet is containing quarks u or d , the event is marked as $t\bar{t} + \text{light}$.
- **Single-top-quark background:** There can also be only one top quark produced in proton-proton collisions. The cross section for this process is lower than that of the top quark pair production. In the s -channel and t -channel, the top quark is produced with another quark, which usually does not pass through the simultaneous cuts on E_T^{miss} and b -jet multiplicity. However, a single top quark can also be produced in association with a W boson, which is the dominant component of the background for this analysis. The modeling of this channel has to be done carefully due to the quantum interference with the $t\bar{t}$ process. The W boson and top quark in the final state can be produced at NLO, leading to a similar topology as LO $t\bar{t}$, which results in the final state with two on-shell W bosons and two b -quarks.

The total cross section for the $WWbb$ final state receives contribution from both topologies, and the matrix element for this process can be written as:

$$|\mathcal{M}_{WWbb}|^2 \propto |\mathcal{M}_{\text{LO-}t\bar{t}}|^2 + |\mathcal{M}_{\text{NLO-}Wt}|^2 + 2\text{Re} \left\{ \mathcal{M}_{\text{LO-}t\bar{t}} \times \mathcal{M}_{\text{NLO-}Wt}^* \right\}.$$

Handling this interference involves introducing a correction in the single-top quark simulated samples while leaving those for $t\bar{t}$ unaffected. It is done at the Monte-Carlo generator level by modifying the matrix element for the process and removing the NLO diagram, which contributes to the $WWbb$ final state. This has to be considered when introducing systematic theoretical uncertainties for the Monte-Carlo modeling of this background.

- **Vector boson + jets background:** There are two major processes - W +jets and Z +jets. Namely, process $Z \rightarrow \nu\nu$ results in large E_T^{miss} in the event, contributing to the regions with high-mass higgsinos. In the W +jets process, W has to decay leptonically to produce E_T^{miss} , which is suppressed by analysis selection requiring zero signal leptons in the final state.
- **Diboson background:** Z and W bosons can also be produced in pairs at the LHC. Events combining $Z \rightarrow b\bar{b}$ and $W \rightarrow \tau\nu_\tau$, or $Z \rightarrow \nu\nu$ and $W \rightarrow c\bar{s}$ where c -quark is mistagged as b -quark can contribute to this background. However, the production cross section of these processes is small, so it is suppressed with respect to the single vector boson production.

- **$t\bar{t} + X$ background:** The top quark can also be produced in association with other particles such as Higgs boson, $t\bar{t}$ pair, or electroweak bosons. Since the production cross section of these processes is small and they do not contribute much to the overall background, they are merged all together in one background process.
- **QCD multijet background:** Events produced by the QCD multijet processes form a small percentage of SM background present after the pre-selection cuts. However, the background has to be estimated accurately. This can be challenging by MC methods, since these processes typically happen at the limit of the perturbative approximation of the QCD. For this reason, a data-driven technique is used to estimate the QCD multijet background. It consists of subtracting non-QCD-multijet background estimated with MC simulations from data. These events are obtained by creating a template that replaces selection $\Delta\phi_{\min}^{4j} > 0.4$ by selection $\Delta\phi_{\min}^{4j} < 0.2$. The contribution of this background to the analysis regions is estimated by using the discriminating BDT in the following way.
 - 1) The fake $\Delta\phi_{\min}^{4j}$ distribution is generated for events in the template, sampled randomly from the expected $\Delta\phi_{\min}^{4j}$ distribution observed in dijet MC simulated samples.
 - 2) Neural-network-assisted reweighting is applied to the template to correctly reflect the correlation between $\Delta\phi_{\min}^{4j}$ and other kinematic variables used in the BDT training. It is done by training the neural network on simulated dijet events to separate $\Delta\phi_{\min}^{4j} < 0.2$ from $\Delta\phi_{\min}^{4j} > 0.4$ events and then applying the event weight based on the per-event neural network output score to the data-driven template.
 - 3) The reweighted template is the QCD multijet estimate.

The main background process is $t\bar{t}$, followed by QCD multijet background at low- $E_{\text{T}}^{\text{miss}}$ regions and Z +jets and single-top backgrounds at high- $E_{\text{T}}^{\text{miss}}$ regions. Smaller contributions are from $t\bar{t} + X$ and diboson production. Table 8.1 summarizes Monte-Carlo generators used to simulate individual backgrounds.

8.3.3 Analysis regions definition

The signal regions are defined using the BDT output scores of preselected events and built using the following iterative procedure for each mass hypothesis. The first signal region is chosen such that events in this region have assigned BDT score in range $(C_{SR_1}, 1]$ where C_{SR_1} is determined such that the SR contains at least 0.5 background events and maximizes statistical significance. After the first region is built, the second region is constructed similarly to the first region for events with BDT output scores in the range $(C_{SR_2}, C_{SR_1}]$. This process is repeated until no more SR can be found. In case there are more than four SRs, the SRs with the lowest score are merged such that there is a maximum number of four signal regions.

Process	Generator	Tune	PDF set	Cross-section order
Higgsino sample	MADGRAPHv2.6.1 + PYTHIAv8.230	A14	NNPDF2.3	NNLO _{apprx} +NNLL [66, 67, 68, 69, 70, 71]
Single top	POWHEG BOXv2 + PYTHIAv8.230	A14	NNPDF3.0 (ME) NNPDF2.3 (UE)	NLO [72] (t/s -channel) NLO+NNLL [73] (Wt)
$t\bar{t}$	POWHEG BOXv2 + PYTHIAv8.230	A14	NNPDF3.0 (ME) NNPDF2.3 (UE)	NNLO+NNLL [74]
$t\bar{t}W/t\bar{t}Z$	MADGRAPH5@NLOv2.3.3 + PYTHIA-8.210	A14	NNPDF3.0 (ME) NNPDF2.3 (UE)	NLO [75]
$t\bar{t}t\bar{t}$	MADGRAPH5@NLOv2.2.2 + PYTHIAv8.186	A14	NNPDF2.3	NLO [75]
$t\bar{t}h$	POWHEG BOXv2 + PYTHIAv8.230	A14	NNPDF3.0 (ME) NNPDF2.3 (UE)	NLO [76]
Dibosons WW, WZ, ZZ	SHERPAv2.2.1	Default	NNPDF3.0	NLO [77, 78]
W/Z+jets	SHERPAv2.2.1	Default	NNPDF3.0	NNLO [79]
Dijet	PYTHIAv8.230	A14	NNPDF2.3	LO

Table 8.1: List of generators used for the different processes. Information about the underlying event tunes, the PDF sets, and the QCD highest-order accuracy to normalize the different samples is given. [62]

After finding all signal regions, a similar procedure is carried out to find the control (CR) and validation (VR) regions. Regions for $t\bar{t}$ are kept orthogonal from high- $m_{T,\min}^{b\text{-jets}}$ regions by applying a cut on $m_{T,\min}^{b\text{-jets}}$, with splitting point $m_{T,\min}^{b\text{-jets}} = 200$ GeV.

The procedure for the low and high- $m_{T,\min}^{b\text{-jets}}$ regions is identical and is done for each region independently of the other. Validation regions are constructed with all of the events with BDT output in the range $(C_{VR}, C_{SR_i}]$ and the value of C_{VR} is chosen so that there are at least 25 weighted background events and the signal contamination is lower than 20%.

Once the high- $m_{T,\min}^{b\text{-jets}}$ region has been found, the procedure is applied for the low- $m_{T,\min}^{b\text{-jets}}$ regions to find the control regions with a requirement of at least 100 weighted background events in the region and the signal contamination lower than 10%.

For the $t\bar{t}$ region, the set of events used to define the region is further split into events containing four and three b -jets. This approach allows us to define two control regions enriched in $t\bar{t}$ events but with different fractions of $t\bar{t} + \text{light}$, $t\bar{t} + \geq 1c$ and $t\bar{t} + \geq 1b$, which is useful to fit separately the normalization of each component.

As described above, Z +jets becomes the dominant background for the high-mass signal regions due to the decay $Z \rightarrow \nu\nu$, which is manifested in events as high E_T^{miss} . In order to define CR and VR for this process, events with exactly

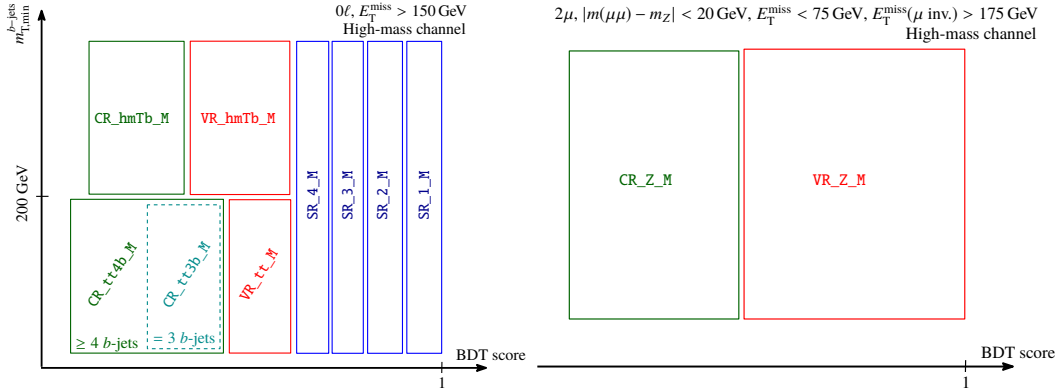


Figure 8.2: Schematic representation of analysis regions construction. [62]

two leptons are selected, and leptons are added to E_T^{miss} to simulate neutrinos from Z decay. For this purpose, the new sample is created with a different set of preselections accepting events with two muons, unlike the sample used for the rest of the analysis, where zero signal leptons are required. On top of that, it is required that muons have opposite charges and that they satisfy condition $|m_{\mu\mu} - m_Z| < 20 \text{ GeV}$. BDT is then used to evaluate these events, and CR and VR are constructed similarly as in the case of regions discussed above, with the only difference that we do not look for the signal regions since these do not exist in this newly constructed sample because of the presence of two leptons.

The construction of the analysis regions is schematically shown in figure 8.3.

8.4 Low-mass channel

The low-mass channel is targeting higgsino masses below 200 GeV. It focuses on the final state characterized by four or more b -jets and the absence of signal-quality leptons. Higgs boson candidates are reconstructed from the b -jets in the event, similarly to the high-mass channel. The event selection in the low-mass part of the analysis cannot rely on the high E_T^{miss} as a high-mass branch of the analysis, and so it relies on the b -jet triggers.

8.4.1 Analysis regions

Analysis regions are then defined based on masses of reconstructed Higgs bosons, which can be depicted in the two-dimensional plane, where axes are masses of reconstructed Higgs bosons. It is shown in figure 8.3 and can be analytically expressed as $X_{hh}^{\text{SR}} < 1.6$ where

$$X_{hh}^{\text{SR}} = \sqrt{\left(\frac{m(h_1) - 120 \text{ GeV}}{0.1m(h_1)}\right)^2 + \left(\frac{m(h_2) - 110 \text{ GeV}}{0.1m(h_2)}\right)^2}, \quad (8.1)$$

and denominators are the approximate resolutions for the Higgs boson candidates.

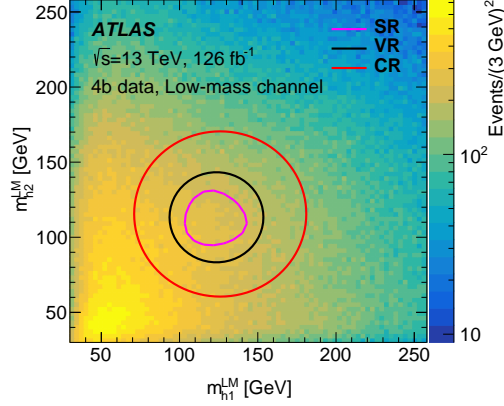


Figure 8.3: Graphical representation of the analysis regions used in the low-mass channel of the analysis. The color scale represents distribution of reconstructed Higgs boson masses using the 4b data. The high event density in the bottom left corner far from the true Higgs boson mass, are the Higgs boson candidates arising from combining together b -tagged jets attributed to the background processes. [62]

8.4.2 Background processes

The main background in the low-mass channel is formed by the QCD multijet process and $t\bar{t}$. The leptonic component of $t\bar{t}$ is reduced by requiring at most two loose leptons. The hadronic $t\bar{t}$ is then suppressed by defining a discriminant based on the reconstruction of top quark decays. Top quarks are reconstructed using three b -jets, where one of these must be from a Higgs boson candidate, and it is considered to be the b -jet from the top quark decay. The other two jets are combined to form a W boson candidate. Moreover, since W boson cannot decay into more than one b -jet, at least one of the W boson candidate jets must not be associated with the Higgs boson candidate. Then quantity

$$X_{Wt} = \sqrt{\left(\frac{m_{jj} - m_W}{0.1m_{jj}}\right)^2 + \left(\frac{m_{jjb} - m_t}{0.1m_{jjb}}\right)^2}, \quad (8.2)$$

is calculated and it is required to be $X_{Wt} < 1.8$. Denominators are, similarly to the SRs definition, representing the fractional mass resolution of reconstructed particle candidates. Mass of W and top mass are $m_W = 80.4 \text{ GeV}$ and $m_t = 172.5 \text{ GeV}$.

Modeling of the QCD background is challenging in simulations, so a data-driven ABCD method with BDT reweighting is used. The method is the following. The SR and CR are split into two smaller sub-regions, one containing events with exactly two b -jets (2b region) and the other with at least four b -jets (4b region). Then the number of events N_{CR-2b} in the 2b and the number of

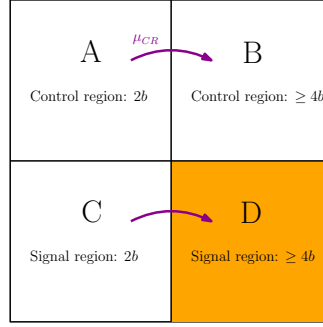


Figure 8.4: Schematic depiction of the ABCD method used for the background estimation in the low-mass channel of the analysis.

events N_{CR-4b} in $4b$ control region is computed, and the transfer factor μ_{CR} is estimated.

$$\mu_{CR} = \frac{N_{CR-2b}}{N_{CR-4b}}$$

The $2b$ regions are reweighted using a BDT³ to correct for any kinematic differences between the $2b$ and $4b$ regions and transfer factor μ_{CR} is used to estimate the final number of events in the $4b$ SR. This is schematically depicted in figure 8.4.

8.5 Systematic uncertainties

Systematic uncertainties entering the analysis in both high and low-mass channels can be split into three categories.

- **Experimental uncertainties:** Experimental uncertainties are systematic uncertainties related to the experimental effects due to mismeasurement of certain quantities. The analysis includes uncertainties associated with the jet energy scale and resolution, jet mass scale, flavor-tagging efficiencies, trigger efficiencies, soft E_T^{miss} terms, pileup conditions, and luminosity estimates. These uncertainties are correlated across all SRs, VRs, and CRs for the high-mass channel, and so they are used for all regions, while for the low-mass channel, they are applied only to the $4b$ SRs, as no other regions are used in the fit. The dominant experimental uncertainties on the background in the SR are those related to the jet reconstruction. Uncertainties related to the jet energy scale and the jet energy resolution are the largest ones, reaching up to 30% on the background prediction in the SRs per source of uncertainty.
- **Theoretical uncertainties:** The theoretical uncertainties are the result of a mismodeling of the signal in Monte-Carlo simulations. These uncertainties are assessed by the effect of varying several parameters, such as

³This is a different BDT than is used in the high-mass channel of the analysis.

factorization and renormalization scales, parton shower tuning, and initial- and final-state radiation parameters. The differences resulting from these variations are applied as systematic uncertainties.

Theoretical uncertainties are also applied to the background samples for the high-mass channel. Uncertainties describing the systematic effects due to possible mismodeling associated with the Monte-Carlo generators and parton shower models are used for the $t\bar{t}$ and single-top backgrounds, as well as the uncertainty associated with the quantum interference between tW and $t\bar{t}$. Uncertainties related to the renormalization, factorization, and matching scales are applied to the W +jets and Z +jets backgrounds. The 50% uncertainties are applied to the $t\bar{t} + X$ and diboson backgrounds, but they have no significant effect due to the small contributions of these backgrounds.

- **Data-driven background uncertainties:** The low-mass channel of the analysis also applies uncertainties related to the data-driven background estimate. These are related to imperfections in the BDT reweighting procedure, extrapolation of results from the CRs to SRs, and the transfer normalization.

8.6 Results

For each mass hypothesis in the high-mass channel, all available signal and control regions are included in the fit. The fit is done simultaneously in all control regions to constraint the background, and then simultaneously in all signal regions to in order to maximize exclusion. After performing the statistical fit, data in the validation regions agree with the background, confirming good background modeling. This is shown in figure 8.5a. [62]

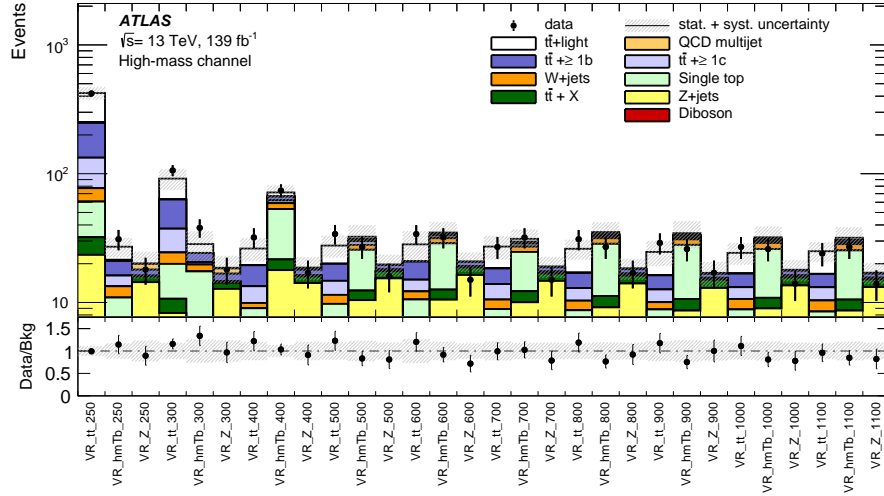
Observations for the SR are shown in figure 8.5b. Also, no statistically significant excess between data and predictions is found here. The largest excess is observed in the SR_1000 with a local statistical significance of 1.9σ . The excesses in SR_900, SR_1000, and SR_1100 are similar due to the highly correlated SR definitions. The same three data events are observed in the first two of these SRs, and one fails the SR_1100 selection.

Also, for the low-mass channel, no significant mismodeling is observed for any of the VRs, and no significant excess is observed for any of the SRs.

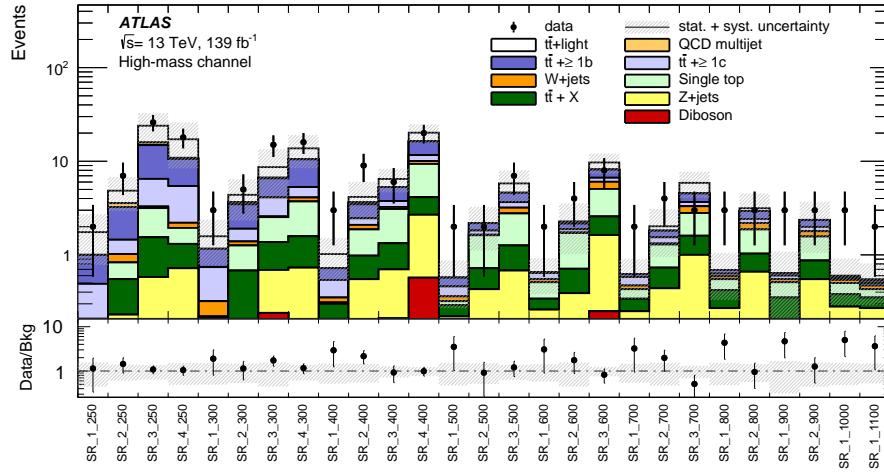
Following the Neyman-Pearson lemma, as described in chapter 7, the upper limits on the higgsino pair production are set using the test statistics based on the profile likelihood ratio. Since no significant excess above SM predictions, the 95% CL upper limits are calculated for the model described in section 8.2, with the transition between low-mass and high-mass channel happening at $m_{\tilde{H}} = 250 \text{ GeV}$. Figure 8.6a shows the upper limit on the higgsino pair-production cross section for a branching ratio of $\mathcal{B}(\tilde{H} \rightarrow h + \tilde{G}) = 100\%$.

The results are also interpreted for the case where $\mathcal{B}(\tilde{H} \rightarrow h + \tilde{G})$ is allowed to vary, with all other decays being $\tilde{H} \rightarrow Z + \tilde{G}$. The higgsino pair-production

8. Search for the higgsino pair production



(a) Validation regions.



(b) Signal regions

Figure 8.5: Agreement between data and background in validation region 8.5a and signal region 8.5b for the high-mass channel of the analysis. [62]

cross section is assumed to match the theoretical prediction. Limits for this interpretation are shown in figure 8.6b.

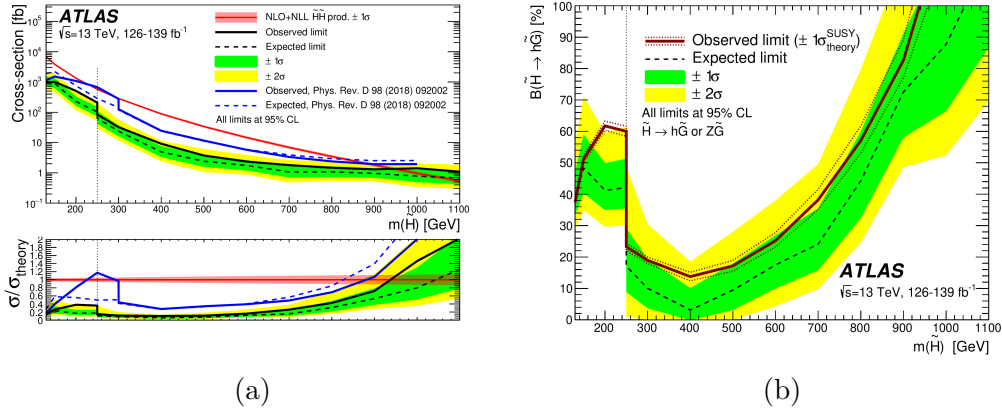


Figure 8.6: The left plot shows the observed (solid) and expected (dashed) 95% CL upper limits on the higgsino pair-production cross section, assuming a higgsino decay branching ratio of $\mathcal{B}(\tilde{H} \rightarrow h + \tilde{G}) = 100\%$. The right plot shows the 95% CL observed (solid) and expected (dashed) upper limits on $\mathcal{B}(\tilde{H} \rightarrow h + \tilde{G})$, assuming the theory cross section for higgsino pair production. The higgsinos are assumed to decay as $\tilde{H} \rightarrow h + \tilde{G}$ or $\tilde{H} \rightarrow Z + \tilde{G}$. For both plots, the phase space above the lines is excluded. [62]

Reinterpretation of the higgsino pair production analysis

9.1 Introduction

Reinterpretation is the process when we assume a different physics model and we process the model in terms of an already existing analysis. Suppose the new model is similar to the one in the original analysis and has the same final state as the original analysis. In that case, we can use the reinterpretation to easily see whether the new model can be excluded. The advantage of this approach is that the analysis regions and background contributions are the same for the reinterpretation as for the original analysis. Reinterpretation can also serve as a starting point for a new analysis that is more suited for the particular features of the physics model than the original analysis.

We studied two other signal models and reinterpreted them in the scope of the high-mass channel of the electroweak higgsino analysis presented in chapter 8. These models are:

- **Heavy and light neutralino model** is the SUSY model assuming production of pair of heavy neutralinos $\tilde{\chi}_3^0$ and $\tilde{\chi}_2^0$ with mass degenerate spectrum, where each of them further decays into a Higgs boson and light neutralino $\tilde{\chi}_1^0$. Two light neutralinos are detected as E_T^{miss} and Higgs bosons decay $b\bar{b}$, which results in the same final state as the higgsino analysis. The process is described in more detail in section 9.2. When referring to heavy neutralinos further in the text, we are not always going to mention both $\tilde{\chi}_2^0$ and $\tilde{\chi}_3^0$ explicitly due to the degeneracy of heavy neutralino masses, and we are often going to talk only about $\tilde{\chi}_2^0$, while assuming that the same holds for $\tilde{\chi}_3^0$, unless stated otherwise. A more detailed description of the model is provided in subsection 9.2.1.
- **Dark-Higgs model** is one of the BSM models proposing the existence of a new s -channel vector boson mediator called Z' , and a new scalar particle,

which is analogous to the Higgs boson in the dark sector (also referred to as mono-s). The vector boson Z' is produced in pp collisions, and it irradiates the dark-Higgs boson in a process similar to bremsstrahlung. Z' decays into two dark matter particles χ , which manifest themselves in the event as E_T^{miss} and dark-Higgs boson decays into two SM Higgs bosons, each of them further decaying into $b\bar{b}$. The process is described in more detail in section 9.3. Despite the same final state as the Higgsino analysis, the topology of the process is different. A more detailed description of the model is provided in subsection 9.3.1.

Each of these processes is described more in detail in dedicated sections 9.2 and 9.3. The interpretation of the dark-Higgs model motivated the development of the new dedicated analysis, which is not part of this thesis. While the author also partly participated in the dark-Higgs analysis, his primary focus was on the reinterpretations presented in this chapter.

9.2 Heavy and light neutralino model

This section describes the reinterpretation of the analysis presented above using the model with heavy and light neutralinos. The signal model and the signal grid used are described at the beginning of this section, followed by the description of the methodology and results of the reinterpretation.

9.2.1 Signal model

For this reinterpretation, pair-production of higgsino-like heavy neutralinos ($\tilde{\chi}_3^0 \tilde{\chi}_2^0$) is considered. Within the MSSM, there are several SUSY production mechanisms. Either via electroweak gauge boson, Higgs-mediated production, or through production via cascade decays of gluinos or via gluino/squark or squarks [80]. The heavy neutralinos then each decay into a Higgs boson and the lightest neutralino ($\tilde{\chi}_1^0$) as shown in figure 9.1. In this scenario, the lightest neutralino is bino-like. The heavy and light neutralino masses are the free parameters in the model, whilst all other sparticle masses are set to be heavy enough not to be in the reach of the LHC and are thus effectively decoupled. The branching ratio for the higgsino-like heavy neutralino to Higgs boson and light neutralino ($\tilde{\chi}_1^0$) decay is set to 100%, unlike the original Higgsino analysis where the heavy neutralinos have a 50% branching ratio to $Z + \tilde{g}$. The masses of the heavy neutralinos $\tilde{\chi}_3^0 \tilde{\chi}_2^0$ are assumed to be degenerate. This reinterpretation targets the final state when both Higgs bosons decay into $b\bar{b}$ and both $\tilde{\chi}_1^0$ manifest themselves in the event as a missing energy. The model is similar to the original electroweak analysis because it has the same event topology and same observable final state as the original analysis¹, but the kinematics is different due to generally non-zero mass of the light neutralino.

¹The light SUSY particles (gravitino or light neutralino) are different in each model but they are observed in the detector as E_T^{miss} .

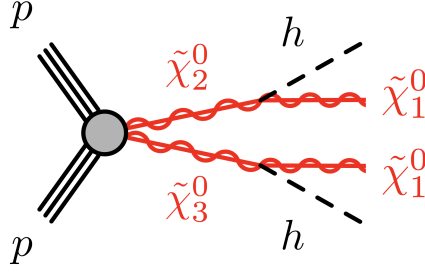


Figure 9.1: Feynman diagram of the model with heavy and light neutralinos. The model has the same final state as the model described in section 8.2, but the kinematics is different due to different masses of particles involved.

We used the Monte-Carlo simulation of the signal process in the signal parameter space shown in figure 9.4a. Matrix elements for neutralino pairs are generated with up to two additional partons using MADGRAPHv2.7.3 at leading order (LO) with the NNPDF 2.3 Parton Density Function (PDF) sets and the A14 tune². PYTHIAv8.244 is subsequently used to model parton showering, hadronization, and underlying event.

In reality, the production of $\tilde{\chi}_2^0 \tilde{\chi}_3^0$ will be accompanied also by production of $\tilde{\chi}_3^0 \tilde{\chi}_1^\pm$, $\tilde{\chi}_2^0 \tilde{\chi}_1^\pm$, and $\tilde{\chi}_1^\pm \tilde{\chi}_1^\pm$. These production modes have similar cross sections (see figure 9.2), but $\tilde{\chi}_1^\pm$ cannot directly produce a Higgs boson. $\tilde{\chi}_1^\pm$ will typically decay through $\tilde{\chi}_1^\pm \rightarrow \tilde{\chi}_1^0 + W$, which will not result in the final state with the Higgs boson. These other production modes were not included as a signal for the reinterpretation because they do not lead to the final state with two Higgs bosons for which the BDT used in the analysis was trained. However, the existence of these other production modes is accounted for in cross sections used in the MC generation.

9.2.2 Results

The topology of the signals model is the same as in the case of the higgsino analysis described in chapter 8. The major difference is in the kinematics for the non-zero mass of the light neutralino, which effectively changes the amount of observed E_T^{miss} in events. In the case of the higgsino analysis, the gravitino is nearly massless, meaning that the signal with light neutralino $m_{\tilde{\chi}_1^0} = 0 \text{ GeV}$, and heavy neutralino with mass $m_{\tilde{\chi}_2^0}$ should have nearly identical kinematic distributions to higgsino with corresponding mass. This can be seen in figure 9.3, where we plotted various kinematic variables used in the analysis. The most obvious effect of changing $m_{\tilde{\chi}_1^0}$ while keeping $m_{\tilde{\chi}_2^0}$ constant is seen in E_T^{miss} and

²Monte-Carlo generators are usually based on models which are typically either approximations to high-multiplicity perturbative QCD calculations or phenomenological attempts to address non-perturbative physics. In order to simulate these effects, a set of parameters has to be introduced into generators, and a particular setting of these parameters is called the tune. [81]

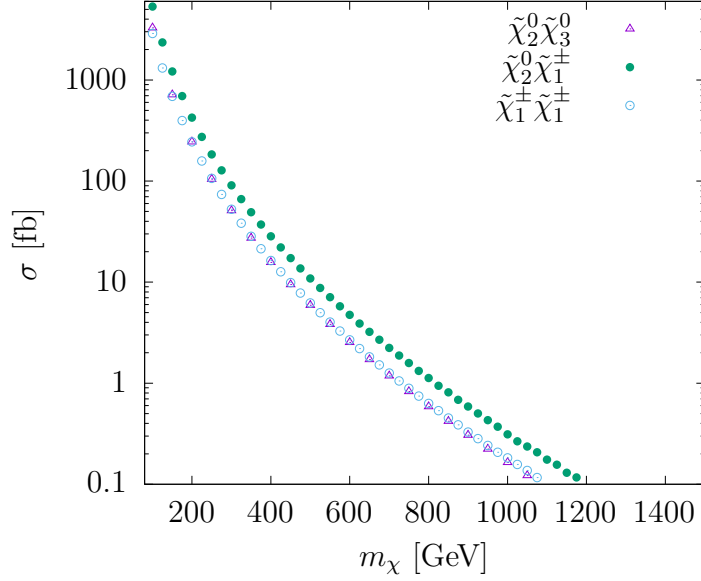


Figure 9.2: Production cross sections for $\tilde{\chi}_2^0\tilde{\chi}_3^0$, $\tilde{\chi}_2^0\tilde{\chi}_1^\pm$, $\tilde{\chi}_1^\pm\tilde{\chi}_1^\pm$ in $\sqrt{s} = 13$ GeV in fully degenerate case where masses of chargino and neutralinos $\tilde{\chi}_2^0$ and $\tilde{\chi}_3^0$ are the same.

H_T as expected, because the amount of E_T^{miss} in the event is related to the mass of undetectable particles in the event.

These differences have to be taken into account while evaluating events using BDTs. The most straightforward choice would be selecting the BDT for the higgsino mass hypothesis $m_{\tilde{H}}$, which is equal to the mass of the heavy neutralino $m_{\tilde{\chi}_2^0}$. However, different BDT might perform better due to the kinematic differences. That is why we performed fits and computed CL_s values using different BDTs, and we picked the BDT that gave us the lowest CL_s value. Using this optimization procedure, we ensured that we always had the best exclusion for the given point in the signal grid. In order to save the computational resources, we ran these optimization fits with 50% flat systematic uncertainties since we do not expect systematic uncertainties to impact the final CL_s values significantly. This was tested for several grid points. After we chose the BDT, we ran the full fit, including all systematic uncertainties and estimated CL_s values, which were used for the final exclusion plot.

Results of this optimization procedure are shown in figure 9.4b, where we show which BDTs were selected for individual signal parameter grid points. It can be seen that the BDT index that corresponds to the higgsino mass hypothesis used for training is increasing as we go more to the right on the x -axis since increasing $m_{\tilde{\chi}_2^0}$ is equivalent to increasing higgsino mass. On the contrary, as we go higher on the y -axis, the BDT index decreases since we are changing the amount of energy that can be used to boost $\tilde{\chi}_2^0$ decay products. It can be noticed that some BDT indices (600 GeV and 800 GeV) are missing even for $m_{\tilde{\chi}_1^0} = 0$ GeV. The reason is that despite the high similarity of heavy neutralino and higgsino signals, there are still differences, such as that the gravitino was nearly

9. Reinterpretation of the higgsino pair production analysis

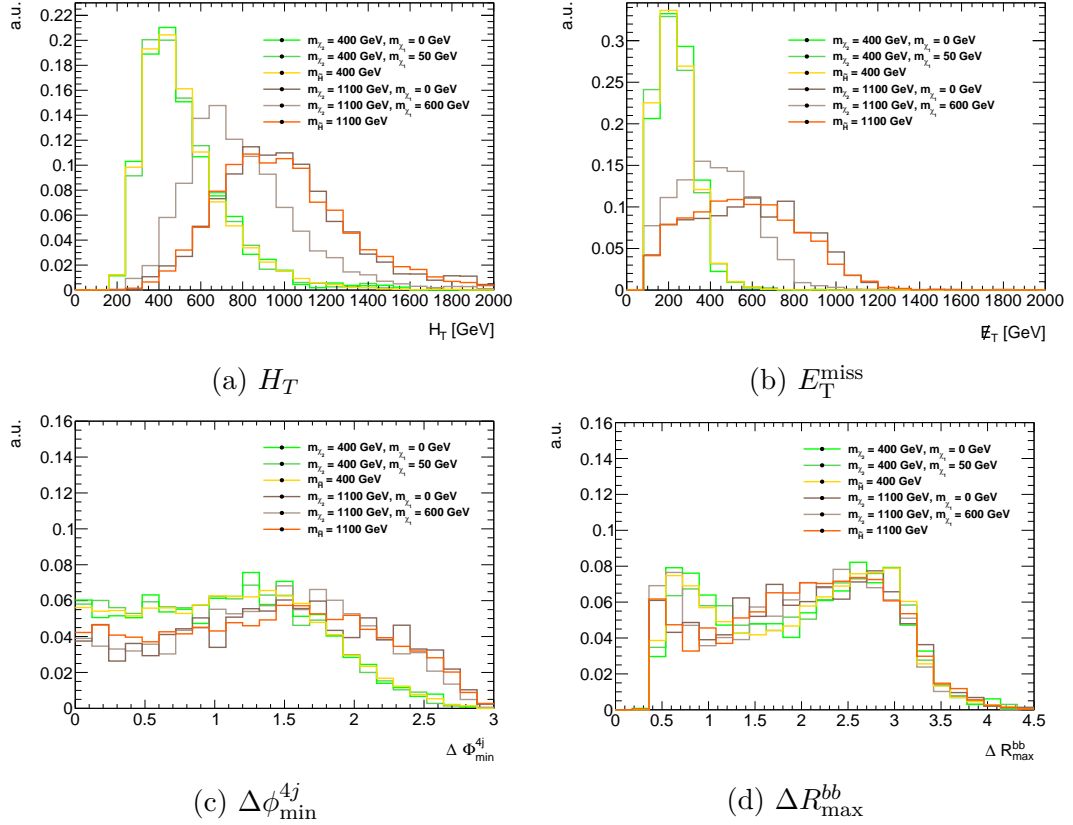


Figure 9.3: Comparison of missing E_T^{miss} , H_t , $\Delta\phi_{\min}^{4j}$, ΔR_{\max}^{bb} for different models. Difference between distributions for the same mass $m_{\tilde{\chi}_2^0}$, but different $m_{\tilde{\chi}_1^0}$ can be seen mainly for E_T^{miss} , and H_t . Distributions for higgsino mass hypotheses $m_{\tilde{H}} = m_{\tilde{\chi}_2^0}$ are plotted as well and they coincide with distributions $m_{\tilde{\chi}_1^0} = 0$ GeV as expected. Histograms are normalized to the unit area, and units on the y -axis are arbitrary.

massless, while heavy neutralino mass is exactly 0 GeV. Since this study was meant to be the reinterpretation, we did not aim for BDT re-training for heavy neutralino samples, which could likely improve the reinterpretation sensitivity.

After selecting the BDT, we checked that the signal contamination in the individual analysis region is comparable to the numbers required by the higgsino analysis. That meant signal contamination lower than 10% for control regions and less than 20% for validation regions. This is shown for all used analysis regions in figure 9.5. The contamination of no CR was above 10%, and no VR had contamination above 20%.

Figure 9.6 shows the final exclusion plot. Although the analysis was initially optimized for the higgsino signal, we still managed to exclude additional phase space in comparison with the previous ATLAS analysis [82] that searched for charginos and neutralinos in final states with two boosted hadronically decaying bosons and missing transverse momentum. This analysis studied several models, and one of them was the same as the one we studied in this reinterpretation.

Its approach also included production modes with charginos ($\tilde{\chi}_3^0 \tilde{\chi}_1^\pm$, $\tilde{\chi}_2^0 \tilde{\chi}_1^\pm$, and $\tilde{\chi}_1^\pm \tilde{\chi}_1^\pm$), which we didn't consider for the reinterpretation for the reason presented at the end of the subsection 9.2.1. This effectively means that the reinterpretation presented in this section had a smaller production cross section, which has to be kept in mind when comparing exclusion plots in figure 9.7.

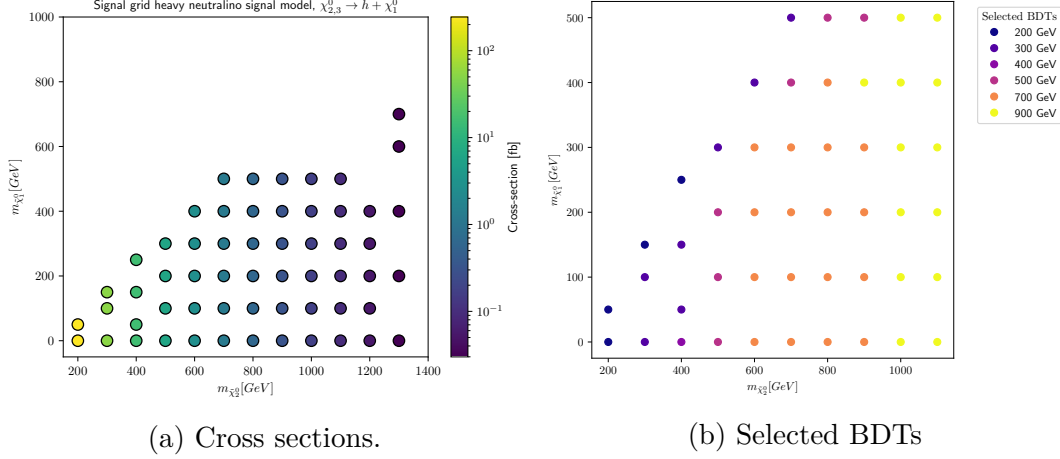
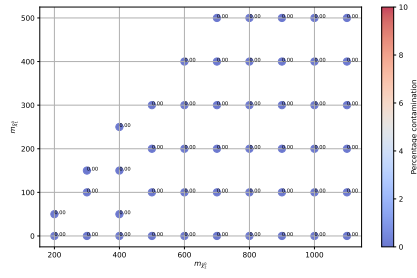
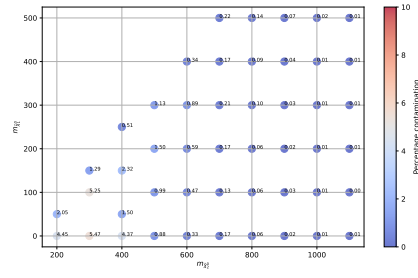


Figure 9.4: The signal grid of the model with heavy neutralino is used for the reinterpretation. Figure (a) shows the cross sections of individual signal hypotheses, and figure (b) shows the BDTs selected for these hypotheses. BDTs are labeled by the higgsino mass hypothesis used for their training.

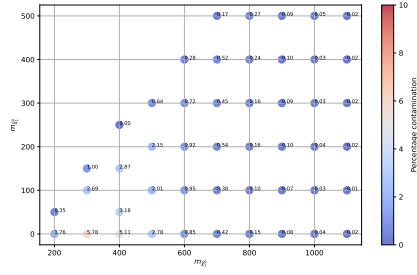
9. Reinterpretation of the higgsino pair production analysis



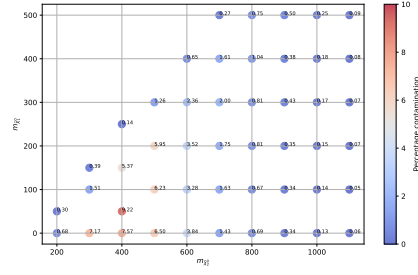
(a) Z+jets CR



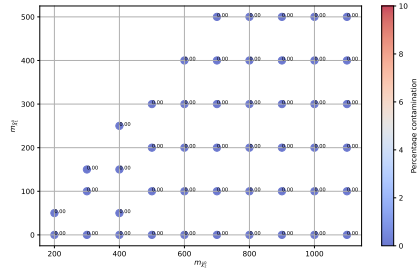
(b) $t\bar{t}$ 4b CR



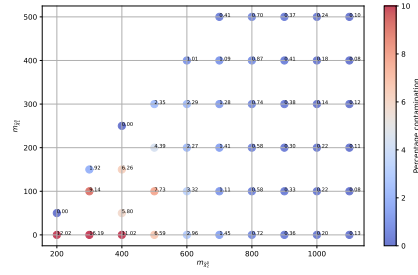
(c) $t\bar{t}$ 3b CR



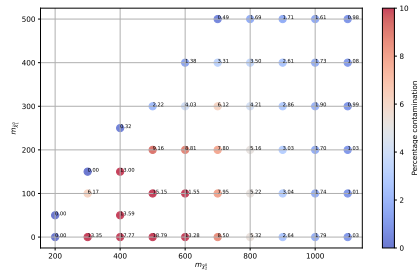
(d) $high - m_{T,min}^b$ CR



(e) Z+jets VR



(f) $t\bar{t}$ VR



(g) $high - m_{T,min}^b$ VR

Figure 9.5: Percentage contamination across the heavy neutralino signal grid for events in all analysis regions.

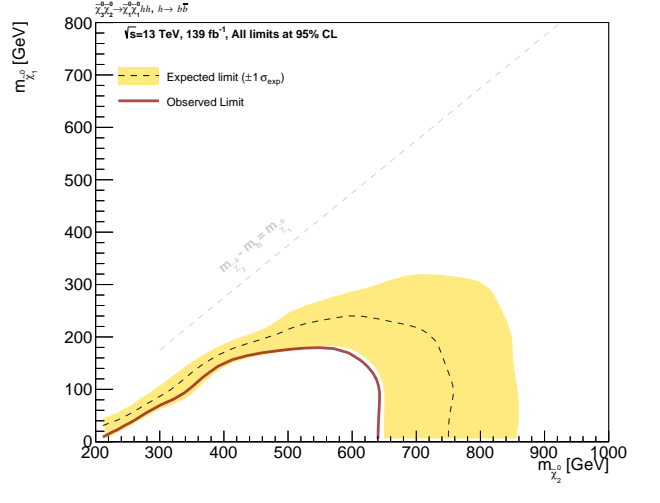


Figure 9.6: Two-dimensional exclusion plot for the model with heavy and light neutralinos. The x-axis of the plot represents the mass of the heavy neutralino, and the y-axis represents the mass of the light neutralino. The area enclosed by the red line and the x-axis is excluded by the data at a 95% confidence level. The area enclosed by the dashed line and the x-axis is excluded by simulation at 95% confidence level, and the yellow band is $\pm 1\sigma$ band. The area above the grey diagonal line is kinematically impossible because the scalar sum of masses of the light neutralino and Higgs boson must always be equal to or smaller than the mass of heavy neutralino, which decays into these two particles.

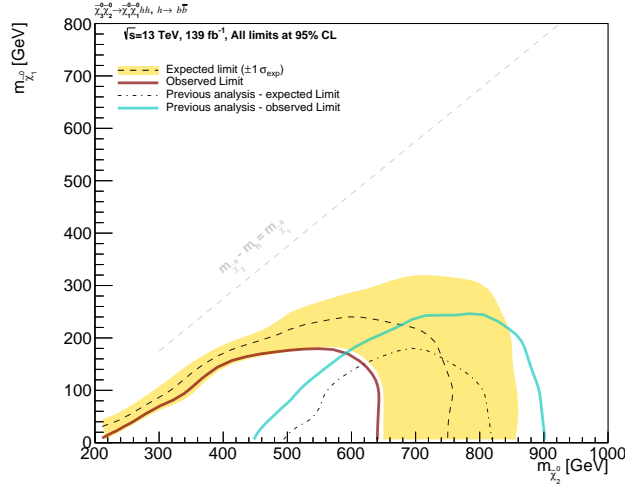


Figure 9.7: Comparison of the two-dimensional exclusion from the reinterpretation using heavy and light neutralino signal with results of the previous ATLAS analysis [82] targeting the same model. However, it has to be kept in mind that previous analysis considered other production modes not included in the reinterpretation, which was justified in the text of this subsection.

9.3 Dark-Higgs model

This section describes the reinterpretation of the high-mass channel of the higgsino analysis described in chapter 8 using the dark-Higgs model. This section is structured similarly to the section describing the reinterpretation using the model with heavy and light neutralinos. It starts with a description of the signal model and the signal grid, followed by the methodology and results.

9.3.1 Signal model

In order to compare different dark matter searches at the LHC, simplified models that incorporate additional dark mediators, to allow communication between the SM and dark matter, have been proposed. One approach to this is to introduce a new single s -channel vector mediator represented by Z' . However, its coupling to the SM particles has to be very small to avoid dark matter overproduction, which would not agree with experimental bounds. This issue can be addressed by introducing a new $U(1)'$ gauge group, similar to the electroweak symmetry-breaking mechanism of the Standard Model. This mechanism gives rise to masses of a new additional Higgs boson in the dark sector and the spin-1 Z' gauge boson. The resulting two-mediator DM (2MDM) model [83] would allow the dark matter particle χ to obtain mass through Yukawa coupling to this dark-Higgs boson. After the symmetry breaking in the hidden sector, the interaction part of the Lagrangian for such a model can be written as

$$\mathcal{L} = -\frac{1}{2}g_\chi Z'^\mu \bar{\chi} \gamma^5 \gamma_\mu \chi - g_\chi \frac{m_\chi}{m_{Z'}} s \bar{\chi} \chi + 2g_\chi Z'^\mu Z'_\mu (g_\chi s^2 + m_{Z'} s), \quad (9.1)$$

where s is the new dark-Higgs boson. Coupling constant g_χ is set to unity to keep consistency with other searches.

The two mediators can interact with the SM particles in various ways. One option is through direct coupling of the Z' to SM particles through its mixing with neutral gauge bosons. In addition, the dark-Higgs interacts with the SM. In this scenario, it mixes with the SM Higgs boson; thus, its coupling to SM particles is proportional to their mass. That means that, depending on the mass of the dark-Higgs, it will preferably decay into SM Higgs boson, vector bosons, or b -quarks.

Because both the mediators are originating from the broken symmetry $U(1)'$, it enables them to interact with each other, resulting in the process such as dark-Higgs strahlung $Z' \rightarrow Z' + s$, as shown in figure 9.8.

If the mass of the Z' is low, the resulting dark-Higgs boson will be relatively soft, meaning that the two dark matter particles decay back-to-back and their contribution to E_T^{miss} cancel out. However, if the mass of the Z' is high enough, it produces boosted dark-Higgs, and thus, the final state with high E_T^{miss} is more likely. In the mass range targeted by this reinterpretation $2m_h \leq m_s \leq 2m_\chi$, for the common benchmark with $m_\chi = 200$ GeV, the decay modes $s \rightarrow VV$ and $s \rightarrow hh$ are dominant.

Dedicated searches for different decay channels and mass ranges have to be employed due to the dependency of the final state on m_s . Low m_s regions are targeted by search using $s \rightarrow b\bar{b}$ [84], while fully hadronic $s \rightarrow VV$ [85] and semileptonic $s \rightarrow WW$ [86] are associated with higher m_s . This reinterpretation³ investigates for the first time $s \rightarrow hh \rightarrow b\bar{b}b\bar{b}$, targeting similar mass ranges as covered by reference [86]. This final state is a viable candidate for the reinterpretation because it has the same observable final state as the higgsino analysis, however, the topology of the event is different which brings some limitations, which are shown in the section with results when discussing CR and VR contamination by the signal.

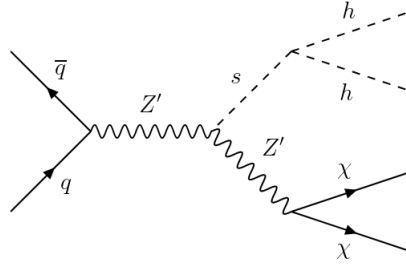


Figure 9.8: Dark-Higgs strahlung - model considered by the reinterpretation.

In the reinterpretation presented in this thesis, the signal process is simulated employing Monte-Carlo methods on the grid shown in figure 9.9a. Matrix elements are generated with up to two additional partons using MADGRAPHv2.9.9 at leading order with NNPDF 2.3 Parton Density Function (PDF) sets and the A14 tune. PYTHIAv8.307 is subsequently used to model parton showering, hadronisation, and underlying event. For compatibility with other analyses, the dark matter mass is set to $m_\chi = 200 \text{ GeV}$. Due to the quickly-changing cross section close to $m_{Z'} = 2m_h$ and $m_{Z'} = 2m_\chi$, extra points are added to the grid.

9.3.2 Results

Similarly to the reinterpretation using the model with heavy and light neutralinos, we selected the BDTs that performed best for given mass points. We followed the same procedure as before, and we ran a statistical fit and computed the CL_s values for each of the mass points using all BDTs; then, we selected the BDT that was giving the lowest CL_s value (i.e., the highest level of exclusion) for the given point. Selected BDTs for each mass point are shown in figure 9.9b.

It can be seen that only three different BDT parametrizations were used. The reason for this is that despite this model having the same final state as studied in the higgsino analysis, the topology of the event is different, which naturally leads to different kinematic distributions of variables used in the analysis. This can also be seen in the analysis regions contamination plots in figure 9.10, where the signal contamination of control and validation regions is above 10%, or 20%

³And the followup analysis, which is not part of this thesis.

respectively, for several grid points. The original higgsino analysis required the signal contamination to be under 10% in all CRs and below 20% in all VRs. While the high contamination of the CRs has a negative impact on the fit quality, the contamination of the VRs is not a problem for the result since VRs are not used in the fit.

The performance would likely improve after the BDTs re-training, but this was not done because we aimed for a pure reinterpretation. Instead, this reinterpretation was a starting point for the new analysis targeting the same model. This newly developed analysis uses a specifically trained neural network, and it also defines new analysis regions optimized for this particular signal ⁴.

The exclusion plot is shown in figure 9.11. Even though the BDTs were optimized for the signal with different topology, we could exclude a part of the two-dimensional parameter space defined by masses of Z' and dark-Higgs boson (mono-s particle). Similarly to the case with heavy and light neutralino model, the BDT retraining was not considered since retraining would not be pure reinterpretation. Instead, a completely new analysis was developed with the optimized neural network. This new analysis, however, is not part of this thesis. It should be mentioned that the excluded region is just a part of a larger signal grid (see figure 9.9a), and the area excluded by observed data has dimensions comparable with the spacing of the grid, so it is susceptible to the interpolation of contours in the plot. We tested several interpolation schemes and picked the interpolation using the RBF method with linear basis function, giving the most reasonable results. The interpolation method is described in depth in appendix A.2.

This reinterpretation is able to exclude only a small new area of the parameter space given by for $m_s > 370$ GeV, compared to analyses in references [84, 85, 86]⁵, however newly developed analysis based on dedicated neural network is expected to improve this result significantly⁶.

⁴Even though the author of this thesis was part of the analysis team, his main focus was on the reinterpretation for the new signals and so the discussion of the analysis is left out from this thesis.

⁵These analyses targeted different final states.

⁶Results of the analysis were not finalized during writing of this thesis.

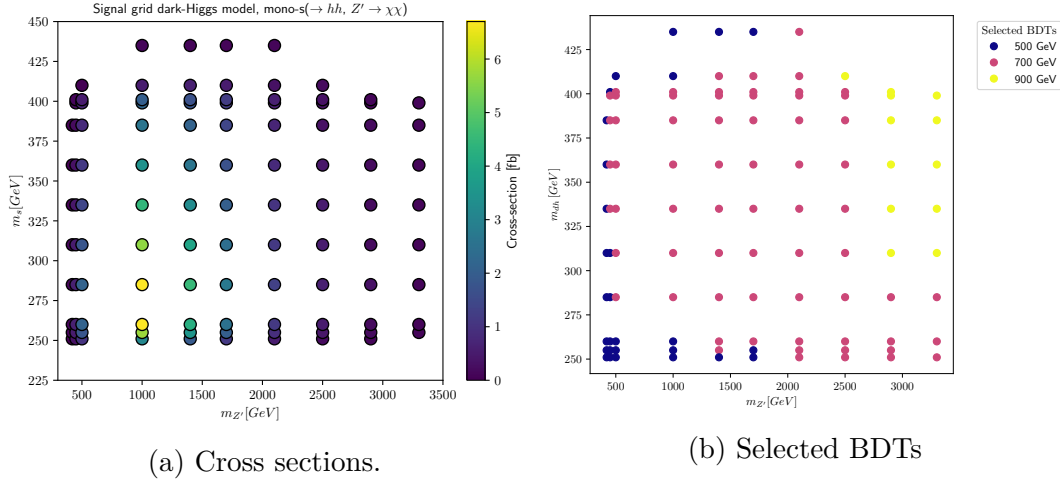


Figure 9.9: The signal grid of the mono-s (dark-Higgs) model used for the reinterpretation. Figure (a) shows the cross sections of individual signal hypotheses, and the figure (b) shows the BDTs selected for these hypotheses. BDTs are labeled by the corresponding higgsino mass hypothesis, which was used for their training.

9. Reinterpretation of the higgsino pair production analysis

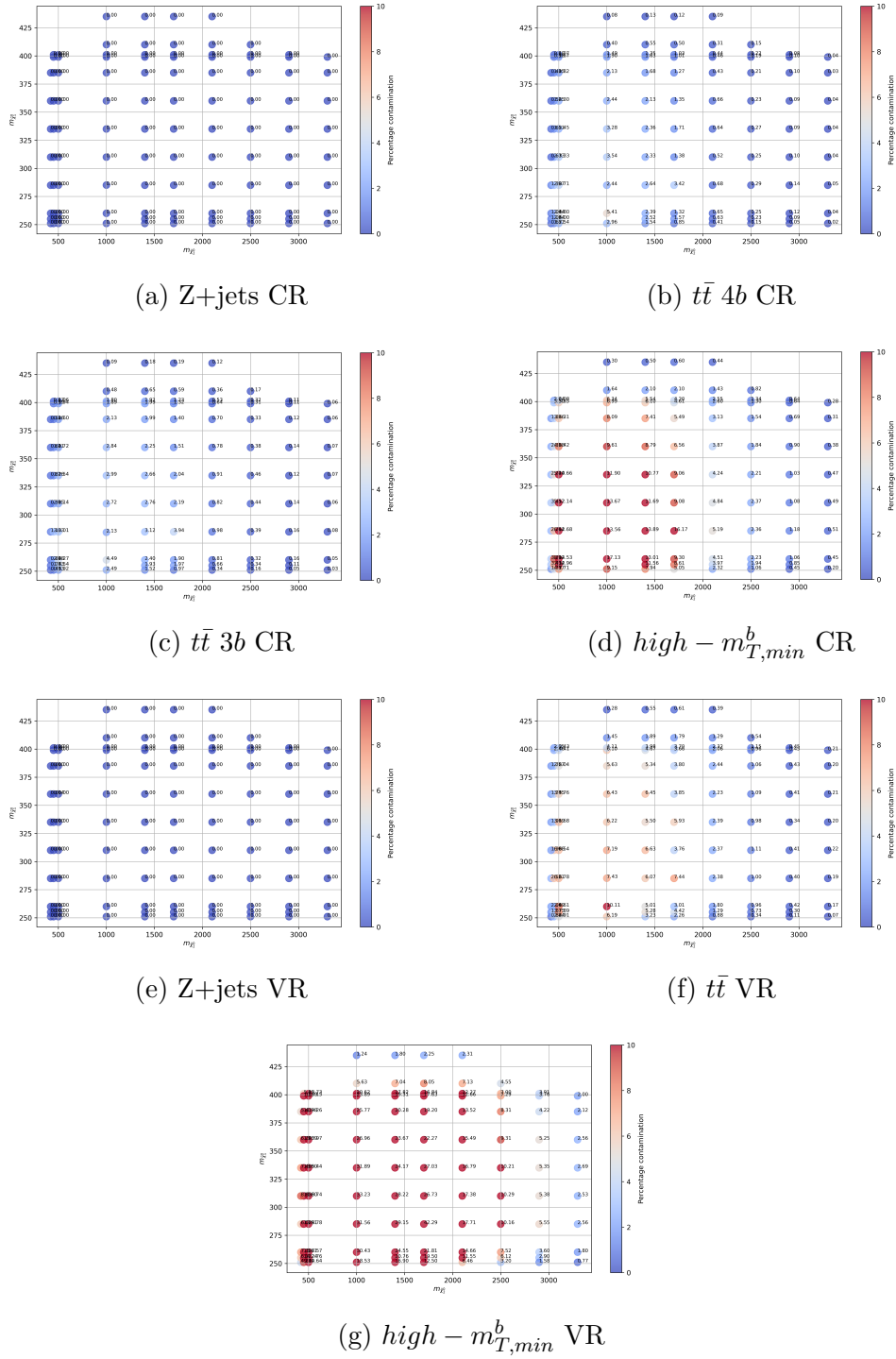


Figure 9.10: Percentage contamination across the dark-Higgs signal grid for events in all analysis regions.

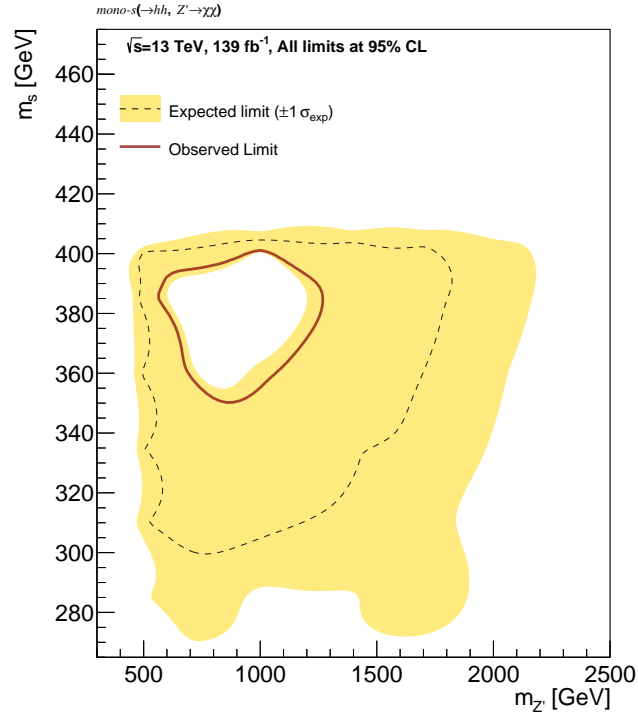


Figure 9.11: Two-dimensional exclusion plot for the dark-Higgs model where we set $m_\chi = 200$ GeV. The x-axis of the plot represents Z' mass, and the y-axis represents the mass of dark-Higgs (mono-s). The area enclosed by the red line is excluded by the data at a 95% confidence level. The area enclosed by the dashed line is excluded by simulation at 95% confidence level, and the yellow band is $\pm 1\sigma$ band.

Analysis preservation

10.1 Introduction

Reinterpretation of the analysis is a process that helps answer the question: "What is the sensitivity of an existing analysis on the alternative signal hypothesis?". Reinterpreting a given analysis using the new signal model is beneficial because it helps to evaluate a new signal model within the framework of an existing analysis without developing a new one. The advantage of this approach is that we do not need new data processing, and we can use the background estimates because the only part that changes in the analysis is the Monte-Carlo simulation of the signal model.

In order to reinterpret the analysis of a different analysis group or even an experiment, it is convenient to preserve the analysis workflow in a form that is easily usable for people who have no previous experience with a given analysis. This requires running individual analysis steps in the same order and using identical software versions as the original analysis team. This is when the concept of *analysis preservation* becomes useful. The tool used in the ATLAS experiment for the analysis preservation is called RECAST [87].

In the context of the analysis preservation, the entire analysis can be viewed as an abstract function that maps data and model hypothesis to the analysis results.

$$\text{result} = f_{\text{analysis}}(\text{data}, \text{model}) \quad (10.1)$$

In an ideal scenario, we want to preserve this mapping in a completely parametrized form independent of specific data and the model on which it has been applied to obtain the result [88]. This requires a description of the steps taken between input data and the final analysis result, as well as a description of the workflow that links these steps and describes how to get from the input data to the result.

In the same way, we described the whole analysis as an abstract function f_{analysis} , we can view each analysis step as a function $f_{\text{step},i}$ where index i indexes different steps. The steps are analysis specific. They can, for example, be the production of ntuples, post-processing of ntuples, and statistical fit. Each step takes as an input some input data σ (this can be either analysis input data or the output of a step that it depends on) and several input parameters p_i .

$$\text{step output} = f_{\text{step}}(p_1, p_2, \dots, p_n, \sigma) \quad (10.2)$$

The last essential ingredient in analysis preservation is describing how individual steps are combined. This can be done by representing the whole analysis pipeline as a directed acyclic graph, where nodes represent the analysis step, and edges describe the data flow from one step to another.

The author of the thesis helped with the preservation of the higgsino analysis presented in chapter 8. Details about RECAST and the particular implementation of the higgsino analysis workflow into RECAST are described in this chapter.

10.2 RECAST

RECAST is a software framework for analysis preservation. The key idea behind RECAST is that the possible new reinterpretation with a different signal needs to run the whole workflow in the exactly same way as the original analysis, only using a different signal Monte-Carlo samples and RECAST makes this easily possible. RECAST uses the description of the workflows in the form of declarative workflow specification *yadage* [89] and Linux containers to preserve the environment of the analysis steps.

The specification is defined as a JSON schema [90]. The language provides an extensible framework for describing arbitrary, runtime-dependent, directed acyclic graphs of individual container workloads. Individual processing stages are defined to be executed on variable inputs provided as a JSON document. [91]

Typical analysis consists of several steps, but some can be the same type of data manipulation executed on different input files or with different input parameters. Viewing steps as runtime instances of processing *stages* is helpful in this context. For example, the processing stage can be the production of ntuples, but this production needs to be executed for different Monte-Carlo campaigns. Instead of defining each step separately and repeating the code, we define the stage for the production of ntuples, and then we run it in several instances (steps) where each instance corresponds to running the ntuples production on different inputs. An example of a stage description is in the code snippet in figure 10.1, and the step description based on this stage is in figure 10.2.

Yadage workflow specification allows individual processing stages as parametrized "packed activities" that can be executed on variable inputs. Workflow directed acyclic graph is described as a set of stages that extend a directed acyclic graph

```
skim:
  process:
    process_type: interpolated-script-cmd
    interpreter: bash
    script: |
      source /release_setup.sh
      echo '{input_folder}'
      ./slim_sig_EWK4_16.sh '{input_folder}' '{year}'
      for i in `ls | grep -E '^[0-9]+$'`; do
        for j in `ls $i/slim*.root`; do
          did=`ls $j | awk -F'[_]' '{{print $4}}`
          mv $j '{output_folder}'/mc16_13TeV_skim.${{did}}.root
        done
      done
  publisher:
    publisher_type: interpolated-pub
    publish:
      output_folder: '{output_folder}'
  environment:
    environment_type: 'docker-encapsulated'
    image: gitlab-registry.cern.ch/otheiner/mbj_utils
    imagetag: recast-a769a35a
  resources:
    - kerberos: true
```

Figure 10.1: Example of description of the processing step used to preserve the electroweak multi-b Higgsino analysis. This description includes a description of the runtime environment in the form of the Docker image specification used, the bash script being run during this stage, and the path where results from this stage are stored so that the following step can be used as input.

```
- name: skim_mc16a
  dependencies: [init, prod_lowmass_mc16a]
  scheduler:
    scheduler_type: singlestep-stage
  parameters:
    input_folder: {step: prod_lowmass_mc16a, output: outputs}
    year: '2016'
    output_folder: '{workdir}'
    step: {$ref: 'steps.yml#/skim'}
```

Figure 10.2: Example of the analysis step description.

by scheduling one or more instances of "packed activities" and defining their execution dependencies, which are represented by graph edges.

Thanks to this approach, the whole analysis can be straightforwardly re-run for different signal models, even by someone who does not know the technical details of the analysis.

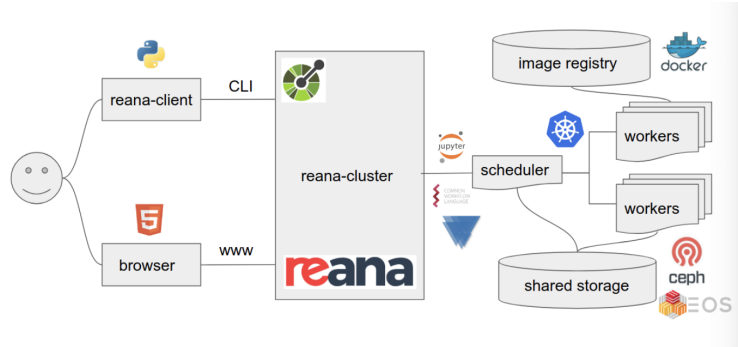


Figure 10.3: Schematic diagram of user communication with the REANA cluster and how REANA manages running workflows. Figure taken from reference [92].

10.3 REANA

Running the whole analysis can be a computationally expensive task, but thanks to the workflow description and containerized environments, it can be run on remote compute clouds. One of the cloud platforms that can be used for this purpose is REANA. REANA is a reproducible analysis platform allowing scientists to run containerized data analysis pipelines on remote compute clouds using workflow description systems such as yadage, which RECAST adopts.

The schema of how REANA works is shown in figure 10.3 and captures well the philosophy behind RECAST, which is running individual analysis steps in containerized environments. The user can communicate with the REANA cluster to schedule and maintain jobs using the web browser interface or the Python-based reana-client tool. Once the workflow is submitted to the REANA cluster, the analysis workflow is run using the specified Docker images, which are coordinated together by Kubernetes according to the workflow description provided by the user.

Workflows using RECAST can also be running locally on the user’s computer following a similar idea as described above; however, due to the computing requirements and long time of individual processing steps, using REANA is a better approach.

10.4 RECAST implementation of the Higgsino search

This section will describe a particular RECAST implementation of the electroweak Higgsino analysis discussed in more detail in section 8. This analysis has two branches which target different analysis regions and employ different cuts. Also, the analysis workflow is slightly different in both cases.

The implemented workflow was verified for two signal mass points (one from the low-mass and the other from the high-mass channel), and we compared the CL_s values from the original analysis and values obtained by RECAST. These

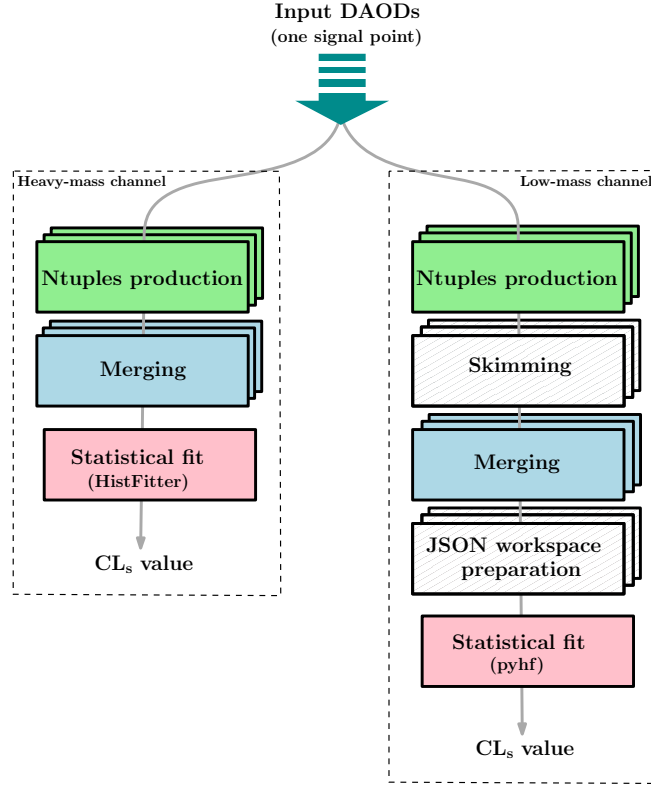


Figure 10.4: Simplified workflow of the higgsino analysis. Each box represents one step in the analysis workflow. Those steps that are stacked three times are performed separately for each MC campaign.

values were expected to be almost the same. The reason for saying "almost" is because we didn't implement signal theory uncertainties to RECAST. The reason for this is that RECAST implementation of the analysis should be general for any type of signal, and theory systematic uncertainties are signal-specific and depend on the modeling. For this reason, it is not possible to implement these into RECAST. Each signal has different sources of theory uncertainties, and that is why there is expected little discrepancy between CL_s from RECAST and from the original analysis.

The simplified analysis workflow is shown in figure 10.4. The full workflow generated automatically by RECAST is shown in appendix A.3. Subsections 10.4.1 and 10.4.2 describe the particularities of both analysis branches.

10.4.1 High-mass channel

In this section, we will describe the RECAST implementation of the high-mass channel of the analysis. It is separated into three stages - ntuples production, merging, and statistical fit - where the first two stages (ntuples production and merging) are performed once per Monte-Carlo campaign¹. These stages are executed in two different runtime environments described by two different Docker

¹Each Monte-Carlo campaign corresponds to a different year of the data-taking.

images. Ntuples production uses a dedicated Docker image, while merging and the statistical fit use different Docker images due to different software requirements.

The following pages describe individual steps in more detail.

Ntuples production

- **Input:** DAOD file with the signal process.
- **Output:** Analysis specific ntuples with variables used in the analysis.

The first task in the analysis chain is producing ntuples. It can be defined as a stage that is then executed on three different Monte-Carlo campaigns². The main input of this step are DAOD files with the signal process of interest for the reinterpretation. Like all other parameters for RECAST, the input files are provided as a path to the file. The analysis code takes the DAOD files as input and produces ntuples that can be used for the statistical fit in the final step of the analysis.

Merging

- **Input:** Ntuples for one Monte-Carlo campaign; weight files
- **Output:** Ntuples from one MC merged into one file with added weights and scale factors.

The merging is another stage performed on ntuples from each Monte-Carlo campaign. This means it will be running in three instances - it will define three steps. The task of this stage is to take ntuples from the previous step and merge them into one file in case there are more files with ntuples for the signal point. The merging is necessary for the statistical fit (another stage) since this data format is expected. The other important purpose of this step is to compute the weight factor, which scales the number of Monte-Carlo simulated events so that the event counts match the number of events corresponding to the integrated luminosity during the data-taking period. It is done in the following way.

By looking at the equation 3.9, it is clear that the signal with a lower cross section σ will be less abundant than the signal with a higher cross-section. We need to reflect this in yields, no matter how many events n_{MC} were generated by the Monte-Carlo simulation, and this is why each event has weight w_{lumi} which is computed

$$w_{lumi} = \frac{\sigma}{n_{MC}}. \quad (10.3)$$

²Different years of the data taking correspond to different Monte-Carlo simulations. In the higgsino analysis, we used three Monte-Carlo campaigns: *mc16a* for years 2015 - 2016, *mc16d* for 2017, and *mc16e* for 2018.

If w_{lumi} is then multiplied by the integrated luminosity L^{int} in the data taking period, we get weight $w_{lumi-real}$. It scales the number of Monte-Carlo-generated events to the number we expect to see in ATLAS.

$$w_{lumi-real} = L^{int} w_{lumi} \quad (10.4)$$

It is clear that this weight is the same for all events corresponding to a particular signal process generated in one Monte-Carlo campaign. That is why the information about the cross section and number of generated events can be stored in a weight file, which is a JSON file provided as an input to the step.

Also, the E_T^{miss} trigger scale factors are added, which account for the turn-on effects of E_T^{miss} triggers used in the analysis.

Input for this step is ntuples produced in the previous step and JSON format weight files for the luminosity reweighting. These new reweighted and merged ntuples can be used in the statistical fit.

Statistical fit

- **Input:** Merged ntuples with all weights
- **Output:** CLs values.

The last step is running the statistical fit as described in chapter 7. It uses the HistFitter [93] software, the framework for statistical data analysis. This step aims to find the CL_s value for the given signal hypothesis.

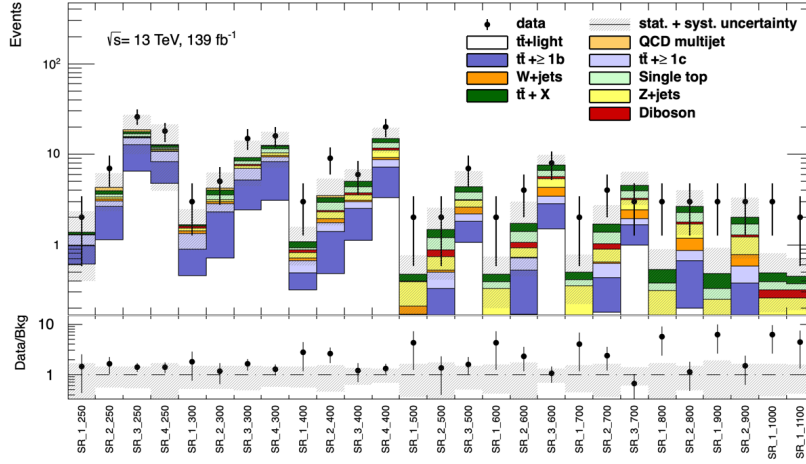
The vital ingredient of this step is the definition of the analysis regions where the fit should be done, but also the file called *cache* containing all the information about the background in the analysis regions. It is hidden from the user because it should not be changed and is the core of the whole reinterpretation process. The advantage of having the cached values of background pre-fit yields and corresponding systematic uncertainties is that the background yields do not need to be estimated during the run time, and the fit is running faster.

The content of the cache used for the high-mass analysis is shown in figures 10.5a and 10.5b.

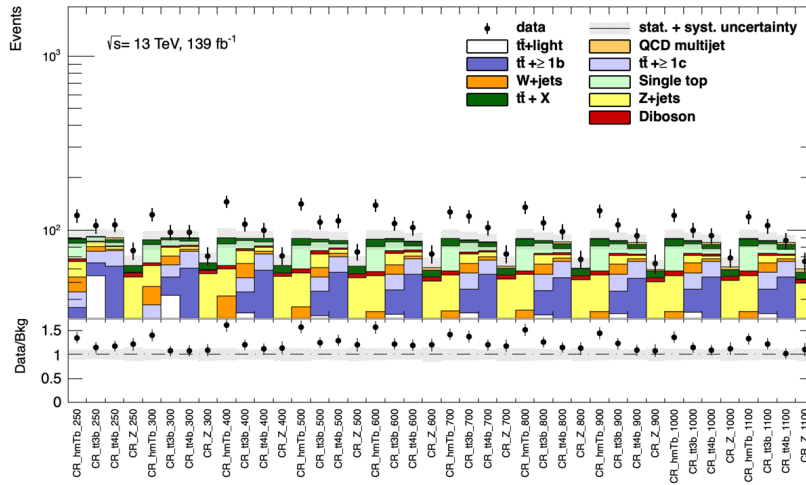
10.4.2 Low-mass channel

The low-mass channel can be split into five stages - ntuples production, skimming, merging, preparation of the JSON workspaces, and the statistical fit - where the first three stages are performed for each Monte-Carlo campaign. Ntuples production and merging use the same runtime environments as their equivalents in the high-mass channel. The skimming step, preparation of workspaces, and the statistical fit are each performed using their dedicated Docker images.

A description of individual steps in the low-mass channel follows.



(a) Signal regions.



(b) Control regions.

Figure 10.5: Content of the cache file used in the RECAST implementation of the Higgsino search.

Ntuples production

- **Input:** DAOD file with the signal process.
- **Output:** Analysis specific ntuples with variables used in the analysis.

Ntuples are produced by the same analysis code used for the high-mass channel, with the only difference being that it does not run the BDT evaluation and runs different pre-selections specific for the low-mass channel.

Skimming

- **Input:** Ntuples.
- **Output:** Skimmed ntuples.

Ntuples are produced by the same code for the analysis's low-mass and high-mass channels, and more additional low-mass-channel-specific selections can be applied to further reduce the size of ntuples. This reduction is done in the skimming step, which saves only necessary variables and discards events not passing selection criteria.

Merging

- **Input:** Skimmed ntuples for one Monte-Carlo campaign; weight files
- **Output:** Ntuples from one MC merged into one file with added weights and scale factors.

This step is identical to the merging step in the high-mass channel of the analysis.

Preparation of JSON workspaces

- **Input:** Merged ntuples with all weights.
- **Output:** Workspaces in form of JSON file.

This is just an intermediate step specific to the low-mass channel, which uses different software to perform the statistical fit than the high-mass channel. However, the primary purpose of this step is to take the information contained in the ROOT files from individual merging steps and write them into a single JSON file that is used as a data input for the statistical fit.

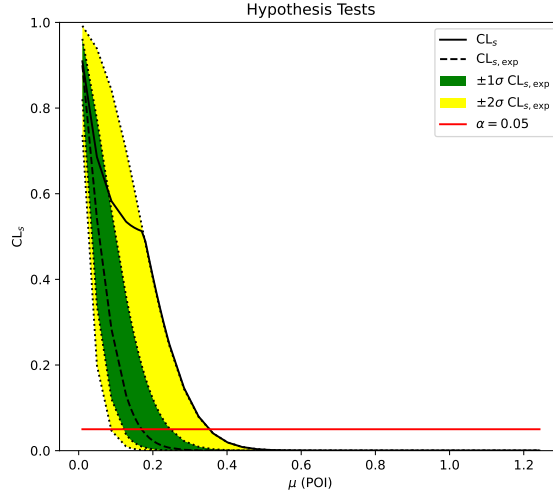


Figure 10.6: Result of hypothesis testing - CL_s values as a function of signal strength μ for the higgsino mass of 200 GeV.

Statistical fit

- **Input:** JSON files from the previous step with all information needed to build a statistical model.
- **Output:** CLs values.

The statistical fit is performed using the pyhf software [94, 95], which is a Python implementation of the HistFactory³ model specifications [96], similar in functionality to HistFitter. Contrary to the high-mass channel, which uses a cache ROOT file with information about background contributions to individual analysis regions, this channel has all the information about background yields in the analysis regions stored inside the plain JSON file. The user does not change this file because it encodes all necessary information for the potential reinterpretation.

The output of this step is the CL_s values for the signal model. Figure 10.6 shows the result of the hypothesis testing where a range of values of μ is scanned and the corresponding CL_s values estimated. This plot is also available in the output.

10.4.3 Drawbacks for the dark-Higgs, and heavy and light neutralino models

RECAST implementation of the higgsino analysis was not used for the reinterpretations described in chapter 9. There were two reasons for that.

³The HistFactory is a tool to build parametrized probability density functions based on the simple ROOT histograms organized in XML files.

The first reason was the long runtime of the ntuples production. In particular, BDT evaluation took an extremely long time with high memory requirements, which made the ntuples production stage run about three days per MC campaign and signal point without evaluation of systematic uncertainties. When the production of full ntuples was used, it took about 10 to 30 days⁴ on the grid. However, the REANA cluster had a two-day time limit for the authentication token that is necessary for access to the input data that are stored on CERN servers and that are used in later stages of the workflow. This meant that the process could not be finished after more than two days. We discussed this issue with REANA cluster administrators, and even with an extended access token lifetime, it was not possible to finish some of the signal points for reinterpretation in time.

The second reason was that one execution of RECAST produced one CL_s value for the BDT evaluation that is specified by the user as one of the input parameters. However, in the process employed by the reinterpretations discussed in chapter 9, we were selecting the fit with the lowest CL_s value, which would mean running ntuples production stage unnecessarily many times or significant modification of the RECAST workflow for the purpose of our reinterpretation would be necessary.

Due to these reasons, we decided not to use RECAST and run individual analysis steps "manually", which allowed us, to run the production and data preparation steps only once and after that run only the statistical fit for each signal mass hypothesis individually.

⁴We later discovered that there was a memory leak in the original analysis code, which was not identified and made the production process CPU extensive.

Conclusion and outlook

The ATLAS experiment has been taking physics data for more than a decade, providing new physics results and helping to push the boundaries of particle physics. Continuous detector development and optimization of the triggering and reconstruction techniques allow moving the boundaries even further. An example of the detector development can be the installation of the New Small Wheel before the start of Run 3 as a part of the ATLAS Upgrade, and the example of trigger optimization can be the use of the Particle Flow reconstruction that was adjusted for the purpose of the at the HLT reconstruction. One of these adjustments was the optimization of track extrapolation for the Particle Flow jet reconstruction, which is presented in this thesis.

The Higgs boson discovery in 2012 was a big success, and it marked an important milestone for particle physics, but also physics in general. Not only did it demonstrate the predictive power of the Standard Model, but this discovery also opened a new observation window to the world of physics beyond the Standard Model. Final states with a Higgs boson and $E_{\text{T}}^{\text{miss}}$ are interesting probes for the BSM physics, such as SUSY, because they could not be used in experiments preceding the Higgs boson discovery. This chapter presented one of these searches, looking for the higgsino pair production and its two reinterpretations with dark-Higgs and heavy and light neutralino models. The work presented in this thesis helped to set the limits on these models - namely, the reinterpretation part, the results of which were not published before.

The exclusion for models used in the reinterpretation can be potentially improved by developing new analyses that are optimized for these models. This is the case of the reinterpretation using the dark-Higgs model, where the dedicated analysis, based on the specifically optimized neural network, was developed.

The reach of physics analyses will improve not only by optimizing analysis strategies but also with more recorded data, which will allow us to look for more rare events. In Run 2, 139 fb^{-1} of integrated luminosity was recorded, and the goal of the Run 3 is to record 300 fb^{-1} , which is more than double the Run 2

dataset. The delivered integrated luminosity will also increase significantly with the transition to the High-luminosity LHC, which will increase the integrated luminosity by a factor of 10.

The upgrade brings up many challenges for the future of the experiment but, most importantly, it will allow to record a lot of new valuable data that can be used in the hunt for physics beyond the Standard Model.

PART II

FASER

This part of the thesis is describing the FASER experiment and its commissioning. Chapter 12 discusses the physics motivation and prospects of the FASER experiment as well as the detector location and its design. The TDAQ system is described more in depth in chapter 13 and commissioning of the experiment is discussed in chapter 14. Chapter 15 then concludes this part of the thesis and shortly presents the first experimental results and future prospects of the experiment.

The author's main contributions to the experiment are described in chapters 13 and 14. He worked on the implementation of some of the TDAQ functionalities, such as data readout error-detecting mechanisms, drivers used to interface communication between hardware GPIO boards and the rest of the TDAQ system, and the testing of Ethernet communication. He also actively participated in the commissioning of the tracking detector, where he performed electronic testing and calibration procedures described in the chapter dedicated to the silicon tracker commissioning.

FASER Detector

12.1 Introduction

The first part of the thesis describes the ATLAS experiment and searches for new physics using that detector. These searches exploit the large center-of-mass energy of the collisions and are often looking for relatively heavy particles in the high- p_T regions, like the searches discussed above where the masses of examined particles were on the order of hundreds of GeV. Nevertheless, this approach can be completely misguided if new particles are light, long-lived, and weakly-coupled. Light particles are typically highly concentrated within a few mrad of the beamline [97], which makes the current big detectors, such as ATLAS or CMS, not well suited for searching for these particles. Experiments ATLAS and CMS can be illustrated as big cylinders with holes along the beamline to let the proton beams in. However, that introduces "blind spots" for potential new physics. This is why searching with a small experiment placed far from the interaction point on the beam axis can be beneficial. This is the case of FASER, a small experiment located 480 m from the ATLAS collision point.

This chapter describes the motivation for building the FASER experiment and also presents the individual detector subsystems. This chapter is purely bibliographical and its aim is to introduce the experiment to the reader, such that the author's contributions to the experiment can be explained more in detail in the following two chapters.

12.2 Physics motivation

The FASER experiment was designed to search for light weakly interacting particles that are potentially created inside collisions in ATLAS and travel hundreds of meters through the rock between the ATLAS IP and FASER locations. This location makes it perfect for searching even for extremely weakly-coupled new

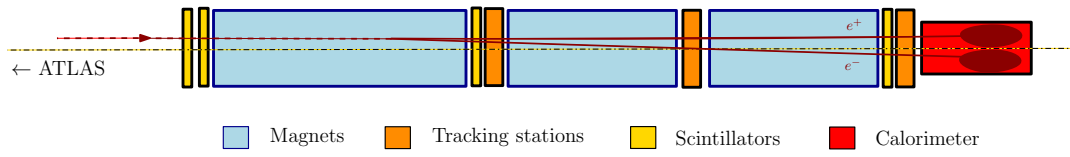


Figure 12.1: A typical signature the FASER experiment is looking for. The "invisible" neutral weakly interacting particle (for example, dark photon – depicted by the brown dashed line with the arrow) comes from the ATLAS and decays inside the decay volume, which is inside the first magnet. This particle then decays into a pair of oppositely charged particles (for example, e^+e^-) that leave hits in three tracking stations and create energy deposits inside the calorimeter. This drawing is simplified and doesn't contain FASER ν . A more detailed description of the whole experiment follows in chapter 12.

particles that are created during pp collisions because of a very low background that, in the case of the FASER experiment, is mostly formed by muons. In addition, a smaller emulsion-based neutrino detector was proposed and added to the main FASER detector.

The experiment doesn't aim to search for one particular type of particle but the whole class of particles that are neutral, weakly interacting, and able to get from ATLAS IP to FASER. These are dark vectors¹, dark scalars², heavy neutral leptons, axion-like particles (ALPs) and dark pseudoscalars [11]. The typical signal that FASER is looking for is a pair of light SM particles (e^+e^- , $\mu^+\mu^-$, $\gamma\gamma$) originating from one vertex that is located inside the detector's decay volume. This is depicted in figure 12.1.

Let us illustrate the typical chain of processes in the case of a dark photon A' .

$$pp \rightarrow A'X \quad , \quad A' \text{ travels } 480 \text{ m} \quad , \quad A' \rightarrow e^+e^-, \mu^+\mu^- \quad (12.1)$$

This process then leads to the signal of two highly energetic, charged tracks created hundreds of meters downstream in the very forward region at ATLAS.

FASER was proposed at the end of the LHC Run 2 and it was built and commissioned during Long Shutdown 2 between the years 2019 and early 2022. This quick progress from initial plans to the realization of the experiment was possible thanks to reusing some technology from the ATLAS and LHCb experiments, but also thanks to the well-working team of people participating on the experiment.

12.3 Experiment location

In the beginning, the initial studies by the CERN survey team were done, and two possible locations were picked. These locations were located inside tunnels

¹dark photons, $B - L$ gauge bosons, $L_i - L_j$ gauge bosons

²dark Higgs bosons

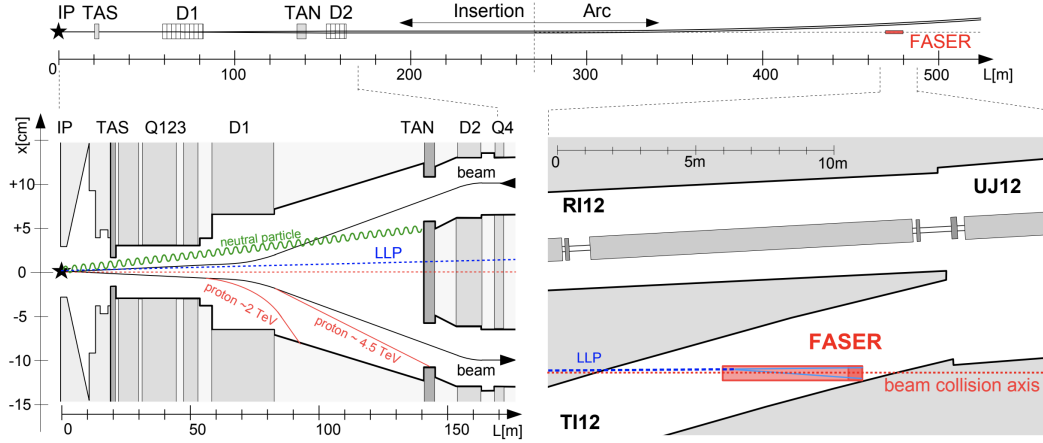


Figure 12.2: Schematic illustration of the FASER experiment inside the LHC tunnel with respect to the position of ATLAS IP. [98]

TI18 and TI12, both of which were located on the beam collision axis or line of sight³. The two tunnels are in symmetric locations with respect to the ATLAS interaction point, both being 480 m from the collision center. In the end, TI12 was chosen for FASER, and the other location in tunnel TI18 is occupied by SND@LHC experiment. The TI12 tunnel is a tunnel formerly used to connect the Super Proton Synchrotron (SPS) to the Large Electron-Positron collider (LEP) and, at the moment of FASER installation, was empty and unused. The schematic location of FASER with respect to the ATLAS interaction point is shown in figure 12.2. The actual placement of the experiment inside the tunnel TI12 is shown in pictures 12.3 and 12.4, which were taken during the FASER installation.

As can be seen from photo 12.4, the floor of the tunnel has a slope and civil engineering works had to be done to excavate the trench where the experiment could be placed to align with the collision axis.

The advantage of the experiment location is that there is rock between the ATLAS IP and FASER, reducing the background to the minimum. The main sources of background are muons and neutrinos produced during collisions in ATLAS. The detector itself is approximately 100 m under the ground, which also reduces the cosmic ray background. Moreover, most of the cosmic ray background is reduced by a well-designed trigger system, which is going to be discussed later. The rate of events seen by FASER is about 1 kHz, which is roughly four orders of magnitude lower than the collision rate inside ATLAS.

³Supposing the zero crossing angle of beams at the interaction point, it is tangent to the proton beam at the collision point. In reality, the crossing angle has a very small value of about $150 \mu\text{rad}$ and causes a shift of a few centimeters at a distance of 480 m where the FASER is located.



Figure 12.3: Location of the FASER experiment. The experiment is installed inside the side tunnel TI12, formerly used to connect the SPS to the LEP. This tunnel is located on the left side of the picture, right next to the LHC. Later, an additional block of shielding for proton scattered from the LHC beam was added parallel to the LHC right next to the entrance to the TI12. The photograph was taken during the FASER installation in February 2021.

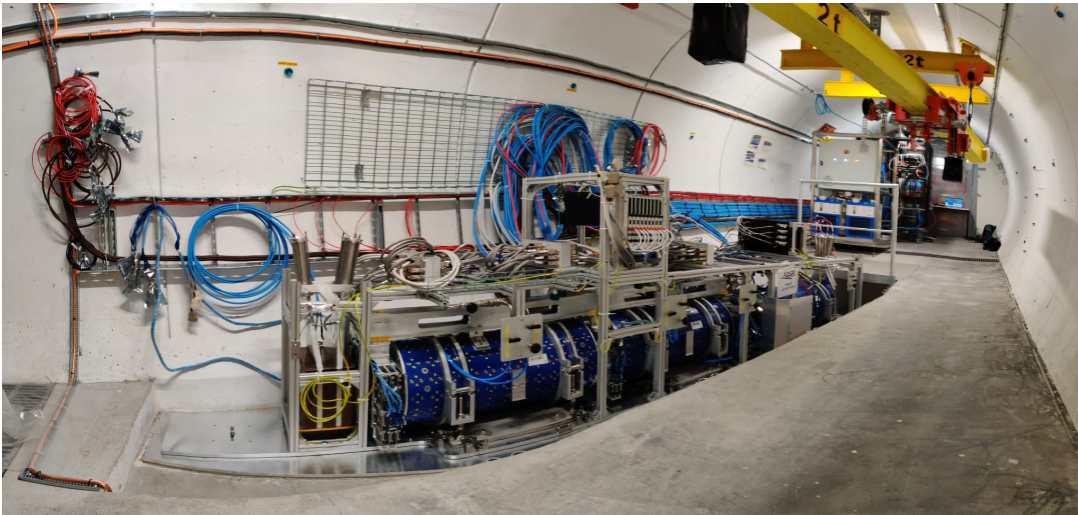


Figure 12.4: Detail of nearly fully installed detector. The calorimeter modules were installed later, as well as FASER ν , which was put into the tunnel shortly before the experiment started to take data. The photograph was taken during the FASER installation in February 2021.

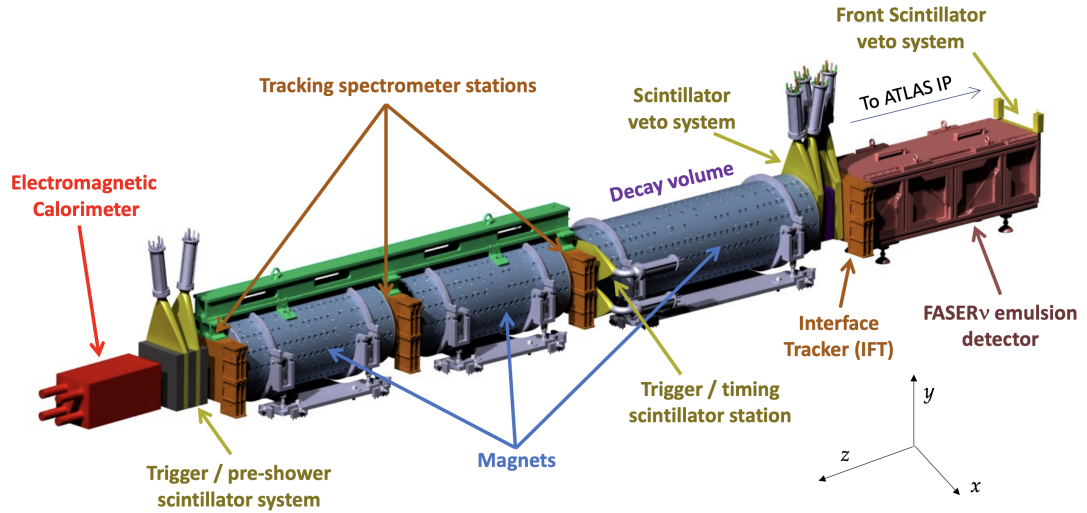


Figure 12.5: A model of the FASER detector, showing the different sub-systems. The figure also shows the orientation of the FASER coordinate system. [98]

12.4 Magnets

FASER is using three permanent dipole magnets to create the magnetic field that can split tracks of oppositely charged particles. The advantage of using permanent magnets is that the experiment doesn't need any cooling of magnets, plus it doesn't need the electric supply to power magnets, which makes operation of the detector easier.

The longest, 1.5 m long, magnet surrounds the decay volume, and is followed by two 1 m long dipoles installed along the tracking spectrometer. All three magnets have a cylindrical shape with a circular hole along their axis of symmetry. The hollow part of a magnet has aperture of 200 mm and is aligned with the beam collision axis. The magnets provide a strong homogeneous field of 0.57 T inside the aperture.

The design of the magnets is based on a Halbach array, which is the particular arrangement of 16 trapezoidal shaped blocks of ferromagnetic material that produces magnetic field confined entirely inside the cylinder and zero field outside.

The magnets can be seen in the model in figure 12.5 and in the photo from the tunnel in figure 12.4. What is actually visible is not a magnet itself but the magnet support and alignment structure (blue cylinders in figure 12.4) that allows precise positioning of each magnet individually.

12.5 Scintillator system

The FASER experiment has four scintillator stations formed by multiple scintillator counter layers in each station. Two of these stations are used as veto

stations, and two are used for triggering. All scintillator stations can be seen in figure 12.5 marked by a yellow color.

The first veto station is located upstream of the FASER ν emulsion detector to veto incoming muons and so provide discrimination between muon-induced background and neutrino interactions.

The second veto station is located between FASER ν and the decay volume magnet. It consists of two pairs of modules placed back-to-back for redundancy and to improve the veto efficiency. The primary purpose of the second veto station is to suppress events with incoming SM particles, which are mostly high-energy muons. A 10 cm-thick lead block is placed between the two pairs of scintillator modules to avoid photons arising from muon bremsstrahlung in front of the detector entering undetected. This block will either generate a shower that is detectable by the second pair of modules or stop these photons completely. This veto station suppresses the background-related muons significantly by requiring the detection of more than 99.99% of incoming muons. This is achieved by a large scintillator signal and efficient light collection.

The third scintillator station is located downstream of the decay volume, in front of the first tracking station. The aim of this station is to provide the trigger and timing information for FASER. It detects the appearance of the charged particle pair from the decay of the long-lived particle in the decay volume, and so it provides the primary trigger signal for the experiment. The non-collision background is suppressed thanks to this station because it uses the precisely measured arrival time of the signal with respect to the pp collisions. This is achieved by a timing resolution of better than 1 ns.

The fourth scintillator station is located after the last magnet and tracker station and in front of the calorimeter system. It has two purposes. The first is to be used as an additional trigger station, which can be used in coincidence with the first trigger station. The second purpose of this station is that it is used as the active sensor in the preshower detector. The two scintillator modules used in this station are identical to the ones used in the second veto station and are preceded by a 3 mm-thick layer of tungsten to create a simple preshower detector. This helps to distinguish a physics signal of two close-by energetic photons, which would otherwise leave one large energy deposit in the calorimeter.

The photo of a single scintillator module is shown in figure 12.6.

12.6 Tracker

The FASER tracking system consists of two main parts - the tracking spectrometer and the interface tracker. The tracking spectrometer is composed of, in total, three tracking stations - two between dipole magnets and one being between the last magnet and the preshower detector and its purpose is to detect two oppositely charged particles coming from the decay of a light, long-lived, hypothetical new particle inside the FASER decay volume.



Figure 12.6: Photo of one of 30 cm \times 30 cm scintillator modules including the light guide.

Each tracking station of the spectrometer is composed of three planes, making in total, nine planes of silicon strip modules that were originally spare for the ATLAS SCT barrel detector. Other parts of the tracker, including mechanical support structures, were developed specifically for FASER.

The interface tracker has an identical design to the single tracking station of the tracking spectrometer, and it enables matching tracks from neutrinos to events in the spectrometer tracking stations. The interface tracker and tracking spectrometer fully cover the aperture of the magnets in the transverse plane.

Modules inside the tracking planes are manufactured from the silicon n -type substrate of $285\,\mu\text{m}$, with p^+ implants. Each module is two-sided and consists of 768 readout strips per side with a constant pitch of $80\,\mu\text{m}$ and the resolution is $\approx 17\,\mu\text{m}$ in the precision coordinate and $\approx 580\,\mu\text{m}$ in the coordinate parallel to the strips, which is thanks to the stereo angle of 40mrad between the sides. [99] This is enough to separate the e^+e^- (or $\mu^+\mu^-$) pair created by the decaying LLP. If we assume a model LLP of mass $100\,\text{MeV}$ and total energy of $2\,\text{TeV}$, the total separation between the two electrons in the first spectrometer tracking station would be about $200\,\mu\text{m}$. This value obviously depends on where exactly in the decay volume particle decays.

Modules are then organized into tracker planes where each plane is formed by 8 modules supported by aluminum frames. Each frame has an inner cooling channel for the water cooling which extracts the heat generated by the readout of modules.

12.7 Calorimeter

The calorimeter is, together with scintillator plates, the second input to the trigger system. It is using four spare LHCb outer ECAL modules that were lent to the FASER by the LHCb collaboration. The modules are of Shashlik-type with interleaved scintillator and lead plates and 64 wavelength shifting fibers going through the whole module and guiding scintillation light to a single photomultiplier tube (PMT) situated at the back of the calorimeter's modules. The modules, including ten-dynode PMT, are $754\,\text{mm}$ long and have transverse

dimensions of $121.2\text{ mm} \times 121.2\text{ mm}$. Each module has a total depth of 25 radiation lengths and is composed of 66 layers of 2 mm lead and 4 mm plastic scintillator and $120\text{ }\mu\text{m}$ -thick Tyvek reflective paper.

The FASER calorimeter consists of four modules positioned in a 2×2 configuration. In order to avoid insensitive regions along gaps between modules and the scintillating fibers, the modules are tilted horizontally and vertically by 50 mrad with respect to the line of sight.

The energy resolution of the FASER calorimeter is given by

$$\frac{\sigma_E}{E} = \frac{9.2\%}{\sqrt{E}} \oplus 0.2\% \quad (12.2)$$

where the first term on the right-hand side of the equation is the stochastic term of the calorimeter resolution attributed to the stochastic fluctuations of the electromagnetic shower, \oplus is a quadratic sum, and the last term is a constant term. The noise term $\propto \frac{1}{E}$ is not included because the electronic noise partially depends on the energy range the system is operated over. The resolution of the calorimeter degrades at energies above 1 TeV due to leakage out of the back of the calorimeter. It is expected that at 1 TeV, about 1.6% of electrons are not fully contained in the calorimeter and leak about 3% of their energy.

Unlike ATLAS and CMS, where the calibration of the energy deposits can be done from known processes, e.g. $Z \rightarrow e^+e^-$, the FASER experiment doesn't have this possibility. The only charged particles crossing the experiment at high rates are muons, which are minimum ionizing particles. The signal from muons, however, is very low, so the PMTs wouldn't be able to detect their signal at the operational voltage. The only way to calibrate the energy using muons is to run with higher gains and then extrapolate down to the nominal operating range. The accuracy of this extrapolation is guaranteed by injecting a known amount of light into the module while lowering the PMT bias voltage in discrete steps. That is why there is a dedicated LED-based calibration system.

Before the installation, all PMTs, scintillator counters, calorimeter modules, and the calibration system underwent a series of tests to ensure they were functional. These tests included tests using light, gamma radiation sources, cosmic rays, and also the test beam, which is described more in section 14.2.

12.8 FASER ν

FASER ν is a detector placed in front of the main FASER detector on the beam collision axis. It is the emulsion-based detector that aims to study neutrino created during pp collisions. It includes a veto station, interface tracker, and the emulsion detector itself.

It consists of a repeated structure of emulsion films interleaved with 1 mm thick tungsten plates. The whole emulsion detector consists of 770 emulsion films with dimensions $25\text{ cm} \times 30\text{ cm}$ and a total tungsten mass of 1.1 tons. The tungsten length is 770 mm, which corresponds to 220 radiation lengths, and 7.8 hadronic interaction lengths. The detector has the ability to identify different

lepton flavors, it can identify muons, it is able to distinguish between electrons and gamma rays, and it can separate between tau and charm decays. Thanks to the fine sampled detector layers, it can measure momenta of muons and hadrons, the energy of electromagnetic showers, and estimate the energy of neutrinos.

The whole detector is fully replaced approximately every three months during technical stops of the LHC, and emulsion plates are developed. These are then sent to Japan for the readout by the Hyper Track Selector system, which is a very precise scanner with a system of lenses that converts information from photographic emulsion into a digital image that can be used for the reconstruction. The emulsion detector readout works for a density up to $\approx 10^6$ tracks/cm², which roughly corresponds to the track density of $0.3 - 1.5 \cdot 10^6$ tracks/cm² that is reached by the end of the three-months period. FASER ν is going to be replaced in total 12 times during LHC Run 3 (three replacements in each of 2022, 2023, 2024, 2025). The new emulsion-tungsten detector will be assembled in the darkroom at CERN just before each installation and transported underground to the experimental site. The placement and the pickup of the heavy detector at the tunnel will be done thanks to the crane that can be seen in figure 12.4 (yellow beam in the upper right corner of the picture).

The emulsion sensitive layers consists of silver bromide crystals dispersed in a gelatine substrate. When a charged particle passes through the crystal, electrons are excited through the electromagnetic interaction to the conduction band, trapped in the lattice defects, and silver atoms group around these locations forming, so-called, latent images. The size of crystal used allows a spatial resolution of 50 nm.

Tungsten, which interleaves the emulsion plates, was chosen for several reasons. Firstly, it has high density, allowing a higher neutrino interaction rate. Second, it has a short radiation length suitable for high-performance electromagnetic shower reconstruction and momentum measurement using multiple Coulomb scattering. And also because of the low levels of radioactivity that can guarantee safe use of the emulsion films.

FASER ν is the first detector to ever observe collider neutrinos, which are of different energy spectrum, compared to neutrinos observed in other neutrino experiments. During the LHC Run 3 data-taking period, assuming the integrated luminosity of 150 fb^{-1} , the FASER ν is expected to observe about 1300 electron neutrinos, $20 \cdot 10^3$ muon neutrinos, and 20 tau neutrinos [100].

Trigger and data acquisition system

13.1 Introduction

The previous chapter described the design of the experiment and its subsystems. However, the trigger and data acquisition system (TDAQ) was omitted. The TDAQ system is crucial for the experiment to record only potentially interesting events. Unlike the TDAQ system of ATLAS, an experiment that has to be able to process events coming in at a rate of about ~ 40 MHz, the TDAQ system of FASER is processing events at the rate of about 1 kHz. Even though FASER has the information about the bunch crossing ID where the particle detected by the experiment originated from, it is not triggering at the moment of the collision, but it is triggering only when it receives the required coincidence of signals from scintillators and the calorimeter. This approach, together with the location of the experiment far from the collision point, reduces the background, which is formed mainly by muons. The design of the system has to be robust and reliable because the location of the experiment does not easily allow maintenance of the experiment inside the tunnel when the LHC is running.

This chapter describes the TDAQ system of the FASER experiment. It starts with a general description of the design, followed by a description of the data acquisition software, which allows communication with the detector readout hardware. This hardware is based on the *General Purpose Input-Output boards* (GPIO). One type of the GPIO board is the *Tracker Readout Board* (TRB), responsible for the readout of the tracker, and the other type is the *Trigger Logic Board* (TLB), responsible for the detector triggering logic.

The author of the thesis contributed to the development of the drivers for these boards and helped incorporate these drivers into the data acquisition software. He implemented the control checksum mechanisms, allowing the identification of data corrupted due to transmission issues, which is described in section 13.5. He also developed software used for the standalone tests of the GPIO boards using the ethernet communication interface used in the experi-

ment. This is described in section 13.6.

13.2 Design

The trigger and data acquisition system of the experiment was designed to be able to handle expected readout rates of about ~ 1 kHz. The core part of the TDAQ system, which makes trigger decisions, is located in TI12 at the experiment's location to minimize time delays in signal transfer, whereas the rest of the system is located on the surface and communicates with the underground part of the system via ethernet and high-speed fiber connections.

In the heart of the whole TDAQ system, there is the *Trigger Logic Board* (TLB), which is a hardware board based on the GPIO board. It is responsible for all trigger decisions and so it has to take input from other parts of the TDAQ system. One type of input is the signal from the digitizer that digitizes the analog signal from 4 calorimeter modules and 12 scintillators, based on which the trigger decision is made. Another input to the TLB is from the clock board, which provides the precise timing information coming from the LHC clock. The last input to the TLB comes from the *Tracker Readout Boards* (TRB), the second type of board based on the same GPIO board as the TLB. The purpose of the TRB is to readout the tracking detector. There is one TRB per tracking layer (3 per station), making it a total of 12 TRBs connected to one central TLB.

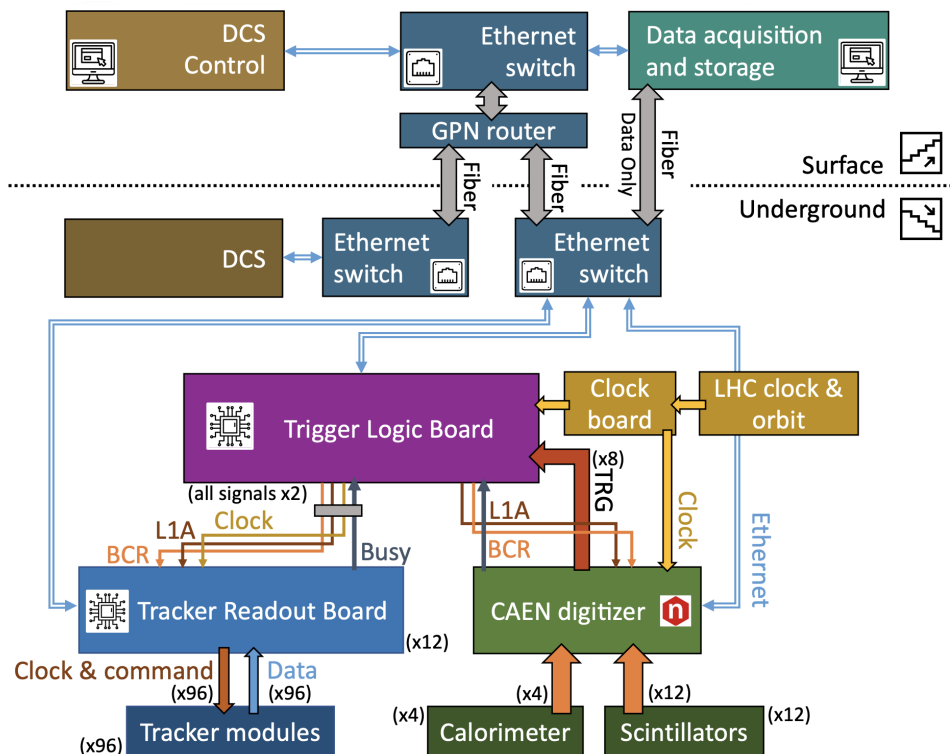
As mentioned above, the trigger information comes from the digitizer using eight trigger lines, which combine signals from the calorimeter and scintillator stations. These eight trigger lines (8 bits) are combined into four physics trigger items (4 bits) based on a lookup table (LUT) with predefined coincidence logic loaded at the configuration time. Two additional trigger bits are defined - an internally generated pseudo-random or fixed rate trigger and another for the LED calibration signal, which can also be activated by a software command. In addition, each trigger item can be prescaled. The final trigger decision, called *L1A* (level-1 accept), is computed as a logical OR between all trigger items and sent further to all readout components unless it is vetoed. [101]

After the readout, all data fragments are sent through the gigabit Ethernet to the event building process running on the dedicated server on the surface. A time stamp and run number is added and the event is recorded to disk.

The whole TDAQ system is based on the open-source lightweight C++ software framework called DAQling [102] developed at CERN.

The control and monitoring of the experiment is done via the *detector control system* (DCS), which can control devices such as high and low-voltage power supplies. For the purpose of monitoring environmental parameters, there is a dedicated electronics board that monitors the parameters of the tracker and, as a hardware-level interlock, ensures the safety of the tracker.

The schematic diagram of the FASER trigger and data acquisition system is shown in figure 13.1.



The DAQ system processes information from the three different types of detectors, which are SCT modules, scintillators, and calorimeter modules, and these are read out by TRBs, digitizers, and the TLB, which sends the L1A signal. Each of these hardware boards has its own readout receiver application running inside the FASER DAQ. These receiver applications are board-specific because they also ensure the communication between the data acquisition system and hardware. They take the raw data payload and add a fragment header that contains important information about the event, such as event ID, bunch-crossing ID, or size of the payload. These data fragments from each receiver application are sent to the event builder, which is the process that takes data fragments, puts together those that have the same event ID, and merges them into a single event with an additional event header. The event builder also performs the basic checks to ensure that data are not corrupted. The basic schema of the event-building process is shown in figure 13.2.

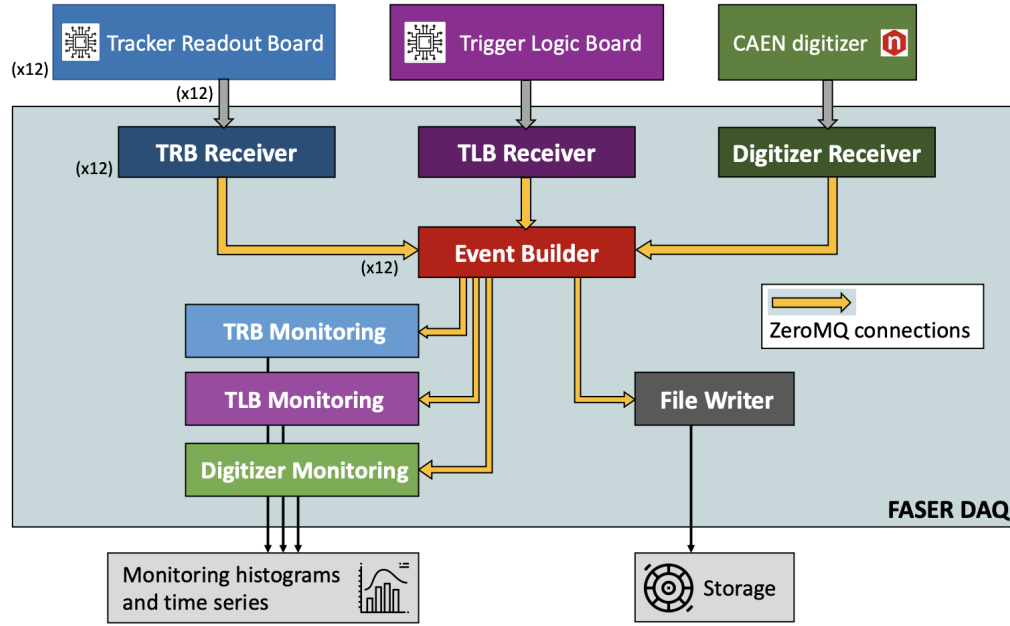


Figure 13.2: Diagram of the FASER DAQ software processes. [101]

13.4 GPIO boards

The important parts of the FASER TDAQ system are the TLB and TRBs, which are responsible for the trigger decision logic of the experiment and the readout of the silicon tracker modules forming the tracker detector. As mentioned above, both the TLB and the TRB are boards based on the General Purpose Input-Output Board developed at the University of Geneva. The core of the board is based on the Intel Cyclone V A7 FPGA, which serves as a main processing unit. The board is able to communicate using the USB3 communication interface, which was used in the early stages of TDAQ system testing and commissioning, and the Ethernet communication interface, which is currently used in the experiment. The board can be interfaced with other hardware using the additional adapter board and mezzanine.

The board communicates with surrounding hardware by sending and receiving chunks of 32-bits, called *words*. The structure of these words is strictly specified by the design of the board and is going to be described more in detail in subsection 13.4.1. We can distinguish between the two modes in which the board can operate, and despite each board (TLB and TRB) having its specifics in the data format of transferred information, these modes are, in principle, similar.

The first is the mode when the board is "listening"; it is ready to receive commands and send answers to the application that requested it. These are usually configuration commands, including resetting various counters¹, setting

¹BCR counter, L1A counter, error counters

more complex parameters such as a silicon strip module mask² or setting the LUT which encodes the main trigger decision logic. This mode is active all the time the board is powered on.

The second mode is the data acquisition mode. This mode is activated by the "enable readout" command sent to the board and the board then starts to send the monitoring data and data from the detector (trigger data, or data from silicon tracker depending on the board) whenever its data buffer is full or when a timeout is reached. Data taking mode can be disabled by the command "disable readout".

In case we are sending a configuration that can't be sent in one single 32-bit word, the checksum mechanism is used to make sure that the configuration received by the board wasn't altered by the data transfer process. This applies, namely, to the LUT, which is in total 1024 bits long³ and we need to be sure that the LUT was transferred without errors. This is why the cyclic redundancy check (CRC) is used, and the 16-bit checksum is computed and attached to the configuration. Another application of the checksum mechanism is used during the data transfer, where a 24-bit modified Fletcher's checksum is computed in order to identify corrupted data. Both CRC and Fletcher checksum mechanisms are discussed in section 13.5.

13.4.1 Communication protocol

Both the GPIO boards are using a communication protocol which is based on sending all transferred information in 32-bits-long words. Bits are then grouped together into sequences, forming the basis of the exchanged information data format. In general we can distinguish between request (request sent by the DAQ PC to the board) and answer (answer to the command sent by the board).

Except for the multi-argument request/answer (which is only the LUT for the TLB), each word that is sent is identified by a request/answer ID, followed by the board ID, which is important for determining the IP address of the board used in the communication. After these pieces of information, the command ID follows. The command ID is a 5-bit sequence identifying different types of commands that the GPIO board can receive. Examples of these commands are board specific⁴ (TLB and TRB have different firmware), but in general, they are commands asking to read board registers, configure registers, and start or stop data readout. After the command ID, the sub-command ID can follow, which is used only in some commands, followed by the request/answer argument. In case of a multi-argument request/answer, the checksum is attached to the exchanged data. This is discussed in more detail in section 13.5.

²enabling and disabling readout of individual silicon strips inside tracker modules

³8 trigger bits from the digitizer can form together $2^8 = 256$ different combinations based on if the given trigger fired or not. Each of the combinations has assigned some trigger decision encoded into four trigger bits. This results in $256 \times 4 = 1024$ -bits configuration.

⁴Examples would be requesting the board ID (which is important to know for initiating the Ethernet communication because the IP address depends on this number), setting and getting the LUT in case of the TLB, requesting the firmware version.

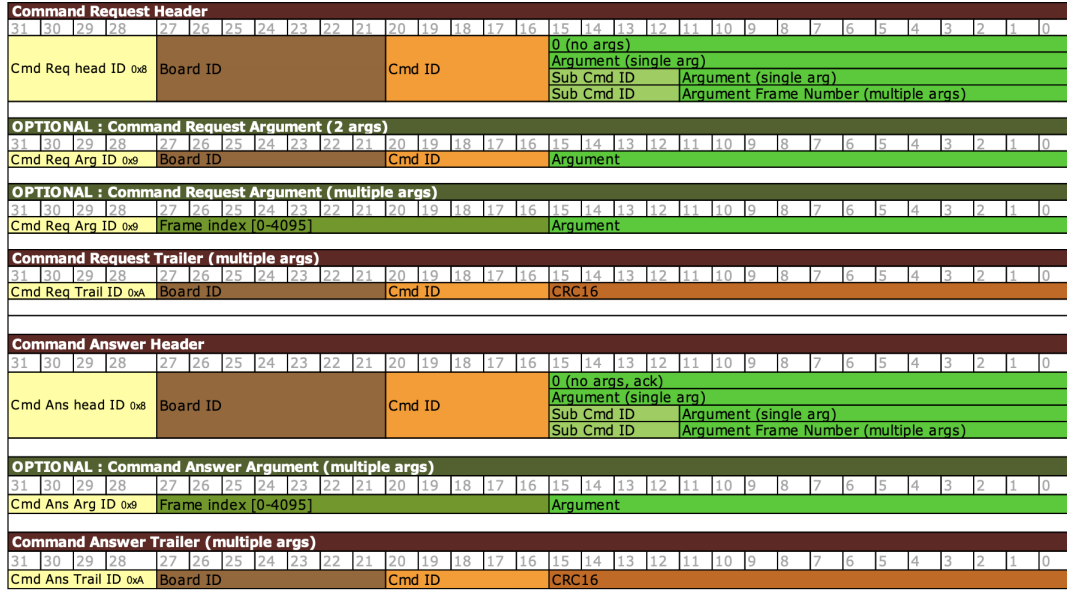


Figure 13.3: Communication protocol used by GPIO boards. [103]

The specifications of the general GPIO board command structure is shown in figure 13.3.

13.4.2 Trigger Logic Board

The TLB is the central trigger processor, and it is responsible for the distribution of a common 40 MHz clock and bunch-crossing reset signal. The clock signal can come from the LHC or be internally generated. It receives eight trigger signals as an input from the digitizer and transmits the final trigger decision to all detector readout components. The additional purpose of the TLB is to veto and prescale incoming triggers.

The purpose of the trigger veto is to minimize the detector *deadtime*. This is when subdetectors are busy reading out event data, and the detector has to wait with the data taking. There are several types of trigger vetos.

- **Tracker busy veto:** When the TRB is reading out the data, it issues a busy signal. The duration of this event depends on the hit multiplicity. The TRB cannot receive another L1A at this moment, and this veto is to prevent this from happening.
- **Digitizer busy veto:** Similar to the TRB behavior, the digitizer will issue a busy signal if its internal readout buffer occupancy reaches a given threshold. This lasts until the occupancy goes back below the threshold.
- **Simple deadtime veto:** All trigger decisions within a fixed number of bunch-crossings after an L1A are vetoed.
- **BCR veto:** SCT modules require 3 clock cycles to process the L1A and 7 clock cycles to process a *bunch counter reset* (BCR) signal, which is

generated by the TLB on every LHC orbit signal. An overlap of these is prevented by vetoing triggers for 9 clock cycles starting from 2 clock cycles before a BCR. The fixed deadtime for random triggers is therefore expected to be 0.25%, but it is zero for collision events as the BCR is designed to occur during the LHC abort gap⁵.

- **Rate limiter:** This is the control mechanism to avoid uncontrolled high rates from an input channel suddenly becoming noisy.

While taking the data, the TLB can be requested to send out the trigger and monitoring data. These data have a well-defined format and are equipped with the checksum so that DAQ can detect corrupted data due to transfer errors. An example of the data format for the TLB is specified in appendix A.4.

13.4.3 Tracker Readout Board

The TRB is a board responsible for the communication between silicon tracker modules and the DAQ PC based on the GPIO board described in chapter 13.4. There can be up to 8 silicon tracker modules connected to the TRB, and the TRB can configure these modules, as well as read out the information about hits upon receiving the L1A signal from the TLB.

The tracker modules are configured by the TRB using the commands and data encoded in bit-streams, which are sent to the tracker modules. The TRB firmware allows the extraction of information from commands sent by the user and converts them into a bit-stream that can be interpreted by the SCT modules. Any combination of modules can be addressed simultaneously. During the data-taking mode, the TRB sends trigger and timing signal only to enabled modules. This happens during the physics data taking when L1A, BCR, and clock signal are received from the TLB or during tracker calibration runs when L1A and clock signal are generated by the TRB.

All TRBs are located inside TI12 right next to the experiment in the mini-crate, located in the support structure just above the middle tracking station.

13.5 Data readout error-detecting mechanisms

The correctness of the data readout is ensured by computing checksums of transferred data. When the readout command for the TLB and TRB is issued, the checksum of the dispatched data is computed directly at the hardware board, and it is later checked by the DAQ software if the checksum attached to the data matches the checksum that is computed by DAQ software on this data. This

⁵The LHC beam dump system needs the short, particle-free, gap in the bunch filling scheme which accounts for the field rise time of the beam dump kicker system. Without this gap, the LHC facilities could get damaged by wrongly deflected bunches during the beam dump magnets turning on.

is a standard mechanism that is used in various communication applications to ensure the correctness of transmitted data.

The data communication in FASER uses two types of checksum for two different applications. The first checksum is the *cyclic redundancy check* (CRC) to make sure that the TLB configuration, the LUT - which is encoded into 1024 bits, is transferred correctly. The second application is the *Fletcher's checksum*, which is used for the TLB and TRB data, in order to make sure that data was not altered by the data transfer process.

The CRC used in FASER is the 16-bit checksum computed from the content of the LUT. The checksum is then attached to the LUT data as specified by the data format.

The checksum used for the data readout in FASER is a modified 24-bit Fletcher's checksum.

The CRC checksum offers stronger detection capabilities and is suitable for high-reliability applications, which is the case when sending configuration to the TLB. We want to be sure that the configuration (in the form of the LUT) that we load is correct, or else the trigger decisions made by the experiment could be wrong. The disadvantage of using CRC as a control mechanism is that the CRC is computationally more complex compared to Fletcher's checksum. This is not a problem since the configuration is sent to the TLB just once before starting the run, and then it stays the same, so we can afford to compute a more robust CRC checksum. However, it could pose a problem when sending data with rates of about 1 kHz. This is why the modified Fletcher's checksum algorithm is used for the TLB data⁶.

The Fletcher's checksum algorithm is explained in the next section, followed by the description of the modified version of this algorithm used in FASER.

13.5.1 Cyclic redundancy check

The cyclic redundancy check is an error detecting mechanism commonly used in the digital communication. Similar to Fletcher's checksum described in the following subsection, it is the redundant information of fixed length that is added to the data in order to allow the receiver see if the message was modified during the transfer process or not.

The n -bit CRC is computed as a remainder after the division of the message by a defined polynomial of length $n + 1$. This is done in the following way. The message is encoded into a sequence of bits, and this sequence is used as a dividend. Then the polynomial of length $n + 1$, which is specified at the beginning and is characteristic of a given CRC checksum. This polynomial can be represented in binary notation by its coefficients, so, for example, the polynomial $x^4 + x^2 + x + 1$ would be represented in binary notation as 10111. Then, the division by the polynomial can be easily implemented using bitwise XOR operation.

⁶TRB also uses the same checksum.

```
110111      original message
10111       polynomial
-----
011000      result
 10111      polynomial
-----
001111      result after last division - the remainder is 1111
```

Figure 13.4: Illustration of the division of the message by polynomial using the bitwise XOR operation. The checksum using polynomial $x^4 + x^2 + x + 1$ for this message would be 1111.

Let's assume we want to compute a 4-bit CRC checksum for the message represented by the sequence 110111. If we use the polynomial $x^4 + x^2 + x + 1$ as a divisor, the resulting 4-bit CRC checksum for this polynomial will be 1111. The process of dividing by the polynomial using the XOR operation is illustrated in figure 13.4.

The CRC checksum that is used in the FASER is a 16-bit CRC.

13.5.2 Fletcher's checksum

Let us first introduce a simple checksum algorithm. Let's assume that we have data that is transmitted in 32-bit packets like in FASER. The simple checksum from the data would be computed by adding together all 32-bit packets, performing modulo $2^{32} - 1$ (the largest unsigned integer that can be stored in 32-bit), and keeping only the remainder. The C++ function that would be computing this simple checksum from the data is shown in the code snippet in figure 13.5.

```
uint32_t SimpleChecksum (const uint32_t* data)
{
    std::vector<uint32_t> packets(data);
    uint32_t checksum = 0;
    for (int i = 0; i < packets.size(); i++)
    {
        checksum += packets[i] % (pow(2.0, 32) - 1);
    }
    return checksum;
}
```

Figure 13.5: Function computing 32-bit simple checksum from the data coming in 32-bit packets.

The checksum computed in this way can be attached to the original data, and if the receiver recomputes the checksum of the data they received, they can figure out if the data was altered by the transmission process. However, this simple checksum is insensitive to the order of received packets.

That's the problem that the Fletcher checksum can solve because it computes a second value along with the simple checksum, which can address the problem of the order of packets. The first value of the checksum is computed as a simple checksum, and the second value is computed as the first value plus the second value. In the beginning, both values are set to 0, but as the data is coming, the sensitivity to the order of packets is introduced because once the packet is added to the first sum, it is repeatedly added to the second value along with every packet after it. Then, the simplest thing to do is to assemble these two values next to each other to form a 64-bit integer. A function computing the 64-bit Fletcher's checksum implemented in C++ is shown in the code snippet in figure 13.6.

```
uint64_t FletcherChecksum (const uint32_t* data)
{
    std::vector<uint32_t> packets(data);
    uint32_t sum1 = 0;
    uint32_t sum2 = 0;

    for (int i = 0; i < packets.size(); i++)
    {
        sum1 += packets[i] % (pow(2.0, 32) - 1);
        sum2 += sum1 % (pow(2.0, 32) - 1);
    }

    return (sum2 & (0xFFFFFFFF << 32)) | (sum1 & 0xFFFFFFFF);
}
```

Figure 13.6: Function computing 64-bit Fletcher's checksum from the data coming in 32-bit packets.

This checksum cannot be used in FASER data format because the format has been designed for the use of the 24-bit checksum. That is where the modification of the presented algorithm has to come because we want to combine `sum1` and `sum2` into a 24-bit number.

13.5.3 Modified Fletcher's checksum used in FASER

The modification of the algorithm presented above consists of modifying the result such that parts of `sum1` and `sum2` are combined such that they form a 24-bit-long checksum as required by the data format. This is achieved by an algorithm nearly similar to the one described in figure 13.6 except the result is a 32-bit unsigned integer where the eight most significant bits are always 0, and the rest is filled by bit substrings extracted from `sum1` and `sum2`. This is schematically illustrated in figure 13.7.

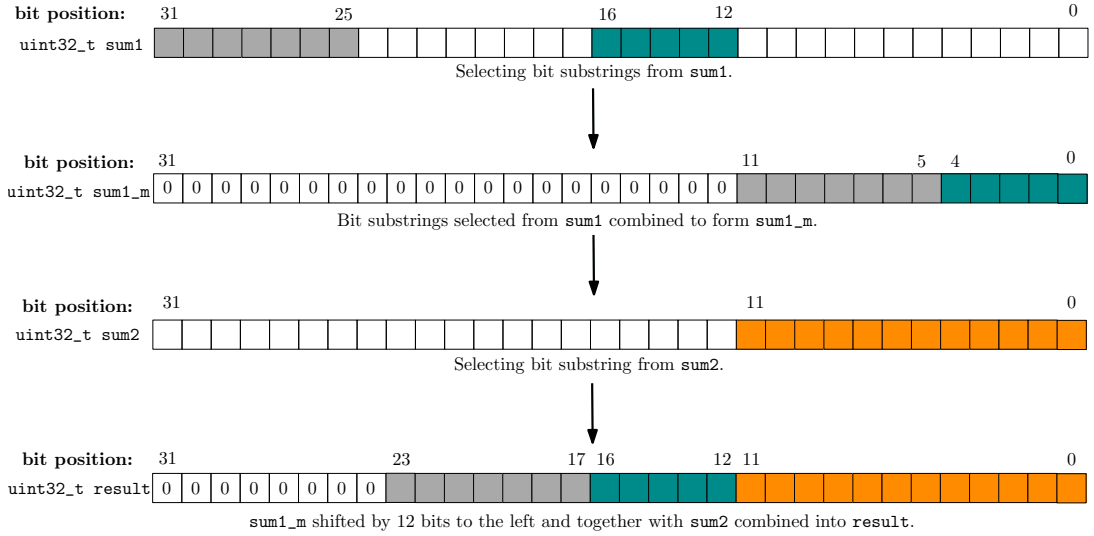


Figure 13.7: Schematic illustration of combining two sums obtained inside the code computing Fletcher’s checksum in figure 13.6 into 24-bits (result returned as 32-bits integer with eight most significant bits set to 0).

13.6 Tests of communication with GPIO boards

GPIO boards, i.e., TLB and TRB, are an integral part of the FASER data acquisition system, and their proper functionality is paramount to the correct data taking. At the development and early commissioning stage of the FASER TDAQ system, a lot of functionality of the GPIO boards was developed with the USB3 communication interface⁷ but the transition to an Ethernet communication interface had to be made due to the distance transfer limitation of the USB3 technology, which is not reliable above approximately 18m of distance, but the data has to be transferred from 100 meters under the ground to the surface where the DAQ PC is located. That is why extensive testing of the newly developed TLB and TRB firmware had to be made in order to detect any possible issues that could arise at the lowest level.

Two separate simple programs (one for the TLB and one for the TRB) were developed to perform these tests. The main purpose was to detect issues that can arise during longer periods of data taking. We were testing the ability to repeatedly receive and correctly process commands, such as reading out the data, setting the configuration, or writing a value to the board’s registers and checking that the value is retrieved unchanged. If there were, for example, an overflow of some of these values, they might not be stored and retrieved correctly. These tests took several hours and checked for any potential issues in communication.

Performing these tests helped to verify the robustness of the whole TDAQ system, which is very important because the experiment is placed underground

⁷The GPIO board was originally developed for the Baby MIND neutrino detector which was using the USB3 communication interface.

next to the LHC, and in-person technical intervention in the tunnel is impossible during LHC data-taking.

Commissioning and detector operations

14.1 Introduction

Before the experiment was placed into the tunnel, it had to be commissioned. The purpose of the commissioning is to ensure the proper working of all detector subsystems and evaluate their performance, which is crucial for the correct data interpretation. The commissioning was performed on the ground and inside the tunnel, and it involved standalone commissioning of individual subsystems and also commissioning of multiple subsystems combined.

This chapter briefly describes calorimeter commissioning using the test beam at CERN, described in section 14.2, where the author participated as one of the shifters who were crucial for taking the data during the week of non-stop operations. Section 14.3 is dedicated to commissioning the silicon tracker detector, where the author, as one of the shifters, helped perform electronic tests and calibrations of the silicon tracker modules. TDAQ commissioning and commissioning of the full detector are described in sections 14.4 and 14.5. The last section presents how the detector is operated thanks to the system of shifters volunteering on a weekly basis and how they monitor the status of the experiment. The author developed simple software that automatizes reporting of the detector status for weekly meetings and to help the shifters.

14.2 Calorimeter commissioning

In August 2021, the FASER calorimeter was commissioned using the beams of high-energy electrons, muons, and pions at the CERN H2 beam line. The beam was used to calibrate the calorimeter modules and measure the relative calorimeter response to high-energy electrons, muons (minimum ionizing particles), and pions for different points across the calorimeter. Six calorimeter modules were

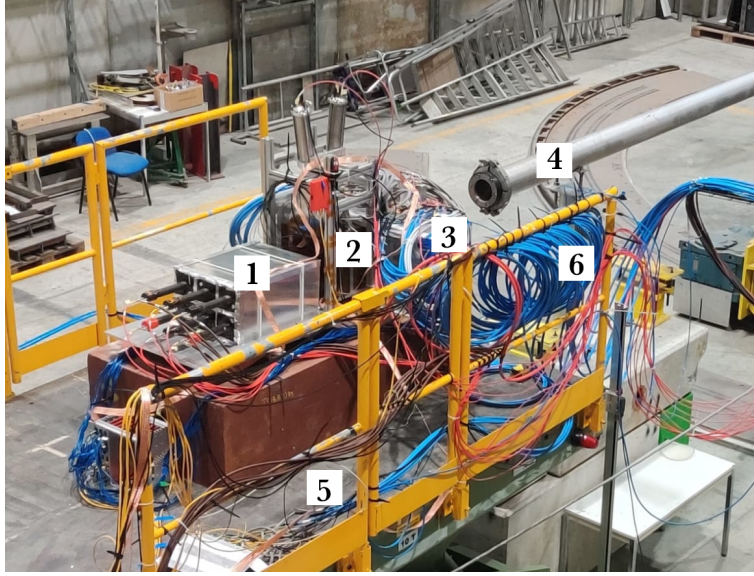


Figure 14.1: The experimental setup used during the FASER test beam. 1) six calorimeter modules under test, 2) trigger preshower scintillator system, 3) tracker station with the trigger scintillators in front (FASER ν veto station), 4) beam pipe, 5) moving table allowing to move the calorimeter modules with respect to the beam position, 6) cabling of the setup (readout and powering).

used for the test beam - four modules used in the experiment and two spare ones - in 3×2 configuration (see figure 14.1).

An electron beam with energy between 10 and 300 GeV was used to calibrate the modules. The uniformity of the muon response was measured with a muon beam at 150 GeV, and the pion scan to study the hadronic response was done at 200 GeV.

The experimental setup is shown in figure 14.1, and it consisted of a tracking station formed by three tracking planes used for the track reconstruction, two scintillators used for triggering, and six calorimeter modules under test. This setup was placed on the scissors table, allowing the setup to be positioned with respect to the beam pipe, which was in place in front.

In order to interpret the results of the experiment, the setup was simulated using the Geant4 package [104], and the simulation was compared to the data.¹

14.3 Silicon tracker commissioning

Individual elements of the FASER tracking detector were tested at each stage of the detector construction. That involved individual tracker planes and the full tracker stations on the surface before the installation into TI12, the location of the FASER experiment. After these tests, the performance was evaluated using

¹Since the author of the thesis was not analyzing the test beam data and the paper with results was not published during the writing of the thesis, the results are not shown.

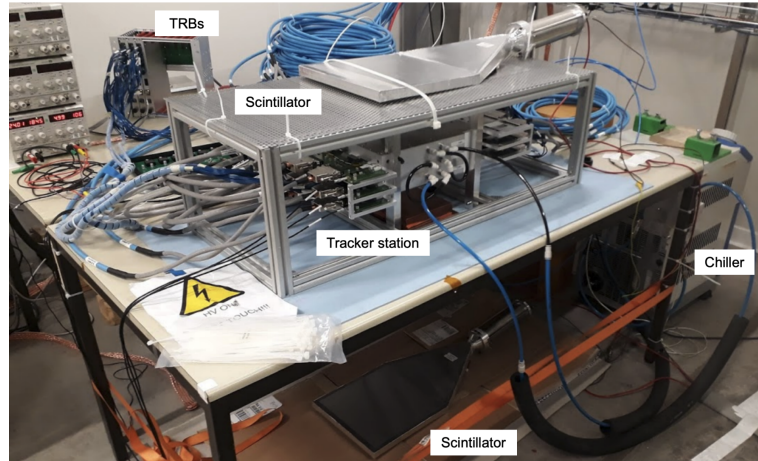


Figure 14.2: The experimental setup used for the station commissioning on the surface. It consisted of the actual tracker station, a chiller for the cooling, TRBs ensuring the tracker plane readouts, and two scintillators used for triggering. Picture taken from reference [99].

cosmic rays. This section describes individual tests in more detail and presents the results of these tests as presented in [99].

The tests were done in three independent stages: tests of single modules, tests of tracker planes, and finally tests of tracker stations.

The single-module tests were to evaluate the performance of single modules. These modules were cooled down by the chiller used to keep the module temperature below 30°C , and the noise value and dependency on applied bias voltage were compared to the results from the module production of the ATLAS SCT detector.

The tracker planes and stations were tested on the surface in test stands using the same equipment and software (DAQ system, powering, cables, calibration software) used in the fully assembled FASER experiment. The monitoring of temperatures, voltage and currents was handled by the Tracker Interlock and Monitoring Board (TIM). Thanks to the surface commissioning with components used in the actual experiment, it was possible to study the long-term behavior early on. The setup used for testing different tracker planes is shown in figure 14.2.

Thermal and electric characterizations were performed after placing the tracker station plane into the test setup. The thermal tests were done in order to study the temperature in three different scenarios - powered-off module, modules after powering, and finally, after configuring the ABCD3TA readout chips, ensuring the readout of the detector. This thermal testing was done for all tracker stations before and after installation into TI12, and it was shown that the temperature of modules always stays under the required 35°C , which is the value required by design.

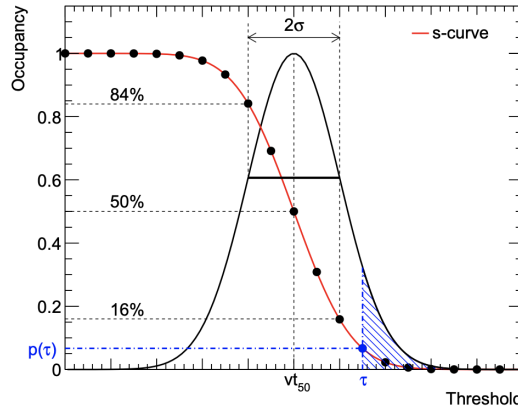


Figure 14.3: Illustration of the concept of s-curve and threshold scan. For a given threshold τ , the hit occupancy is the fraction of signals above the threshold (dashed area). In the case of only Gaussian noise and constant injected charge, the hit occupancy is the complementary error function. $p(\tau)$ is the probability that the signal is above threshold τ . Figure is taken from reference [99].

14.3.1 Threshold scan

Since the readout chips are capable of only binary readout², their calibration is crucial for the proper data interpretation. For this purpose, the chip contains an internal calibration circuit that enables the simulation of a hit pulse in a strip. Each strip has a 100 fF calibration capacitor connected to its input, and thanks to that and the dedicated chopper circuit, it is possible to simulate the voltage pulse while bypassing the sensor strips. The delay of the pulse with respect to the clock phase can be adjusted in 64 steps within 50 ns, and the amplitude of the pulse allows to simulate charges up to 16 fC, which allows to simulate a wide range of scenarios when a particle passes through the detector.

The calibration is based on the *threshold scans*, in which the range of values of the discriminator threshold is scanned, and a set of well-defined fixed-amplitude charges is sent at every step. This allows us to estimate the hit occupancy of the injected charge for a given discriminator threshold. Plotting the hit occupancy as a function of a threshold gives us the so-called *s-curve*. If there was no electronic noise, we would get instead a step function; however, due to the presence of the electronic noise, which follows a normal distribution, the hit efficiency follows the s-curve. In actual experiments, when a particle passes through the silicon, this s-curve corresponds to the cumulative distribution function of the charge deposited by the particle, which approximately follows the Landau distribution. The point at which the occupancy is 50% is called vt_{50} . The concept of the s-curve is shown in figure 14.3

²They only give the information if there was a hit or not.

14.3.2 Electronic tests and calibration procedure

The calibration procedure adopted by the FASER tracker is based on a procedure established by the ATLAS SCT collaboration, and it consists of the following steps.

- The first step is the **mask scan**. Its purpose is to determine dead/non-responsive channels and very noisy channels. Dead strips are detected by setting a very low threshold, then sending a number of trigger signals to read the data stored in the digital pipelines, and finally checking the detection efficiency. A similar thing is done to detect noisy channels, except the threshold is set high, and no charge is injected, and only readout is performed. Channels identified as defective are disabled by loading their list into a dedicated in-chip mask register.

The modules that had the lowest number of masked strips were mounted inside the tracker planes to positions corresponding to the central region of FASER's magnet central acceptance. The station with the lowest number of masked strips was chosen to be placed at the front of the detector (upstream) because that is where the separation between the electron-positron pair from the decay of a dark photon is smallest and gets more significant as the pair travels through the detector.

- **Strobe delay** is the second test, and it is used to determine, for each chip, the optimal delay between the calibration charge and the clock. This is achieved by varying the delay and computing the hit occupancy after the injection. The optimum delay is estimated as a plateau of the maximum occupancy.
- In the next step, we estimate the gain and the noise of the preamplification stage³. This test is called the **Three-Point-Gain**. For each strip, a linear fit of the vt_{50} threshold versus injected charge is carried out for three different input charges to obtain the slope and the threshold offset in mV.

The gain measured for the FASER tracker stations was 54 mV/fC, which is in good agreement with 55 mV/fC from the module specifications.

- **Trimming** is the fourth step in the calibration procedure. The readout chips are designed to provide the uniformity of thresholds across the whole module, and this is achieved through the trimming procedure by applying threshold corrections to compensate for the discriminator offset in each channel. This is because the readout chips were designed for the ATLAS detector to operate in the LHC environment in which the threshold spread across the modules between different channels increases due to the sensor's irradiation. The effect of the trimming procedure can be seen in figure 14.4.

³The front-end electronics of each readout chip consists of a preamplifier, shaper, and discriminator, and the purpose of the preamplifier is to amplify the signal before further electronics processing.

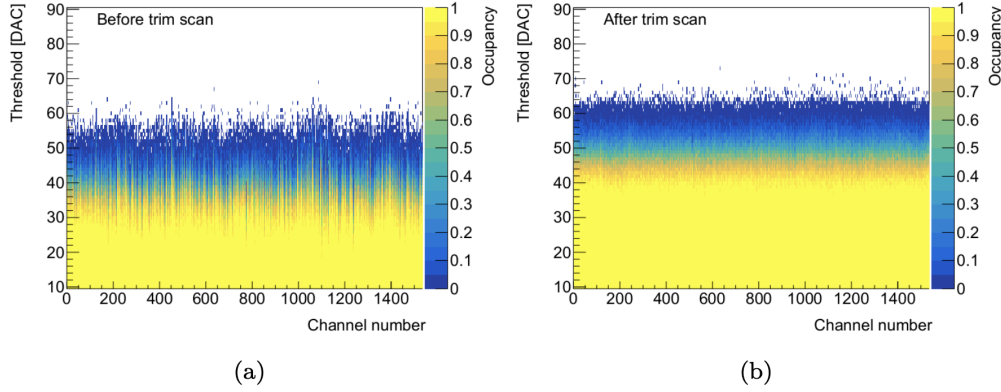


Figure 14.4: Threshold scan for a module with 1.5 fC injected charge before optimal trim settings (a) and after optimal trim settings (b). The figure is taken from reference [99]

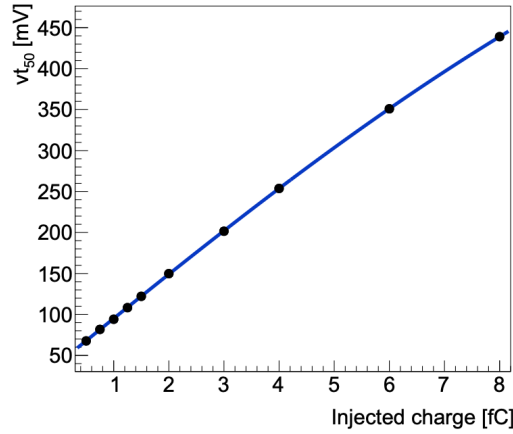


Figure 14.5: Response curve fit for a single strip. [99]

- The conversion between the signal from the detector in mV to a charge created by a particle in fC is not a linear function. In order to find this conversion, the **response curve** is estimated. Threshold scans are performed for ten input charges, ranging from 0.5 fC to 0.8 fC, and vt_{50} is estimated for each. These are then plotted as a function of the input charge, and the first-degree polynomial of form $\tau = p_2 + \frac{p_0}{1+e^{-q/p_1}}$ is fitted to the data. p_0 , p_1 , p_2 are parameters of the fit and τ , and q are threshold and injected charge. The polynomial then represents the relation between the threshold in mV and the charge in fC. An example of the response curve is shown in figure 14.5.
- The last test, which is the **noise occupancy** scan, is not part of the chip calibration procedure because no parameters are derived from it. However, it is used to determine the goodness of the above calibration procedure. The noise occupancy is defined as the probability that a strip will give rise to a hit due to the noise. This is done by performing threshold scans with-

out input charge while increasing the threshold. The number of triggers sent is increasing as the threshold is rising. For the ATLAS SCT modules, the noise occupancy per strip was specified to be less than $5 \cdot 10^{-4}$ at 1 fC threshold at the nominal operating temperature. After performing the tests, over 99.7% of the strips in the tracker satisfy these performance criteria.

The above tests were performed during the module, plane, and station testing. The station testing was performed both on the surface and in TI12, and the results were consistent with each other.

In addition to the tests described above, tests with a magnetic field were done. There were concerns about the presence of a residual magnetic field during lowering tracker planes, and the purpose of these tests was to check if the magnetic field from the magnets did not damage the tracker planes. However, the number of noisy and non-responsive strips was very consistent between different measured positions of the tracker plane with respect to the magnet.

Finally, the tracker was also commissioned using cosmic rays together with the whole TDAQ system. These tests are described in more detail in the section 14.4.

14.4 TDAQ commissioning

The commissioning of the TDAQ system can be split into two phases. In the first phase, individual system components (digitizer, TLB, TRB, and the DAQ software) were tested in standalone tests, and the second phase consisted of combined system measurements. The results of the TDAQ testing are described in reference [101], and this section summarizes the results presented there.

14.4.1 Standalone tests

The standalone tests of the digitizer, TLB, and TRB were performed to ensure the proper functionality of these components, which are paramount to the whole TDAQ system.

First, the digitizer's readout performance was checked and it was demonstrated that the digitizer can handle a maximum readout rate of more than 2.5 kHz at the nominal data fragment size of 19 kB. This corresponds to a maximum bandwidth usage of almost 50 MB/s.

After ensuring the digitizer's proper workings, the TLB was checked in several standalone tests. These tests were conducted using a lab setup in which a signal generator provided various signal configurations to the digitizer, and the digitizer's trigger output rate was used as input for the TLB. The results were then verified by checking the signal input and output on the oscilloscope and analyzing the data output from the board. In these tests, the following TLB functionalities were tested.

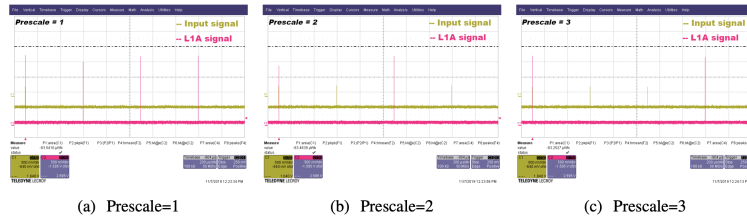


Figure 14.6: The output from an oscilloscope of 2 kHz input signal sent from the digitizer to the TLB. Prescale setting n means that only every n -th trigger gives rise to an L1A signal. [101]

- **Signal timing** - The TLB trigger LUT is configured to trigger only on the coincidence of the two input signals from the digitizer. However, it can happen that signal from different scintillators/calorimeter corresponding to one particle does not arrive at the TLB at the same bunch-crossing due to the different cable lengths, signal processing times., or time-of-flight. The TLB allows to correct for this effect and allows to synchronize trigger input signals that would arrive at different times. This functionality was successfully tested using the pulse generator and signal splitter, where one of the signals was delayed with respect to the other one such that it fell into a different clock cycle⁴
- **Rate control** - The TLB can control the rate either by vetoing triggers due to several sources as described in section 13.4.2, or by prescaling individual trigger items, which is when only every n -th item is selected. The prescaling functionality was tested by sending a 2 kHz input signal from the digitizer to the TLB, and based on the prescale settings, every n -th trigger gave rise to an L1A signal, which was seen in the signal from the oscilloscope in figure 14.6.

The veto sources asserted by the TLB were tested in the lab setup. This included simple deadtime veto and rate limiter. The simple deadtime veto and rate limiter were tested by supplying a 10 MHz 10-pulse signal burst to the digitizer-TLB system for simple deadtime veto windows of 0 and 10 bunch-crossings. While the former shows three L1A signals every 100 ns, the latter shows three consecutive L1A signals for every third input signal 300 ns after, as seen in figure 14.7.

The TRB was tested through hardware communication to ensure that the values that the TRB is sending match the expected values. That was done by configuring the tracker modules, reading the configured values, and checking that the sent and received values match. The other TRB test verified the correct data readout by injecting a test pulse into some tracker strips while performing the data readout. The information recorded by the TRB was checked with respect to hits in expected strips, and it was verified that no errors from tracker modules

⁴One clock cycle corresponds to 25 ns, which is the time window between two bunch crossings.

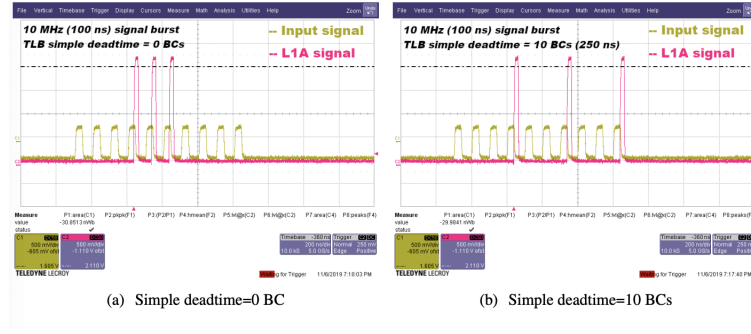


Figure 14.7: An oscilloscope image of a 10 MHz 10-pulse signal burst from the digitizer to the TLB. For a simple deadtime of 0 BC, the L1A occurs for three consecutive signals. For the 10 BCs, the two input signals after the L1A are vetoed. [101]

were received. Finally, tests of the data throughput were performed. In these tests, the repeated bursts of triggers of 1000 events were issued while injecting charge into 25% of all strips to generate hits. The TRB firmware automatically adjusted the delay between triggers to avoid the overflow of data FIFO, and a maximum recorded data rate of 51 MB/s with trigger rate regulated to 6 kHz was observed.

14.4.2 Combined measurements

To test the functionality of the TDAQ system after the FASER installation inside TI12, a series of tests was performed to ensure that the whole system was working as expected. These tests included stress tests by running at various high rates and also running with cosmic muons.

The setup of the system was the following. The signal from the PMTs at each scintillator or calorimeter station were mapped to the final trigger item output of the TLB using the combination of digitizer logic and the TLB trigger LUT logic. A trigger is fired in case of the presence of a signal in any calorimeter module, in the top or bottom part of the timing station, in either of the veto layers, or in the preshower layer.

The first important step in combined testing was to tune the timing for the PMT and tracker components to make the signals correspond to the same bunch crossing arriving at the same time. This included synchronizing the signals from the scintillators and calorimeter to make them come simultaneously, which was done based on the signal waveform using the signal from cosmic muons. In the case of the tracker, there is a signal propagation delay of the L1A to the SCT modules. This delay needs to be accounted for to ensure that the SCT modules are read out at the moment when there is a signal, and it is different for each tracker plane. The tuning of this parameter was done using the hit pattern in cosmic ray data, and the final fine-tuning was done with high-energy muons from pp collisions synchronized to the LHC clock.

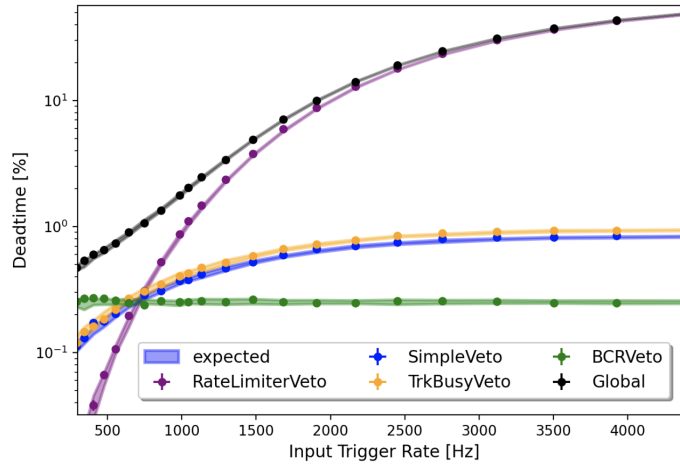


Figure 14.8: The measured deadtime fraction due to various sources as a function of input trigger rate. Random pulses were generated using the signal generator. [101]

Once the timing between individual components was done and the event data for each subdetector was verified to be in the center of the readout window, it was further checked that all data fragments from a common event were assigned to the same BCID.

After the whole TDAQ system was set up, it underwent system stress testing. The FASER physics rate is about 1 kHz for the pp data taking, and so it was crucial that the whole system was stress tested at higher rates using the pulse generator delivering rates between 250 Hz to 5.3 kHz. The maximum recorded event rate achieved in this setup was 2.2 kHz, limited mainly by the rate limiter as was estimated in the standalone test in a lab with one tacker plane (see figure 14.8).

Also, the FASER DAQ software has proven itself to handle the fully integrated TDAQ system up to the maximum hardware readout limited to 2.2 kHz and data throughput of 47 MB/s.

14.5 Commissioning of the full detector

After standalone testing of individual FASER subsystems, they were all installed in TI12 in March 2021.⁵ This section describes commissioning studies done in situ using cosmic rays and an LHC pilot beam towards the end of Long Shutdown 2 in October 2021.

⁵FASER ν emulsion detector, FASER ν veto scintillator, and the interface tracking station were installed later.

14.5.1 Commissioning with cosmic rays

The commissioning with cosmic rays was used to test the functionality of the assembled detector, but it couldn't be used to test real data-taking scenarios where particles are traversing through all three tracking stations due to the very low probability of cosmic rays arriving at such a big incidence angle. This probability is also lowered because the FASER detector is under the ground at a depth of 80 m.

However, cosmic-ray data were used by the tracker, calorimeter, scintillators, and the TDAQ system for various performance studies.

The long-term operations of the tracker during the cosmic-ray data taking with the full detector showed that all SCT modules could be kept under 30° C and that the tracker was able to operate efficiently and safely for single runs over many days. Also, the noise occupancy was measured at the nominal 1 fC thresholds using randomly triggered events during cosmic-ray runs, and it was shown that the results were in good agreement with numbers obtained during the tests of single SCT modules as described in section 14.3.

During the cosmic-ray data-taking period, the calorimeter system was tested by taking the cosmic rays and noise data for nearly 82 days, corresponding roughly to the expected time of stable beam collisions in a full year of the LHC. It was shown that the cosmic-ray background can be suppressed by additional selection on signal timing and will not be significant in physics data analysis. In addition, the LED calibration system, which was already mentioned in section 12.7, was used to monitor the calorimeter response versus time, and it was shown that the system and the PMTs were stable within 1%.

The long-term stability of the TDAQ system for the detector in its final location was continuously tested during the combined cosmic-ray data taking, and the limitations of the TDAQ hardware and software were probed by dedicated high-rate tests as described in subsection 14.4.2. The TDAQ system was proven to run without signs of limitations during these high-rate tests.

14.5.2 Commissioning during the LHC pilot beam

The LHC carried out a pilot beam test in which proton beams were circulated in the LHC during the last two weeks of October 2021. The LHC operated with a maximum of four circulating bunches per beam, with the nominal number of protons per bunch and a beam energy of 450 GeV. During these two weeks, the FASER experiment continuously collected data using cosmic triggers (triggers on a single signal per scintillator station or calorimeter module) and coincidence trigger that required signal in the veto and pre-shower scintillators. The primary purpose of these tests was to check the LHC beam pipe aperture.

Several hundred events were observed containing charged particles traversing the detector, such that they can be traced back to the ATLAS interaction point. Since the LHC circulated two bunches colliding inside ATLAS and two non-colliding bunches, and an equal number of events traversing FASER was observed for colliding and non-colliding bunches, it is strongly suggested that the observed

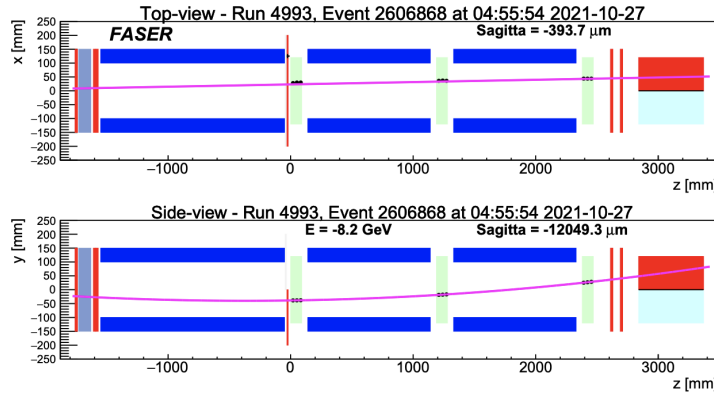


Figure 14.9: An event display of a charged particle traversing the full detector during the LHC stable beam run with two 450 GeV colliding beams. [98]

signals are arising only from the beam background rather than collision products. An example of the charged particle traversing the whole FASER detector is shown in figure 14.9.

14.6 Detector conditions monitoring

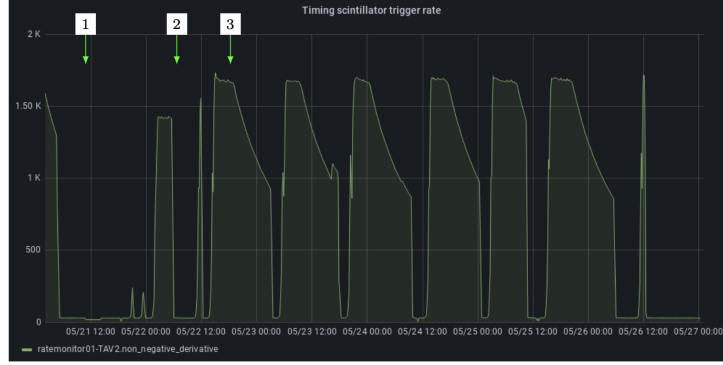
FASER is operated thanks to the run manager and monitoring shifter, which are the roles volunteered by the collaboration members on a weekly basis.

The run manager's role is to ensure the detector's smooth operation and to coordinate interventions on the subsystems that need to be done by different people, such as tests or, in rare cases, interventions in the tunnel.

The role of the monitoring shifter is to check for possible problems during the daily detector operations. The detector doesn't have a dedicated control room and is controlled via a web-based run control system. It is designed to allow data-taking for long periods without human intervention. However, it still needs to be regularly checked to see if it is working correctly to ensure the proper collection of the data and prevent detector damage due to unexpected issues. These checks include monitoring histograms related to the detector operations (temperature, currents, voltages,...). Each monitoring shifter has to report on the detector's status at the end of their weekly shift. Shifter reports include the time evolution of monitored quantities with annotation of events that can influence them, such as, for example, hardware tests, calibrations, or LHC beam-related issues, since these annotations can help trace potential issues.

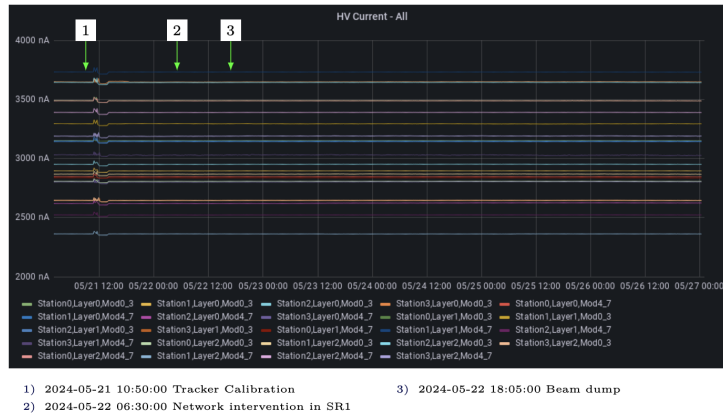
Due to the repetitive nature of the task of preparing a presentation summarizing the status of the detector, a script that automatizes this task and allows the simultaneous annotation of selected events in all plots is used. The example of the output slides prepared by the script is shown in figure 14.10.

Trigger rate



(a) FASER trigger rate.

Leakage currents



(b) Leakage current of SCT modules.

Figure 14.10: Snippet of the FASER monitoring weekly summary. Timeline annotations are defined in a text configuration file and are automatically marked in all plots. Figure 14.10a shows the FASER trigger rate that reflects the variance in ATLAS instantaneous luminosity. It can be seen that during the period with no triggers, the tracker calibration was performed, which caused a short change in the leakage current in silicon strip detectors. This is how this automatic annotation can help trace potential issues across various plots.

Conclusion and outlook

FASER is one of the most recently installed experiments at the LHC, and it can be classified as a small and cheap experiment that complements the physics program of the large LHC experiments, thanks to its location far from the proton-proton collision point. It was commissioned and built during the three-year-long LHC maintenance break, and it has been taking data since the beginning of Run 3 (July 2022). Due to its placement deep under the ground, far from the interaction point, and its design, it can provide physics data with a very low background. During the short time it took to collect data, it already brought valuable physics results.

In particular, the first data set of 27.0 fb^{-1} taken between September and November 2022 was used to search for dark photons and B-L gauge bosons. The results of this analysis are one of the first probes of these regions of parameter space since the 1990s, and they exclude previously viable models motivated by dark matter, which can be seen in exclusion plots 15.1 from the paper in reference [105] presenting these results.

In addition, FASER managed to observe the first ever neutrino interaction at a particle collider experiment as presented in reference [106]. Neutrino candidate events were identified in a 13.6 TeV center-of-mass energy pp collision data set of 35.4 fb^{-1} using the active electronic components of the FASER detector.

Finally, FASER ν managed to observe high-energy electron and muon neutrinos and measure their cross-sections in energy ranges of around $\sim 0.5 - 1.7 \text{ TeV}$, which are the first measurements of neutrino interaction cross sections in these energy ranges.

With more recorded data, FASER should be able to extend its reach and probe unexplored parameter space of models predicting long-lived weakly interacting particles. An improvement is also expected with the new high-precision preshower detector [107] allowing to distinguish the predicted axion-like particles signature of two very closely spaced highly energetic photons. The FASER collaboration showed that FASER is the experiment that can push the boundaries

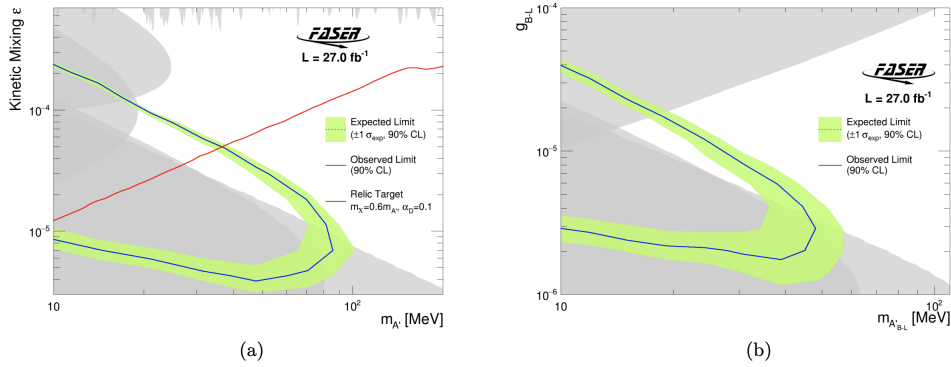


Figure 15.1: 90% confidence level exclusion contours in (a) the dark photon and (b) the B - L gauge boson parameter space. Regions excluded by previous experiments are shown in grey. The red line shows the region of parameter space that yields the correct dark matter relic density. [105]

of particle physics and is expected to contribute even more knowledge about BSM physics.

Moreover, there are plans for building the new Forward Physics Facility [108] located several hundred meters from the ATLAS interaction point, shielded by concrete and rock. This facility will host a suite of experiments to probe SM processes and search for BSM physics, and FASER2 and FASER ν 2 are two of them. FASER and FASER ν inspire these two proposed experiments, and the expertise gained during the commissioning and operations of the FASER detector will help with building these experiments in the future.



Summary

The first two chapters presented the Standard Model of particle physics and theories beyond the SM, which were discussed later in the thesis, followed by the chapter describing the LHC and basics of the collider physics. The introductory part is then followed by the two major parts of the thesis, which present the authors' work at experiments ATLAS and FASER, motivated by searches for physics beyond the Standard Model.

The first part of the thesis was dedicated to the experiment ATLAS at the LHC, where in chapter 4 we described various subsystems of the ATLAS experiment.

Chapter 5 was dedicated to event reconstruction, discussing both online and offline reconstruction algorithms. In particular, we discussed jet reconstruction techniques because jets are important experimental signatures when probing the Standard Model and for searches beyond the Standard Model, some of which are presented later in the thesis.

In chapter 6, we described the track extrapolation process used in Particle Flow jet reconstruction and the optimization of the extrapolation algorithm, which was employed in ATLAS at the HLT level during Run 3. Although this change only slightly reduced CPU usage, it allows running other more complex trigger algorithms, leading to better triggering performance. The importance of such improvements will be crucial in the future when getting closer to the transition to the High-Luminosity LHC¹, which will be able to increase the sensitivity of future physics searches.

Chapter 7 presented statistical methods used in physics searches and, in

¹The High luminosity LHC is the project that aims to improve the LHC performance by increasing the integrated luminosity by a factor of 10 beyond the LHC's design value. This is connected with technical challenges, and the ATLAS experiment is continuously being upgraded to prepare for the change. The luminosity increase will be connected with pile-up increase from $\langle\mu\rangle = 55$ up to $\langle\mu\rangle = 200$, which emphasizes the importance of the efficient trigger system even more.

chapter 8, we presented two reinterpretations of the search probing the higgsino pair production model using these methods. Despite not observing any significant excess between data and simulation predictions in these two reinterpretations, we were able to exclude part of the phase space and so put constraints on masses $m_{\tilde{\chi}_1^0}$, $m_{\tilde{\chi}_2^0}$, and $m_{\tilde{\chi}_3^0}$ in the SUSY model with heavy and light neutralinos, and on masses $m_{Z'}$, m_s in the dark-Higgs (mono- s) model. The reinterpretation of the dark-Higgs model also served as a starting point for a new dedicated analysis of this signal.

Chapter 10 described the preservation of the analysis targeting the higgsino pair production using RECAST. Even though we were not able to use the RECAST implementation for the reinterpretations presented in chapter 8 (ntuples production was too slow using the REANA cluster, and we needed to perform the BDT selection, which was easier to do outside of RECAST), it can be used as a starting point for future searches targeting the same final state.

Finally, chapter 11 concluded the ATLAS part briefly presented the outlook of the presented analyses and plans of the ATLAS detector for the future.

The second part of the thesis was dedicated to FASER. Although FASER is a small, inexpensive experiment compared with ATLAS, it proved during its first years of data-taking that it can complement ATLAS's physics program well and search for particles that leave ATLAS undetected.

Chapter 12 introduced the physics motivation for the FASER experiment and described its components.

The second chapter of the part dedicated to FASER, chapter 13, described the detector's TDAQ system with a focus on work performed by the author of the thesis, namely his contribution to testing and development of the drivers to the GPIO boards.

Chapter 14 described different stages of commissioning of the individual detector subsystems as well as the basics of the detector operations during its first years of data-taking.

Chapter 15 briefly presented the first FASER results and discussed the outlook for the future.



Appendix

A.1 ATLAS jet trigger naming convention

Triggers in ATLAS are usually complex sets of rules for selecting interesting events, and they are called by the string that uniquely specifies these rules. We will briefly describe the naming convention relevant to jet triggers mentioned in this thesis.

The trigger name specifies the trigger level **HLT** stands for the trigger executed at the HLT level and **L1** stands for trigger at the Level-1 trigger.

Jet triggers at the HLT level are called by the jet multiplicity, jet signature specifier **j**, and the jet p_T . Single jet trigger with jet $p_T > 400$ GeV would be **j400**, 3-jet trigger with all jets above $p_T > 190$ GeV would be **3j190**, and 4-jet trigger with all jets above $p_T > 110$ GeV **4j110**.

Name can also specify algorithms used for the jet reconstruction such as **pf_ftf**, which stands for Particle Flow with tracks using Fast Track Finding algorithm and preselection criteria which follow afterword **presel**.

Jet triggers at Level-1 follow a similar convention as HLT triggers with the jet signature specifier **J**. Random triggers are designated by specifier **RD0**.

Finally, if the name contains **FILLED** at the end, the trigger was active only during bunch crossings filled with protons since some bunches can be empty as described in chapter 3.

A.2 Interpolating in exclusion plots

When producing the two-dimensional exclusion plot, we face the following problem. We know CLs values in discrete points, but we need to draw continuous lines to connect points with CLs values in the whole plane, which, in reality, is not discrete but continuous. We need to connect points with a value of CLs = 0.05 to draw the exclusion line. In order to do this in the discrete grid, we have to interpolate between known grid points, for which we can use different interpolation strategies. When producing these plots using HistFitter, we have two options - triangular interpolation and RBF (radial basis function interpolation), which need to be carefully chosen because we have a grid with rapidly changing CLs values close to its edges, and each approach can lead to different results.

Radial basis function (RBF) interpolation

Radial basis functions (RBFs) are a series of exact interpolation methods, meaning the surface must pass through each measured sample value. RBFs are conceptually similar to fitting a rubber membrane through the measured sample values while minimizing the total curvature of the surface.

With the RBF interpolation, the problem is the following. We have a set of points $X = \{x_1, x_2, \dots, x_n\}$ where each point is defined by two coordinates and its functional value². These points lay on the surface defined by the function $f(x)$, but we don't know $f(x)$, and we only know $f(x_i)$ where $x_i \in X$. Our task is to interpolate $f(x)$ by a new function $s(x)$, which means that we require

$$s(x_i) = f(x_i), \quad x_i \in X. \quad (\text{A.1})$$

In case of RBF interpolation, $s(x)$ is of form

$$s(x) = \sum_{i=1}^n w_i \varphi(\|x - x_i\|), \quad (\text{A.2})$$

function φ is called radial basis function, and w_i are weights we are trying to find. The requirement is that φ depends only on the distance from some point³. Function $s(x)$ can be then found using prescription (A.2) and condition (A.1) solving the system of linear equations

$$\begin{bmatrix} \varphi(\|x_1 - x_1\|) & \varphi(\|x_2 - x_1\|) & \dots & \varphi(\|x_n - x_1\|) \\ \varphi(\|x_1 - x_2\|) & \varphi(\|x_2 - x_2\|) & \dots & \varphi(\|x_n - x_2\|) \\ \vdots & \vdots & \ddots & \vdots \\ \varphi(\|x_1 - x_n\|) & \varphi(\|x_2 - x_n\|) & \dots & \varphi(\|x_n - x_n\|) \end{bmatrix} \begin{bmatrix} w_1 \\ w_2 \\ \vdots \\ w_n \end{bmatrix} = \begin{bmatrix} f(x_1) \\ f(x_2) \\ \vdots \\ f(x_n) \end{bmatrix} \quad (\text{A.3})$$

²In our case, axes are defined by masses of dark Higgs and Z' and the value is the CLs value obtained by the fit in HistFitter.

³Some of the radial basis functions that can be used are gaussian $\varphi(r) = e^{-(\epsilon r)^2}$, multi-quadric $\varphi(r) = \sqrt{1 + (\epsilon r)^2}$, linear $\varphi(r) = r$, ...

The advantage of this approach is that we get a nice smooth surface that interpolates our data. However, the disadvantage is that the fitted surface can have a minimum below the minimum of interpolated data points. This becomes problematic if we are close to the exclusion limit and "artificially" create an excluded region not backed up by any data - see figure A.3. This can be avoided by choosing different radial basis function.

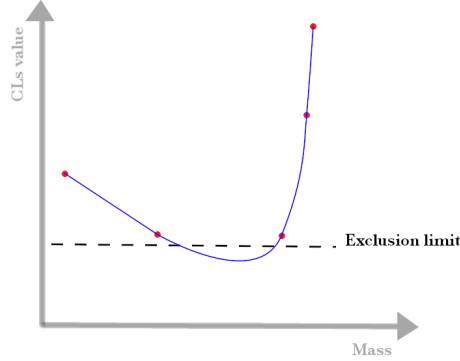


Figure A.2: Schematic illustration of the RBF interpolation in the two-dimensional section using multiquadric (or similar) radial basis function. The red points are points we want to interpolate, and the blue line is the section through the interpolated surface.

In our case, we used HistFitter scripts, which use the SciPy Python package to perform RBF interpolation.

Delaunay triangular interpolation

Triangulation is a set of lines connecting each point to its natural neighbors in scattered data, such that the created grid consists of triangular faces. Delaunay triangulation is a triangulation in which the unique circle circumscribed about the triangle contains no data points for each triangle. If we have a set of points $X = \{x_1, x_2, \dots, x_n\}$, the surface of the interpolated function is found by triangulating scattered data and linearly interpolating the surface within each triangle.

Using this method will ensure that the generated surface won't have minimum (maximum) below (above) the extreme values in our data set, i.e., we can avoid the problem that arises when using RBF interpolation described above when an "artificially" excluded region can be created. This is schematically depicted in figure A.4. The resulting exclusion plot using this approach combined with smoothing of the interpolated surface can be seen in figure A.5

Delaunay triangulation is used in ROOT⁴ for plotting 2D graphs (TGraph2D) for surface interpolation.

⁴The software package used in particle physics for data processing, manipulation with the

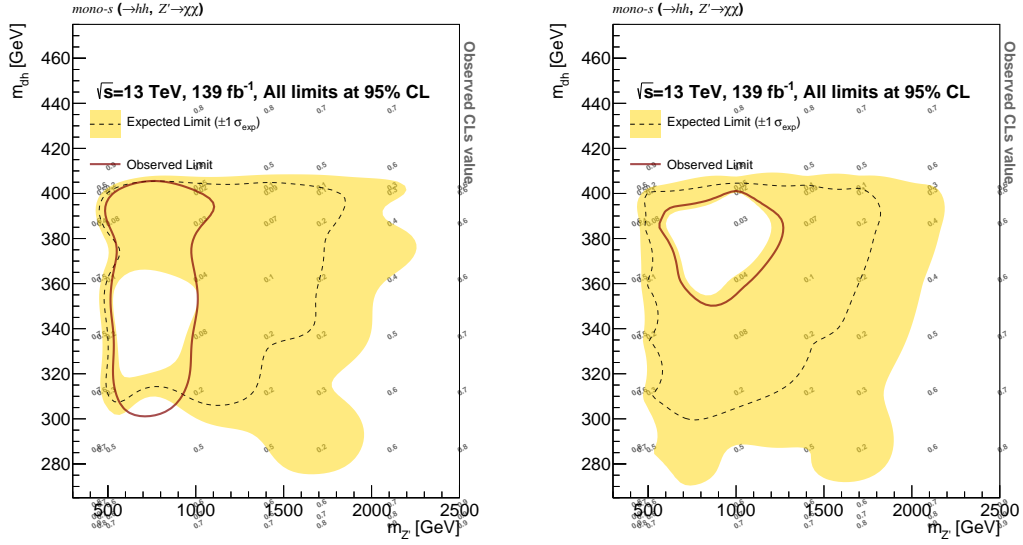


Figure A.3: Two-dimensional exclusion plot created using RBF interpolation method. The plot on the left was created using multiquadric RBF, which suffers from an artificially created excluded region because of abruptly changing CLs values at the grid's border. The plot on the right was created using the linear radial basis function, which does not create "downward fluctuation," and the excluded area is much better backed up by data points.

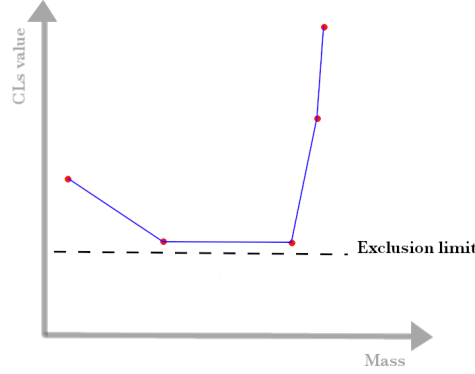


Figure A.4: Schematic illustration of a triangular interpolation in the two-dimensional section. The red points are the points we want to interpolate, and the blue line is the section through the interpolated surface. Because the interpolation is linear between data points, we avoid having a minimum of the interpolated blue line (surface in three dimensions) below the minimum present in the data (red points).

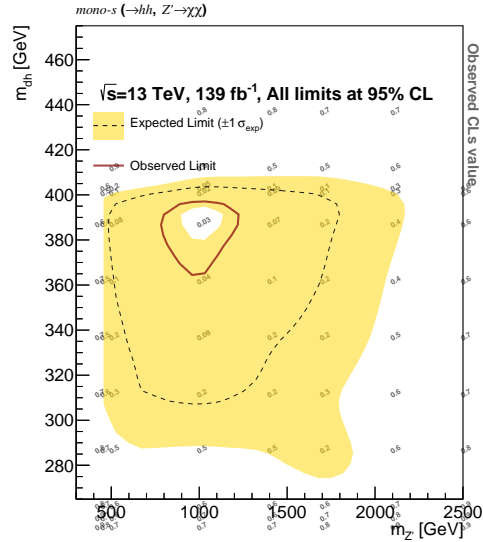


Figure A.5: Exclusion limit plot using Delaunay triangulation method with subsequent smoothing to produce interpolated surface and draw exclusion limit contours.

A.3 RECAST workflow

The schema in the figure A.6 shows the workflow of the higgsino analysis generated automatically by RECAST. A little blue square at the top of the figure where all the lines start is the entry point of the analysis. Items connected directly to the entry point are input files and parameters the user specifies. Dashed grey boxes represent individual processing stages; blue boxes represent analysis steps. There can be several stages in principle, but the presented preserved analysis contains only single-step stages. Outputs from steps are circled in red. Arrows show the direction of the information flow from one processing stage/step to another.

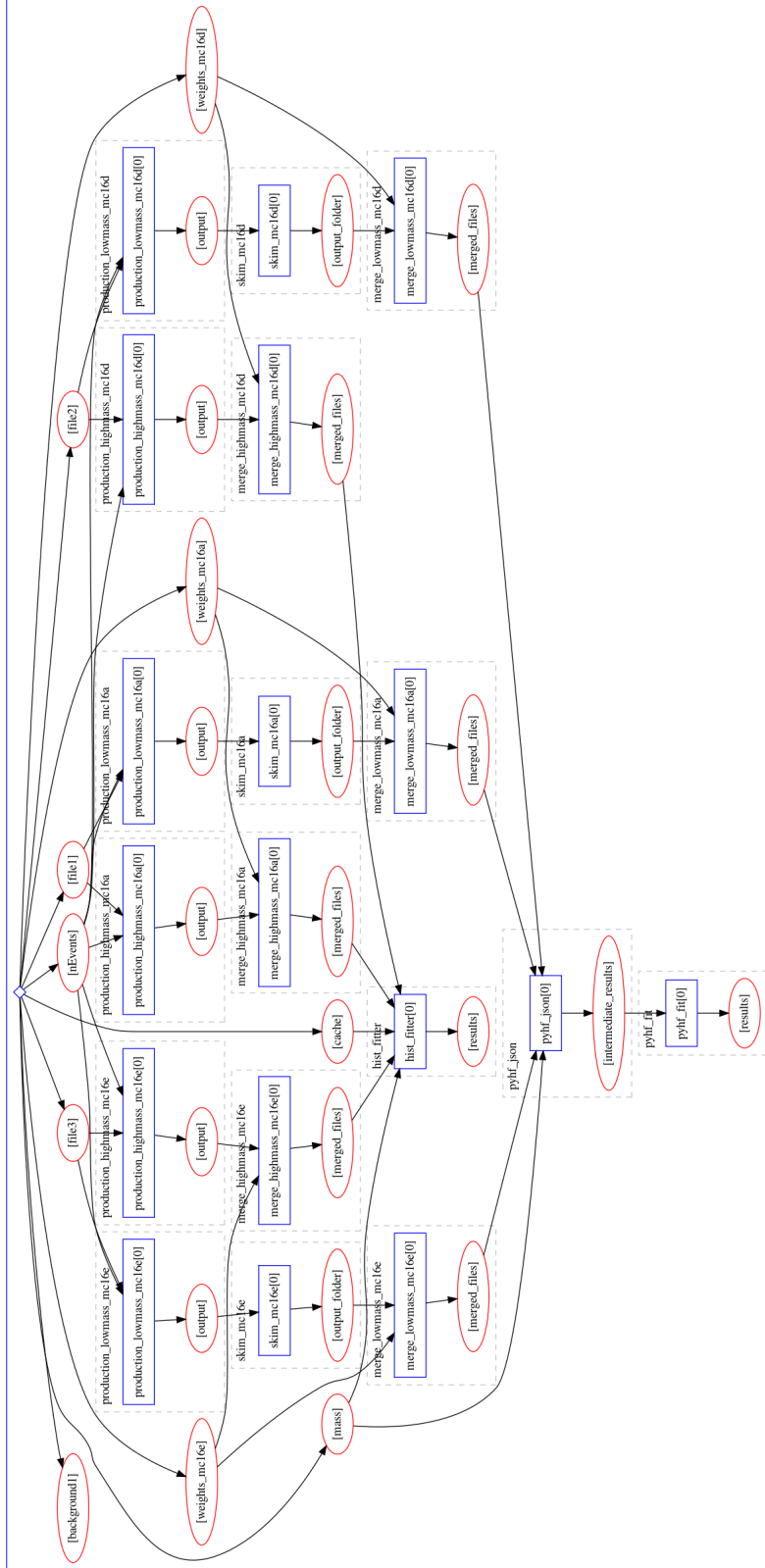


Figure A.6: Schematics of the higgsino analysis generated by RECAST.

A.4 TLB and TRB data format specifications

This appendix shows the data format specifications for the TLB and TRB.

A.4.1 TRB data

The data structure for the TRB is shown in figure A.7. Data can be split into header, data payload and trailer. These are always identified by the two most significant bits, followed by the three bits encoding the frame count. Then the structure of 32-bits words depends if it's header, data payload, or trailer.

The information that is encoded in header is the event count.

Payload data can be split into TRB data and module data. The TRB data contain information such as BCID and information about errors, and the module data carry the raw information from the silicon tracker modules.

The trailer then encodes the 24-bits Fletcher's checksum computed for the data by the TRB board.

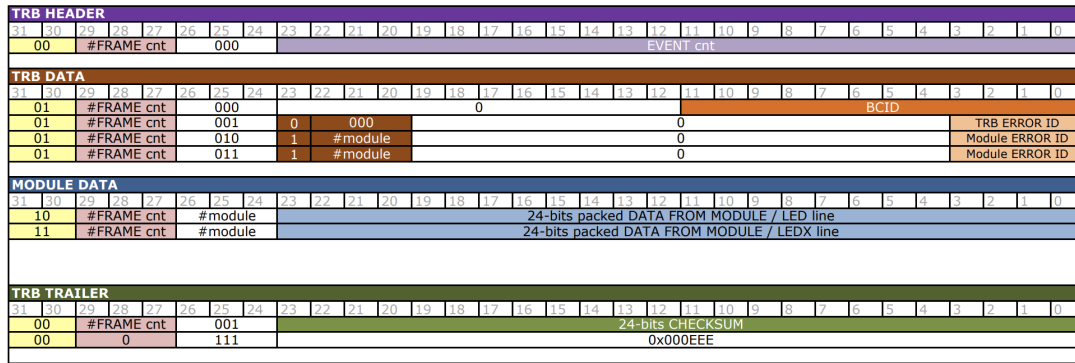


Figure A.7: The TRB data structure. [103]

A.4.2 TLB data

The TLB data can be split into two types. The first type is the TLB trigger data. The format of this data is shown in figure A.8.

The data always start with the header, which is followed by the payload. The payload encodes information such as event number, orbit counter, bunch counter (0 to 3563), trigger after prescale (TAP), trigger before prescale (TBP) and values of eight trigger bits. The data is always finished by the trailer containing the 24-bits Fletcher's check sum.

The second type of the data provided by the TLB is the TLB monitoring data. This type of data is read out as often as trigger data and so it consists of more words, because we can afford to read it less frequently⁵. The monitoring data consists of header, followed by the data payload with event counter, orbit counter, bunch counter, trigger before and after prescale, trigger after veto

⁵The trigger data rate is close to 1 kHz but the monitoring rate is usually in order of $\mathcal{O}(1)$ Hz or below.

TLB Trigger Data

Word 0																																			
31	30	29	28	27	26	25	24	23	22	21	20	19	18	17	16	15	14	13	12	11	10	9	8	7	6	5	4	3	2	1	0				
Header																																			
Word 1																																			
31	30	29	28	27	26	25	24	23	22	21	20	19	18	17	16	15	14	13	12	11	10	9	8	7	6	5	4	3	2	1	0				
0	0	0	1	0	0	0	0	Event Counter																											
Word 2																																			
31	30	29	28	27	26	25	24	23	22	21	20	19	18	17	16	15	14	13	12	11	10	9	8	7	6	5	4	3	2	1	0				
Orbit Counter																																			
Word 3																																			
31	30	29	28	27	26	25	24	23	22	21	20	19	18	17	16	15	14	13	12	11	10	9	8	7	6	5	4	3	2	1	0				
0	0	1	1	0	0	0	0	0	0	0	0	0	0	0	0	0	0	0	Bunch Counter																
Word 4																																			
31	30	29	28	27	26	25	24	23	22	21	20	19	18	17	16	15	14	13	12	11	10	9	8	7	6	5	4	3	2	1	0				
1	1	0	0	TAP								TBP								Input Bits								Input Bits (next CLK)							
Word 5																																			
31	30	29	28	27	26	25	24	23	22	21	20	19	18	17	16	15	14	13	12	11	10	9	8	7	6	5	4	3	2	1	0				
1	1	1	0	0	0	0	0	Checksum																											

Figure A.8: The TLB trigger data structure. [103]

(TAV), deatime veto counter, busy veto counter, rate limiter veto counter, BCR veto counter and digitizer busy counter. Data is then terminated by the trailer containing 24-bits Fletcher's checksum.



List of Acronyms

ALP	Axion Like Particle
ATLAS	A Toroidal LHC Aparatus
BCR	Bunch Counter Reset
BDT	Boosted Decision Tree
BSM	Beyond Standard Model
CLs	Confidence Levels
CR	control region
CRC	Cyclic Redundancy Check
CSC	Cathode-Strip Chambers
CTP	Central Tigger Processor
DAQ	Data Acquisition System
DCS	Detector Control System
eFEX	electron Feature Extractor
FASER	Forward Search Experiment
FEX	Feature Extractor
gFEX	global Feature Extractor
GPIO (board)	General Purpose Input-Output board
HLT	High Level Trigger

HNL	heavy neutral lepton
IBL	Insertable B-Layer
ID	Inner Detector
IP	Interaction Point
jFEX	jet Feature Extractor
JVT	Jet Vertex Tagger
LAr	Liquid Argon
LEP	Large Electron–Positron Collider
LHC	Large Hadron Collider
LLP	Long-lived particle
LO	Leading Order
LS	Long Shutdown
LSP	lightest supersymmetric particle
LUT	Lookup table
MDT	Monitor Drift Tube chamber
MET	Missing transverse momentum; E_T^{miss}
MS	Muon Spectrometer
MSSM	Minimal Supersymmetric Standard Model
NLO	Next-to-Leading Order
NSW	New Small Wheel
PDF	Probability Density Function
PFlow	Particle Flow
PFO	Particle Flow Object
PMT	Photomultiplier tube
<i>pp</i>	proton – proton
QCD	quantum chromodynamics
ROB	Read-Out Buffer
RoI	Region of Interest

RPC	Resistive Plate Chambers
SCT	Semiconductor Tracker
SM	Standard Model
SPS	Super Proton Synchrotron
SR	signal region
SUSY	Supersymmetry
TDAQ	Trigger and Data Acquisition System
TGC	Thin Gap Chambers
TIM (board)	Tracker Interlock and Monitoring Board
TLB	Trigger Logic Board
TRB	Tracker Readout Board
VR	validation region



Bibliography

- [1] Baron Kelvin, William Thomson. Baltimore lectures on molecular dynamics and the wave theory of light, 1904.
- [2] Andrew Purcell. Go on a particle quest at the first CERN webfest. Le premier webfest du CERN se lance à la conquête des particules. (35/2012):10, 2012. <https://cds.cern.ch/record/1473657>.
- [3] S. Navas et al. Review of particle physics. *Phys. Rev. D*, 110(3):030001, 2024. <https://doi.org/10.1103/PhysRevD.110.030001>.
- [4] D. Griffiths. *Introduction to Elementary Particles*. John Wiley and Sons, New York, USA, 1987.
- [5] John Ellis. Higgs physics. 2013. <https://arxiv.org/abs/1312.5672>.
- [6] J Goldstone. Field theories with "superconductor" solutions. *Nuovo Cimento*, 19:154–164, 1961. <https://cds.cern.ch/record/343400>.
- [7] Yoichiro Nambu. Quasi-particles and gauge invariance in the theory of superconductivity. *Phys. Rev.*, 117:648–663, Feb 1960. <https://link.aps.org/doi/10.1103/PhysRev.117.648>.
- [8] V. A. Bednyakov, N. D. Giokaris, and A. V. Bednyakov. On the Higgs mass generation mechanism in the Standard Model. *Physics of Particles and Nuclei*, 39(1):13–36, January 2008. <http://dx.doi.org/10.1134/S1063779608010024>.
- [9] ATLAS Collaboration . Summary plots from the ATLAS Standard Model physics group. <https://atlas.web.cern.ch/Atlas/GROUPS/PHYSICS/CombinedSummaryPlots/SM/index.html>.

-
- [10] J. S. Farnes. A unifying theory of dark energy and dark matter: Negative masses and matter creation within a modified λ cdm framework. *Astronomy and Astrophysics*, 620:A92, December 2018. <http://dx.doi.org/10.1051/0004-6361/201832898>.
- [11] Akitaka Ariga et al. (FASER Collaboration). FASER’s physics reach for long-lived particles. *Phys. Rev. D*, 99, May 2019.
- [12] STEPHEN P. MARTIN. *A SUPERSYMMETRY PRIMER*, pages 1–98. WORLD SCIENTIFIC, July 1998.
- [13] Jonathan L. Feng, Iftah Galon, Felix Kling, and Sebastian Trojanowski. Forward search experiment at the lhc. *Physical Review D*, 97(3), February 2018. <http://dx.doi.org/10.1103/PhysRevD.97.035001>.
- [14] Jonathan L. Feng, Iftah Galon, Felix Kling, and Sebastian Trojanowski. Axionlike particles at FASER: The LHC as a photon beam dump. *Physical Review D*, 98(5), September 2018. <http://dx.doi.org/10.1103/PhysRevD.98.055021>.
- [15] CERN. How an accelerator works, 2021. <https://home.cern/science/accelerators/how-accelerator-works>.
- [16] E. Mobs. The CERN accelerator complex. Complexe des accélérateurs du CERN, July 2019. <https://cds.cern.ch/record/2684277>.
- [17] Jacques Gareyte. LHC main parameters. *Part. Accel.*, 50, 1995.
- [18] Public ATLAS Luminosity Results for Run-3 of the LHC, 2024. <https://twiki.cern.ch/twiki/bin/view/AtlasPublic/LuminosityPublicResultsRun3>.
- [19] ATLAS Collaboration. The ATLAS Experiment at the CERN Large Hadron Collider. *Journal of Instrumentation*, 3(08):S08003–S08003, August 2008.
- [20] ATLAS. <https://public-archive.web.cern.ch/en/LHC/ATLAS-en.html>.
- [21] Takubo Yosuke, editor. *ATLAS IBL operational experience*. The ATLAS collaboration, 2016. <https://cds.cern.ch/record/2235541/files/ATL-INDET-PROC-2016-012.pdf>.
- [22] Experiment Briefing: Keeping the ATLAS Inner Detector in perfect alignment, 2020. <https://cds.cern.ch/record/2723878>.
- [23] The Inner Detector. <https://atlas.cern/Discover/Detector/Inner-Detector>.
- [24] ATLAS Collaboration. Performance of the electronic readout of the ATLAS liquid argon calorimeters. *JINST*, 5, September 2010.

- [25] Maximilien Brice. Installing the ATLAS calorimeter. vue centrale du détecteur ATLAS avec ses huit toroïdes entourant le calorimètre avant son déplacement au centre du détecteur. <https://cds.cern.ch/record/910381>.
- [26] T. Kawamoto et al. New Small Wheel Technical Design Report. 6 2013. <https://cds.cern.ch/record/1552862/>.
- [27] Nir Amram. *Hough Transform Track Reconstruction in the Cathode Strip Chambers in ATLAS*. PhD thesis, Tel Aviv University, 2008.
- [28] ATLAS Collaboration. The ATLAS Trigger System for LHC Run 3 and Trigger performance in 2022. *JINST*, 19, 2024. <https://doi.org/10.1088/1748-0221/19/06/P0602>.
- [29] ATLAS Collaboration. Athena, April 2019. <https://doi.org/10.5281/zenodo.2641997>.
- [30] ATLAS Collaboration. Performance of the reconstruction of large impact parameter tracks in the Inner Detector of ATLAS. ATL-PHYS-PUB-2017-014, 2017. <https://cds.cern.ch/record/2275635>.
- [31] ATLAS Collaboration. Performance of the ATLAS Silicon Pattern Recognition Algorithm in Data and Simulation at $\sqrt{s} = 7$ TeV. ATLAS-CONF-2010-072, 2010. <https://cds.cern.ch/record/1281363>.
- [32] ATLAS Collaboration. Performance of primary vertex reconstruction in proton–proton collisions at $\sqrt{s} = 7$ TeV in the ATLAS experiment. ATLAS-CONF-2010-069, 2010. <https://cds.cern.ch/record/1281344>.
- [33] ATLAS Collaboration. Performance of the reconstruction of large impact parameter tracks in the inner detector of atlas. *The European Physical Journal C*, 83(11), November 2023. <http://dx.doi.org/10.1140/epjc/s10052-023-12024-6>.
- [34] ATLAS Collaboration. Software Performance of the ATLAS Track Reconstruction for LHC Run 3. ATL-PHYS-PUB-2021-012, 2021. <https://cds.cern.ch/record/2766886>.
- [35] ATLAS Collaboration. The ATLAS Trigger System for LHC Run 3 and Trigger performance in 2022, 2024.
- [36] ATLAS Collaboration. Topological cell clustering in the ATLAS calorimeters and its performance in LHC Run 1. *The European Physical Journal C*, 77(7), jul 2017. <http://dx.doi.org/10.1140/epjc/s10052-017-5004-5>.
- [37] ATLAS Collaboration. Jet reconstruction and performance using Particle Flow with the ATLAS Detector. *The European Physical Journal C*, 77(7), jul 2017. <http://dx.doi.org/10.1140/epjc/s10052-017-5031-2>.

-
- [38] ATLAS Collaboration. Performance of the ATLAS Inner Detector Track and Vertex Reconstruction in the High Pile-Up LHC Environment. ATLAS-CONF-2012-042, 2012. <https://cds.cern.ch/record/1435196>.
 - [39] ATLAS Collaboration. $R = 0.4$ jets input comparison and Monte Carlo calibration with the ATLAS Detector. ATL-PHYS-PUB-2022-038, 2022. <https://cds.cern.ch/record/2824558>.
 - [40] ATLAS Collaboration. Topological cell clustering in the ATLAS calorimeters and its performance in LHC Run 1. *The European Physical Journal C*, 77(7), jul 2017. <http://dx.doi.org/10.1140/epjc/s10052-017-5004-5>.
 - [41] ATLAS Collaboration. The performance of missing transverse momentum reconstruction and its significance with the atlas detector using 140 fb^{-1} of $\sqrt{s} = 13 \text{ tev}$ pp collisions, 2024. <https://arxiv.org/abs/2402.05858>.
 - [42] Matteo Cacciari, Gavin P Salam, and Gregory Soyez. The anti-ktjet clustering algorithm. *Journal of High Energy Physics*, 2008(04):063–063, April 2008. <http://dx.doi.org/10.1088/1126-6708/2008/04/063>.
 - [43] S Catani, Yu L Dokshitzer, Michael H Seymour, and Bryan R Webber. Longitudinally-invariant k_{\perp} -clustering algorithms for hadron-hadron collisions. *Nucl. Phys. B*, 406:187–224, 1993. <https://cds.cern.ch/record/246812>.
 - [44] ATLAS Collaboration. Jet energy scale and resolution measured in proton–proton collisions at $\sqrt{s} = 13 \text{ TeV}$ with the ATLAS detector. *Eur. Phys. J. C*, 81:689, 2021. <https://doi.org/10.1140/epjc/s10052-021-09402-3>.
 - [45] ATLAS Collaboration . Public Jet Trigger Plots for Collision Data. https://twiki.cern.ch/twiki/bin/view/AtlasPublic/JetTriggerPublicResults#2022_pp_data.
 - [46] ATLAS Collaboration. Fast b-tagging at the high-level trigger of the ATLAS experiment in LHC Run 3. *Journal of Instrumentation*, 18(11):P11006, nov 2023. <https://dx.doi.org/10.1088/1748-0221/18/11/P11006>.
 - [47] ATLAS Collaboration . Jet Flavour Tagging With GN1 and DL1d. Generator dependence, Run 2 and Run 3 data agreement studies. <https://atlas.web.cern.ch/Atlas/GROUPS/PHYSICS/PLOTS/FTAG-2023-01/>.
 - [48] ATLAS Collaboration. Electron and photon performance measurements with the ATLAS detector using the 2015–2017 LHC proton-proton collision data. *Journal of Instrumentation*, 14(12):P12006–P12006, December 2019. <http://dx.doi.org/10.1088/1748-0221/14/12/P12006>.

- [49] ATLAS Collaboration. Muon reconstruction performance of the atlas detector in proton–proton collision data at $\sqrt{s} = 13$ tev. *The European Physical Journal C*, 76(5), May 2016. <http://dx.doi.org/10.1140/epjc/s10052-016-4120-y>.
- [50] ATLAS Collaboration. Reconstruction of hadronic decay products of tau leptons with the atlas experiment. *The European Physical Journal C*, 76(5), May 2016. <http://dx.doi.org/10.1140/epjc/s10052-016-4110-0>.
- [51] Reconstruction, Identification, and Calibration of hadronically decaying tau leptons with the ATLAS detector for the LHC Run 3 and reprocessed Run 2 data. Technical report, CERN, Geneva, 2022. <https://cds.cern.ch/record/2827111>.
- [52] ATLAS Collaboration. Performance of algorithms that reconstruct missing transverse momentum in $\sqrt{s} = 8$ TeV proton–proton collisions in the ATLAS detector. online. <https://arxiv.org/abs/1609.09324>.
- [53] Tagging and suppression of pileup jets with the ATLAS detector. Technical report, CERN, Geneva, 2014. <https://cds.cern.ch/record/1700870>.
- [54] ATLAS Collaboration. The performance of missing transverse momentum reconstruction and its significance with the atlas detector using 140 fb^{-1} of $\sqrt{s} = 13$ tev pp collisions, 2024. <https://arxiv.org/abs/2402.05858>.
- [55] E Lund, L Bugge, I Gavrilenko, and A Strandlie. Track parameter propagation through the application of a new adaptive Runge-Kutta-Nystrom method in the ATLAS experiment. *JINST*, 4:P04001, 2009. <https://cds.cern.ch/record/1113528>.
- [56] H.H.J. ten Kate. The ATLAS superconducting magnet system at the Large Hadron Collider. *Physica C: Superconductivity*, 468:2137–2142, September 2008.
- [57] E Lund, L Bugge, I Gavrilenko, and A Strandlie. Transport of covariance matrices in the inhomogeneous magnetic field of the ATLAS experiment by the application of a semi-analytical method. *JINST*, 4:P04016, 2009. <https://cds.cern.ch/record/1114177>.
- [58] The ATLAS Inner Detector Trigger performance in pp collisions at 900 GeV and 13.6 TeV for LHC Run 3 operation during 2022. Technical report, CERN, Geneva, 2023. <https://cds.cern.ch/record/2881679>.
- [59] S. S. Wilks. The large-sample distribution of the likelihood ratio for testing composite hypotheses. *The Annals of Mathematical Statistics*, 9(1):60–62, 1938. <http://www.jstor.org/stable/2957648>.

-
- [60] ATLAS Collaboration. Search for squarks and gluinos in final states with jets and missing transverse momentum at $\sqrt{s} = 13$ TeV with the ATLAS detector. ATLAS-CONF-2015-062, 2015. <https://cds.cern.ch/record/2114828>.
- [61] ATLAS Collaboration. Search for squarks and gluinos in final states with same-sign leptons and jets using 139 fb^{-1} of data collected with the ATLAS detector. ATLAS-CONF-2019-015, 2019. <https://cds.cern.ch/record/2676590>.
- [62] ATLAS Collaboration. Search for pair production of higgsinos in events with two higgs bosons and missing transverse momentum in $\sqrt{s} = 13$ TeV pp collisions at the atlas experiment. *Phys. Rev. D*, 109:112011, Jun 2024. <https://link.aps.org/doi/10.1103/PhysRevD.109.112011>.
- [63] G.F. Giudice and R. Rattazzi. Theories with gauge-mediated supersymmetry breaking. *Physics Reports*, 322(6):419–499, December 1999. [http://dx.doi.org/10.1016/S0370-1573\(99\)00042-3](http://dx.doi.org/10.1016/S0370-1573(99)00042-3).
- [64] ATLAS Collaboration. Electron efficiency measurements with the atlas detector using 2012 lh proton–proton collision data. *The European Physical Journal C*, 77(3), March 2017. <http://dx.doi.org/10.1140/epjc/s10052-017-4756-2>.
- [65] ATLAS Collaboration. Object-based missing transverse momentum significance in the ATLAS Detector. ATLAS-CONF-2018-038, 2018. <https://cds.cern.ch/record/2630948>.
- [66] W. Beenakker et al. Squark and gluino hadroproduction. *Int. J. Mod. Phys. A*, 26:2637–2664, 2011. <https://doi.org/10.1142/S0217751X11053560>.
- [67] W. Beenakker et al. Soft-gluon resummation for squark and gluino hadroproduction. *J. High Energy Phys.*, 0912:041, 2009. <https://doi.org/10.1088/1126-6708/2009/12/041>.
- [68] A. Kulesza and L. Motyka. Soft gluon resummation for the production of gluino-gluino and squark-antisquark pairs at the LHC. *Phys. Rev. D*, 80:095004, 2009. <https://doi.org/10.1103/PhysRevD.80.095004>.
- [69] A. Kulesza and L. Motyka. Threshold resummation for squark-antisquark and gluino-pair production at the LHC. *Phys. Rev. Lett.*, 102:111802, 2009. <https://doi.org/10.1103/PhysRevLett.102.111802>.
- [70] W. Beenakker et al. Squark and gluino production at hadron colliders. *Nucl. Phys. B*, 492:51–103, 1997. [https://doi.org/10.1016/S0550-3213\(97\)00084-9](https://doi.org/10.1016/S0550-3213(97)00084-9).

- [71] Jon Butterworth et al. PDF4LHC recommendations for LHC Run II. *J. Phys.*, G43:023001, 2016. <https://doi.org/10.1088/0954-3899/43/2/023001>.
- [72] P. Kant, O. M. Kind, T. Kintscher, T. Lohse, T. Martini, S. Mölbitz, P. Rieck, and P. Uwer. HatHor for single top-quark production: Updated predictions and uncertainty estimates for single top-quark production in hadronic collisions. *Comput. Phys. Commun.*, 191:74–89, 2015. <https://doi.org/10.1016/j.cpc.2015.02.001>.
- [73] Nikolaos Kidonakis. NNLL resummation for s-channel single top quark production. *Phys. Rev. D*, 81:054028, 2010. <https://doi.org/10.1103/PhysRevD.81.054028>.
- [74] Michal Czakon and Alexander Mitov. Top++: A Program for the Calculation of the Top-Pair Cross-Section at Hadron Colliders. *Comput. Phys. Commun.*, 185:2930, 2014. <https://doi.org/10.1016/j.cpc.2014.06.021>.
- [75] J. Alwall, R. Frederix, S. Frixione, V. Hirschi, F. Maltoni, O. Mattelaer, H. S. Shao, T. Stelzer, P. Torrielli, and M. Zaro. The automated computation of tree-level and next-to-leading order differential cross sections, and their matching to parton shower simulations. *JHEP*, 07:079, 2014. [https://doi.org/10.1007/JHEP07\(2014\)079](https://doi.org/10.1007/JHEP07(2014)079).
- [76] S Heinemeyer et al. Handbook of LHC Higgs Cross Sections: 3. Higgs Properties: Report of the LHC Higgs Cross Section Working Group. (arXiv:1307.1347. CERN-2013-004), 2013. <https://cds.cern.ch/record/1559921>.
- [77] T. Gleisberg et al. Event generation with SHERPA 1.1. *JHEP*, 02:007, 2009. <https://doi.org/10.1088/1126-6708/2009/02/007>.
- [78] Stefan Höche, Frank Krauss, Marek Schönherr, and Frank Siegert. QCD matrix elements + parton showers: The NLO case. *JHEP*, 04:027, 2013. [https://doi.org/10.1007/JHEP04\(2013\)027](https://doi.org/10.1007/JHEP04(2013)027).
- [79] Stefano Catani, Leandro Cieri, Giancarlo Ferrera, Daniel de Florian, and Massimiliano Grazzini. Vector boson production at hadron colliders: a fully exclusive QCD calculation at NNLO. *Phys. Rev. Lett.*, 103:082001, 2009. <https://doi.org/10.1103/PhysRevLett.103.082001>.
- [80] M. Bisset, N. Kersting, J. Li, F. Moortgat, S. Moretti, and Q. L. Xie. Pair-produced heavy particle topologies: MSSM neutralino properties at the LHC from gluino/squark cascade decays. *The European Physical Journal C - Particles and Fields*, 45(2):477–492, 2006. <https://doi.org/10.1140/epjc/s2005-02433-4>.

-
- [81] ATLAS Collaboration. ATLAS Pythia 8 tunes to 7 TeV data. ATL-PHYS-PUB-2014-021, 2014. <https://cds.cern.ch/record/1966419>.
- [82] ATLAS Collaboration. Search for charginos and neutralinos in final states with two boosted hadronically decaying bosons and missing transverse momentum in pp collisions at $\sqrt{s} = 13$ TeV with the atlas detector. *Phys. Rev. D*, 104:112010, Dec 2021. <https://link.aps.org/doi/10.1103/PhysRevD.104.112010>.
- [83] Michael Duerr, Felix Kahlhoefer, Kai Schmidt-Hoberg, Thomas Schwetz, and Stefan Vogl. How to save the WIMP: global analysis of a dark matter model with two s-channel mediators. *Journal of High Energy Physics*, 2016(9), 9 2016. <https://doi.org/10.1007/2Fjhep09%282016%29042>.
- [84] RECAST framework reinterpretation of an ATLAS Dark Matter Search constraining a model of a dark Higgs boson decaying to two b -quarks. Technical report, CERN, Geneva, 2019. <https://cds.cern.ch/record/2686290>.
- [85] Georges Aad, Brad Abbott, and Dale Charles Abbott. Search for dark matter produced in association with a dark Higgs boson decaying into $W^\pm W^\mp$ or ZZ in fully hadronic final states from $\sqrt{s} = 13$ TeV pp collisions recorded with the ATLAS detector. *Phys. Rev. Lett.*, 126:121802, 2021. <https://cds.cern.ch/record/2741385>.
- [86] ATLAS Collaboration. Search for dark matter produced in association with a dark Higgs boson decaying into W^+W^- in the one-lepton final state at $\sqrt{s}=13$ TeV using 139 fb $^{-1}$ of pp collisions recorded with the ATLAS detector, 2022. <https://doi.org/10.1007/JHEP07%282023%29116>.
- [87] Kyle Cranmer and Itay Yavin. Recast — extending the impact of existing analyses. *JHEP 1104:038,2011*, April 2011. <https://arxiv.org/abs/1010.2506>.
- [88] L. Heinrich K. Cranmer. Yadage and packtivity – analysis preservation using parametrized workflows. 2017. <https://arxiv.org/abs/1706.01878>.
- [89] Yadage. <https://github.com/yadage/yadage>.
- [90] JSON Schema, 2024. <https://json-schema.org/>.
- [91] L. Heinrich K. Cranmer. Analysis Preservation and Systematic Reinterpretation within the ATLAS experiment. *J. Phys: Conf. Ser.*, 1085(4), 2018. <https://iopscience.iop.org/article/10.1088/1742-6596/1085/4/042011>.
- [92] REANA documentation website. <https://docs.reana.io/>.

- [93] M. Baak, G. J. Besjes, D. Cote, A. Koutsman, J. Lorenz, and D. Short. Histfitter software framework for statistical data analysis. *The European Physical Journal C*, 75(4), April 2015. <http://dx.doi.org/10.1140/epjc/s10052-015-3327-7>.
- [94] Lukas Heinrich, Matthew Feickert, and Giordon Stark. pyhf: v0.7.6. <https://github.com/scikit-hep/pyhf/releases/tag/v0.7.6>.
- [95] Lukas Heinrich, Matthew Feickert, Giordon Stark, and Kyle Cranmer. pyhf: pure-python implementation of histfactory statistical models. *Journal of Open Source Software*, 6(58):2823, 2021. <https://doi.org/10.21105/joss.02823>.
- [96] Kyle Cranmer, George Lewis, Lorenzo Moneta, Akira Shibata, and Wouter Verkerke. HistFactory: A tool for creating statistical models for use with RooFit and RooStats. Technical report, New York U., New York, 2012. <https://cds.cern.ch/record/1456844>.
- [97] Jonathan L. Feng, Iftah Galon, Felix Kling and Sebastian Trojanowski. ForwArd Search ExpeRiment at the LHC. *Phys. Rev. D*, 95, February 2018. <https://doi.org/10.1103/PhysRevD.97.035001>.
- [98] FASER Collaboration. The FASER Detector. *JINST*, 19, May 2024. <https://doi.org/10.1088/1748-0221/19/05/P05066>.
- [99] FASER Collaboration. The tracking detector of the FASER experiment. *Nucl. Instrum. Meth. A*, 1034, 2022. <https://doi.org/10.1016/j.nima.2022.166825>.
- [100] FASER Collaboration. Technical Proposal: FASERnu. January 2020. <https://doi.org/10.48550/arXiv.2001.03073>.
- [101] FASER Collaboration. The trigger and data acquisition system of the FASER experiment. *JINST*, 16, 2021. <https://doi.org/10.1088/1748-0221/16/12/P12028>.
- [102] M. Boretto, W. Brylinski, G. Lehmann Miotto, E. Gamberini, R. Sipos, and V. V. Sonesten. DAQling: an open-source data acquisition framework. *EPJ Web Conf.*, 245, 2020.
- [103] Yannick Favre. Technical specification for the UniGe GPIO board.
- [104] S. Agostinelli et al. Geant4—a simulation toolkit. *Nuclear Instruments and Methods in Physics Research Section A: Accelerators, Spectrometers, Detectors and Associated Equipment*, 506(3):250–303, 2003. [https://doi.org/10.1016/S0168-9002\(03\)01368-8](https://doi.org/10.1016/S0168-9002(03)01368-8).
- [105] FASER Collaboration. Search for dark photons with the FASER detector at the LHC. *Physics Letters B*, 848:138378, 2024. <https://doi.org/10.1016/j.physletb.2023.138378>.

- [106] FASER Collaboration. First direct observation of collider neutrinos with faser at the lhc. *Physical Review Letters*, 131(3), July 2023. <http://dx.doi.org/10.1103/PhysRevLett.131.031801>.
- [107] Jamie Boyd. The FASER W-Si High Precision Preshower Technical Proposal. 2022. <https://cds.cern.ch/record/2803084>.
- [108] Jonathan L Feng, Felix Kling, Mary Reno, and et. al. The forward physics facility at the high-luminosity lhc. *Journal of Physics G: Nuclear and Particle Physics*, 50(3):030501, January 2023. <http://dx.doi.org/10.1088/1361-6471/ac865e>.